# Evaluation of Millimetre-wave Coherent Scattering from a Sea Surface covered by Foam modelled as Sequences of Thin Phase-Scattering Screens using Split-Step Fourier Method

Ayibapreye Kelvin Benjamin

A thesis submitted for the degree of *Doctor of Philosophy*

School of Computer Science and Electronic Engineering

University of Essex

Date of Submission: Tuesday 23rd July, 2019

# DEDICATION

**To my late elder brother Kingley Ayibaemi Benjamin and best friend**
**Uzoamaka Wisdom Osuji**

# ABSTRACT

This research focused on developing a physical based model of foam covered sea surface as air-bubble coated with thin layers of seawater, that is suitable for investigation of millimetre wave coherent scattering. The propagation media was described as a flat sea-surface covered by foam and modelled as sequences of thin and deep phase scattering screens. The propagation media is a dense random media which comprise randomly distributed air-bubbles that follow a log-normal distribution pattern. The log-normal distribution is a skewed distribution with low geometric mean and large variance which can not be negative but cut-off at zero. The log-normal distribution is a good candidate for modelling random variability from the multiplicative version of the central limit theorem, which proves that many independent, positive random variables are approximately log-normal. The locations and bubble radii of the air-bubbles were described by uniform random numbers. To obtain the bubble size distribution (BSD) and bubble radii the uniform random variate was transformed to normal variate by computing the error function, complementary error function and cumulative error function. The probability density function (PDF) of the inverse error function was obtained by Newton's method. We estimated the BSD and bubble radii by assuming a geometric mean $\mu_g = 500\mu m$ and geometric standard deviation $\sigma_g = 2.0$. Three dimensional ($3D$) sphere packing approach was implemented for filling the air-bubbles in a cubic domain as we assumed that the air-bubbles are spherical in shape. There was need to avoid two adjacent spheres overlapping to ensure efficient packing density. The $3D$ packed spheres were converted to $2D$ slices of annuli with the outer circle being a thin layer of seawater and the inner circle $80-95\%$ air. The model of sea foam accounts for its mechanical and optical properties which comprises of foam layer thickness, bubble size distribution, foam void fraction, bubble radius, refractive index, sea surface temperature etc. Sea surface roughness and wind speed are physical processes which are significant in evaluation of the sea surface emissivity which helps in measuring brightness temperature of the sea. The split-step Fourier method was adopted as a marching technique well suited for evaluation of the refraction and diffraction effects of scattered millimetre wave due to its interaction with five (5) $2D$ slices of sea foam layer. Results obtained from the split-step Fourier method represent the angular spectrum as a distorted wavefront and field intensity at the sea surface after forward and backward propagation for thin and deep phase screens. The attenuation in $dB$ and specific attenuation (dB/mm) for incident angles $\theta_i = 30°, 45°$ and $60°$ with $\phi = 0°$ for thin and deep phase screens at various WindSat frequencies 6.8 $GHz$, 10.7 $GHz$, 18.7 $GHz$, 23.8 $GHz$ and 37 $GHz$ are presented. Diffuse scattering is a major attenuation factor for thin phase screen at moderate frequencies while absorption is dominant at high frequencies for deep phase screens.

# Acknowledgements

My sincere gratitude goes to Almighty God and everyone who contributed in various ways to my completion of this PhD thesis.

Special thanks goes to my supervisor David H.O. Bebbington for giving me the opportunity to work with him and gave me the guidance and direction to explore Electromagnetic propagation and scattering by random media and modelling of these media through numerical computations using FORTRAN compiler. He introduced me to the field of remote sensing and use of FORTRAN computation software in modelling Electromagnetic propagation problems. I am very grateful to you for accepting me as your PhD student.

My special gratitude goes to Felix Ngobigha for helping in setting down at the University of Essex. He was always there in time of need and never stopped encouraging and motivating me. I deeply appreciate your guidance and support. My gratitude also goes to Mrs Ngobigha for her hospitality and support.

I am very grateful to my lovely wife Mrs Benjamin Bienumugha Confidence for her support and understanding. She has always been beside me through this journey. She played a significant role in ensuring that I never gave up during the toughest moments of my PhD adventure.

Finally, my thanks goes to Pastor John Ogbuagu and his wife Mrs Chrissy Ogbuagu. Many thanks to Deaconess Loveth, PTDF for sponsoring me, Olali Princewill, Dr Collins Ouserigha, Jewad Shaker, My mother and father, the staff of computer science and electronic engineering that have suported me in one way or the other.

# CONTENTS

**Abstract** **ii**

**Acknowledgements** **iv**

**Acronyms** **x**

**List of Figures** **xii**

**List of Tables** **xxxi**

**1 Introduction** **1**

1.1 Why PWE models? . . . . . . . . . . . . . . . . . . . . . . . . . . . . . . 6

1.2 Research Motivation . . . . . . . . . . . . . . . . . . . . . . . . . . . . 6

**2 Background and Literature Review** **10**

2.1 Overview of Ocean Remote Sensing . . . . . . . . . . . . . . . . . . . . . . 10

2.1.1 Introduction . . . . . . . . . . 10

2.2 Remote Sensing . . . . . . . . . . 13

2.2.1 Passive Remote Sensing . . . . . . . . . . 14

2.2.2 Active Remote Sensing . . . . . . . . . . 15

2.3 Polarimetry . . . . . . . . . . 15

2.4 Vertical and Horizontal Polarization . . . . . . . . . . 16

2.5 Boundary Conditions by Fresnel's Equation . . . . . . . . . . 18

2.5.1 Single and Multiple scattering . . . . . . . . . . 20

2.5.2 Fluctuating Fields . . . . . . . . . . 20

2.5.3 Elastic and Inelastic Scattering . . . . . . . . . . 21

2.5.4 Propagation Media Characteristics . . . . . . . . . . 21

2.5.5 Conductivity . . . . . . . . . . 22

2.5.6 Dielectric Constant and Refractive index . . . . . . . . . . 22

2.5.7 Permeability . . . . . . . . . . 23

2.5.8 Lossless and Lossy Media . . . . . . . . . . 23

2.5.9 Scattering Parameters . . . . . . . . . . 24

2.6 Formation of Oceanic Foams . . . . . . . . . . 27

2.6.1 Sea Foam Formation . . . . . . . . . . 27

2.7 Significant Ocean Parameters . . . . . . . . . . 28

2.8 Sea Surface Temperature (SST) . . . . . . . . . . 29

2.9 Salinity . . . . . . . . . . 29

2.10 Brightness Temperature . . . . . . . . . . 30

2.11 Review of Dielectric Constant of Sea Foam at Microwave Frequency . . . . . 31

2.12 Modelling of Sea Foam using Effective Medium Theories . . . . . . . . . . 34

2.12.1 Sea Foam Properties . . . . . . . . . . . . . . . . . . . . . . . . . . 35
2.12.2 Classical Mixing Rule . . . . . . . . . . . . . . . . . . . . . . . . . . 35
2.12.3 Maxwell Garnet's Method . . . . . . . . . . . . . . . . . . . . . . . . 36
2.12.4 Polder Van Santen (Bruggeman or De Loor) Formula . . . . . . . . . 39
2.13 Critical Review of Sea foam Dielectric Constant . . . . . . . . . . . . . 41
2.14 Summary . . . . . . . . . . . . . . . . . . . . . . . . . . . . . . . . . . 47

**3 Parabolic Wave Equation Method 49**

3.1 Problem Formulation . . . . . . . . . . . . . . . . . . . . . . . . . . . . 52
3.2 Derivation of the Parabolic Wave Equation . . . . . . . . . . . . . . . . 53
3.2.1 The Split Step Fourier Transform Solution . . . . . . . . . . . . . . 56
3.2.2 Two dimensional form of PE . . . . . . . . . . . . . . . . . . . . . . 58
3.2.3 Inhomogeneous Helmholtz Equation . . . . . . . . . . . . . . . . . . 59
3.3 Summary . . . . . . . . . . . . . . . . . . . . . . . . . . . . . . . . . . 63

**4 Seafoam Model Implementation 65**

4.1 Modelling of Sea-foam properties and shape . . . . . . . . . . . . . . . . 65
4.1.1 Introduction . . . . . . . . . . . . . . . . . . . . . . . . . . . . . . . 65
4.2 Random Sphere Packing Problem . . . . . . . . . . . . . . . . . . . . . . 68
4.3 Inverse Cumulative Distribution Method . . . . . . . . . . . . . . . . . . 70
4.4 Bubble Size Distribution and Bubble Radius . . . . . . . . . . . . . . . . 77
4.4.1 Foam Layer Thickness . . . . . . . . . . . . . . . . . . . . . . . . . . 78
4.4.2 Foam Void Fraction . . . . . . . . . . . . . . . . . . . . . . . . . . . 79
4.5 Sphere Packing Model and Implementation . . . . . . . . . . . . . . . . . 80
4.5.1 Non-linear Model . . . . . . . . . . . . . . . . . . . . . . . . . . . . . 81

4.5.2 Non-overlapping Constraints . . . . . . . . . . . . . . . . . . . . . 81

4.5.3 Bubble Placement and Three Spheres Intersection . . . . . . . . . . . 82

4.6 Summary . . . . . . . . . . . . . . . . . . . . . . . . . . . . . . . . 88

**5 Code implementation of Split-step Fourier Method 89**

5.1 Introduction . . . . . . . . . . . . . . . . . . . . . . . . . . . . . . 89

5.2 Investigative approach . . . . . . . . . . . . . . . . . . . . . . . . 90

5.2.1 SSFM Computation for Investigation of seafoam layer model . . . . . 93

5.2.2 Sea-foam Boundary Condition . . . . . . . . . . . . . . . . . . . . . 98

5.2.3 Phase Fluctuations in Thin Phase Scattering Screen at Low Windsat Frequencies and slice thicknessses . . . . . . . . . . . . . . . . . . 98

5.2.4 Phase Fluctuations in Deep Phase Scattering Screen at High Windsat Frequencies and slice thicknessses . . . . . . . . . . . . . . . . . . 106

5.3 Angular Spectrum of Backscattered E-fields at WindSat Frequencies . . . . . 114

5.4 Field Intensity $|E|^2$ at WindSat Frequencies . . . . . . . . . . . . . . . . 125

5.4.1 Attenuation of the Field Intensity in dB with Depth of Sea Foam at WindSat Frequencies . . . . . . . . . . . . . . . . . . . . . . . . . 134

5.5 Comparison of Simulated Emissivity of Sea Foam with Experimental Results 151

5.6 Comparison of Simulated Brightness Temperature of Sea Foam with Experimental Results . . . . . . . . . . . . . . . . . . . . . . . . . . . . . 156

5.7 Summary . . . . . . . . . . . . . . . . . . . . . . . . . . . . . . . . 160

**6 Conclusion and Further Work 161**

**Appendices 180**

**A Derivations 181**

A.1 Wide angle Split-step Algorithm . . . . . . . . . . . . . . . . . . . . . . . . . 181

**B Publications 185**

B.1 List OF Publications . . . . . . . . . . . . . . . . . . . . . . . . . . . . . . . 185

# ACRONYMS AND ABBREVIATIONS

BSD - Bubble Size Distribution

CDF - Cumulative Distribution Function

DDA - Discrete Dipole Approximation

EM - Electromagnetic

EMT - Effective Medium Theory

FCC - Face Centred Cubic

FD - Finite Difference

FE - Finite Element

FFTs - Fast Fourier Transforms

GUI - Graphical User Interface

MCM - Monte-Carlo Method

mmW - Millimetre wave

PDF - Probability Density Function

PE - Parabolic Equation

PEM - Parabolic Equation Method

PETOOL - Parabolic Equation Toolbox

PSD - Particle Size Distribution

PWE - Parabolic Wave Equation

SMOS - Soil Moisture Ocean Salinity

SPE - Standard Parabolic Equation

SSFM - Split-Step Fourier Method

SSFT - Split-Step Fourier Transform

SST - Sea Surface Temperature

TE - Transverse Electric

TM - Transverse Magnetic

VHF - Very High Frequency

W - Whitecap Fraction

# LIST OF FIGURES

2.1 Scattering with incident direction $(\theta_i, \phi_i)$ and scattered direction $(\theta_s, \phi_s)$. [1] 17

2.2 Sea Foam at Ocean Beach in San Francisco [2] . . . . . . . . . . . . . . . . . 28

2.3 Geometry of Sea-foam as a heterogeneous mixture of air, seawater and impurities 34

2.4 Bubble cluster of ellipsoidal inclusions in a dielectric base material . . . . . . 37

2.5 Showing Real Dielectric Constant for Maxwell Garnet's and Bruggeman's Model of Seawater . . . . . . . . . . . . . . . . . . . . . . . . . . . . . . 43

2.6 Showing Imaginary Dielectric Constant for Maxwell Garnet's and Bruggeman's Model of Seawater . . . . . . . . . . . . . . . . . . . . . . . . . . 44

2.7 Showing Real Dielectric Constant for Maxwell Garnet's and Bruggeman's Model of Seawater . . . . . . . . . . . . . . . . . . . . . . . . . . . . . . 45

2.8 Showing Imaginary Dielectric Constant for Maxwell Garnet's and Bruggeman's Model of Seawater . . . . . . . . . . . . . . . . . . . . . . . . . . 46

2.9 Variation of Dielectric Constant for Maxwell Garnet's and Bruggeman's Model of Seawater . . . . . . . . . . . . . . . . . . . . . . . . . . . . . . . . . . . . 46

4.1 Plot of the inverse error function against uniform random variate U(0,1). . . 75
4.2 Histogram of the PDF of Standard Normal Variate . . . . . . . . . . . . . 75
4.3 Histogram of PDF of Scaled Normal Variate . . . . . . . . . . . . . . . . . . . 75
4.4 Histogram of $N(r)$ against Bubble radii for $\sigma_g = 0.5$ . . . . . . . . . . . . . . 76
4.5 Histogram of $N(r)$ against Bubble radii for $\sigma_g = 0.2$ . . . . . . . . . . . . . . 76
4.6 Structure of Research Implementation . . . . . . . . . . . . . . . . . . . . 76
4.7 BSD $N(r)$ against Bubble radii for $\sigma_g = 2.0$ and $\mu_g = 500 microns$ . . . . . . 78
4.8 BSD $N(r)$ against Bubble radii . . . . . . . . . . . . . . . . . . . . . . . . 78
4.9 Two spheres cannot overlap if the distance between their centres is greater or equal to the sum of their radii . . . . . . . . . . . . . . . . . . . . . . . . . 82
4.10 Intersection of three spheres within a plane . . . . . . . . . . . . . . . . . . 83
4.11 Randomly packed spheres in slice 1 . . . . . . . . . . . . . . . . . . . . . . . 87
4.12 Randomly packed spheres in slice 2 . . . . . . . . . . . . . . . . . . . . . . . 87
4.13 Randomly packed spheres in slice 3 . . . . . . . . . . . . . . . . . . . . . . . 87
4.14 Randomly packed spheres in slice 4 . . . . . . . . . . . . . . . . . . . . . . . 87

5.1 Schematic of incident E-Field propagated through slices of sea foam layers . 90
5.2 Flowchat of Split-step Fourier Transform Algorithm . . . . . . . . . . . . . 92
5.3 The phase gradient of an incident plane wave for horizontal polarization (TE) with zenith $\theta_i = 30°$ and azimuth $\phi = 0°$ as a function of the spatial coordinates X and Y of the propagation media at 1.42 $GHz$. . . . . . . . . . . . . . . . . 100

5.4 The phase gradient of an incident plane wave for vertical polarization (TM) with zenith $\theta_i = 30°$ and azimuth $\phi = 0°$ as a function of the spatial coordinates X and Y of the propagation media at 1.42 $GHz$. . . . . . . . . . . . . . . . . 100

5.5 The phase gradient of an incident plane wave for horizontal polarization (TE) with zenith $\theta_i = 30°$ and azimuth $\phi = 45°$ as a function of the spatial coordinates X and Y of the propagation media at 1.42 $GHz$. . . . . . . . . . . . . 100

5.6 The phase gradient of an incident plane wave for vertical polarization (TM) with zenith $\theta_i = 30°$ and azimuth $\phi = 45°$ as a function of the spatial coordinates X and Y of the propagation media at 1.42 $GHz$. . . . . . . . . . . . . 100

5.7 The phase gradient of E-field in free space for horizontal polarization (TE) with zenith $\theta_i = 30°$ and azimuth $\phi = 0°$ as a function of the spatial coordinates X and Y of the propagation media at 6.8 $GHz$. . . . . . . . . . . . . . . . . . 101

5.8 The phase gradient of E-field in free space for vertical polarization (TM) with zenith $\theta_i = 30°$ and azimuth $\phi = 0°$ as a function of the spatial coordinates X and Y of the propagation media at 6.8 $GHz$. . . . . . . . . . . . . . . . . . 101

5.9 The phase gradient of an E-field in free space for horizontal polarization (TE) with zenith $\theta_i = 30°$ and azimuth $\phi = 45°$ as a function of the spatial coordinates X and Y of the propagation media at 6.8 $GHz$. . . . . . . . . . . . . 101

5.10 The phase gradient of E-field in free space for vertical polarization (TM) with zenith $\theta_i = 30°$ and azimuth $\phi = 45°$ as a function of the spatial coordinates X and Y of the propagation media at 6.8 $GHz$. . . . . . . . . . . . . . . . 101

5.11 The phase variation of E-field in free space for horizontal polarization (TE) with zenith $\theta_i = 30°$ and azimuth $\phi = 0°$ as a function of the spatial coordinates X and Y of the propagation media at 6.8 $GHz$, $\delta_t = 0.1$ $mm$. . . . . . . . . . 104

5.12 The phase variation of E-field in free space for vertical polarization (TM) with zenith $\theta_i = 30°$ and azimuth $\phi = 0°$ as a function of the spatial coordinates X and Y of the propagation media at 6.8 $GHz$, $\delta_t = 0.1$ $mm$. . . . . . . . . . . 104

5.13 The phase variation of E-field in slice 1 for horizontal polarization (TE) with zenith $\theta_i = 30°$ and azimuth $\phi = 0°$ as a function of the spatial coordinates X and Y of the propagation media at 6.8 $GHz$,$\delta_t = 0.1$ $mm$. . . . . . . . . . . 104

5.14 The phase variation of E-field in slice 1 for vertical polarization (TM) with zenith $\theta_i = 30°$ and azimuth $\phi = 0°$ as a function of the spatial coordinates X and Y of the propagation media at 6.8 $GHz$,$\delta_t = 0.1$ $mm$. . . . . . . . . . . 104

5.15 The phase variation of E-field in slice 2 for horizontal polarization (TE) with zenith $\theta_i = 30°$ and azimuth $\phi = 0°$ as a function of the spatial coordinates X and Y of the propagation media at 6.8 $GHz$,$\delta_t = 0.1$ $mm$. . . . . . . . . . . 105

5.16 The phase variation of E-field in slice 2 for vertical polarization (TM) with zenith $\theta_i = 30°$ and azimuth $\phi = 0°$ as a function of the spatial coordinates X and Y of the propagation media at 6.8 $GHz$,$\delta_t = 0.1$ $mm$. . . . . . . . . . . 105

5.17 The phase variation of E-field in slice 3 for horizontal polarization (TE) with zenith $\theta_i = 30°$ and azimuth $\phi = 0°$ as a function of the spatial coordinates X and Y of the propagation media at 6.8 $GHz$,$\delta_t = 0.1$ $mm$. . . . . . . . . . . 105

5.18 The phase variation of E-field in slice 3 for vertical polarization (TM) with zenith $\theta_i = 30°$ and azimuth $\phi = 0°$ as a function of the spatial coordinates X and Y of the propagation media at 6.8 $GHz$,$\delta_t = 0.1$ $mm$. . . . . . . . . . . 105

5.19 The phase variation of E-field in free space for horizontal polarization (TE) with zenith $\theta_i = 30°$ and azimuth $\phi = 45°$ as a function of the spatial coordinates X and Y of the propagation media at 23.8 $GHz$,$\delta_t = 2$ $mm$. . . . . . . 107

5.20 The phase variation of E-field in free space for vertical polarization (TM) with zenith $\theta_i = 30°$ and azimuth $\phi = 45°$ as a function of the spatial coordinates X and Y of the propagation media at 23.8 $GHz$ and $\delta_t = 2\ mm$. . . . . . . . 107

5.21 The phase variation of E-field in slice 1 for horizontal (TE) with zenith $\theta_i = 30°$ and azimuth $\phi = 45°$ as a function of the spatial coordinates X and Y of the propagation media at 23.8 $GHz$,$\delta_t = 2\ mm$. . . . . . . . . . . . . . . . . . . 107

5.22 The phase variation of E-field in slice 1 for vertical polarization (TM) with zenith $\theta_i = 30°$ and azimuth $\phi = 45°$ as a function of the spatial coordinates X and Y of the propagation media at 23.8 $GHz$,$\delta_t = 2\ mm$. . . . . . . . . . 107

5.23 The phase variation of E-field in slice 2 for horizontal polarization (TE) with zenith $\theta_i = 30°$ and azimuth $\phi = 45°$ as a function of the spatial coordinates X and Y of the propagation media at 23.8 $GHz$,$\delta_t = 2\ mm$. . . . . . . . . . 108

5.24 The phase variation of E-field in slice 2 for vertical polarization (TM) with zenith $\theta_i = 30°$ and azimuth $\phi = 45°$ as a function of the spatial coordinates X and Y of the propagation media at 23.8 $GHz$ and $\delta_t = 2\ mm$. . . . . . . . 108

5.25 The phase variation of E-field in slice 3 for horizontal (TE) with zenith $\theta_i = 30°$ and azimuth $\phi = 45°$ as a function of the spatial coordinates X and Y of the propagation media at 23.8 $GHz$,$\delta_t = 2\ mm$. . . . . . . . . . . . . . . . . . . 108

5.26 The phase variation of E-field in slice 3 for vertical polarization (TM) with zenith $\theta_i = 30°$ and azimuth $\phi = 45°$ as a function of the spatial coordinates X and Y of the propagation media at 23.8 $GHz$,$\delta_t = 2\ mm$. . . . . . . . . . 108

5.27 The phase variation of E-field in slice 4 for horizontal polarization (TE) with zenith $\theta_i = 30°$ and azimuth $\phi = 45°$ as a function of the spatial coordinates X and Y of the propagation media at 23.8 $GHz$,$\delta_t = 2\ mm$. . . . . . . . . . 109

5.28 The phase variation of E-field in slice 4 for vertical polarization (TM) with zenith $\theta_i = 30°$ and azimuth $\phi = 45°$ as a function of the spatial coordinates X and Y of the propagation media at 23.8 $GHz$ and $\delta_t = 2\ mm$. . . . . . . . 109

5.29 The phase variation of E-field in slice 5 for horizontal (TE) with zenith $\theta_i = 30°$ and azimuth $\phi = 45°$ as a function of the spatial coordinates X and Y of the propagation media at 23.8 $GHz$,$\delta_t = 2\ mm$. . . . . . . . . . . . . . . . . . . 109

5.30 The phase variation of E-field in slice 5 for vertical polarization (TM) with zenith $\theta_i = 30°$ and azimuth $\phi = 45°$ as a function of the spatial coordinates X and Y of the propagation media at 23.8 $GHz$,$\delta_t = 2\ mm$. . . . . . . . . . 109

5.31 The phase variation of E-field in free space for horizontal polarization (TE) with zenith $\theta_i = 30°$ and azimuth $\phi = 45°$ as a function of the spatial coordinates X and Y of the propagation media at 37 $GHz$ and $\delta_t = 2\ mm$. . . . . . 111

5.32 The phase variation of E-field in free space for vertical polarization (TM) with zenith $\theta_i = 30°$ and azimuth $\phi = 45°$ as a function of the spatial coordinates X and Y of the propagation media at 37 $GHz$ and $\delta_t = 2\ mm$. . . . . . . . . 111

5.33 The phase variation of E-field in slice 1 for horizontal (TE) with zenith $\theta_i = 30°$ and azimuth $\phi = 45°$ as a function of the spatial coordinates X and Y of the propagation media at 37 $GHz$, $\delta_t = 2\ mm$. . . . . . . . . . . . . . . . . . . 111

5.34 The phase variation of E-field in slice 1 for vertical polarization (TM) with zenith $\theta_i = 30°$ and azimuth $\phi = 45°$ as a function of the spatial coordinates X and Y of the propagation media at 37 $GHz$, $\delta_t = 2\ mm$. . . . . . . . . . . 111

5.35 The phase variation of E-field in slice 2 for horizontal polarization (TE) with zenith $\theta_i = 30°$ and azimuth $\phi = 45°$ as a function of the spatial coordinates X and Y of the propagation media at 37 $GHz$ and $\delta_t = 2\ mm$. . . . . . . . . 112

5.36 The phase variation of E-field in slice 2 for vertical polarization (TM) with zenith $\theta_i = 30°$ and azimuth $\phi = 45°$ as a function of the spatial coordinates X and Y of the propagation media at 37 $GHz$ and $\delta_t = 2\ mm$. . . . . . . . . 112

5.37 The phase variation of E-field in slice 3 for horizontal (TE) with zenith $\theta_i = 30°$ and azimuth $\phi = 45°$ as a function of the spatial coordinates X and Y of the propagation media at 37 $GHz$, $\delta_t = 2\ mm$. . . . . . . . . . . . . . . . . . . . 112

5.38 The phase variation of E-field in slice 3 for vertical polarization (TM) with zenith $\theta_i = 30°$ and azimuth $\phi = 45°$ as a function of the spatial coordinates X and Y of the propagation media at 37 $GHz$, $\delta_t = 2\ mm$. . . . . . . . . . . 112

5.39 The phase variation of E-field in slice 4 for horizontal polarization (TE) with zenith $\theta_i = 30°$ and azimuth $\phi = 45°$ as a function of the spatial coordinates X and Y of the propagation media at 37 $GHz$ and $\delta_t = 2\ mm$. . . . . . . . . 113

5.40 The phase variation of E-field in slice 4 for vertical polarization (TM) with zenith $\theta_i = 30°$ and azimuth $\phi = 45°$ as a function of the spatial coordinates X and Y of the propagation media at 37 $GHz$ and $\delta_t = 2\ mm$. . . . . . . . . 113

5.41 The phase variation of E-field in slice 5 for horizontal (TE) with zenith $\theta_i = 30°$ and azimuth $\phi = 45°$ as a function of the spatial coordinates X and Y of the propagation media at 37 $GHz$, $\delta_t = 2\ mm$. . . . . . . . . . . . . . . . . . . . 113

5.42 The phase variation of E-field in slice 5 for vertical polarization (TM) with zenith $\theta_i = 30°$ and azimuth $\phi = 45°$ as a function of the spatial coordinates X and Y of the propagation media at 37 $GHz$, $\delta_t = 2\ mm$. . . . . . . . . . . 113

5.43 Angular spectrum of diffused reflected wave field at $6.8GHz$ and $\delta_t = 0.1mm$ for TE polarization with effective dielectric constant of seawater $\epsilon_{sw} = 62.6425+j27.8729$ and foam void fraction $f_a = 0.8$ at constant $SST = 20^\circ$ and salinity $(34psu)$ for seed = 4. . . . . . . . . . . . . . . . . . . . . . . . . . . . . 114

5.44 Angular spectrum of diffused reflected wave field at $6.8GHz$ and $\delta_t = 0.1mm$ for TM polarization with effective dielectric constant of seawater $\epsilon_{sw} = 62.6425+j27.8729$ and foam void fraction $f_a = 0.8$ at constant $SST = 20^\circ$ and salinity $(34psu)$ for seed = 4. . . . . . . . . . . . . . . . . . . . . . . . . . . . . 114

5.45 Angular spectrum of diffused reflected wave field at 6.8 $GHz$ and $\delta_t = 0.1$ $mm$ for TE polarization with effective dielectric constant of seawater $\epsilon_{sw} = 62.6425 + j27.8729$ and foam void fraction $f_a = 0.8$ at constant $SST = 20^\circ$ and salinity $(34psu)$ for seed = 5 . . . . . . . . . . . . . . . . . . . . . . . 115

5.46 Angular spectrum of diffused reflected wave field at $6.8GHz$ and $\delta_t = 0.1$ $mm$ for TM polarization with effective dielectric constant of seawater $\epsilon_{sw} = 62.6425 + j27.8729$ and foam void fraction $f_a = 0.8$ at constant $SST = 20^\circ$ and salinity $(34psu)$ for seed = 5. . . . . . . . . . . . . . . . . . . . . . . . 115

5.47 Angular spectrum of diffused reflected wave field at 6.8 $GHz$ and $\delta_t = 0.2$ $mm$ for TE polarization with effective dielectric constant of seawater $\epsilon_{sw} = 62.6425 + j27.8729$ and foam void fraction $f_a = 0.8$ at constant $SST = 20^\circ$ and salinity $(34psu)$ . . . . . . . . . . . . . . . . . . . . . . . . . . . . . 116

5.48 Angular spectrum of diffused reflected wave field at $6.8GHz$ and $\delta_t = 0.2$ $mm$ for TM polarization with effective dielectric constant of seawater $\epsilon_{sw} = 62.6425 + j27.8729$ and foam void fraction $f_a = 0.8$ at constant $SST = 20^\circ$ and salinity $(34psu)$ . . . . . . . . . . . . . . . . . . . . . . . . . . . . . 116

5.49 Angular spectrum of diffused reflected wave field at 6.8 $GHz$ and $\delta_t = 2$ $mm$ for TE polarization with effective dielectric constant of seawater $\epsilon_{sw} = 62.6425 + j27.8729$ and foam void fraction $f_a = 0.8$ at constant $SST = 20^\circ$ and salinity $(34psu)$ . . . . . . . . . . . . . . . . . . . . . . . . . . . . . . 117

5.50 Angular spectrum of diffused reflected wave field at 6.8 $GHz$ and $\delta_t = 2$ $mm$ for TM polarization with effective dielectric constant of seawater $\epsilon_{sw} = 62.6425 + j27.8729$ and foam void fraction $f_a = 0.8$ at constant $SST = 20^\circ$ and salinity $(34psu)$ . . . . . . . . . . . . . . . . . . . . . . . . . . . . . . 117

5.51 Angular Spectrum of Diffused Reflected Wavefront at 10.7 $GHz$ and $\delta_t = 0.1$ $mm$ for TE polarization with effective dielectric constant of seawater $\epsilon_{sw} = 53.5604 + j32.8054$ and foam void fraction $f_a = 0.8$ at constant $SST = 20^\circ$ and salinity $(34psu)$. . . . . . . . . . . . . . . . . . . . . . . . . . . . . . 118

5.52 Angular Spectrum of Diffused Reflected Wavefront at 10.7 $GHz$ and $\delta_t = 0.1$ $mm$ for TM polarization with effective dielectric constant of seawater $\epsilon_{sw} = 53.5604 + j32.8054$ and foam void fraction $f_a = 0.8$ at constant $SST = 20^\circ$ and salinity $(34psu)$. . . . . . . . . . . . . . . . . . . . . . . . . . . . . . 118

5.53 Angular Spectrum of Diffused Reflected Wavefront at 10.7 $GHz$ and $\delta_t = 2$ $mm$ for TE polarization with effective dielectric constant of seawater $\epsilon_{sw} = 53.5604 + j32.8054$ and foam void fraction $f_a = 0.8$ at constant $SST = 20^\circ$ and salinity $(34psu)$. . . . . . . . . . . . . . . . . . . . . . . . . . . . . . 118

5.54 Angular Spectrum of Diffused Reflected Wavefront at 10.7 $GHz$ and $\delta_t = 2$ $mm$ for TM polarization with effective dielectric constant of seawater $\epsilon_{sw} = 53.5604 + j32.8054$ and foam void fraction $f_a = 0.8$ at constant $SST = 20^\circ$ and salinity $(34psu)$. . . . . . . . . . . . . . . . . . . . . . . . . . . . . . 118

5.55 Angular Spectrum of Diffused Reflected Wavefront at 18.7 $GHz$ and $\delta_t = 0.1$ $mm$ for TE polarization with effective dielectric constant of seawater $\epsilon_{sw} = 36.5500 + j34.9728$ and foam void fraction $f_a = 0.8$ at constant $SST = 20°$ and salinity ($34psu$). . . . . . . . . . . . . . . . . . . . . . . . . . . . . . 119

5.56 Angular Spectrum of Diffused Reflected Wavefront at 18.7 $GHz$ and $\delta_t = 0.1$ $mm$ for TE polarization with effective dielectric constant of seawater $\epsilon_{sw} = 36.5500 + j34.9728$ and foam void fraction $f_a = 0.8$ at constant $SST = 20°$ and salinity ($34psu$). . . . . . . . . . . . . . . . . . . . . . . . . . . . . . 119

5.57 Angular Spectrum of Diffused Reflected Wavefront at 18.7 $GHz$ and $\delta_t = 2$ $mm$ for TE polarization with effective dielectric constant of seawater $\epsilon_{sw} = 36.5500 + j34.9728$ and foam void fraction $f_a = 0.8$ at constant $SST = 20°$ and salinity ($34psu$). . . . . . . . . . . . . . . . . . . . . . . . . . . . . . 120

5.58 Angular Spectrum of Diffused Reflected Wavefront at 18.7 $GHz$ and $\delta_t = 2$ $mm$ for TM polarization with effective dielectric constant of seawater $\epsilon_{sw} = 36.5500 + j34.9728$ and foam void fraction $f_a = 0.8$ at constant $SST = 20°$ and salinity ($34psu$). . . . . . . . . . . . . . . . . . . . . . . . . . . . . . 120

5.59 Angular Spectrum of Diffused Reflected Wavefront at 23.8 $GHz$ and $\delta_t = 0.2$ $mm$ for TE polarization with effective dielectric constant of seawater $\epsilon_{sw} = 28.9247 + j33.2233$ and foam void fraction $f_a = 0.8$ at constant $SST = 20°$ and salinity ($34psu$). . . . . . . . . . . . . . . . . . . . . . . . . . . . . . 121

5.60 Angular Spectrum of Diffused Reflected Wavefront at 23.8 $GHz$ and $\delta_t = 0.2$ $mm$ for TM polarization with effective dielectric constant of seawater $\epsilon_{sw} = 28.9247 + j33.2233$ and foam void fraction $f_a = 0.8$ at constant $SST = 20°$ and salinity ($34psu$). . . . . . . . . . . . . . . . . . . . . . . . . . . . . . 121

5.61 Angular Spectrum of Diffused Reflected Wavefront at 23.8 $GHz$ and $\delta_t = 2$ $mm$ for TE polarization with effective dielectric constant of seawater $\epsilon_{sw} = 28.9247 + j33.2233$ and foam void fraction $f_a = 0.8$ at constant $SST = 20°$ and salinity ($34psu$). . . . . . . . . . . . . . . . . . . . . . . . . . . . . 121

5.62 Angular Spectrum of Diffused Reflected Wavefront at 23.8 $GHz$ and $\delta_t = 2$ $mm$ for TM polarization with effective dielectric constant of seawater $\epsilon_{sw} = 28.9247 + j33.2233$ and foam void fraction $f_a = 0.8$ at constant $SST = 20°$ and salinity ($34psu$). . . . . . . . . . . . . . . . . . . . . . . . . . . . . 121

5.63 Angular Spectrum of Diffused Reflected Wavefront at 37 $GHz$ and $\delta_t = 0.1$ $mm$ for TE polarization with effective dielectric constant of seawater $\epsilon_{sw} = 17.7537 + j26.8554$ and foam void fraction $f_a = 0.8$ at constant $SST = 20°$ and salinity ($34psu$). . . . . . . . . . . . . . . . . . . . . . . . . . . . . 123

5.64 Angular Spectrum of Diffused Reflected Wavefront at 37 $GHz$ and $\delta_t = 0.1$ $mm$ for TM polarization with effective dielectric constant of seawater $\epsilon_{sw} = 17.7537 + j26.8554$ and foam void fraction $f_a = 0.8$ at constant $SST = 20°$ and salinity ($34psu$). . . . . . . . . . . . . . . . . . . . . . . . . . . . . 123

5.65 Angular Spectrum of Diffused Reflected Wavefront at 37 $GHz$ and $\delta_t = 0.2$ $mm$ for TE polarization with effective dielectric constant of seawater $\epsilon_{sw} = 17.7537 + j26.8554$ and foam void fraction $f_a = 0.8$ at constant $SST = 20°$ and salinity ($34psu$). . . . . . . . . . . . . . . . . . . . . . . . . . . . . 123

5.66 Angular Spectrum of Diffused Reflected Wavefront at 37 $GHz$ and $\delta_t = 0.2$ $mm$ for TM polarization with effective dielectric constant of seawater $\epsilon_{sw} = 17.7537 + j26.8554$ and foam void fraction $f_a = 0.8$ at constant $SST = 20°$ and salinity ($34psu$). . . . . . . . . . . . . . . . . . . . . . . . . . . . . 123

5.67 Angular Spectrum of Diffused Reflected Wavefront at 37 $GHz$ and $\delta_t = 2$ $mm$ for TE polarization with effective dielectric constant of seawater $\epsilon_{sw} = 17.7537 + j26.8554$ and foam void fraction $f_a = 0.8$ at constant $SST = 20°$ and salinity ($34psu$). . . . . . . . . . . . . . . . . . . . . . . . . . . . . . 124

5.68 Angular Spectrum of Diffused Reflected Wavefront at 37 $GHz$ and $\delta_t = 2$ $mm$ for TM polarization with effective dielectric constant of seawater $\epsilon_{sw} = 17.7537 + j26.8554$ and foam void fraction $f_a = 0.8$ at constant $SST = 20°$ and salinity ($34psu$). . . . . . . . . . . . . . . . . . . . . . . . . . . . . . 124

5.69 Field intensity of backscattered wave for horizontal polarization (TE) with zenith $\theta_i = 30°$ and azimuth $\phi = 0°$ as a function of the spatial coordinates X and Y of the propagation media at 6.8 $GHz$ and $\delta_t = 0.1$ $mm$. . . . . . . . . 126

5.70 Field intensity of backscattered wave for vertical polarization (TM) with zenith $\theta_i = 30°$ and azimuth $\phi = 0°$ as a function of the spatial coordinates X and Y of the propagation media at 6.8 $GHz$ and $\delta_t = 0.1$ $mm$. . . . . . . . . . . . . 126

5.71 Field intensity of backscattered wave for horizontal polarization (TE) with zenith $\theta_i = 30°$ and azimuth $\phi = 0°$ as a function of the spatial coordinates X and Y of the propagation media at 6.8 $GHz$ and $\delta_t = 0.2$ $mm$. . . . . . . . . 126

5.72 Field intensity of backscattered wave for horizontal polarization (TM) with zenith $\theta_i = 30°$ and azimuth $\phi = 0°$ as a function of the spatial coordinates X and Y of the propagation media at 6.8 $GHz$ and $\delta_t = 0.2$ $mm$. . . . . . . . . 126

5.73 Field intensity of backscattered wave for horizontal polarization (TE) with zenith $\theta_i = 30°$ and azimuth $\phi = 0°$ as a function of the spatial X and Y of the propagation media at 10.7 $GHz$ and $\delta_t = 0.1$ $mm$. . . . . . . . . . . . . . 127

5.74 Field intensity of backscattered wave for vertical polarization (TM) with zenith $\theta_i = 30°$ and azimuth $\phi = 0°$ as a function of the spatial X and Y of the propagation media at 10.7 $GHz$ and $\delta_t = 0.1$ $mm$. . . . . . . . . . . . . . . . 127

5.75 Field intensity of backscattered wave for horizontal polarization (TE) with zenith $\theta_i = 30°$ and azimuth $\phi = 0°$ as a function of the spatial coordinates X and Y of the propagation media at 10.7 $GHz$ and $\delta_t = 0.2$ $mm$. . . . . . . . 127

5.76 Field intensity of backscattered wave for horizontal polarization (TM) with zenith $\theta_i = 30°$ and azimuth $\phi = 0°$ as a function of the spatial coordinates X and Y of the propagation media at 10.7 $GHz$ and $\delta_t = 0.2$ $mm$. . . . . . . . 127

5.77 Field intensity of backscattered wave for horizontal polarization (TE) with zenith $\theta_i = 30°$ and azimuth $\phi = 0°$ as a function of the spatial X and Y of the propagation media at 18.7 $GHz$ and $\delta_t = 0.1$ $mm$. . . . . . . . . . . . . . 128

5.78 Field intensity of backscattered wave for vertical polarization (TM) with zenith $\theta_i = 30°$ and azimuth $\phi = 0°$ as a function of the spatial X and Y of the propagation media at 18.7 $GHz$ and $\delta_t = 0.1$ $mm$. . . . . . . . . . . . . . . . 128

5.79 Field intensity of backscattered wave for horizontal polarization (TE) with zenith $\theta_i = 30°$ and azimuth $\phi = 0°$ as a function of the spatial coordinates X and Y of the propagation media at 18.7 $GHz$ and $\delta_t = 0.2$ $mm$. . . . . . . . 128

5.80 Field intensity of backscattered wave for horizontal polarization (TM) with zenith $\theta_i = 30°$ and azimuth $\phi = 0°$ as a function of the spatial coordinates X and Y of the propagation media at 18.7 $GHz$ and $\delta_t = 0.2$ $mm$. . . . . . . . 128

5.81 Field intensity of backscattered wave for horizontal polarization (TE) with zenith $\theta_i = 30°$ and azimuth $\phi = 0°$ as a function of the spatial X and Y of the propagation media at 23.8 $GHz$ and $\delta_t = 0.1$ $mm$. . . . . . . . . . . . . . 129

5.82 Field intensity of backscattered wave for vertical polarization (TM) with zenith $\theta_i = 30°$ and azimuth $\phi = 0°$ as a function of the spatial X and Y of the propagation media at 23.8 $GHz$ and $\delta_t = 0.1$ $mm$. . . . . . . . . . . . . . . . . 129
5.83 Field intensity of backscattered wave for horizontal polarization (TE) with zenith $\theta_i = 30°$ and azimuth $\phi = 0°$ as a function of the spatial coordinates X and Y of the propagation media at 23.8 $GHz$ and $\delta_t = 0.2$ $mm$. . . . . . . . 129
5.84 Field intensity of backscattered wave for horizontal polarization (TM) with zenith $\theta_i = 30°$ and azimuth $\phi = 0°$ as a function of the spatial coordinates X and Y of the propagation media at 23.8 $GHz$ and $\delta_t = 0.2$ $mm$. . . . . . . . 129
5.85 Field intensity of backscattered wave for horizontal polarization (TE) with zenith $\theta_i = 30°$ and azimuth $\phi = 0°$ as a function of the spatial X and Y of the propagation media at 37 $GHz$ and $\delta_t = 0.1$ $mm$. . . . . . . . . . . . . . . 130
5.86 Field intensity of backscattered wave for vertical polarization (TM) with zenith $\theta_i = 30°$ and azimuth $\phi = 0°$ as a function of the spatial X and Y of the propagation media at 37 $GHz$ and $\delta_t = 0.1$ $mm$. . . . . . . . . . . . . . . . . 130
5.87 Field intensity of backscattered wave for horizontal polarization (TE) with zenith $\theta_i = 30°$ and azimuth $\phi = 0°$ as a function of the spatial coordinates X and Y of the propagation media at 37 $GHz$ and $\delta_t = 0.2$ $mm$. . . . . . . . . 130
5.88 Field intensity of backscattered wave for horizontal polarization (TM) with zenith $\theta_i = 30°$ and azimuth $\phi = 0°$ as a function of the spatial coordinates X and Y of the propagation media at 37 $GHz$ and $\delta_t = 0.2$ $mm$. . . . . . . . . 130
5.89 Field intensity of backscattered wave for horizontal polarization (TE) with zenith $\theta_i = 30°$ and azimuth $\phi = 0°$ as a function of the spatial X and Y of the propagation media at 1.42 $GHz$ and $\delta_t = 2$ $mm$. . . . . . . . . . . . . . . 131

5.90 Field intensity of backscattered wave for vertical polarization (TM) with zenith $\theta_i = 30°$ and azimuth $\phi = 0°$ as a function of the spatial X and Y of the propagation media at 1.42 $GHz$ and $\delta_t = 2\ mm$. . . . . . . . . . . . . . . . . 131

5.91 Field intensity of backscattered wave for horizontal polarization (TE) with zenith $\theta_i = 30°$ and azimuth $\phi = 0°$ as a function of the spatial coordinates X and Y of the propagation media at 6.8 $GHz$ and $\delta_t = 2\ mm$. . . . . . . . . . 131

5.92 Field intensity of backscattered wave for horizontal polarization (TM) with zenith $\theta_i = 30°$ and azimuth $\phi = 0°$ as a function of the spatial coordinates X and Y of the propagation media at 6.8 $GHz$ and $\delta_t = 2\ mm$. . . . . . . . . . 131

5.93 Field intensity of backscattered wave for horizontal polarization (TE) with zenith $\theta_i = 30°$ and azimuth $\phi = 0°$ as a function of the spatial X and Y of the propagation media at 10.7 $GHz$ and $\delta_t = 2\ mm$. . . . . . . . . . . . . . . 132

5.94 Field intensity of backscattered wave for vertical polarization (TM) with zenith $\theta_i = 30°$ and azimuth $\phi = 0°$ as a function of the spatial X and Y of the propagation media at 10.7 $GHz$ and $\delta_t = 2\ mm$. . . . . . . . . . . . . . . . . 132

5.95 Field intensity of backscattered wave for horizontal polarization (TE) with zenith $\theta_i = 30°$ and azimuth $\phi = 0°$ as a function of the spatial coordinates X and Y of the propagation media at 18.7 $GHz$ and $\delta_t = 2\ mm$. . . . . . . . . 132

5.96 Field intensity of backscattered wave for horizontal polarization (TM) with zenith $\theta_i = 30°$ and azimuth $\phi = 0°$ as a function of the spatial coordinates X and Y of the propagation media at 18.7 $GHz$ and $\delta_t = 2\ mm$. . . . . . . . . 132

5.97 Field intensity of backscattered wave for horizontal polarization (TE) with zenith $\theta_i = 30°$ and azimuth $\phi = 0°$ as a function of the spatial X and Y of the propagation media at 23.8 $GHz$ and $\delta_t = 2\ mm$. . . . . . . . . . . . . . . 133

5.98 Field intensity of backscattered wave for vertical polarization (TM) with zenith $\theta_i = 30°$ and azimuth $\phi = 0°$ as a function of the spatial X and Y of the propagation media at 23.8 $GHz$ and $\delta_t = 2\ mm$. . . . . . . . . . . . . . . . . 133

5.99 Field intensity of backscattered wave for horizontal polarization (TE) with zenith $\theta_i = 30°$ and azimuth $\phi = 0°$ as a function of the spatial coordinates X and Y of the propagation media at 23.8 $GHz$ and $\delta_t = 2\ mm$. . . . . . . . . 133

5.100 Field intensity of backscattered wave for horizontal polarization (TM) with zenith $\theta_i = 30°$ and azimuth $\phi = 0°$ as a function of the spatial coordinates X and Y of the propagation media at 23.8 $GHz$ and $\delta_t = 2\ mm$. . . . . . . . . 133

5.101 Attenuation of Field Intensity for horizontal polarization (TE) with zenith $\theta_i = 30°$ and azimuth $\phi = 0°$ with depth of sea foam at 6.8 $GHz$ and $\delta_t = 0.1$ $mm$. . . . . . . . . . . . . . . . . . . . . . . . . . . . . . . . . . . . . . . 135

5.102 Attenuation of Field Intensity for vertical polarization (TM) with zenith $\theta_i = 30°$ and azimuth $\phi = 0°$ with depth of sea foam at 6.8 $GHz$ and $\delta_t = 0.1\ mm$. 135

5.103 Attenuation of Field Intensity for horizontal polarization (TE) with zenith $\theta_i = 30°$ and azimuth $\phi = 0°$ with depth of sea foam at 6.8 $GHz$ and $\delta_t = 0.2$ $mm$. . . . . . . . . . . . . . . . . . . . . . . . . . . . . . . . . . . . . . . 137

5.104 Attenuation of Field Intensity for vertical polarization (TM) with zenith $\theta_i = 30°$ and azimuth $\phi = 0°$ with depth of sea foam at 6.8 $GHz$ and $\delta_t = 0.2\ mm$. 137

5.105 Attenuation of Field Intensity for vertical polarization (TM) with zenith $\theta_i = 30°$ and azimuth $\phi = 0°$ with depth of sea foam at 1.42 $GHz$ and $\delta_t = 2\ mm$. 137

5.106 Attenuation of Field Intensity for vertical polarization (TM) with zenith $\theta_i = 30°$ and azimuth $\phi = 0°$ with depth of sea foam at 1.42 $GHz$ and $\delta_t = 2\ mm$. 137

5.107 Attenuation of Field Intensity for horizontal polarization (TE) with zenith $\theta_i = 30°$ and azimuth $\phi = 0°$ with depth of sea foam at 10.7 $GHz$ and $\delta_t = 10$ $mm$. . . . . . . . . . . . . . . . . . . . . . . . . . . . . . . . . . . . . . . 139

5.108 Attenuation of Field Intensity for vertical polarization (TM) with zenith $\theta_i = 30°$ and azimuth $\phi = 0°$ with depth of sea foam at 10.7 $GHz$ and $\delta_t = 10$ $mm$. 139

5.109 Attenuation of Field Intensity for vertical polarization (TM) with zenith $\theta_i = 30°$ and azimuth $\phi = 0°$ with depth of sea foam at 10.7 $GHz$ and $\delta_t = 20$ $mm$. 139

5.110 Attenuation of Field Intensity for vertical polarization (TM) with zenith $\theta_i = 30°$ and azimuth $\phi = 0°$ with depth of sea foam at 10.7 $GHz$ and $\delta_t = 20$ $mm$. 139

5.111 Attenuation of Field Intensity for horizontal polarization (TE) with zenith $\theta_i = 30°$ and azimuth $\phi = 0°$ with depth of sea foam at 18.7 $GHz$ and $\delta_t = 0.2$ $mm$, and 2 $mm$. . . . . . . . . . . . . . . . . . . . . . . . . . . . . . . . 140

5.112 Attenuation of Field Intensity for vertical polarization (TM) with zenith $\theta_i = 30°$ and azimuth $\phi = 0°$ with depth of sea foam at 18.7 $GHz$ and slice thickness $\delta_t = 0.2$ $mm$, and 2 $mm$. . . . . . . . . . . . . . . . . . . . . . . . . . . 140

5.113 Attenuation of Field Intensity for vertical polarization (TM) with zenith $\theta_i = 30°$ and azimuth $\phi = 0°$ with depth of sea foam at 23.8 $GHz$ and $\delta_t = 0.2$ $mm$, and 2 $mm$. . . . . . . . . . . . . . . . . . . . . . . . . . . . . . . . 140

5.114 Attenuation of Field Intensity for vertical polarization (TM) with zenith $\theta_i = 30°$ and azimuth $\phi = 0°$ with depth of sea foam at 23.8 $GHz$ and $\delta_t = 0.2$ $mm$, and 2 $mm$. . . . . . . . . . . . . . . . . . . . . . . . . . . . . . . . 140

5.115 Attenuation of Field Intensity for horizontal polarization (TE) with zenith $\theta_i = 30°$ and azimuth $\phi = 0°$ with depth of sea foam at 37 $GHz$ and $\delta_t = 0.1$ $mm$ . . . . . . . . . . . . . . . . . . . . . . . . . . . . . . . . . . . . . 142

5.116 Attenuation of Field Intensity for vertical polarization (TM) with zenith $\theta_i = 30^\circ$ and azimuth $\phi = 0^\circ$ with depth of sea foam at 37 $GHz$ and $\delta_t = 0.1\ mm$ 142
5.117 Attenuation of Field Intensity for vertical polarization (TM) with zenith $\theta_i = 30^\circ$ and azimuth $\phi = 0^\circ$ with depth of sea foam at 37 $GHz$ and $\delta_t = 0.2\ mm$ 142
5.118 Attenuation of Field Intensity for vertical polarization (TM) with zenith $\theta_i = 30^\circ$ and azimuth $\phi = 0^\circ$ with depth of sea foam at 37 $GHz$ and $\delta_t = 0.2\ mm$ 142
5.119 Attenuation ($dB$) of $|E|^2$ for TE and TM POL against depth of sea foam with zenith $\theta_i = 30^\circ$ and azimuth $\phi = 0^\circ$ for thin phase scattering screens. . . . . 143
5.120 Attenuation ($dB$) of $|E|^2$ for TE and TM POL against depth of sea foam with zenith $\theta_i = 45^\circ$ and azimuth $\phi = 0^\circ$ for thin phase scattering screens. . . . . 143
5.121 Attenuation ($dB$) of $|E|^2$ for TE and TM POL against depth of sea foam with zenith $\theta_i = 60^\circ$ and azimuth $\phi = 0^\circ$ for thin phase scattering screens. . . . . 145
5.122 Specific attenuation ($dB/mm$) against frequency ($GHz$) with propagation angles zenith $\theta_i = 30^\circ, 45^\circ$ and $\theta = 60^\circ$ for thin phase scattering screens. . . . . 145
5.123 Attenuation ($dB$) of $|E|^2$ for TE and TM POL against depth of sea foam with zenith $\theta_i = 30^\circ$ and azimuth $\phi = 0^\circ$ for deep phase scattering screens. . . . . 147
5.124 Attenuation ($dB$) of $|E|^2$ for TE and TM POL against depth of sea foam with zenith $\theta_i = 45^\circ$ and azimuth $\phi = 0^\circ$ for deep phase scattering screens. . . . . 148
5.125 Attenuation ($dB$) of $|E|^2$ for TE and TM POL against depth of sea foam with zenith $\theta_i = 60^\circ$ and azimuth $\phi = 0^\circ$ for deep phase scattering screens. . . . . 149
5.126 Specific attenuation ($dB/mm$) against frequency ($GHz$) with propagation angles zenith $\theta_i = 30^\circ, 45^\circ$ and $\theta = 60^\circ$ for deep phase scattering screens. . . . . 150

5.127 Comparison between simulation results and measurements of microwave emissivity at 10.7 $GHz$ for horizontal and vertical polarization as a function of incidence angle. . . . . . . . . . . . . . . . . . . . . . . . . . . . . . . . . 152

5.128 Comparison between simulation results and measurements of microwave emissivity at 37 $GHz$ for horizontal and vertical polarization as a function of incidence angle. . . . . . . . . . . . . . . . . . . . . . . . . . . . . . . . . 153

5.129 Comparison between simulation results and measurements of microwave emissivity at 10.7 $GHz$ for horizontal and vertical polarization as a function of foam layer thickness. . . . . . . . . . . . . . . . . . . . . . . . . . . . . . 154

5.130 Comparison between simulation results and measurements of microwave emissivity at 37 $GHz$ for horizontal and vertical polarization as a function of foam layer thickness. . . . . . . . . . . . . . . . . . . . . . . . . . . . . . . . 155

5.131 Comparison between simulation results and measurements of brightness temperature at 10.7 $GHz$ for horizontal and vertical polarization as a function of incidence angle. . . . . . . . . . . . . . . . . . . . . . . . . . . . . . . . . 156

5.132 Comparison between simulation results and measurements of brightness temperature at 37 $GHz$ for horizontal and vertical polarization as a function of incidence angle. . . . . . . . . . . . . . . . . . . . . . . . . . . . . . . . . 157

5.133 Comparison between simulation results and measurements of brightness temperature at 10.7 $GHz$ for horizontal and vertical polarization as a function of foam layer thickness. . . . . . . . . . . . . . . . . . . . . . . . . . . . . . 158

5.134 Comparison between simulation results and measurements of brightness temperature at 37 $GHz$ for horizontal and vertical polarization as a function of foam layer thickness. . . . . . . . . . . . . . . . . . . . . . . . . . . . . . 159

# LIST OF TABLES

2.1 Results for Dielectric Constant of sea water at fixed salinity(34psu) and SST(20 degrees celsius) . . . . . . . . . . . . . . . . . . . . . . . . . . . . . . . . . 42

2.2 Results for Dielectric Constant of sea water at fixed salinity(34psu) and SST(20 degrees celsius) . . . . . . . . . . . . . . . . . . . . . . . . . . . . . . . . . 43

2.3 Results for Dielectric Constant of sea water at fixed salinity(34psu) and SST(20 degrees celsius) . . . . . . . . . . . . . . . . . . . . . . . . . . . . . . . . . 43

4.1 Results for Dielectric constants of seafoam at frequencies of 1.42 $GHz$, 6.8 $GHz$ and 23.8 $GHz$ for 5 $2D$ slices of randomly packed air bubbles covered with thin layer of seawater. . . . . . . . . . . . . . . . . . . . . . . . . . . 87

5.1 Results for Dielectric Constant of sea foam at 10.7 $GHz$ and 37 $GHz$ for 5 2-D slices of randomly packed air-bubbles covered with thin-layer of sea water 151

# CHAPTER 1

# INTRODUCTION

Computational electromagnetics have gained widespread use in microwave remote sensing, weather radar, bio-medical diagnosis, astrophysics and meteorology. In polarimetry, satellite radiometers and other sensors are used to measure EM waves with unique polarizations to the atmosphere or earth surface in order to interpret, deduce or predict the properties of objects or targets within the surrounding environment. The process of using satellite sensors for characterization of particles is referred to as remote sensing. Satellite sensors can use measured observations of responses by particles or objects to incident EM waves to describe their compositions and other properties without any form of physical or direct contact with these objects. Microwave radiometers are more prominent in remote sensing of oceanic foams due to their advantage over in situ and remote sensing instruments [3]. For enhancement of radiometer performance, a weather remote sensing tool must depend on assessment of the physical conditions governing scattering and absorption of millimetre waves which are determined by wavelength, sea surface temperature, salinity, particle properties (shape, foam layer thickness, bubble size distribution, foam void fraction, bubble radii and refractive index) [4].

Foam generated by breaking waves under strong wind conditions has significant effect on the average brightness temperature of the ocean surface [5]. This can be attributed to the fact that cloud radiates thermally and scattering of this radiation by the sea surface affects the effective brightness temperature observed by satellite radiometers. Hence, ignoring the specular reflections from the cloud which radiates on the foam covered sea-surface leads to modelling of the emissivity of the sea surface incorrectly. Due to the important role sea foam plays in passive microwave remote sensing, there is need to estimate the effects of sea foam on microwave radiation. Earlier models of sea foam were based on wind speeds. For example, [6] observed that effects of foam formations to the brightness temperature of sea surface can be modelled as a function of wind speed. Droppleman [7] asserted that foam induced effects may contribute as much as half the total sea surface signature to an orbiting microwave radiometer, for a surface wind speed greater than 15m/s. These earlier models are empirical fitting procedures which use experimental data and could not explore how a sea foam layer affects sea surface emission. The aforementioned challenge inspired the need for researchers to develop theoretical models of sea foam.

It is invaluable to note that microwave remote sensing procedures based on satellite radar are faced with propagation challenges under strong wind and other atmospheric conditions. The presence of hydrometeors in the atmosphere (fog, mist, water droplet, ice particles, snow, cloud, etc) distorts EM wave propagation significantly in millimetre and centimetre wavelengths [8]. Propagation challenges such as reflection (scattered and specular), diffraction, refraction, interference (constructive and destructive) and absorption are well known as these mechanisms results in attenuation of signals as they propagates through indoor, outdoor and complex environments. Transmission loss of millimetre waves is mainly due to free-space path loss and other contributing factors such as atmospheric gaseous losses, precipitation attenuation, foliage blockage, scattering and diffraction by particles, buildings, hills, moving targets and stationary objects [9]. In radio wave communication it is essential that signals or waveforms that carries information or data are received with minimal or no distortion at the receiver. Hence, absorption and scattering of electromagnetic waves by hydrometeor such as sea foam have stimulated research interest in this area. The passive remote sensing of ocean surface from aircraft deals with the microwave characteristics of small water droplets in water sprays produced by wind wave breaking [10]. Thermal emission from foam bubbles seems to be of great significance as the foam on the ocean surface increases the emissivity and brightness temperature measured by a passive microwave radiometer and is a main component of the wind vector [11]. The characterization of these hydrometeors depends on knowledge of their geometric (shape) and electrical properties as well as how they respond to propagating EM waves at millimetre and microwave frequencies. Computational electromagnetics play significant roles in evaluating and determining the optical and electrical properties of hydrometeors and also evaluation of the scattering effects of irregular hydromeoters. This process is not easy to attain as there will be strong interactions such as scattering, diffraction and absorption when an incident EM wave is propagated to probe these irregular hydrometeors which have random particle compositions.

Artificial and natural media such as atmosphere, ocean, geophysical media, biological media, composite and disordered materials that possess random spatial inhomogeneities and changes randomly in time could be referred to as random media [12].

It is worth noting that waves in random media are often difficult problems to solve theoretically. Lax, Foldy and Twersky were among researchers that developed early multiple scattering theories for randomly distributed particles [13, 14].

Multiple scattering by distribution of discrete scatterers is observed in optical and millimetre wave scattering by rain drops, fog, smog, snow, ice particles, vegetation and oceanic foams, optical and ultrasound scattering by tissues and blood, optical and acoustic scattering in the ocean and composite materials [15]. A discrete random medium which consists of scatterers of simple shapes and material properties could be randomly distributed in a homogeneous background.

Generally, the characteristics of such a medium is described in an ensemble averaging sense. The discrete random medium provides a convenient model for a variety of geophysical, biological, and artificial systems. Discrete random medium can be classified into two forms according to its scattering properties: sparse and dense [14]. Multiple scattering in sparse medium is negligible due to low particle concentration such that the mean separation of scatterers is much larger than wavelength, low material contrast which results in weak scattering strength from each scatterer and the scattered field falling off quickly in the background medium [16]. In sparse medium, the total response is the sum of the individual responses from each isolated scatterer. A dense medium, in contrast, have closely packed scatterers with significant scattering. Hence, in a dense media, multiple scattering effects must be properly included to get the correct results.

The need to understand and predict low-elevation electromagnetic propagation in the troposphere has been a major concern to researchers which stimulated the development of models to describe and predict electromagnetic propagation in the lower atmosphere and these models have been deployed alongside system simulations to evaluate operational system performance with good success.

The development of efficient numerical solutions of the Parabolic Wave Equation (PWE) offered a major breakthrough in EM propagation modelling by allowing accurate calculations for realistically complicated refractive environments. The PWE is a forward-scatter, narrow-angle approximation to the full Helmoltz wave equation and inherently includes effects due to spherical-Earth diffraction, atmospheric refraction, and surface reflections (i.e., multipath). Advanced PWE models may include impedance boundaries, complicated antenna patterns, rough surfaces, and irregular terrain, atmospheric absorption and other scattering phenomena. PWE based methods result in less complicated propagation models in the sense that direct numerical evaluation of the wave equation eliminates the need to use different approximations and algorithms for different geometries (e.g., multipath interference, transition, and diffraction regions), or for different frequency regimes (e.g., surface-wave formulation for HF and simple Fresnel reflection theory for higher frequencies). Also, there is no need to express the solution as a complicated sum of normal or coupled modes. For these reasons, PWE methods have become the preferred propagation modelling approach for many applications ranging from frequency and propagtion geometry for radar, weapon, and electromagnetic support measures systems. PWE models are currently used in trade-off studies and design evaluations, analyses of experiments and sea tests, operational performance assessment, and mission planning programs.

## 1.1 Why PWE models?

PWE models have some general characteristics that set them apart from other propagation modelling techniques. The PWE is an initial-value problem amenable to numerical solutions using matching methods that starts at the near field and matches out in range and altitude. It becomes imperative to define an initial field solution at a reference range or altitude, as well as boundary conditions in the other dimension. The most popular PWE models match in range, calculating the field along a vertical strip during each range step. It is also possible to march in altitude using an initial solution specified in range at a reference altitude. The Split-step Fourier method and implicit finite-difference equations are two popular numerical methods for solving the PWE which engage stepping in range or altitude and deploys similar initial solution and boundary conditions. PWE methods possess an inherent potential to generate a range-height grid of calculated values which has both its merits and demerits. PWE codes can be quite fast, they generally remain too computationally burdensome for use in a time-step tracking simulation in which the modelled antenna pointing direction is changing frequently. On the other hand, other types of models such as finite-difference and finite-element methods often take substantially longer than PWE-based codes to calculate a large grid of values for range-height plots. The PWE technique appears to be the most reliable method capable of handling realistic complicated atmospheric conditions.

## 1.2 Research Motivation

The motivation of this work is attributed to inadequate physically based models of sea foam that accounts for microscopic properties of sea foam at millimetre wavelength. Earlier research used satellite based models of sea foam to evaluate brightness temperature which enhances computation of sea surface emissivity. A prominent application of this research is in ocean wind remote sensing. In the absence of foam, absorption is the main cause of energy loss when EM radiation is incident on the sea surface or ocean. At millimetre wavelength the sea surface roughness accounts for scattering as the ocean particle size becomes much larger than the wavelength of the incident EM radiation. This is due to more interactions that occurs at the air sea surface interface. Under strong wind conditions scattering is dominated by the presence of sea foam on the surface of sea water thus increase foam coverage on sea water. The increase in foam coverage on the sea surface induces a corresponding increase in the sea surface emissivity but the impact of foam on the retrieval of ocean surface wind vector from satellite-mounted microwave instruments or radiometers is a major concern. This is due to the difficulty in making measurements at high wind conditions when significant foam coverage is present. The need to model brightness temperature to an accuracy of tens of milli-Kelvin implies that there should be improvement in EM modelling of sea foam for remote sensing applications. To achieve this we need to model accurately the dielectric constant of sea foam by taking account of the micro-structural properties of foam [17]. Considering the micro-structure of foam, enhances the likelihood of modelling the effective dielectric constant of sea foam accurately, which helps to treat current models of sea foam as black or grey body. This model will integrate future models to improve observations of scattering properties and emissivity of sea foams.

For effective analysis of millimeter-wave (mmW) propagation challenges in the ocean and sea surface there is need to have exquisite understanding of the electromagnetic properties of the media of propagation. The effective complex dielectric constant of sea-foam plays a vital role in achieving this objective. In this research, we model the propagation phenomena that occurs when mmW at frequencies between 6.8 $GHz$ and 37 $GHz$ travels through a sea-foam layer $0 \leq Z \leq d$ , where $d$ is the depth of the seafoam layer. The sea-foam layer is a diphasic composite with numerous isotropic-coated spherical particles, randomly embedded in an isotropic host with permittivity with no overlap between adjacent spherical air-bubbles. These air-bubbles consist of core air with permittivity $\epsilon_{air}$ and coating shell with permittivity $\epsilon_{seawater}$ . For $N$ spherical particles with outer radii $r_{out}$ and inner radii $r_{in}$ randomly distributed in the host medium. The radii are represented by the bubble size distribution of the particles $N(r)$. For a given plane wave with incident angle and foam-covered sea surface, the Split-step Fourier transform is used to compute the field profile for each range step until the desired range is reached.

In our approach, we intend to develop a theoretical model that seems appropriate to describe the interactions that occur as the mmW propagates through 2D (two dimensions) slices of sea-foam layer with depth $0.1mm$ using split-step Fourier transform as a numerical solution of the parabolic equation which describes the EM propagation problem. For accurate modelling of the emissivity and brightness temperature of sea foam which necessitates satellite based geophysical retrievals of environmental variables from radiometric measurements, it is important that we predict with precision the effective complex dielectric constant of sea-foam based on its microstructural properties. In Chapter 2, we review vital literatures on millimetre wave scattering and remote sensing of random media, Chapter 3 discusses parabolic wave equation method and its significant for modelling electromagnetic wave propagation problems which describes the split-step Fourier transform (SSFT) method and problem formulation, Chapter 4 explains the development of the randomly packed sea-foam model. SSFT technique is applied to calculate the field profile from depth $d = 0$ to the desired depth at each depth step

$\Delta z$ as the incident $mmW$ transverses through various layers of the sea foam layer. We shall analyze the $mmW$ interactions with the sea-foam layer,simulation results and discussion in Chapter 5. Finally, in Chapter 6 we discuss conclusions and present possible works.

# CHAPTER 2

# BACKGROUND AND LITERATURE REVIEW

## 2.1 Overview of Ocean Remote Sensing

### 2.1.1 Introduction

In atmosphere-ocean remote sensing we usually intend to determine the state of physical and optical properties of the media. To enhance retrieval of sea-surface emissivity (radiative properties) and scattering properties of the ocean there is need to take into account the importance of breaking waves [18]. High wind speeds induce breaking gravity waves which create large sea-foam coverage at the atmosphere-ocean interface. Sea-foam significantly influences the accuracy of ocean colour remote sensing and aerosol optical thickness [19–21], it also plays significant role in marine aerosol production, heat and mass exchange across air-sea interface and the ambient noise sound generation [22–24]. Satellite radiometers are deployed for such purposes as measuring radiance backscattered into the atmosphere from below the ocean surface and the strong scattering characteristics of the coated bubbles comprising the foam are measured as brightness temperature by satellite radiometers [25].

Many air-sea interaction processes are quantified in terms of whitecap fraction W because oceanic whitecaps are the most visible and direct way of observing the breaking of wind waves in the open ocean. Enhanced by breaking waves, surface fluxes of momentum, heat, and mass are critical for ocean atmosphere coupling and thus affect the accuracy of models used for weather forecasting, prediction of storm intensification and climate change. Whitecap fraction is defined as the fraction of a unit sea surface covered by foam [2]. It has been traditionally measured by extracting the high intensity pixels marking white water in still photographs or video images collected from towers, ships and aircraft. Satellite-based passive remote sensing of whitecap fraction is a recent development which allows long term consistent observations of whitecapping on a global scale. The remote sensing method relies on change of ocean surface emissivity at microwave frequencies (6 $GHz$ to 37 $GHz$) due to the presence of sea foam on a rough sea surface. These changes at the ocean surface are observed from the satellite as brightness temperature $T_B$ [2, 26]. The algorithm to obtain W from satellite observations of $T_B$ was developed at the Naval Research Laboratory within the framework of WindSat mission. It improved upon the feasibility study of this remote sensing technique by using independent sources for the input variables of the algorithm, physically based models for the emissivity of rough sea surface and emissivity of foam, improved rain flag, and atmospheric model necessary for the atmospheric correction.

The database built with this algorithm compiles W for entire year 2006 matched in time and space with data for the wind vector, wave field (such as significant wave height and peak wave period), and environmental parameters (such as sea surface temperature and atmospheric stability). This data base has proved useful in analysing and quantifying the variability of W. Magdalena et.al presented an updated algorithm for estimating W from WindSat $T_B$ data using new sources and products for the input variables. This approach replaces the originally used QuikSCAT data for ocean wind vector with new wind vector fields [2, 26, 27].

Xiaobin Tin et.al [28] found large discrepancies when comparing measurements and model simulations as wind speed (WS) rise above $12ms^{-1}$. Over the open ocean and for moderate wind speeds ($WS_s$), the Soil Moisture and Ocean Salinity (SMOS) brightness temperature ($T_B$) was initially consistent with $T_B$ computations made by theoretical prelaunch models implemented in European Space Level 2 Ocean Salinity processor [1, 27, 28], [29]. A new approach was proposed using new set of parameters for sea wave spectrum and foam coverage model that can be used for simulating L-band radiometer data over a large range of WS based on the deduction of wind induced components from the SMOS data [16, 30, 31].

Previous calculations assumed particles with size parameter $ka << 1$ using DMRT. An extension to moderate sized particle is vital for millimetre wave remote sensing because at high frequency range above 10GHz, the particle size in geographical media are comparable to the wavelength (Mie Scattering) [1, 30, 31]. Contributions by Chi-Te Chan et.al shows that analytical results were consistent with Monte Carlo simulations of exact solutions of Maxwells equations for randomly distributed finite size sphere without adjusting parameters. Input parameters of the model are all physical parameters of sizes, concentrations (volume fractions) and permittivities. The results of the models were used to obtain brightness temperatures in passive remote sensing of ocean foam at 19GHz and 37GHz. Mie scattering was used with QCA and QCA-CP (quasi-crystalline approximation with coherent potential) to provide solution that is consistent for particle sizes comparable to or larger than the wavelength. With results obtained from [31] , the extinction behaviour of sea foam was illustrated, thermal emission from sea foam was evaluated and it was shown that the extinction was dominated by absorption. A physical model of foam emission was obtained that relates observed brightness temperature to the micro-structure of foam as well as ocean surface wind vector. The brightness temperature of sea foam was presented as a function of observed angle and frequency with the radiative transfer equation solved using derived QCA parameters.

It is well known that radar technology, remote sensing, radiometry, medical diagnosis, astronomy, meteorology, geosciences and other space technologies deploy scattering theory to study the properties of objects, particles, aerosols, precipitation and other hydrometeors. In scattering theory, the underlying physics of the interaction between incident EM wave and the object is invaluable. We shall review electromagnetic wave scattering from densely packed particles.

## 2.2 Remote Sensing

Remote sensing as a concept involves the detection, interpretation and deduction of the shape, colour, size, physical properties and internal constitution of objects, particles, molecules, etc., without seeing or the use of natural sensors. It is well known that the eyes, nose, ears, tongue and skin are natural sensors. For example, the eye detects colours, shapes, and size of objects by scattered light which travels to the eyes. The detection of objects without the use of natural sensors could be referred to as remote sensing.

In geosciences and meteorology remote sensing connotes the capacity of satellites to detect electromagnetic radiations from observations on the earth's surface or the atmosphere. Electromagnetic radiations emitted from the sun comprises ultra-violet light, visible light, thermal infrared, microwave, millimetre wave and x-rays. Most substance with temperature greater than the absolute zero $(-273.15°C)$ or $(-459°F)$ emits some type of electromagnetic radiation. Some satellite sensors interprets visible light scattered from the surface of the earth or atmosphere while others deduce emitted radiation from the earth's surface. Artificial sensors can easily measure sea ice in the visible, infrared and microwave regions of the electromagnetic spectrum but they have their limitations. The spectral regions do not allow scientists to optimally evaluate sea ice in all conditions as "whiter objects" (those with high albedo) reflects more light than "darker" objects. Remote sensing can be distinguished into passive and active remote sensing.

### 2.2.1 Passive Remote Sensing

Passive remote sensing could be referred to as passive microwave. Obviously, objects at the surface of the earth emit not only infrared but also microwaves at relatively low energy levels. The detection of microwave radiation naturally emitted by the earth via a sensor is called passive remote sensing. For example, clouds emits much less microwave radiation as compared to sea ice. Therefore, microwaves can penetrate clouds and be used to detect sea ice during night and day irrespective of cloud cover. Further reading on sea ice can be found in [32].

### 2.2.2 Active Remote Sensing

Active remote sensing is the use of satellite sensors which actively emit radiation towards the earth's surface which bounces off the surface returning back to the sensors. This form of remote sensing could be referred to as active microwave or radar. Radar is a well known technology deployed to track aircraft, ships and fast moving automobile. Comparatively, the physical properties of objects at the earth's surface regulate the amount and characteristics of microwave radiation that reflects to the sensor. Active microwave sensors such as imaging radar, non-imaging radar and altimetry are used to detect sea ice [32].

## 2.3 Polarimetry

The concept of interpreting and measuring the polarization of transverse waves, mainly electromagnetic waves in the form of light and radio-waves is termed polarimetry. The characterization of objects and complex materials in the atmosphere and earth surface could be achieved by polarimetry on EM waves propagated through these materials and complex structures which have undergone reflection,refraction and diffraction. Polarimetry is very useful in remote sensing applications namely; weather radar, astronomy, interferometry,bio-medical diagnosis and planetary science. A polarimetric radar can be used for post-processing to enhance characterization of targets in computational analysis of EM waves. This can be achieved by estimating the fine texture of a material which helps to resolve the orientation of small structures in the target.

Polarimetric radar antenna can transmit and receive EM waves with a clearly stated polarization (the orientation of the E-field vector in the plane perpendicular to poynting vector propagation direction). SAR (Synthetic Aperture Radar) systems have the capacity to provide data on polarimetric properties of an observed surface by changing the polarization of the transmitted signal. The structure of the surface elements inside a resolution element is shown by these polarimetric properties. Scattered signals are depolarized by randomly oriented structures while oriented structures namely; buildings or aligned natural features in the form of sand ripples react in preference to oriented polarizations and opt to maintain polarimetric coherence.

## 2.4 Vertical and Horizontal Polarization

In EM wave propagation problems there is need to propagate waves in a preferred direction. For a plane wave propagating at oblique incidence with angle $\theta_i$ to the normal along the +z direction, the plane containing the normal to the boundary and the direction of propagation of the incidence wave is defined as the plane of incidence.

When the electric field $E$ is travelling in a direction parallel to the plane of incidence it is termed as transverse magnetic $TM$ polarized field. The transverse electric field $TE$ is perpendicular to the plane of incidence. Other names for the $TM$ polarized field are parallel, vertical and $P$-polarized field and others for the $TE$ polarized field are perpendicular, horizontal and $S$-polarized field.

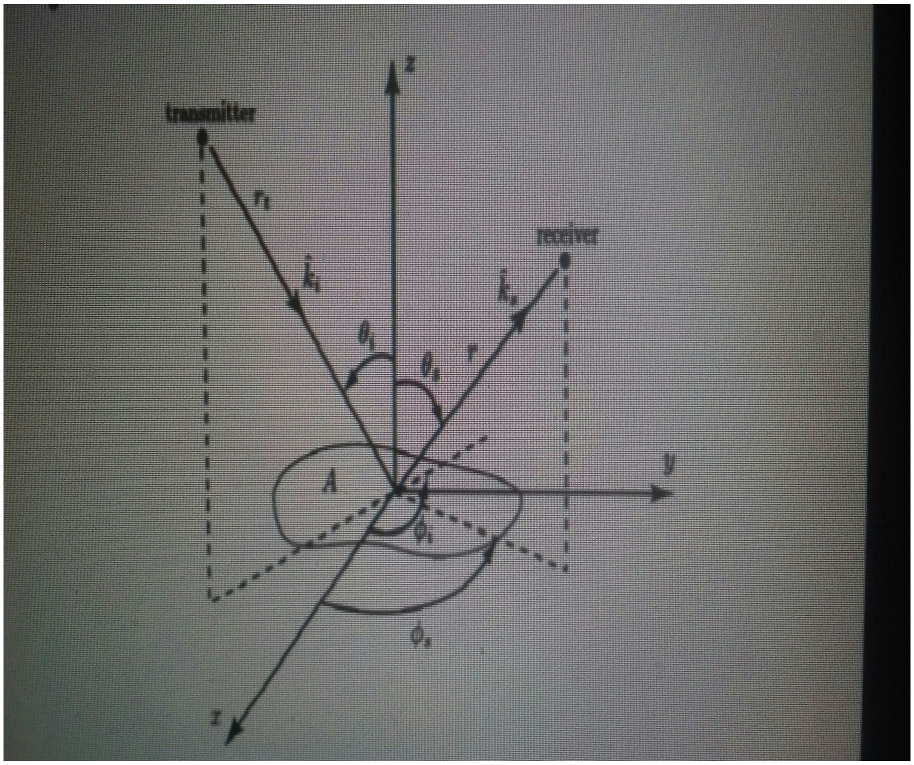

Figure 2.1: Scattering with incident direction $(\theta_i, \phi_i)$ and scattered direction $(\theta_s, \phi_s)$. [1]

Considering a wave vector $k_i$ in the incident plane described by zenith and azimuth angles $\theta_i$ and $\phi_i$ in spherical coordinates. The incident wave vectors $\hat{k}_i$, $\hat{v}_i$ and $\hat{h}_i$ are expressed mathematically as

$$\hat{k}_i = \sin\theta_i \cos\phi_i \hat{x} + \sin\theta_i \sin\phi_i \hat{y} + \cos\theta_i \hat{z} \tag{2.1}$$

$$\hat{v}_i = \cos\theta_i \cos\phi_i \hat{x} + \cos\theta_i \sin\phi_i \hat{y} - \sin\theta_i \hat{z} \tag{2.2}$$

$$\hat{h}_i = -\sin\phi_i \hat{x} + \cos\phi_i \hat{y} \tag{2.3}$$

Likewise, the wave vectors $\hat{k}_s$, $\hat{v}_s$ and $\hat{h}_s$ in the scattering plane associated with angles $\theta_s$ and

$\phi_s$ are

$$\hat{k}_s = \sin\theta_s \cos\phi_s \hat{x} + \sin\theta_s \sin\phi_s \hat{y} + \cos\theta_s \hat{z} \tag{2.4}$$

$$\hat{v}_s = \cos\theta_s \cos\phi_s \hat{x} + \cos\theta_s \sin\phi_s \hat{y} - \sin\theta_s \hat{z} \tag{2.5}$$

$$\hat{h}_s = -\sin\phi_s \hat{x} + \cos\phi_s \hat{y} \tag{2.6}$$

## 2.5 Boundary Conditions by Fresnel's Equation

For a plane wave incident at angle $\theta_n$ at an interface separating the sea foam bottom layer (fifth layer) and medium 2 (seawater) with dielectric constants $\epsilon_n$ and $\epsilon_{sw}$ respectively, the Fresnel's factor or reflection coefficient for vertical and horizontal polarizations are

$$\Gamma_\perp = \frac{\cos\theta_n - \sqrt{\frac{\epsilon_{sw}}{\epsilon_n} - \sin^2\theta_n}}{\cos\theta_n + \sqrt{\frac{\epsilon_{sw}}{\epsilon_n} - \sin^2\theta_n}} \tag{2.7}$$

where $\Gamma_\perp$ denotes Fresnel's reflection coefficient for $TE$ polarization and $\Gamma_\parallel$ is the $TM$ Fresnel's reflection factor.

$$\Gamma_\parallel = \frac{\frac{\epsilon_{sw}}{\epsilon_n}\cos\theta_n - \sqrt{\frac{\epsilon_{sw}}{\epsilon_n} - \sin^2\theta_n}}{\frac{\epsilon_{sw}}{\epsilon_n}\cos\theta_n + \sqrt{\frac{\epsilon_{sw}}{\epsilon_n} - \sin^2\theta_n}} \tag{2.8}$$

Given the field intensity incident angle $\theta_n = 30^0$ and the azimuth angle of the sea foam bottom layer $\phi_n = 30^0$ onto the interface, we obtained the reflected angle using Snell's law.

$$\theta_n = \theta_{sw} \tag{2.9}$$

The transmitted angle is obtained from Snell's law

$$\eta_n \sin\theta_n = \eta_{sw} \sin\theta_{sw} \tag{2.10}$$

where $\eta_n$ is the refractive index of sea-foam bottom layer and $\eta_{sw}$ denotes refractive index of sea-water.

The Fresnels reflection coefficients are used for the computation of sea surface emissivity $e^{foam}$ and brightness temperature $T_B$ in the radiative transfer equations given below.

$$e_p^{foam} = 1 - |R_p^{foam}|^2 \tag{2.11}$$

$$e_v^{foam} = 1 - |R_v^{foam}|^2 \tag{2.12}$$

Where $e_p^{foam}$ is the sea surface emissivity, $p = h$ (horizontal polarization) and $v = s$ (vertical polarization).

$$T_{Bp} = e_p^{foam} T_s \tag{2.13}$$

$$T_{Bv} = e_v^{foam} T_s \tag{2.14}$$

where $T_s$ denotes sea surface temperature. The expressions of reflection coefficients for multi-layered foam structure for both horizontal $R_p^{foam}$ and vertical $R_v^{foam}$ polarized fields are given in [30].

### 2.5.1 Single and Multiple scattering

Single scattering occurs when the incident electric field is scattered by a localized scattering centre. Scattering centres are often grouped together, which is accounted for multiple scattering. The disparity between the effects of single and multiple scattering is that multiple scattering is treated as a stochastic process while single scattering is described as a random process [16]. In most cases, the location of a single scattering centre is not usually well known relative to the path of radiation, the outcome, which tends to rely strongly on the incident electric field trajectory, appears random to an observer [16]. The final path of the radiation in multiple scattering appears to be a deterministic distribution intensity as the randomness of the interaction tends to be averaged out by large number of scattering events. For example, a light beam passing through thick fog. Multiple scattering and diffusion are relatively analogous, and the terms could be used interchangeably in many context. Coherent backscattering, an enhancement of backscattering that is observed when coherent radiation is multiply scattered by a random medium, is often accredited to weak localization [31].

### 2.5.2 Fluctuating Fields

In random scattering problems, since the inhomogeneities are randomly distributed, the fields and intensity are fluctuating. In the case of random discrete scatterers, the particles are randomly distributed in positions, shapes, sizes and orientations so that the scattered fields are randomly distributed. It is note-worthy that the concept of random fields is the foundation of random media and random rough surface scattering problems. Unlike a deterministic problem in which there is only one solution, random media problems only have a unique solution for a single realization. As realizations changes, the positions of the scatterers change and height profiles change, and the fields will fluctuate. Realizations changes can be due to motion of the random media and rough surfaces or the motion of the transmitter and receiver as they would view different parts of the surfaces and random media. Reported works on the phenomenon of random fields include Booker and Gordon [33] , Foldy [34], Lax [35], Twersky [36], Frisch [37], Beran [38], Tatarskii [39], and Ishimaru [12].

### 2.5.3 Elastic and Inelastic Scattering

In elastic scattering the wavelength of the scattered field remain unchanged as the incident field. For example, Mie and Rayleigh scattering. Inelastic scattering is a contrast to elastic scattering as the scattered radiation has a wavelength different from that of the incident radiation (Raman scattering, Compton scattering, an inverse Compton scattering). The momentum of the incident energy does not affect the scattering of the particles in elastic scattering. Small frequency energy signal does not influence the scattering of the particle. It is the dipole moment orientation and distribution that is responsible for the scattering of the incident electric field. This concept is analogous to Doppler Effect in radar.

### 2.5.4 Propagation Media Characteristics

Electromagnetic waves propagate in free space or air with acceptable losses while they attenuates rapidly in sea water or inside lands, with increase in frequency. The propagation media characteristics are described by the electromagnetic constitutive parameters of the material medium. They are conductivity, permittivity (dielectric constant) and permeability [40].

### 2.5.5 Conductivity

The conductivity of a media is one of the three constitutive EM parameters of a material medium. A material is said to be homogeneous if its constitutive parameters do not vary from point to point, and it is isotropic if its constitutive parameters are independent of direction. A perfect conductor is a material with conductivity $\sigma = \infty$ and electric field $E = 0$, while a perfect dielectric is a material with conductivity $\sigma = 0$ and current density $J = 0$. In plane wave propagation, the conductivity and dielectric properties of the media determines if the media is lossless or lossy.

### 2.5.6 Dielectric Constant and Refractive index

The knowledge of the dielectric properties of hydrometeors is fundamental to determining their various scattering properties. For a linear, isotropic, and homogeneous medium with conductivity $\sigma$, the complex permittivity $\epsilon_c = \epsilon - \frac{\sigma}{\omega}$, where $\epsilon_c = \epsilon^{'} - \epsilon^{''}$, with $\epsilon^{'}$ as the real component and $\epsilon^{''}$ the imaginary component [41]. An applied electric field $\vec{E}$ exposed to a dielectric material causes the polarization of the atoms or molecules of the material to create dipole moments that augment the total displacement flux $\vec{D}$. The appended polarization vector is called the electric polarization $\vec{P_e}$, where

$$\vec{D} = \epsilon_o \vec{E} + \vec{P_e} \tag{2.15}$$

In a linear medium, the relationship between $\vec{P_e}$ and $\vec{E}$ is given by

$$\vec{D} = \vec{P_e} = \epsilon_o \chi_e \vec{E} \tag{2.16}$$

where $\chi_e$, which may be complex is known as the electrical susceptibility. Then

$$\vec{D} = \epsilon_o\vec{E} + \vec{P}_e = \epsilon_o\vec{E} + \chi_e\epsilon_o\vec{E} \tag{2.17}$$

where $\epsilon_c \cong \epsilon^{'} - \epsilon^{''} = \epsilon(1 + \chi_e)$, is the complex permittivity of the medium.

For a lossless medium with $\sigma = 0$, $\epsilon^{''} = 0$ and $\epsilon_c = \epsilon^{'} = \epsilon$. The higher the dielectric constant the more scattering we expect from a particle after collision. For a material with complex permittivity such as oceanic foam, snow flakes, ice crystals, raindrops, water and aerosols, the imaginary part of the complex permittivity accounts for losses. Dielectric properties are often expressed as complex dielectric constant $\epsilon_c \cong \epsilon^{'} - \epsilon^{''}$ or complex refractive index $n = n^{'} - n^{''}$ with the two quantities related by $n = \sqrt{\epsilon}$.

### 2.5.7 Permeability

The magnetic permeability of a material could be expressed as $\mu_c = \mu_o(1 + \chi_m)$, where $\chi_m$ is the magnetic susceptibility. The magnetic properties of material are often described by its relative permeability $\mu_r$. Mathematically, $\mu_r = \frac{\mu}{\mu_o}$ where $\mu_o$ is the permitivity of free space. For most metals and dielectric materials $\mu_r = 1$ or $\mu = \mu_o$.

### 2.5.8 Lossless and Lossy Media

For a lossless medium, the conductivity $\sigma = 0$ and the attenuation constant $\alpha = 0$. There is no attenuation and energy absorption due to conductivity in this medium. Losses are accounted for by the dielectric properties of the medium. The dielectric constant in lossless media contains the real component of the complex dielectric constant only. Conversely, the lossy medium attenuates energy due to conductivity of the medium which is accounted for losses or absorption of incident radiation. The attenuation depends on the imaginary part of the complex dielectric constant. Considering wave propagation in a conducting medium with propagation constant

$$\gamma^2 = -\omega^2 \mu \epsilon_c \tag{2.18}$$

$$\gamma^2 = -\omega^2 \mu (\epsilon^{'} - \epsilon^{''}) \tag{2.19}$$

where $\gamma^2 = -\omega^2 \mu \epsilon_c$ and $\epsilon^{'} = \Re\epsilon, \epsilon^{''} = \Im\epsilon = \dfrac{\sigma}{\omega\epsilon}$

### 2.5.9 Scattering Parameters

Scattering plane is described by the plane containing incident field propagating along the direction of the poynting vector of the scattered field or the plane containing the incident field and the line from the centre of the scattering target or systems to the observer.

Scattering cross-section ($\sigma_{sca}$) represents the amount of scattered incident field or particles after interaction with with a scatterer. It describes the portion of the incident field that becomes scattered field through the impact of the area of the scatterer. Differential cross-section is the ratio of the scattered field to the incident field. In quantum mechanics, the differential cross-section can be expressed as $\dfrac{d\theta}{d\Omega} = |f(\theta)|^2$.

Absorption cross-section ($\sigma_{abp}$) describes the amount of incident field that is absorbed or converted to heat energy by the scatterer. For a conducting medium or lossy dielectric with imaginary refractive index, most of the incident energy is absorbed, thus the extinction cross-section is equal to the absorption cross-section. For lossless dielectric scatterer with real refractive index, the extinction cross-section is equal to the scattering cross-section [42].

Extinction cross-section ($\sigma_{ext}$) which can be referred to as total cross-section describes the total energy lost after interaction with a scatterer. This is dependent on the refractive index or dielectric constant of the scatterer. For a scatterer with complex dielectric constant or refractive index such as sea foam which is a mixture of air and water bubbles, the total cross-section consists of energy losses of the incident field due to scattering and absorption. Hence, the extinction cross-section is the sum of the scattering cross-section and the absorption [42].

$$\sigma_{ext} = \sigma_{abp} + \sigma_{sca} \tag{2.20}$$

#### 2.5.9.1 Size Parameter

The size parameter of a scatterer is a very significant scattering parameter and can be defined as the product of the wavelength and the radius of the scatterer in the case of a sphere. In scattering theory, spherical particles are considered due to the availability of rigorous scattering solutions in Mie theory. For a spherical scatterer with size parameter $x = ka$, $x$ denotes the size parameter, $k$ is the wavenumber and $a$ denotes the radius of the sphere [13]. The single scattering properties of aerosols or wavelength scaled particles can be evaluated using Discrete Dipole Approximation (DDA) but the computation becomes very slow when the particle size considerably exceeds the wavelength of radiation. For instance, computations above $x = 20$, are highly challenging for supercomputers. It is important to know that scattering becomes interesting when scatterers size approaches a wavelength. However, scatterers with dimensions smaller than the incident wavelength with complex dielectric constant could deviate from the Rayleigh law.

Scattering efficiency ($Q_{sca}$) is also called scattering efficiency factor. It is defined as the ratio of the scattering cross-section to the geometric cross-section of the particle. The geometric cross-section is the area of the particle projected onto the plane perpendicular to the incident beam in quantum mechanics. The geometric cross-section of a spherical particle is expressed as $G = \pi r^2$, G denotes the geometric cross-section of the particle and the scattering efficiency is given by

$$Q_{sca} = \frac{\sigma_{sca}}{G} \tag{2.21}$$

Absorption efficiency or absorption efficiency factor ($Q_{abs}$) is the ratio of the absorption cross-section to the geometric cross-section of the particle. This is given by

$$Q_{abp} = \frac{\sigma_{abp}}{G} \tag{2.22}$$

Extinction efficiency ($Q_{ext}$) which is also referred to as extinction efficiency factor is defined as the ratio of the extinction cross-section to the geometric cross-section of the material or the sum of the scattering efficiency and absorption efficiency of the material. It is written mathematically as

$$Q_{ext} = \frac{\sigma_{ext}}{G} \quad Q_{ext} = Q_{abs} + Q_{sca} \tag{2.23}$$

For non-absorbing medium, the extinction efficiency is equal to the scattering efficiency while the extinction efficiency is equal to the absorption efficiency for an absorbing medium with negligible scattering.

## 2.6 Formation of Oceanic Foams

### 2.6.1 Sea Foam Formation

Foam formation is enhanced by the presence of impurities in water. Foam is a dispersion of a gas in a liquid or solid separated by thin films or lamellae. It has been observed that a pure liquid cannot foam unless a surface-active material is present. Surface-active forming materials comprise particles, detergents and soap, polymers, specific absorbed cations or anions from organic salts etc [2, 43]. In aquatic habitat, sea foam forms when dissolved organic matter in the ocean is churned up but on a grander scale when the ocean is agitated by wind and waves [44]. The formation of sea foam is governed by different conditions on each coastal region. Sea water contains higher concentration of dissolved organic matter (proteins, salts, lipids and lignins, decaying algae or phytoplankton bloom and decaying fish). These acts as surfactants or foaming agents. As the sea water is agitated by breaking waves in the surf zone next to the shore, the existence of these surfactants under these turbulent conditions traps air, forming persistent bubbles which stick to each other through surface tension [43]. Foam on ocean surface consists of densely packed air bubbles coated with thin layer of water.

Due to its low density and persistence, foam can be blown by strong on-shore winds from the beach face inlands onto sidewalks and street as shown in figure 2.1. Human waste forms a great contribution to sea foam in addition to overflow from plants, factory waste and sewer spills. Sea foam produced by non-pollutants or algae bloom is white. Foams formed by pollutants is often brown in colour. However, sea foam produced by red tide or other organic source also appear brownish.

Figure 2.2: Sea Foam at Ocean Beach in San Francisco [2]

## 2.7 Significant Ocean Parameters

There are several important ocean parameters that helps to characterize its absorption and scattering properties. The most popular are sea surface temperature, salinity, effective dielectric constant of seawater, brightness temperature etc. We shall explain these parameters briefly.

## 2.8 Sea Surface Temperature (SST)

Sea surface temperature is an important geophysical parameter, providing the boundary condition used in the estimation of heat flux at the air-sea interface. On the global scale, this is important for climate modelling, study of the earth's heat balance and insight into atmosphere and ocean circulation patterns and anomalies such as El Nino. On a more local scale, SST can be used operationally to access eddies, fronts and upwellings for marine navigation and to tract biological productivity. Satellite technology has improved measurement of SST by allowing frequent and global coverage. Earlier measurements of SST were done by ships and bouys whose ranges were limited. Thermal infrared and passive microwave radiometry are two methods for determining SST.

## 2.9 Salinity

Salinity is the degree of saltiness in seawater. It is about 3.1% and 3.8% in seawater and its concentration can be expressed in parts per thousand or parts per million (ppm) and practical salinity scale (psu) which was adopted in 1978. The United States Geological Survey classifies saline water in three salinity categories. Salt concentration in slightly saline water is around 1,000 to 3,000 ppm $0.1\% - 0.3\%$, in moderately saline water 3,000 to 10,000 ppm $0.3\% - 1\%$ and in highly saline water 10,000 to 35,000 ppm $1\% - 3.5\%$. Seawater has a salinity of roughly 35,000 ppm, equivalent to 35 grams of salt per one litre (or kilogram) of water. The saturation level is dependent on the temperature of the water. At 20 °C, 1 $ml$ of water can dissolve about 0.357 grams of salt; a concentration of 26.3%. At boiling (100 °C), the amount that can be dissolved in 1 $ml$ of water increases to about 0.391 grams or 28.1%

saline solution [45]. Salinity is also significant in the determination of the effective dielectric constant of seawater. It increases electrical conductivity and absorption of incident EM waves on the Ocean which is a major contributor to transmission losses in the medium. In contrast, thermal conductivity decreases with increase in salinity but increases with increase in temperature [46].

## 2.10 Brightness Temperature

We often normalize specific intensities to obtain brightness temperatures. For thermal emissions from a half-space medium with dielectric constant $\epsilon_1$ in passive remote sensing. The specific intensity $I_\beta(\theta_o, \phi_o)$ emitted by an observed medium with $\beta$ as the polarization and $(\theta_o, \phi_o)$ denotes angular dependence, see Tsang.et.al [30]. The specific intensity of the medium at temperature $T$ is

$$I = \frac{KT}{\lambda^2}\frac{\epsilon_1}{\epsilon_o} \tag{2.24}$$

and should be propagated through the boundary.

## 2.11 Review of Dielectric Constant of Sea Foam at Microwave Frequency

A systematic insight into the application of various mixing rules (effective medium theories) for evaluating the dielectric constant (permittivity) of sea foam (whitecaps) at microwave frequencies between 1.4 to 37 $GHz$ was reported by [47]. It is significant to note that foam scattering is weak at these frequencies which explains the interest of [47] in evaluating the dielectric constant of whitecaps using inexplicit scattering computations such as the Maxwell Garnett, Bruggeman, Coherent potential, Looyenga, and Refractive models [47]. This approach relies on previous findings on various heterogeneous dielectric mixtures and reported characterization of sea foam in order to evaluate the availability of various permittivity models for obtaining acceptable predictions of sea foam dielectric constant. Numerous experimental and field observations were presented which characterized deep bubble plumes well but measurements characterizing the surface foam layers are few and usually simulated artificial sea foam [48–52].

Due to limited knowledge of the microscopic characteristics of sea foam from previously published work and experiments, recent models evaluating the foam emissivity and effective permittivity uses exclusively macroscopic foam characteristics, such as void fraction (whitecap coverage) and foam thickness thereby ignoring scattering losses in sea foam. This could be attributed to the fact that previous foam emissivity models that computed the attenuation and permittivity in foam with several scattering theories using as input the microscopic characteristics of foam such as bubble diameters, bubble wall thicknesses, bubble size distribution, filling factor, and stickiness parameter [30, 53–55] introduced uncertainties which affected the accuracy of the foam emissivity models.

To restrict these uncertainties and enhance use in retrieval algorithms, Bordonskiy, G. S. et al suggested the use of exclusively macroscopic quantities instead, namely; void fraction profile and foam layer thickness [56]. Avoiding the use of microscopic quantities implies foregoing modelling of the scattering losses in sea foam. Based on the aforementioned consideration the foam emissivity was obtained by one of the classical permittivity models (mixing rules) which involve only the sea water permittivity $\epsilon$, air permittivity $\epsilon_0 = 1 - j0$ and void fraction $f_a$. In [57] the foam layer was assumed to be much thicker than the penetration depth of the radiation, thus ignoring the emissivity of the water below the foam layer. Evaluations of extinction, scattering and absorption coefficients were carried out at 19.35 $GHz$ for foam consisting of large bubbles with inner radius of 4.3 $mm$ with relatively thick walls (0.13) $mm$. Zhang et.al obtained results which represents a numerical analogue of Williams experimental observations for foam spread over an aluminium plate [57]. The model in [57] eliminated a major contributor to absorption (the water below the foam) and considered large thick-walled bubbles at relatively high frequency. This, unsurprisingly, predicts low absorption (about 28% of the total extinction) and significant scattering, which appear consistent with the other analytical and experimental findings.

Scattering, absorption and extinction efficiency factors ($Q_s, Q_{abs}, Q_e$) were evaluated by Mie theory for spherical water bubbles with different sizes and wall thicknesses [58]. The results obtained depict that absorption was the main attenuation factor which was further clarified by conclusions from Militskii et.al [48, 49] work that the observed small attenuation in dry foam is predominated by absorption within the bubble walls, not scattering. Scattering, however, increases as radiation frequency and bubble dimensions (radius and wall thickness) increases. Based on Raizer's observations [55], various models can be created with significant scattering by using microscopic characteristics of sea foam such as bubble diameter, bubble wall thickness, bubble size distribution, filling factor and stickiness without the introduction of uncertainties by considering two input parameters in the models at different intervals instead of many parameters when computing the scattering losses [55]. However, existing models of sea water can be used coupled with effective medium theories for evaluating the effective dielectric constant of sea foam. In the next section, some existing models for evaluating the dielectric constant of sea water will be mentioned as well as the various mixing rules for sea foam evaluation. Strogryn's model [6] for seawater at fixed sea surface temperature (SST) at ($20^o$) and salinity (34) $psu$ at 1.4 $GHz$, 6.8 $GHz$, 10.7 $GHz$, 18.7 $GHz$, 23.8 $GHz$ and 37.0 $GHz$ was used to evaluate the effective dielectric constant of sea foam. The dielectric constants obtained at aforementioned frequencies were used as the dielectric constants of the of the host medium $\epsilon_B$ (base medium) while the dielectric constant of air $\epsilon_{air} = 1.0006$ which is approximately equal to the dielectric constant of vacuum $\epsilon_o$ is the dielectric constant of the inclusion. Therefore, $\epsilon_{air} \approx \epsilon_o = 1$ for sea foam (sea water-air interface). It was also used for sea spray (air-sea water interface) which implies that air represents the base medium with sea water as inclusion. Magdalena's model [26] depends on the void fraction ($f_a$) (air or water) inclusions. This method was developed using the famous Maxwell Garnet's approximation, Polder van Santen (Bruggeman), Looyenga (cubic) law, refractive (quadratic rule) and coherent potential [47] . It is worth noting that the void fraction changes abruptly with depth. $(f_a) \approx 100\%$ at the interface adjacent to the air to $\ll 1\%$ at the interface adjacent to sea water and below. More information on void fraction can be found in [47].

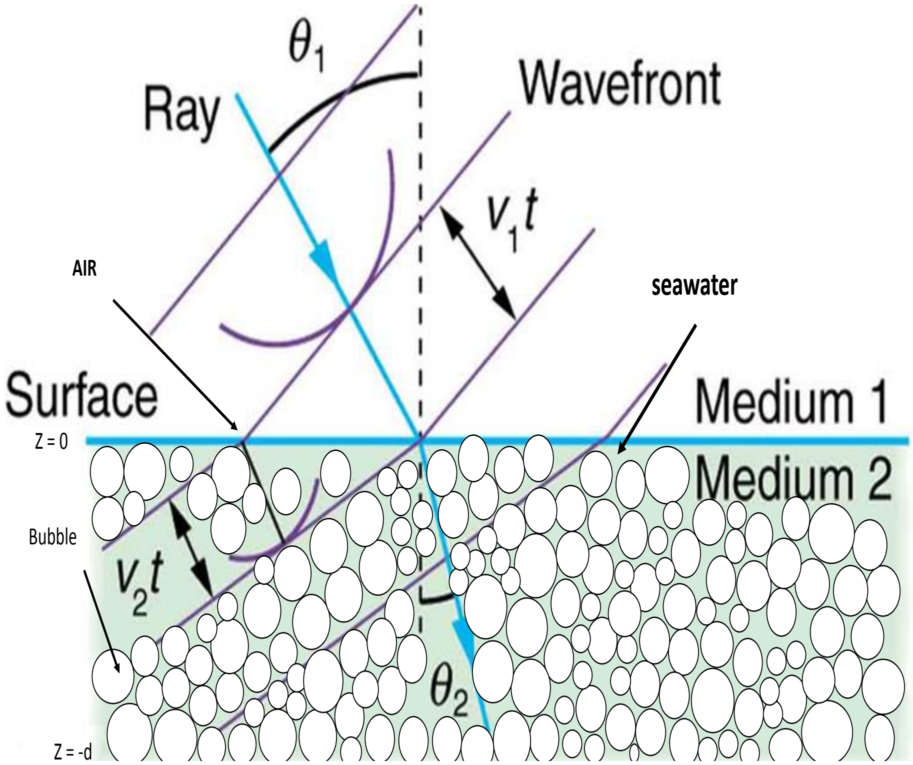
$\theta_1$
Ray
Wavefront
$v_1t$
AIR
seawater
Surface
Medium 1
Z = 0
Medium 2
Bubble
$v_2t$
$\theta_2$
Z = -d

Figure 2.3: Geometry of Sea-foam as a heterogeneous mixture of air, seawater and impurities

## 2.12 Modelling of Sea Foam using Effective Medium Theories

Sea foam is a heterogeneous mixture composed of air, sea water and impurities as shown in figure 2.2. Such a mixture could be referred to a polyphasic mixture. The dielectric properties of a polyphasic mixture can be evaluated using a suitable mixing rule. The mixing rule is an approach of homogenizing an inhomogeneous medium. This is achieved by representing a complex material with a uniform effective permittivity. The mixing rule is also known as effective medium theory (EMT). EMT is a very useful tool for evaluating and analysing the dielectric and radiative properties of composite materials [59]. It matches the effective permittivity $\epsilon_{eff}$ of a heterogeneous mixture to the permittivity of its constituents. To develop a consistent model of sea foam it is necessary to study sea foam properties. A concise survey of sea foam properties is explained below.

### 2.12.1 Sea Foam Properties

Sea foam and whitecap at microwave frequencies are routinely modelled by a polydisperse systems of bubbles. Two layered spherical particles with a thin salt water shell, with air inclusions as shown in figure 5.1. Sea foam and the processes within can be characterize in microscopic and macroscopic form. Microscopic characteristics such as bubbles dimensions (radius $r$, and wall thickness $w$) and size distribution or concentration $N(r)$ are necessary. Macroscopic characteristics such as foam layer thickness $t$ and foam void fraction $f_a$ describe the foam layer. The specific mechanical structure of sea foam is represented by a group of medium variables established by micro and macro characteristics of sea foam. In [27] an overview of sea foam properties in formulating several dielectric models of sea foam was discussed.

### 2.12.2 Classical Mixing Rule

The sea foam modelling based on classical mixing rule assuming explicit macroscopic characteristics of sea foam is a diphasic mixture with constituents described as an host medium with inclusions, each with permittivity $\epsilon_b$ and $\epsilon_i$, respectively. The void fraction $f_a$ (defined as the unit volume of ocean occupied by air) of the total mixture occupied by the inclusions determines the nature and character of the mixture. In Anguelova's [27] model, sea water is the host medium and air bubbles represent the inclusions thus denoting $\epsilon_{eff} = \epsilon_f$, $\epsilon_e = \epsilon$, $\epsilon_i = 1$, and $f_v = f_a$. Most natural media are material-in-air mixtures with a dielectric constant $\frac{\epsilon_i}{\epsilon_e} < 1(\epsilon_e = \epsilon_0 = 1 - j0)$ and has been more extensively studied than air-in-material mixtures, like the sea foam, with $\frac{\epsilon_i}{\epsilon_e} > 1$. Effective medium theory has been widely deployed for dense media in which the dipole interactions and resonance in closely packed inclusions need to be evaluated. Examples of these are Maxwell Garnets (MG) method, the Polder-van Santen (Bruggeman or De Loor formula), Coherent Potential (CP) or Power law formula and refractive method [47]. There is need to investigate the most appropriate and best suitable mixing rule with the potency to model a consistent foam permittivity to meet the desired remote sensing application. De Loor reported that it is impossible to choose one particular relation to fully describe the permittivity of a specific mixture.

### 2.12.3 Maxwell Garnet's Method

From previous studies [7, 51, 52, 54], the Maxwell Garnet's formula is a very famous mixing rule. It was reported that different mixing rule used to evaluate sea foam permittivity approximates to the expression for Maxwell Garnet's rule with appropriate notations of the variables and some algebraic re-arrangements. For example, see Anguelova et.al [60]. The Maxwell Garnet's method is derived for a diphasic composite, where spherical dielectric inclusions are present in a homogeneous host, and could be extended for arbitrary ellipsoid inclusions and for multiphase mixtures. This derivation is based on polarizability of a dielectric sphere. Considering a composite where ellipsoidal inclusions with dielectric constant $\epsilon_i$

occupy random positions within the host medium $\epsilon_b$ as shown in figure 2.3. Assuming the volume fraction of inclusions to be $v_i$, and host material $v_b = 1 - v_i$.

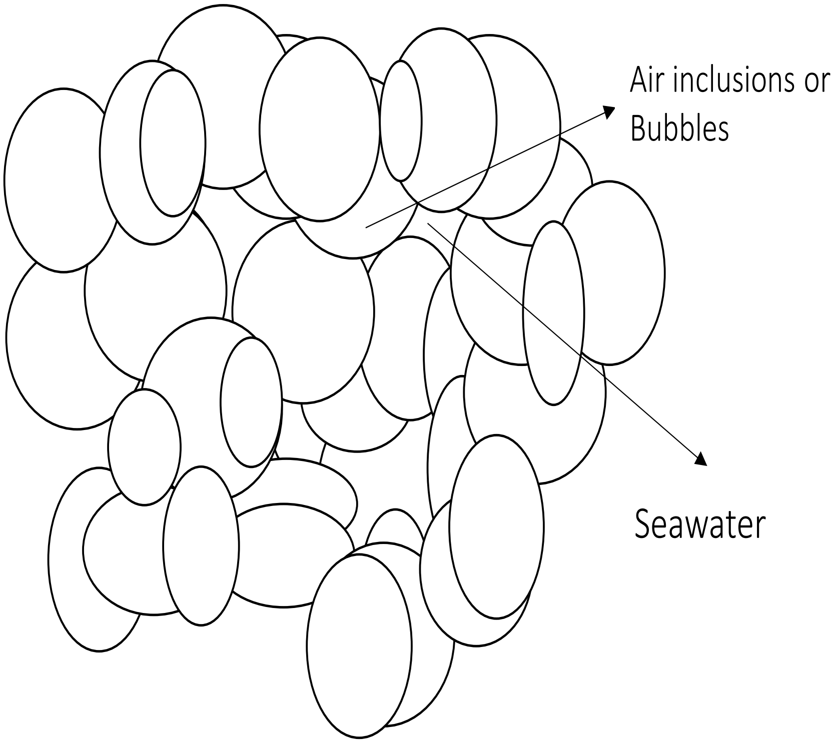

Figure 2.4: Bubble cluster of ellipsoidal inclusions in a dielectric base material

Consider an average displacement vector and an average electric field. For a linear isotropic mixture, these parameters are related by

$$\bar{D} = \epsilon_{eff} \bar{E} \tag{2.25}$$

where $\epsilon_{eff} = \epsilon_0 \epsilon_{effr}$ is the absolute permittivity, complex in general case.

The average field and displacement vector could be written weighted with corresponding volume fractions of phases with absolute complex permittivity $\epsilon_b = \epsilon_0 \epsilon_{br}$ for base medium, and $\epsilon_i = \epsilon_0 \epsilon_{ir}$ for inclusions. This is usually done for real and frequency-dependent dielectric constant, but it could be generalized for lossy and frequency-dispersive materials.

$$\bar{D} = v_i \epsilon_i \bar{E_i} + (1 - v_i)\epsilon_b \bar{E_b} \tag{2.26}$$

$$\bar{E} = v_i \bar{E_i} + (1 - v_i)\bar{E_b} \tag{2.27}$$

we further obtain

$$\epsilon_{\tilde{eff}} = \frac{v_i \epsilon_i A + (1 - v_i)\epsilon_b \bar{E_b}}{v_i A + (1 - v_i)\bar{E_b}} \tag{2.28}$$

where $A$ is proportionality coefficient between the internal field inside an inclusion and external field in the host medium.

$$\bar{E_i} = A\bar{E_b} \tag{2.29}$$

For spherical inclusions, by solving a rigorous boundary problem for electrostatic potential, it is possible to express the proportionality coefficient as

$$A = \frac{3\epsilon_b}{2\epsilon_b + \epsilon_i} \tag{2.30}$$

substituting the expression for $A$ in (2.29) into (2.30) gives

$$\epsilon_{eff} = \frac{v_i \epsilon_i (\frac{3\epsilon_b}{2\epsilon_b + \epsilon_i}) + (1 - v_i)\epsilon_b \bar{E_b}}{v_i (\frac{3\epsilon_b}{2\epsilon_b + \epsilon_i}) + (1 - v_i)\bar{E_b}} \tag{2.31}$$

which is further expressed as

$$\epsilon_{eff} = \frac{v_i \epsilon_i 3\epsilon_b + (1 - v_i)(2\epsilon_b + \epsilon_i)}{v_i 3\epsilon_b + (1 - v_i)\epsilon_b (2\epsilon_b + \epsilon_i)} \tag{2.32}$$

factorizing (2.32) we have

$$\epsilon_{eff} = \epsilon_b + 3v_i\epsilon_b\frac{(\epsilon_i - \epsilon_b)}{\epsilon_i + 2\epsilon_b - v_i(\epsilon_i - \epsilon_b)} \tag{2.33}$$

This result is the famous Mawell Garnet's mixing formula for diphasic mixture with randomly dispersed spherical inclusions. For volume fraction $v_i \rightarrow 0$, $\epsilon_{eff} \rightarrow \epsilon_b$; for volume fraction $v_i \rightarrow 1$, $\epsilon_{eff} \rightarrow \epsilon_i$

### 2.12.4 Polder Van Santen (Bruggeman or De Loor) Formula

The unified mixing formula expressed as

$$\frac{\epsilon_{eff} - \epsilon_e}{\epsilon_{eff} + 2\epsilon_e + v(\epsilon_{eff} - \epsilon_e)} = f_v\frac{\epsilon_i - \epsilon_e}{\epsilon_i + 2\epsilon_e + v(\epsilon_{eff} - \epsilon_e)} \tag{2.34}$$

which was published in Table 1. of Anguelova et.al [60], for $v = 0$, we obtain the Maxwell Garnet's formula as shown in (2.33) for $v = 2$, the Polder Van Santen formula could be expressed as

$$2\epsilon_{eff}^2 + \epsilon_{eff}[1 - 2\epsilon + 3f_a(\epsilon - 1)] - \epsilon = 0 \tag{2.35}$$

$$\frac{\epsilon_{eff} - \epsilon_e}{\epsilon_{eff} + 2\epsilon_{eff}} = f_v\frac{\epsilon_i - \epsilon_e}{\epsilon_i + 2\epsilon_{eff}} \tag{2.36}$$

Expanding (2.36) gives

$$\epsilon_{eff}\epsilon_e - \epsilon_e\epsilon_i + 2\epsilon_{eff}^2 - 2\epsilon_{eff}\epsilon_e = \epsilon_{eff}f_v\epsilon_i - f_v\epsilon_e\epsilon_{eff} + 2\epsilon_{eff}f_v\epsilon_i - 2\epsilon_{eff}f_v\epsilon_e \tag{2.37}$$

This can be further expressed as

$$\epsilon_{eff}\epsilon_e - \epsilon_e\epsilon_i + 2\epsilon_{eff}^2 - 2\epsilon_{eff}\epsilon_e = 3\epsilon_{eff}f_v\epsilon_i - f_v\epsilon_e\epsilon_{eff} - 2\epsilon_{eff}f_v\epsilon_e \tag{2.38}$$

For sea foam with $\epsilon_e$ as base dielectric constant and $\epsilon_i$ as dielectric constant of inclusions, $\epsilon_i = 1$ , equation (2.38) becomes

$$\epsilon_{eff} - \epsilon_e + 2\epsilon_{eff}^2 - 2\epsilon_{eff}\epsilon_e = 3\epsilon_{eff}f_v - f_v\epsilon_e\epsilon_{eff} - 2\epsilon_{eff}f_v\epsilon_e \tag{2.39}$$

which can be written as

$$\epsilon_{eff} - \epsilon_e + 2\epsilon_{eff}^2 - 2\epsilon_{eff}\epsilon_e = 3\epsilon_{eff}f_v - f_v - 3\epsilon_{eff}f_v\epsilon_e \tag{2.40}$$

and further written as

$$2\epsilon_{eff}^2 + \epsilon_{eff} - 2\epsilon_{eff}\epsilon_e - 3\epsilon_{eff}f_v + 3\epsilon_{eff}f_v\epsilon_e - \epsilon_e = 0 \tag{2.41}$$

factorizing (2.41) gives

$$2\epsilon_{eff}^2 + \epsilon_{eff}[1 - 2\epsilon_e + 3f_v(\epsilon_e - 1)] - \epsilon_e = 0 \tag{2.42}$$

Other models could be derived from the unified mixing formula [47].

At RF and microwave frequencies, inclusions are much smaller in size as compared to the wavelength of electromagnetic waves, which implies that composite materials can be assumed to be in quasi-stable regime from an electromagnetic standpoint. Hence, the effects of propagation and multiple reflections within inclusions will be ignored.

Coherent potential (CP) and Polder van Santen(PS) models respond to multipole interaction at a higher density of inclusions by assigning to the particle surroundings the dielectric properties of the mixture. CP and PS are very significant for scattering in dense media as they are identical to the low frequency limit of their respective exact formulae which explicitly involve scattering. It was reported that dielectric measurements of dry and wet snow between 3 to 37GHz gives close results with PS model predictions and CP mixing model within low frequency limit was not suitable for modeling the permittivity of sea foam in macroscopic terms [27]. Ignoring scattering properties of sea foam, at frequencies between 1 to 37 $GHz$, mixing rules to be considered for obtaining the dielectric constant of sea foam floating on the ocean surface for $0 \leq f_a \leq 1$ in terms of suitability are listed as follows:

1. Refractive (quadratic) model
2. Looyenga (cubic) model
3. Maxwell Garnet's model
4. Polder van Santern model.

## 2.13 Critical Review of Sea foam Dielectric Constant

For fixed salinity ($34psu$), sea surface temperature ($20^{o}C$) and frequency range betweeen 1.4 $GHz$ to 37.0 $GHz$, the dielectric constant of seawater was calculated by adopting existing methods by Stogryn, Guillou, Wentz, English, Klein and Swift [26]. These calculated dielectric constants were used to evaluate the effective permittivity of sea foam. The estimate was carried out using Bruggeman and Maxwell Garnette's method. The permittivity of phytoplanktones was taken into consideration which accounts for the optical effects of impurities in sea water. Dead decay organisms and phytoplanktones contribute impurities in 95% of the

Table 2.1: Results for Dielectric Constant of sea water at fixed salinity(34psu) and SST(20 degrees celsius)

| Wentz Permittivity of seawater | frequency(GHz) | English Permittivity of seawater | frequency(GHz) |
|---|---|---|---|
| 71.8419+j65.3482 | 1.42 | 70.9660+j66.5496 | 1.4 |
| 63.4152+j34.7004 | 6.8 | 63.3405+j34.1233 | 6.8 |
| 54.2341+j37.2669 | 10.7 | 54.5612+j36.6399 | 10.7 |
| 37.1811+j37.8001 | 18.7 | 37.8060+j37.3359 | 18.7 |
| 29.4553+j35.6590 | 23.8 | 30.1423+j35.2509 | 23.8 |
| 17.9840+j28.7506 | 37.0 | 18.7605+j28.4104 | 37.0 |

worlds ocean [61]. Reported estimates of the refractive index of bulk algae with $70\% - 80\%$ water content expected range was adopted and used to estimate the effective dielectric constant of sea foam. For cells suspended in sea water, the refringence can only originate from dry mass which amounts to about $20\% - 30\%$ of the total mass. The diatom(opal) has a low refractive index of about $(1.07 \pm 0.02)$ while calcite has a value of $n = 1.19(\pm 0.01)$. The estimated imaginary refractive index of Chla dissolved in acetone is 0.0025 as reported by [61] and relative index for lipids 1.10, carbohydrates 1.15 and 1.20 for proteins. Based on these estimates a refractive index of $(1.1449 \pm 0.000065)$ was chosen.

The variation of effective dielectric constant of seawater with frequency $(GHz)$ in Table 2.1 based on Wentz and English models show that permittivity of seawater decreases with increase in frequency $(GHz)$. This is valid for the real part of seawater effective dielectric constant while the imaginary part decreases in a non-linear way.

Table 2.2 and 2.3 which illustrates variation of effective dielectric constant of seawater with frequency $(GHz)$ based on Stogryn, Guillou, Klein and Swift models behaves in similar pattern for both real and imaginary part of the effective dielectric constant of seawater, as the effective dielectric constant decreases with increase in frequency $(GHz)$.

Table 2.2: Results for Dielectric Constant of sea water at fixed salinity(34psu) and SST(20 degrees celsius)

| Stogryn permittivity of seawater | frequency | Guillou permittivity of seawater | frequency |
|---|---|---|---|
| 70.6301+j34.0112 | 1.42 | 70.3719+j63.8775 | 1.4 |
| 62.6425+j27.8729 | 6.8 | 62.3736+j33.7977 | 6.8 |
| 53.5604+j32.8054 | 10.7 | 53.3282+j36.3177 | 10.7 |
| 36.5500+j34.9728 | 18.7 | 36.5362+j36.5429 | 18.7 |
| 28.9247+j33.2233 | 23.8 | 29.4553+j35.6596 | 23.8 |
| 17.7537+j26.8554 | 37.0 | 18.1987+j27.1685 | 37.0 |

Table 2.3: Results for Dielectric Constant of sea water at fixed salinity(34psu) and SST(20 degrees celsius)

| **Klein and Swift Model for sea water** | **Frequency(GHz)** |
|---|---|
| 70.6301+j34.0112 | 1.4 |
| 62.6425+j27.8729 | 6.8 |
| 53.5604+j32.8054 | 10.7 |
| 36.5500+j34.9728 | 18.7 |
| 28.9247+j33.2233 | 23.8 |
| 17.7537+j26.8554 | 37.0 |

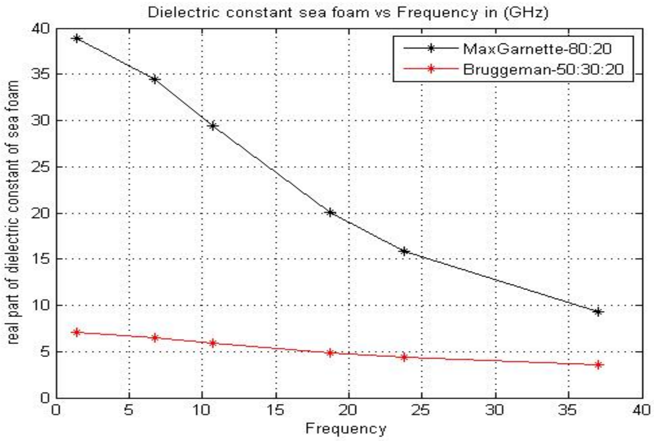

Figure 2.5: Showing Real Dielectric Constant for Maxwell Garnet's and Bruggeman's Model of Seawater

Figure 2.5 and Figure 2.6 gives variation of the effective dielectric constant of wet foam with frequency for real and imaginary part. The dielectric constant and dielectric loss of wet foam follows similar pattern as that shown by Klein and Swift model of seawater. It is is obvious that the real part of the effective dielectric constant of wet sea foam decreases with frequency ($GHz$). The dielectric loss decrease with increase in frequency up to 10 $GHz$, then increases gradually to 18.7 $GHz$ and decreases at 18.7 $GHz$ to 37 $GHz$.

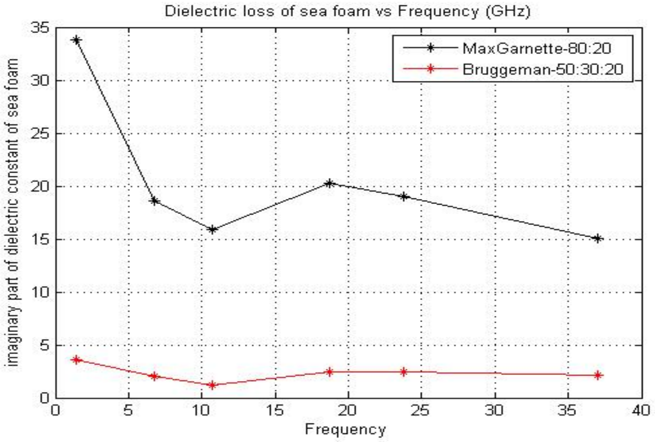

Figure 2.6: Showing Imaginary Dielectric Constant for Maxwell Garnet's and Bruggeman's Model of Seawater

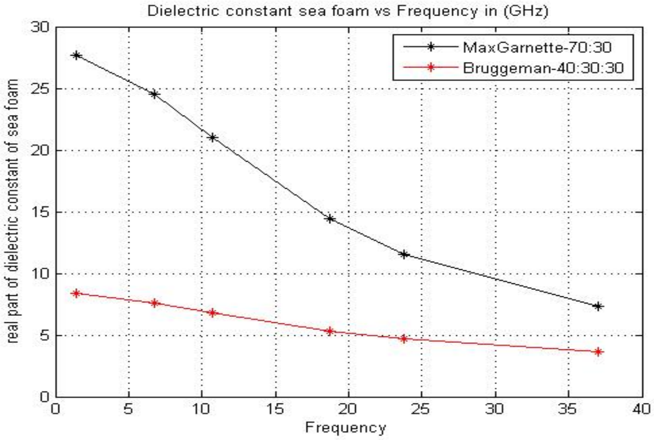

Figure 2.7: Showing Real Dielectric Constant for Maxwell Garnet's and Bruggeman's Model of Seawater

Figure 2.7 and Figure 2.8 gives variation of the effective dielectric constant of wet foam with frequency for real and imaginary part. The dielectric constant and dielectric loss of wet foam follows similar pattern as that shown by Klein and Swift model of seawater. It is is obvious that the real part of the effective dielectric constant of wet sea foam decreases with frequency $(GHz)$. The dielectric loss decrease with increase in frequency up to 6.8 $GHz$, then increases gradually to 10.7 $GHz$ and becomes constant upto 18.7 $GHz$ then decreases at 18.7 $GHz$ to 37 $GHz$.

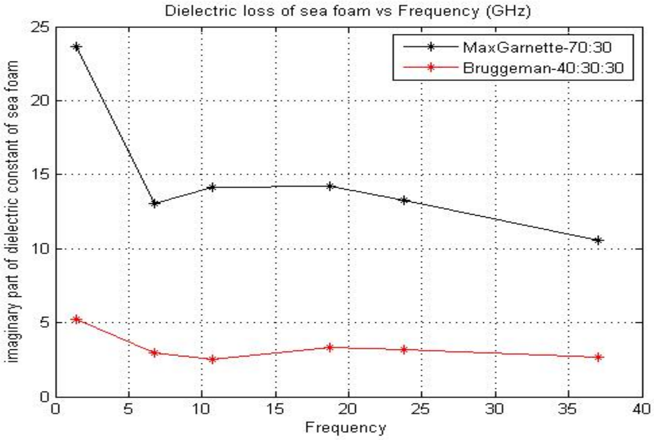

Figure 2.8: Showing Imaginary Dielectric Constant for Maxwell Garnet's and Bruggeman's Model of Seawater

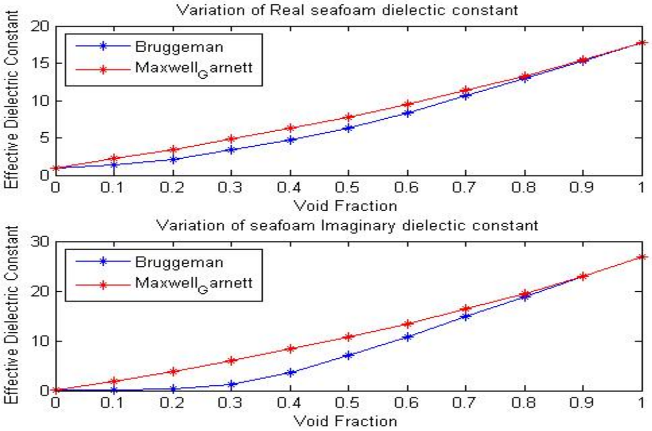

Figure 2.9: Variation of Dielectric Constant for Maxwell Garnet's and Bruggeman's Model of Seawater

The effective dielectric constant and dielectric loss of sea foam increase with increase in wet foam void fraction for both Maxwell Garnett's and Bruggeman's methods. Millimetre wave scattering properties of sea foam with known effective dielectric constants could be evaluated by the numerical methods discussed below.

## 2.14 Summary

An overview of ocean remote sensing and terminologies were explained explicitly in this chapter. We also explore the concept of polarization, single and multiple scattering, fluctuating fields, elastic and inelastic scattering as various ways of investigating and describing the interaction between electromagnetic wave and random inhomogeneous media. Propagation medium characteristics such as conductivity, dielectric constant and permeability are very significant in evaluating and predicting the emission of electromagnetic wave scattered through layers of the sea-foam and back to the surface from the ocean-bottom.

Lossy and lossless media, scattering parameters such as scattering cross-section, scattering plane, scattering efficiency and size parameters were also discussed, due to their importance in evaluating the emissivity and brightness temperature of the ocean surface. Sea-foam formation and ocean parameters such as sea-surface salinity, sea-surface temperature, and brightness temperature were briefly discussed as very important factors in modelling ocean surface wind-vector.

A short review of the effective dielectric constant of sea-water and sea-foam at millimetre wavelength was mentioned, with reference to existing models by Wentz, English, Stogryn, Guillou, Klein and Swift shown in Tables 2.1, 2.2 and 2.3. The use of effective medium theories such as Maxwell Garnett's method and Bruggeman's model to evaluate the effective dielectric constant of sea-foam at microwave frequency was described. We showed that these models are inconsistent when the constituents are interchanged from host medium to inclusion medium and vice versa.

Finally, the parabolic equation method that was used to investigate the scattering effects and emission of thermal radiation from the ocean surface shall be discussed in detail in the next chapter. Also, the inconsistency of effective medium theory prompted the need to use a discrete method for evaluating the effective dielectric constant of sea-foams modelled as sequences of thin phase screens.

# CHAPTER 3

# PARABOLIC WAVE EQUATION METHOD

The parabolic wave equation method is one of the numerous computational and numerical approximations used in modelling the interactions of EM fields with physical objects and the environment. Parabolic equation method (PEM) provides efficient approximation to the Helmholtz equation which is derived by decoupling of Maxwell's equations to evaluate radiowave propagation in random and inhomogeneous media.

Leontovich and Fock [62] introduced the parabolic wave equation which is very powerful in its application for analysing the problem of radiowave diffraction around the earth or in the atmosphere. Malyuzhinets, Fock and Wainstein generalized the PEM based on studies of ray-coordinates and transverse diffusion. Malyuzhinets unified geometric optics with the parabolic approximate method to establish an efficient theory diffraction of obstacles [63]. The split-step Fourier solution of the parabolic wave equation for solving underwater acoustic problems was developed by Tappert et.al [64].

PEM applications span from radiowave propagation problems in VHF to millimetre wave affected by atmospheric refraction, diffraction and reflection by irregular terrains and rough sea surface. More views and references of the parabolic equation method can be in [65, 66].

The principal advantages of the various parabolic wave equations derived below is that it constitutes an initial value problem in range and hence can be solved by a range marching numerical technique, given a source field distribution over depth at the initial range.

Over the years, several different solution techniques have been implemented using numerical computations, but only the split-step Fourier technique and various finite-difference/finite element techniques have gained widespread use in the underwater acoustic community.

Before going into details on the numerical solution schemes, let us brief point out some advantages and disadvantages of these two techniques. The split-step algorithm has been extensively used to solve the standard parabolic equation (SPE) ever since it was developed by Hardin and Tappert [64] in the early 1970s. The technique is computationally efficient for long-range,narrow-angle propagation problems with weak bottom interactions.

For short range, deep water and shallow water problems in general, propagation is basically more wide-angled and bottom interacting paths become more important. This requires the use of wide-angle PEs, which can be solved only by finite-difference or finite-element methods. Moreover, the strong speed and density contrasts encountered at the water-bottom interface adversely affect the computational efficiency of the split-step technique, which in cases of strong bottom interaction requires an excessively fine computational grid $(\Delta x, \Delta z)$. However, the advantage of higher computational efficiency of the split-step technique is entirely lost in situations with strong bottom interactions.

Finite-difference and finite-element solutions are applicable to PE for large arbitrary angle. The main drawback of these schemes is that, for long range and narrow angle with minimal or no bottom interaction, the split-step solution is more efficient. It remains the most adopted technique for performance prediction as it is more suitable to solving many practical ocean surface problems.

Conversely, the finite-difference and finite element schemes have widespread application for wide-angle and bottom interacting boundaries. It is prominent for providing higher accuracy in these domains.

The most recent development in terms efficient PE solution schemes is a split-step Padé approximations derived in [64–66] . The result has a considerable gain through the use of a higher range step. Thus the scheme claimed to be more than an order magnitude faster than the standard FD/FE solution techniques. This could create a unified PE solution approach where high accurate angle PEs can be solved with the efficiency of the classical split-step Fourier scheme. The fast Fourier transform provides an efficient numerical implementation but has the drawback that suitable filters must be applied to avoid aliasing.

## 3.1 Problem Formulation

For a plane incident EM wave propagating along the positive $z$ direction with an incident angle of 30° and azimuth angle $\phi = 0°$, with single frequency of 6.8 $GHz$ absorbed and scattered by a foam layer of depth $\delta_{foam} = 50\ mm$ with axis parallel or perpendicular to the plane of incidence, the total E-field ($E_T$) for horizontal polarization will be the sum of the incident and scattered field if there is negligible absorption by foam covered sea surface.

$$E_T = E_{inc} + E_{sca} \tag{3.1}$$

Otherwise,

$$E_T = E_{abs} + E_{sca} \tag{3.2}$$

The scattering of the incident plane wave in a foam covered sea surface is a three dimensional ($3D$) problem in principle but we shall reduced it to a two dimensional ($2D$) boundary value problem. Here we explore the marching potential of the split-step Fourier technique by slicing the $3D$ foam structure into $2D$ layers and determine the vertical field profiles of the propagating E-field at successive depth steps until the final depth is reached. The scatterer (foam layer) comprises of randomly distributed packed bubbles with estimated complex dielectric constant of sea foam which is a mixture of air coated with thin layer of sea water [67]. It has internal and external radii $r_{in}$ and $r_o$. The bubble size distribution $N(r)$ follows a log-normal distribution pattern. We consider a cluster of $N$ bubbles randomly packed closely such that there exist no overlap between any two adjacent bubbles. The bubbles are assumed to be spherical in shape and are placed in a finite domain in the form of a cube with dimensions L(length) = B(width) = H(height). The sea foam model is described by three regions embedded in inequality $0 \leq z \leq d$, the incident field $u(z, x, y)$ satisfies the Helmholtz equation

$$\nabla^2 u + k^2 u = 0 \tag{3.3}$$

which is a form of the Laplace equation. It was shown in section 3.2, from equation (3.5-3.9) that the inhomogeneous form of equation 3.3 is given by

$$\nabla^2 u + k^2(n^2 - 1)u = 0 \tag{3.4}$$

For narrow-angle PE approximation the analytic PE solution was expressed as equation 3.12.

The numerical implementation of the Split-step Fourier transform solution depends on the boundary conditions to be satisfied at the top and bottom of the domain. The equation provides a numerical recipe for calculating the field: transform of the initial field $u(0, x, y) = u(z_0, x, y) = u(x, y)$ from $x, y$-domains to $p, q$-domains $U(0, p, q) = U(z_0, p, q) = U(p, q)$, multiply by spectral propagator $exp(i\Delta x \frac{-p^2 - q^2}{2k})$ and inverse transform to the z-domain, multiply by the the phase screens $exp(ik(n^2(z, x, y) - 1)\frac{\Delta x}{2})$ at successive depths of sea foam layer [68].

## 3.2 Derivation of the Parabolic Wave Equation

Using a simple model which describe the propagation of a reduced function

$$\psi\left(z, x\right) = u\left(z, x\right) e^{ikz} \tag{3.5}$$

associated with the direction of propagation $z$, where $u\left(x,z\right)$ can be expressed as

$$\psi\left(x,z\right) = u\left(z,x\right)e^{ikz} \tag{3.6}$$

The Helmholtz equation of the reduced function is obtained by decoupling Maxwell's equations which yields

$$\nabla^2\psi + k^2n^2\left(z,x\right)\psi = 0 \tag{3.7}$$

where $n^2\left(z,x\right)\psi$ is the refractive index and $k$ is the wavenumber. The refractive index is assumed to possess smooth variations. The reduced function implies that the propagation energy varies slowly at angles close to the paraxial direction. The Laplacian of $\nabla\left(z,x\right)$ can be expresssed as

$$\nabla^2\psi = [\nabla^2 u + 2ik(\nabla)u - k^2u]e^{ikz} \tag{3.8}$$

$\psi$ is the product of a plane wave solution, by substituting (3.4) into (3.3) yields

$$[\nabla^2 u + 2ik(\nabla)u - k^2u]e^{ikx} + k^2n^2(x,z)ue^{ikz} = 0 \tag{3.9}$$

The Laplacian operator for $2D$ scalar wave equation can be expressed as $\left(\frac{\partial^2}{\partial x^2} + \frac{\partial^2}{\partial z^2}\right)$, in the atmosphere where $n-1$ is small, we neglect $\frac{\partial^2}{\partial x^2}$ as small (paraxial approximation) and equation (3.9) becomes

$$\frac{\partial^2 u}{\partial x^2} + 2ik\frac{\partial u}{\partial z} + k^2(n^2-1)u = 0 \tag{3.10}$$

Equation (3.10) is the standard parabolic equation and can be expressed as

$$2ik\frac{\partial u}{\partial x} = (1-n^2)k^2u - \frac{\partial^2 u}{\partial z^2} = 0 \tag{3.11}$$

The analytic solution of the parabolic wave equation can be evaluated by

$$\frac{\partial u}{\partial x} = i\{(1-n^2)k^2 - \frac{p^2}{2k}\}u = 0 \tag{3.12}$$

Substitution of $A = (1-n^2)k^2 - \frac{p^2}{2k}$ into 3.12 gives

$$\frac{\partial u}{\partial z} = iAu \tag{3.13}$$

The analytic solution of parabolic wave equation becomes

$$u(z_0 + \Delta z, x) = u(z_0)e^{iAz} \tag{3.14}$$

It is worth noting that (3.10) can be factored out to obtain

$$\{\frac{\partial}{\partial u} + ik(1-Q)\}\{\frac{\partial}{\partial u} + ik(1-Q)\} = 0 \tag{3.15}$$

This gives us

$$\frac{\partial u}{\partial z} = -ik(1-Q)u \tag{3.16}$$

and

$$\frac{\partial u}{\partial z} = -ik(1+Q)u \tag{3.17}$$

where Q is the pseudo-differential operator and is expressed as

$$Q = \sqrt{\frac{1}{k^2}\frac{\partial^2}{\partial z^2} + n^2(z,x)} \tag{3.18}$$

The outgoing parabolic equation is (3.16) and (3.17) the incoming parabolic wave equation. For a homogeneous medium with refractive index $n$, the field component $\psi$ satisfies the $2D$ scalar wave equation

$$\frac{\partial^2 \psi}{\partial x^2} + \frac{\partial^2 \psi}{\partial z^2} + k^2 n^2 = 0 \tag{3.19}$$

The refractive index varies with the range $x$ and height $z$ and equation (3.19) is a good approximation provided $n$ varies slowly with wavelength. It is worth noting that equation (3.19) is not exact [66]. If the propagation medium is vacuum, the standard parabolic wave equation in (3.19) becomes

$$\frac{\partial^2 \psi}{\partial x^2} + 2ik\frac{\partial u}{\partial z} = 0 \tag{3.20}$$

The solution of equation (3.16) is expressed as

$$u(z_0 + \Delta z, x) = u(z_0)e^{i\frac{p^2}{2k}\Delta z} \tag{3.21}$$

### 3.2.1 The Split Step Fourier Transform Solution

The split-step Fourier method is a very efficient PEM which separate the refractive effect from the diffractive part of the propagator [69]. Considering a two dimensional scalar wave equation for horizontally and vertically polarised wave, Hardin et.al introduced the split-step Fourier method which transforms the rough surface problem with propagation through a sequence of phase screens [66].

The standard parabolic equation (SPE) in equation (3.6) can be written as

$$\frac{\partial u}{\partial z} = \frac{ik}{2}(\frac{1}{k^2}\frac{\partial^2}{\partial x^2} + (n^2 - 1))u \tag{3.22}$$

Let

$$A = \frac{1}{k^2}\frac{\partial^2}{\partial z^2} \tag{3.23}$$

and

$$B = n^2(z,x) - 1 \tag{3.24}$$

Equation (3.18) becomes the standard parabolic equation (SPE) in equation (3.6) can be written as

$$\frac{\partial u}{\partial z} = \frac{ik}{2}(A+B)u \tag{3.25}$$

The analytic solution of the SPE becomes

$$u(z+\Delta z, x) = u(z,x)e^{\frac{ik}{2}\Delta z(A+B)} \tag{3.26}$$

Using

$$\delta = \frac{ik\Delta z}{2} \tag{3.27}$$

Equation (3.22) yields

$$u(z+\Delta z, x) = u(z,x)e^{\delta(A+B)} \tag{3.28}$$

Equation (3.28) is the split-step solution which represent the field propagating through a series of phase screens. The field is first propagated through a slice of homogeneous medium characterised by the exponent of $A$ and apply a phase screen modulated by refractive index variations with the exponent of B. The effect of factors in A are well illustrated using Fourier transforms but B works by simple multiplication. It is very important to note that the two operators $A$ and $B$ are not commutative except there is a constant refractive index. Hence, the split is approximate except A and B are commutative.

Taking the non-commutative property of operator A and B into considerations, we have the following forms of Split-step solutions

### 3.2.2 Two dimensional form of PE

The $2D$ standard PE in equation (3.6) can be written as

$$\frac{\partial u}{\partial z} = \frac{ik}{2}(\frac{1}{k^2}(\frac{\partial^2}{\partial x^2} + \frac{\partial^2}{\partial y^2}) + (n^2(z, x, y) - 1))u(z, x, y) \tag{3.29}$$

Let

$$df = \frac{1}{k^2}(\frac{\partial^2}{\partial x^2} + \frac{\partial^2}{\partial y^2}) \tag{3.30}$$

and

$$sf = (n^2(z, x, y) - 1)) \tag{3.31}$$

The standard $2D$ PE in 3.29 can be written as

$$\frac{\partial u}{\partial z} = \frac{ik}{2}(df + sf)u \tag{3.32}$$

The analytic solution of the standard $2D$ PE becomes

$$u(z + \Delta z, (x, y)) = u(z, (x, y))e^{\frac{ik}{2}\Delta z(df+sf)} \tag{3.33}$$

substituting the expression for $\delta$ in 3.27 into 3.33 yields

$$u(z+\Delta z,(x,y)) = u(z,(x,y))e^{\delta(df+sf)} \tag{3.34}$$

### 3.2.3 Inhomogeneous Helmholtz Equation

The Maxwell's macroscopic equations are used to describe the interaction of fields with different media and to define wave equations with particular interest in irregular hydrometeors which can be modelled as inhomogeneous dielectric medium. Maxwell's equations for time varying field is given as

$$\nabla \cdot E = \frac{\rho}{\varepsilon} \tag{3.35}$$

$$\nabla \times E = -j\omega\mu H \tag{3.36}$$

$$\nabla \cdot H = 0 \tag{3.37}$$

$$\nabla \times H = J + j\omega\varepsilon E \tag{3.38}$$

The field components, $E$,$D$,$B$ and $H$ denote the electric field, electric flux density, magnetic flux density, and the magnetic field. Their sources, the charge density $\rho$ and current density $J$ are functions of the spatial co-ordinate $(x, y, z)$. The electric flux density $D$ and electric field $E$ are mathematically related by

$$D = \varepsilon_r\varepsilon_0 E \tag{3.39}$$

Similarly, the magnetic flux density and magnetic field are related by

$$B = \mu_r \mu_0 H \tag{3.40}$$

To describe the EM wave propagation in an inhomogeneous varying space, we use the vector identity expressed below to evaluate equation (3.28)

$$\nabla \times (\nabla \times A) = \nabla(\nabla \cdot A) - \nabla^2 A \tag{3.41}$$

This becomes

$$\nabla \times (\nabla \times E) = -j\omega\mu(\nabla \times H) \tag{3.42}$$

$$\nabla \times (\nabla \times E) = -j\omega\mu(J + j\omega\varepsilon E) \tag{3.43}$$

where $J = \sigma E$, for non-conducting or charge free medium ($\sigma = 0$) the current density $J = 0$. Equation (3.35) reduces to the form

$$\nabla \times (\nabla \times E) = -j\omega\mu(j\omega\varepsilon E) \tag{3.44}$$

$$\nabla \times (\nabla \times E) = \omega^2 \mu\varepsilon E \tag{3.45}$$

For a lossless or non-conducting media the propagation constant $\gamma^2 = -\omega^2\mu\varepsilon E$, since the wave is not attenuated as it propagates we introduce the wavenumber $k = \omega\sqrt{\mu\varepsilon}$. From these assumptions we can say that

$$-\gamma^2 = k^2 \tag{3.46}$$

$$\omega^2 \mu \varepsilon E = \nabla(\nabla \cdot E) - \nabla^2 E \tag{3.47}$$

For a homogeneous medium this becomes

$$\nabla^2 E + \omega^2 \mu \varepsilon E = 0 \tag{3.48}$$

$$\nabla^2 E + k^2 E = 0 \tag{3.49}$$

where $\nabla \cdot E = 0$ but for conducting media $\nabla \cdot D = \rho$ and $\nabla \cdot E \neq 0$ in a time varying space where $\varepsilon_r = n^2$. Hence, equation (3.49) for inhomogeneous medium can be written as

$$\nabla^2 E + k^2 E = \nabla(\nabla \cdot E) \tag{3.50}$$

From equation (3.39) the electric field $E$ is

$$E = \frac{1}{\varepsilon_0} \frac{D}{n^2} \tag{3.51}$$

Applying product rule of differentiation yields

$$\nabla \cdot E = \frac{1}{\varepsilon_0} \nabla \cdot \frac{D}{n^2} = \frac{1}{\varepsilon_0} \frac{1}{n^2} \nabla \cdot D + \frac{1}{\varepsilon_0} D \cdot \nabla \frac{1}{n^2} \tag{3.52}$$

substitute $\nabla \cdot D = 0$ and $E = \frac{1}{\varepsilon_0}\frac{D}{n^2}$ into equation (3.52) to obtain

$$\nabla \cdot E = n^2 E \cdot \nabla(\frac{1}{n^2}) \tag{3.53}$$

$$\nabla \cdot E = n^2 E \cdot (\frac{-2}{n^3})\nabla(n) \tag{3.54}$$

$$\nabla \cdot E = -\frac{2}{n} E \cdot \nabla(n) = -2E(\frac{1}{n})\nabla(n) \tag{3.55}$$

$$\nabla \cdot E = -\frac{2}{n} E \cdot \nabla(n) = -2E(\frac{1}{n})\nabla(n) \tag{3.56}$$

$$\nabla \cdot E = -2E \cdot \nabla(\ln n) \tag{3.57}$$

Hence,

$$\nabla(\nabla \cdot E) = \nabla\{-2E \cdot \nabla(\ln n)\} \tag{3.58}$$

The inhomogeneous Helmholtz equation can be expressed as

$$\nabla^2 E + k^2 E = \nabla\{-2E \cdot \nabla(\ln n)\} \tag{3.59}$$

The equations expressed above show that Maxwell's equations are set of relations linking the values of a number of quantities that describe electric E and magnetic H fields. Therefore, the foundation of our theoretical approach in this study are the Maxwell's macroscopic equations that describe the origin of fields propagating in space and time, where the physical properties of the material medium (characterized by $\epsilon$ and $\mu$) are continuous. Equation (3.59) implies that the gradient of the logarithm of the refractive index is relatively small.

## 3.3 Summary

The parabolic equation have been widely used to solving EM scattering and radio wave propagation problems. It has been realized that PE method may be adopted as an efficient numerical tool for EM field calculation and may bridge the gap between rigorous numerical methods such as MOM and FDTD, and asymptotic methods based in ray tracing or physical optics.

Applying PE method can avoid the limitation of CPU time and memory required by these rigorous methods. It can also reduce the error caused by high frequency approximations. SSFT and finite difference algorithms is very popular for solving PE. SSFT technique is frequency domain algorithm, when used to solve the PE, the step of SSFT is almost free from restrictions and can be selected as large discrete element. Therefore, the SSFT algorithm of PE is suitable for large scale wave propagation problems.

SSFT algorithm is complicated when dealing with irregular boundary, so it is not easy to be used in the calculation of electromagnetic scattering problems with complex structures.

FD algorithm is carried out through the mesh of computation domain, and process computations according to the electromagnetic field on the adjacent grid-points. Since precise mesh is used, FD algorithm can directly calculate the field on arbitrary boundaries, therefore it is more convenient to deal with irregular boundaries, but the discretized step in FD is restricted by the wavelength.

Therefore, we must take small step, which results in large scale matrix operations. Solving the high-frequency, large-scale wave propagation problems based on PE, FD algorithm is slow and computer memory consumption is also high.

This chapter reviews the parabolic equation method and split-step Fourier transform which is widely used in (2-D) two dimensional radio-wave and ground wave propagation modelling. Maxwell's equation as a governing equation provides us with the mathematical relationship between the electric and magnetic field and their constitutive parameters such as conductivity, permittivity and permeability. Decoupling of Maxwell's equations helps us to obtain the inhomogeneous Helmholtz equation which describes the random propagation media with small varying effective dielectric constant.

The next chapter deals with sea-foam model implementation as a random distribution of spherical bubbles coated with thin layer of sea-water.

# CHAPTER 4

# SEAFOAM MODEL IMPLEMENTATION

## 4.1 Modelling of Sea-foam properties and shape

### 4.1.1 Introduction

Earlier models used empirical microwave emissivity [6, 70–73] to estimate the effect of foam presence at the crest of the ocean surface. This was achievable by passive microwave remote sensing measurements. These measurements were done by assuming physical micro-structure of foam and foam layer thickness. Measurement procedures were empirical fitting and based on experimental data.

Foam dynamics has gained prominence in recent times. Huang et. al proposed a composite model of foam scatterers and two scaled wind driven rough sea surface [74]. In [75], controlled field experiments were used to measure foam dynamics and the microwave emissivity of calm water. A fully polarimetric passive model for wind generated and foam covered rough sea can be represented by empirical Durden-Versecky spectrum [76]. [77] used a face-centred cubic (FCC) structure to model high density spheres which represents air bubbles placed inside a cube. Ding et.al [77] reported that polarization and frequency of the brightness temperatures are influence by the physical micro-structure properties of foam and foam layer thickness.

We shall focus on developing a theoretical model for evaluating millimetre wave scattering by oceanic foam. Numerous methods such as Radiative transfer theory, Quasi-crystalline approximation method, Monte-Carlo and other hybrid methods are available for the evaluation of millimetre wave scattering by sea surface and sea foam [1, 31]. At low wind speed and frequency, scattering becomes negligible due to low foam coverage on the sea surface and the wavelength of the incident EM radiation becomes larger than the size parameter of sea water while absorption effect becomes dominant. Sea surface roughness is responsible for scattering at microwave frequency under moderate wind conditions due to increased interactions at the air-sea interface as the wavelength of the incident field becomes smaller than the size parameter of the particles in sea water. Under strong winds, sea surface roughness and breaking waves are actuated which leads to increased foam coverage on the sea surface and foam presence on the sea surface accounts for significant scattering. These effects contribute high transmission losses, which makes scattering effect significant.

A new approach of modelling sea foam is proposed to account for the optical properties such as foam layer thickness, foam void fraction, bubble radius, bubble size distribution and bubble shape. The bubble size distribution and bubble radius are evaluated by inverse cumulative error function using the Newton-Raphson method [68]. Three dimensional sphere packing approach is applied for filling the bubbles in the domain. The domain could be a cube, cuboid, prism or cylinder, and the packing is done such that no two bubbles overlapped. The random close packing method of spheres is used for the irregular arrangement of spheres so that they are densely packed [78] with the bubble volume fraction of 74% while the space within the cube or other domain geometry is 26% for maximum packing density. Finally, Split-Step Fourier solution of the Parabolic Wave Equation (PWE) [66] is used to evaluate the refractive and the diffraction effects of the scattered field.

The sea foam model is implemented by considering the 3-dimensional (3-D) sphere packing into a 3-D finite domain in the form of a cube/box. We adopt sphere packing of $N$ randomly distributed spheres, having maximum radius 0.95 $cm$ and minimum radius 6.9 $mm$ with restriction on overlap between two spheres at a given neighbourhood. These values were obtained from the bubble size distribution with geometric mean radius $\mu_g = 500\ \mu m$ and geometric mean deviation $\sigma_g = 2.0$ [79] . The steps taken to implement the inverse method and obtain the bubble size distribution $N(r)$ and log-normally distributed bubble radii is explained in section 4.3. The structure of sea foam could be ideally described by spherical bubbles with void fraction of 99% for dry foam and void fraction of 1% for wet foam. The effective dielectric constant for dry foam is close to that of air while the effective dielectric constant of wet foam is close to that of seawater.

A realistic model of the bidirectional scattering effects of sea foam requires knowledge of its optical properties and geometrical characteristics of the sea foam layer. These characteristics are bubble thickness, bubble size distribution (BSD), and foam void fraction [79]. Reported evidence of microwave remote sensing considered foam layer thickness and void fraction [80] as important parameters that give adequate description of the sea foam layer .

Foam layer thickness in the open sea varies with coalescence and breaking of whitecaps which depend on wind speed. Physical quantities such as wind speed, air temperature, refractive index, wind waves in form of gravity or surface waves are prone to certain level of randomness. Wind speed actuate sea surface roughness and breaking waves. Sea surface roughness and breaking waves are more intense at high wind speed which is a major factor responsible for the creation of sea foams. The presence of foams on the ocean surface has profound effect on brightness temperatures usually measured by microwave radiometers [79]. Although foam typically covers only a few percentage of sea surfaces, increasing foam coverage on the sea surface substantially increases the sea surface emissivity.

## 4.2 Random Sphere Packing Problem

Sphere packing as a form of optimization problem involves packing objects together (usually inside a container), as densely as possible. The container could be a two or three dimensional convex region, or an infinite space and objects of same or different shapes, some or all of the objects must be packed into the container. Usually the packing must be without any overlap with an aim to obtain the maximum density. According to [81] the densest packing of circles in a plane is the hexagonal arrangement where centre of circles are arranged in a hexagonal lattice. The Packing density of this arrangement is given by

$$h = \frac{\pi}{\sqrt{12}} \approx 0.9069 \tag{4.1}$$

Axel Thue in 1890 proved that the hexagonal lattice is the densest of all possible circle packings, both regular and irregular.

In sphere packing, the close packing of spheres in 3D is the regular (or lattice) arrangement of identical spheres in space so that they are as densely packed as possible. There are three kinds of lattice arrangements or periodic packings for identical spheres namely cubic lattice, face-centred cubic lattice, and hexagonal (close-packed) lattice [82]. These lattice arrangements or periodic packings can easily be formed by hand. The face-centred cubic lattice, and hexagonal (close-packed) lattice arrangements are discussed with detail in [82]. The Kepler Conjecture [83] in 1611 stated that no packing of identical spheres in 3D has density greater than that of the face-centred cubic or hexagonal packing. This density is expressed as

$$h = \frac{\pi}{3\sqrt{2}} \approx 0.74048 \tag{4.2}$$

And perhaps this was the first investigation about the densest packing of spheres. This conjecture was proved by Thomas Hales using computer calculations but it is not yet completely verified [84]. The packing density of random close packing is about 0.64 [85]. The random close packing of spheres is the irregular arrangement of spheres so that they are as densely packed as possible and this packing technique will be used in the sphere filling problem.

Numerous studies of random sphere packing in multi-dimensions have been carried out via Monte-Carlo Method (MCM) or Molecular Dynamics simulations. These studies were reportedly achieved by randomly placing spheres in 3-Dimensional box to obtain a highly densed packed box. Particle scaling procedures or compression algorithm could be used to obtain higher packing fractions. Marsaglia's proposed test of random number generators has a close relationship with the initial placing of spheres in a box [85].

## 4.3 Inverse Cumulative Distribution Method

The inverse cumulative distribution function method (CDF) also called inversion method is used for transforming uniform random variates monotonically into non-uniform variates. It has been extensively used in cases where the inverse CDF can be simulated directly from a simple function or analytically. Numerical methods are deployed when the CDF is represented by simple functions that are available in computing libraries. Monte Carlo method in principle exploit the inverse CDF approach.

Over the years, several inverse CDF's have been used for estimation of particle size distribution (PSD) but the direct and rejection methods are popular [86]. The direct method also known as inversion method, transform method or Smirnov transform requires inverting a cumulative probability function $F(X) = P_r(X \leqslant x)$ linked with the random variable $U(0,1)$. $U(0,1)$ is mapped with $F(X)$ such that $0 \leqslant F(X) \leqslant 1$. Hence, we can generate random samples of $X$ from the CDF via inversion. The inverse transform is used when $F^{-1}$ can be determined by either analytical or empirical expressions.

To implement the inverse method, we generate uniform random variates of size 1000 and assume a standard normal CDF $\Phi(X)$. The relationship between $\Phi(X)$ and $U$ is given by

$$\Phi(X) = U \tag{4.3}$$

where $X = \Phi^{-1}(U)$, $X$ denotes the Normal distribution which is characterized by $X \sim N(\mu, \sigma^2)$ where $\mu$ is the mean $= 0$ and $\sigma^2$ the variance $= 1$. Hence, $X \sim N(0, 1)$ is the true representation of the standard Normal distribution. The random uniform generator could be generated using linear congruential generator but we used built-in Fortran random number generator. The standard normal CDF $\Phi(X)$ can be expressed mathematically in terms of the error function and complementary error function as follows:

$$\Phi(X) = \frac{1}{2} + \frac{1}{2} erf(\frac{X}{\sqrt{2}}) \tag{4.4}$$

$$\Phi(X) = \frac{1}{2} erfc(\frac{-X}{\sqrt{2}}) \tag{4.5}$$

The inverse method of generating random Normal deviates from uniformly distributed random variate $U(0, 1)$ is obtained by solving the equation below

$$\Phi(X) = U \tag{4.6}$$

where $U$ is the uniformly distributed random variate between 0 and 1 and $erfc(X)$ is the complementary error function of variable $X$. We solve for $X$ numerically using Newton Raphson's iteration. Equation (4.4) is written as

$$\Phi(X) - U = 0 \tag{4.7}$$

Equation (4.5) conforms with $f(X) = 0$ which is a root finding problem and is solved by deploying Newton-Raphson method. The complementary error function $erfc(X)$ is obtained from the error function $erf(X)$ by the relation

$$erfc(X) = 1 - erf(X) \tag{4.8}$$

The error function can be written as

$$erf(X) = \frac{2}{\sqrt{\pi}} \int_0^X \exp(-t^2)dt \tag{4.9}$$

and the complementary error function expressed as

$$erfc(X) = \frac{2}{\sqrt{\pi}} \int_0^\infty \exp(-t^2)dt \tag{4.10}$$

$$erfc(X) = e^{-X^2} erf(X) \tag{4.11}$$

Where erfc(X) is referred to as the scaled complementary error function used to prevent arithmetic underflow. Abramowitz and Stegun give approximations of varying accuracies which helps us to choose the fastest error function approximation suitable for this application. We choose an approximation with a maximal error of $1.2 \times 10^{-7}$ for any real argument.

$$erf(X) = \begin{cases} 1 - \tau & \text{for} \quad X \geq 0 \\ \tau - 1 & \text{for} \quad X < 0 \end{cases} \tag{4.12}$$

with

$$\tau = texp(-x^2 - 1.26551223 + 1.00002368t + 0.37409196t^2 + 0.09678418t^3 - 0.18628806t^4$$
$$+0.27886807t^5 - 1.13520398t^6 + 1.48851587t^7 - 0.82215223t^8 + 0.17087277t^9) \tag{4.13}$$

and $t = \frac{1}{1+0.5|X|}$ or $t = \frac{1}{1+0.5|X/\sqrt{2}|}$

The inverse error function was computed with the approximation below

$$erf^{-1}(X) = sgn(X)\sqrt{\sqrt{(\frac{2}{\pi a} + \frac{ln(1-X^2)}{2})^2 - \frac{ln(1-X^2)}{a}} - (\frac{2}{\pi a} + \frac{1-X^2}{2})} \tag{4.14}$$

The cumulative distribution function $\Phi(X)$ and the inverse error function $erf^{-1}(X)$ are related as shown

$$\Phi^{-1}(X) = \sqrt(2)erf^{-1}(2X-1) \tag{4.15}$$

The steps taken to implement the inverse method are stated below.

1. Generate uniform random variate $U(0,1)$ of size $N = 1000$.

2. Transform uniform random variate to normal variate using inverse method by computing the error function $erf(X)$, complementary error function $erfc(X)$, inverse error function $erf^{-1}(X)$ and cumulative distribution function CDF $\Phi(X)$.

3. Compute the probability density function ($PDF$) of the inverse error function by Newton's method and store the inverse error function solution as $X$ and the Newton's iteration values as $XN$.

4. Assuming a mean $\mu = 2.0$ and standard deviation $\sigma = 0.5$, the scaled normal variate $\bar{X}$ was computed using

$$\bar{X} = X\sigma + \mu \tag{4.16}$$

5. Assuming a geometric mean $\mu_g = 500\mu$m and geometric standard deviation $\sigma_g = 2.0$ as suggested in the table below. The bubble radii $r_b$ was computed for $N = 1000000$ using

$$r_b = \mu_g + exp(\bar{X} ln(\sigma_g)) \tag{4.17}$$

with the $r_b$ known it was easy to compute the BSD $N(r)$ using

$$N(r) = \frac{1}{ln(\sigma_g) r_b \sqrt{2\pi}} exp(-0.5ln(\frac{r_b - \bar{r}}{\sigma_g})^2) \tag{4.18}$$

where $\bar{r} = \mu_g$ is the mean bubble radius.

Table 4.1 shows several cumulative distribution functions used for inverse transformation.

| Distribution | CDF F(X) | Inverse |
|---|---|---|
| Exponential | $1 - e^{-\frac{x}{a}}$ | $-a \ln(u)$ |
| Extreme value | $1 - e^{-e^{(\frac{x-a}{b})}}$ | $a + b \ln\ln(u)$ |
| Geometric | $1 - (1-p)^x$ | $\frac{\ln u}{ln(1-p)}$ |
| Weibull | $1 - e^{(\frac{x}{a})^b}$ | $a(lnu)^{\frac{1}{b}}$ |

The inverse CDF method are used in estimation of the bubble size distribution and bubble radius.

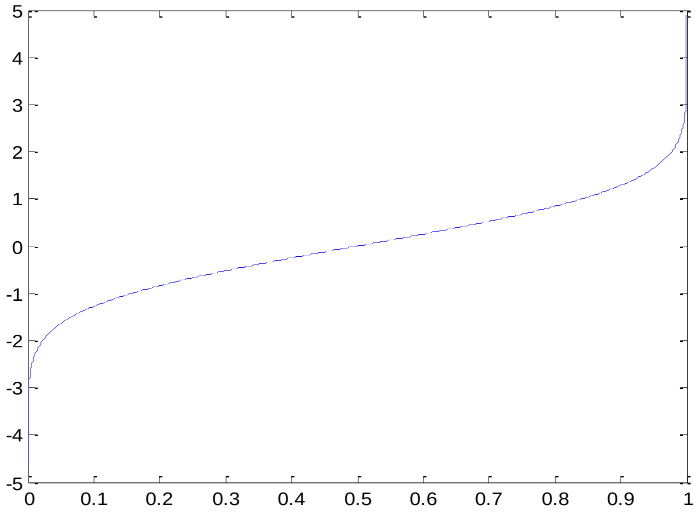

Figure 4.1: Plot of the inverse error function against uniform random variate U(0,1).

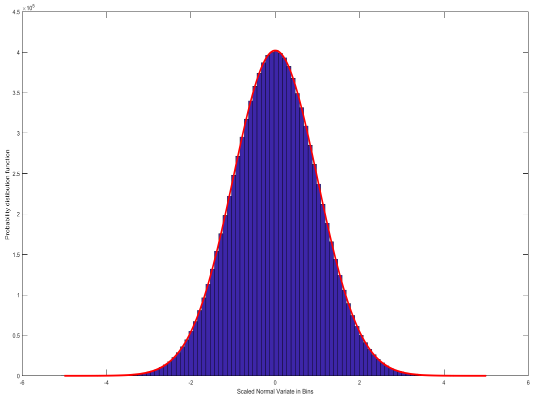

Figure 4.2: Histogram of the PDF of Standard Normal Variate

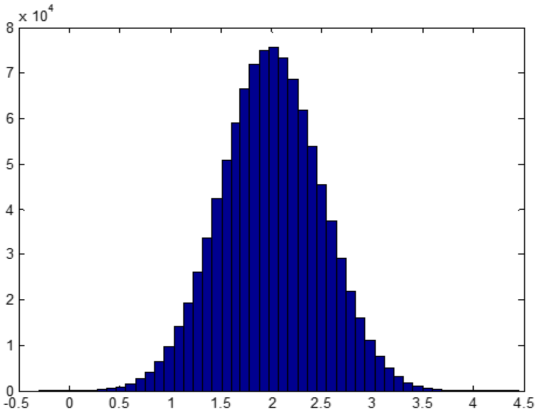

Figure 4.3: Histogram of PDF of Scaled Normal Variate

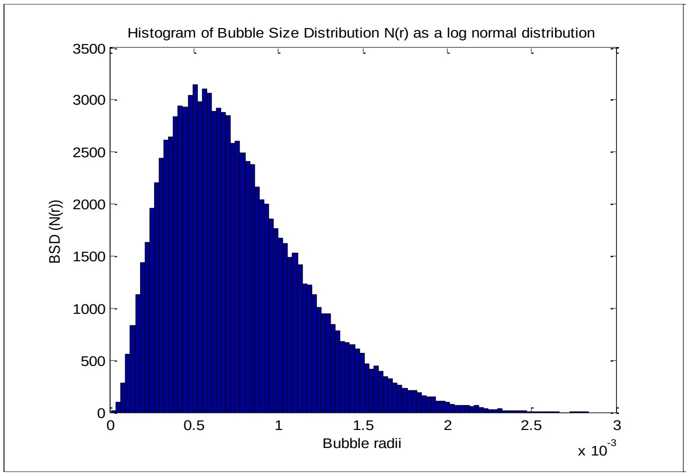

Figure 4.4: Histogram of $N(r)$ against Bubble radii for $\sigma_g = 0.5$

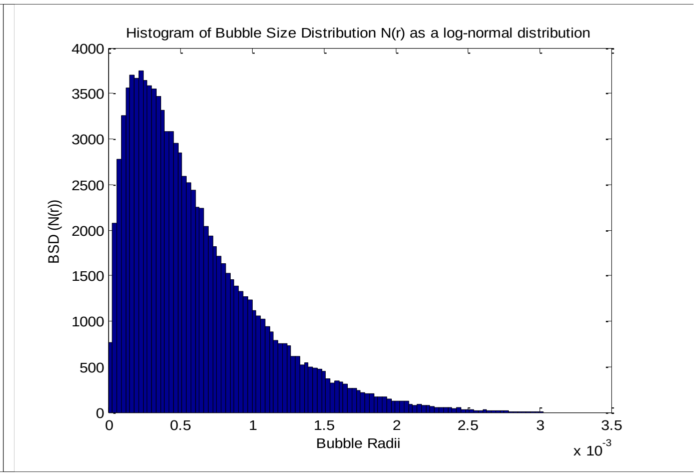

Figure 4.5: Histogram of $N(r)$ against Bubble radii for $\sigma_g = 0.2$

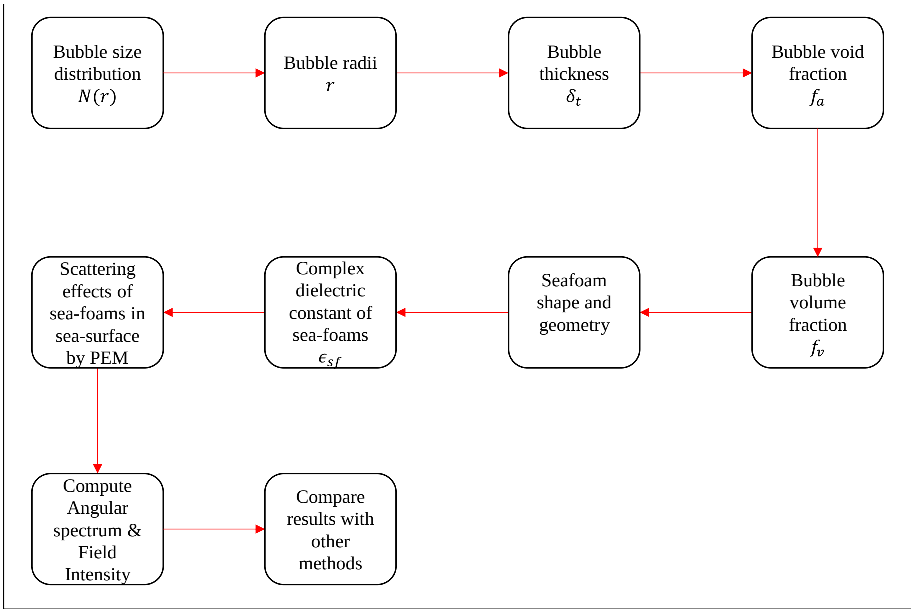
Bubble size distribution $N(r)$
Bubble radii $r$
Bubble thickness $\delta_t$
Bubble void fraction $f_a$
Bubble volume fraction $f_v$
Seafoam shape and geometry
Complex dielectric constant of sea-foams $\epsilon_{sf}$
Scattering effects of sea-foams in sea-surface by PEM
Compute Angular spectrum & Field Intensity
Compare results with other methods

Figure 4.6: Structure of Research Implementation

## 4.4 Bubble Size Distribution and Bubble Radius

Bubble size distribution (BSD) and bubble radius are very significant in modelling forward and backscattering effects of sea foam. The bubble size distribution gives us insight into the shape, thickness and foam void fraction.

It was reported that three types of functions have been deployed to describe BSDs in the foam and bubble layer. They are: gamma distribution [87], power-law distribution [88] and log-normal distribution [89]. The bubble size distribution is a distribution of bubble radii from $r_{min}$ to $r_{max}$ where $r_{min}$ denotes minimum radius and $r_{max}$ the maximum radius. The choice of modelling the BSD as a log-normal distribution was based on the fact that distribution of particles, chemicals and organisms are often log-normal [90]. It was asserted that many chemicals and atmospheric physical properties follow a log-normal distribution law such as size distributions of aerosols and clouds and turbulent processes parameters [91]. The distribution of sensitivity to fungicides in populations and distribution of population size for microbiology and phytomedicine application are log-normal [92], many species in the plant and animal communities follows log-normal distribution [93]. Finally, many applications of log-normal distribution is associated with characterization of structures in food technology and food processing engineering. For example, size and frequency of particles, droplets and bubbles generated in dispersing processes [94].

Anguelova et al. carried an extensive probe on bubble cloud size distribution at varying wind speeds and depths under sea water. [48] asserted a $0.1 - 1$ $mm$ bubble radius range in the foam layer with values probably falling from $0.1 - 0.25$ $mm$. In [95] a review of foam layer thickness $\delta = r_{in} - r_o$ was carried out and it was reported that bubble thickness spans from

1 $cm$ to $\geqslant 12$ $cm$ under strong wind speed and 0.1 $cm$ to $\geqslant 1$ $cm$ under low wind speed.

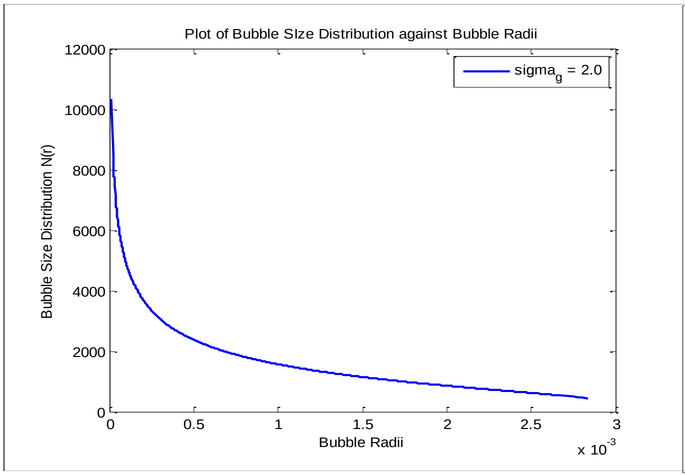

Figure 4.7: BSD $N(r)$ against Bubble radii for $\sigma_g = 2.0$ and $\mu_g = 500 microns$

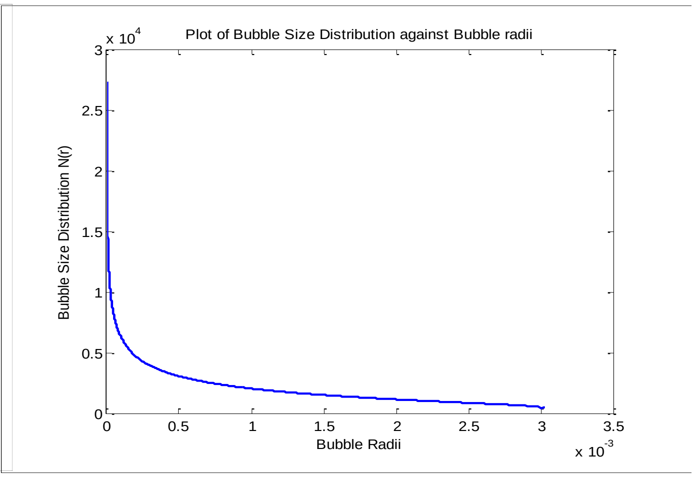

Figure 4.8: BSD $N(r)$ against Bubble radii

### 4.4.1 Foam Layer Thickness

It was earlier stated that sea foam structure can be described a a diphasic mixture of air trapped in seawater. For simplicity, sea foam as cloud of bubbles are assumed to have spherical shapes and seen as two concentric spheres with inner and outer radii. Sea foam can be classified into wet foam and dry foam. The dry foam is a larger volume air coated with thin layer of seawater while the wet foam is smaller volume of air coated with less thinner layer of seawater. The foam layer thickness is the difference between the inner radius and the outer radius. Let $\delta$ denote the foam layer thickness such that

$$\delta = r_{in} - r_o \tag{4.19}$$

The growth and decay of oceanic whitecaps determines foam layer thickness variation in the open ocean and depends on the wind speed. An artificial foam with layer thickness distribution between 0.5 to 4 *cm* with an obvious peak of about 3.3 *cm* and small peak at 1.3 *cm* was reported. Whitecap fraction $W$ is a function of wind speed and foam layer thickness $\delta$. The whitecap coverage increase as wind speed increases, several reporters proposed that each layer of foam has the same thickness and total depth from 9 *mm* to 90 *mm*, which is the most probable thickness in the ocean [79] and a good reason for choosing a foam depth of 50 *mm* as well as dividing it into 5 $2D$ slices.

### 4.4.2 Foam Void Fraction

Foam void fraction describes the volume of bubble in the sea foam layer, it can be expressed as a function of the number of bubbles per unit volume and the volume of the polydispersed spherical sea foam. It is defined mathematically in [60] as

$$f_a \approxeq f_b = \frac{1}{N_b} \sum_{N_b} \frac{\frac{4\pi r_o^3}{3}}{\frac{4\pi r_{in}^3}{3}} \Rightarrow (\frac{r_o}{r_{in}})^3 = s_f^3 \tag{4.20}$$

where $f_a$ denotes the foam void fraction and is approximately equal to the bubble void fraction $f_b$, $N_b$ denotes the number of bubbles, $r_o$ and $r_{in}$ are the outer and inner radius respectively while the scale factor is $s_f^3$. We can evaluate the total number of bubbles given the volume fraction of bubbles $f_v$. $f_v \approxeq 0.74$ for the highest packing density of random packed spheres. However, $f_v$ can be expressed mathematically [60] as

$$f_v = N_{tot} \frac{4\pi}{3} \int_{r_{min}}^{r_{max}} r^3 N(r) dr \tag{4.21}$$

and $N_{tot}$ is obtained from (4.21) as

$$N_{tot} = \frac{3f_v}{\int_{r_{min}}^{r_{max}} 4\pi r^3 N(r)dr} \tag{4.22}$$

We can assume that the bubble size distribution function $N(r)$ is a log-normal distribution which matches experimental results in [96]. $N(r)$ is given by

$$N(r) = \frac{N_{tot}}{r\sqrt{2\pi}\ln\sigma_g} exp[\frac{-(\ln(\frac{r}{r_{gmean}}))^2}{2(\ln\sigma_g)^2}] \tag{4.23}$$

$\sigma_g$ is the geometric standard deviation of the log-normal distribution and $r_{gmean}$ denotes the geometric mean radius of the bubbles.

Calculation of the bubble size distribution function $N(r)$ and bubble radius $r$ will help us to implement the sea foam model.

## 4.5 Sphere Packing Model and Implementation

The non-linear formulation is prominent as it maximizes the spheres radius and assumes that the spheres do not overlap and fits inside the cubic object. Non-linear models have been very successful in packing infinite number of identical items into an N-dimensional object, all with fixed dimensions. Most non-linear model based strategies are common such that the number of non-overlapping constraints between items is $O(N^2)$, where $N$ is the number of items being packed. To be able to solve problems that involves packing large number of items, it is vital to develop a methodology and their corresponding data structure to reduce asymptotic computational complexity based on efficient algorithms.

### 4.5.1 Non-linear Model

The non-linear model used is structured as follows:

Minimize: the object dimensions

Subject to: fitting the items inside the object

Non-overlapping of items

The object dimension should be minimized so we can pack the items as densely as possible. We need to define the constraints of the items to be placed within the object. Finally, the non-overlapping constraint between the items.

### 4.5.2 Non-overlapping Constraints

The region bounding the object will be divided into small grid like regions and the given spheres are distributed randomly within the region using probability distribution function. This section describes the non-overlapping constraints. A methodology is described on strategies developed for the N-body problem to reduce the complexity of computing the non-overlapping constraints. We denote $c_i, i = 1, \ldots N$ as the centres of $N$ spherical items with radii $r_i, i = 1, \ldots N$. The models for non-overlapping between two spheres is given as

$$d(c_i, c_j) \geqslant (r_i + r_j), \forall i < j \tag{4.24}$$

where $d(c_i, c_j)$ denotes the Euclidean distance between sphere $i$ and sphere $j$.

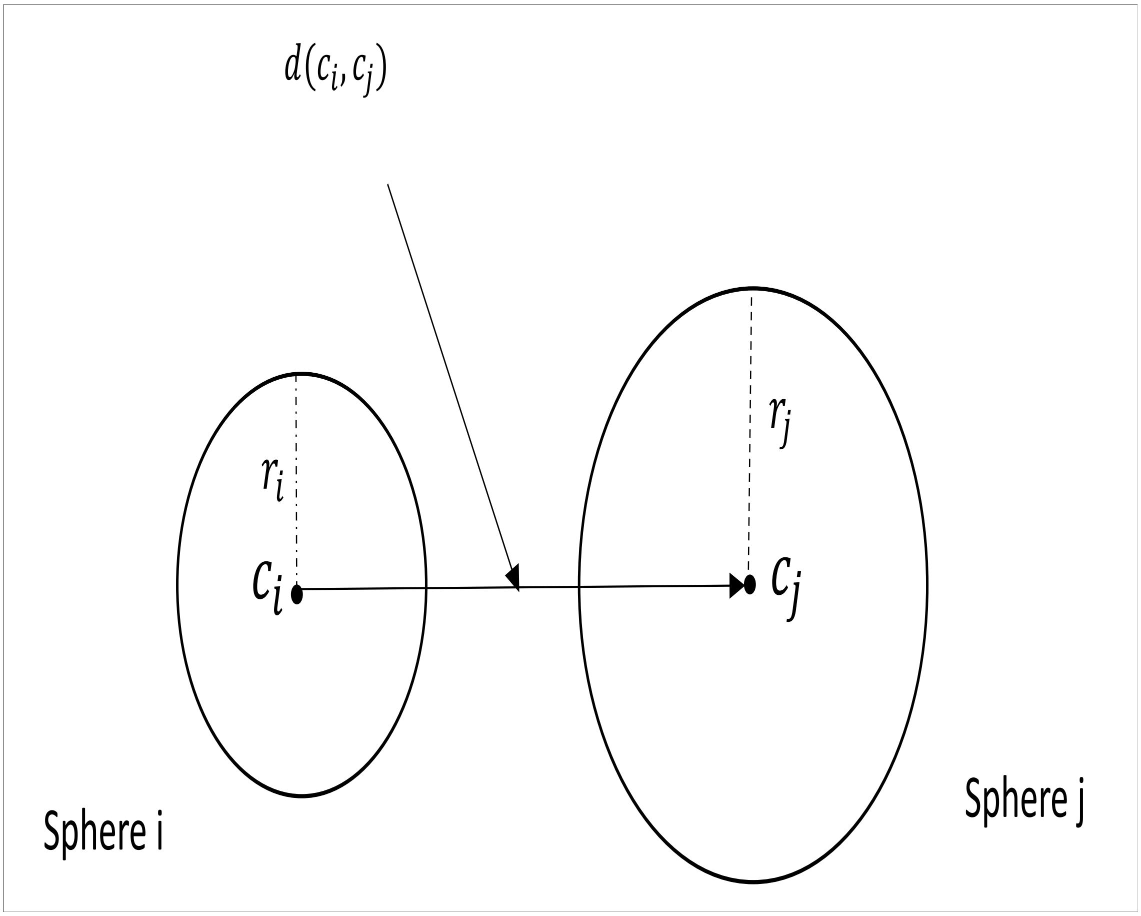

Figure 4.9: Two spheres cannot overlap if the distance between their centres is greater or equal to the sum of their radii

### 4.5.3 Bubble Placement and Three Spheres Intersection

The problem of bubble placement requires the bubble to touch three other bubbles in 3D. This can be equivalently stated as that three augumented spheres intersect at the centre of the fourth bubble. The concept of bubble intersection can be descibed with the 2D diagram below.

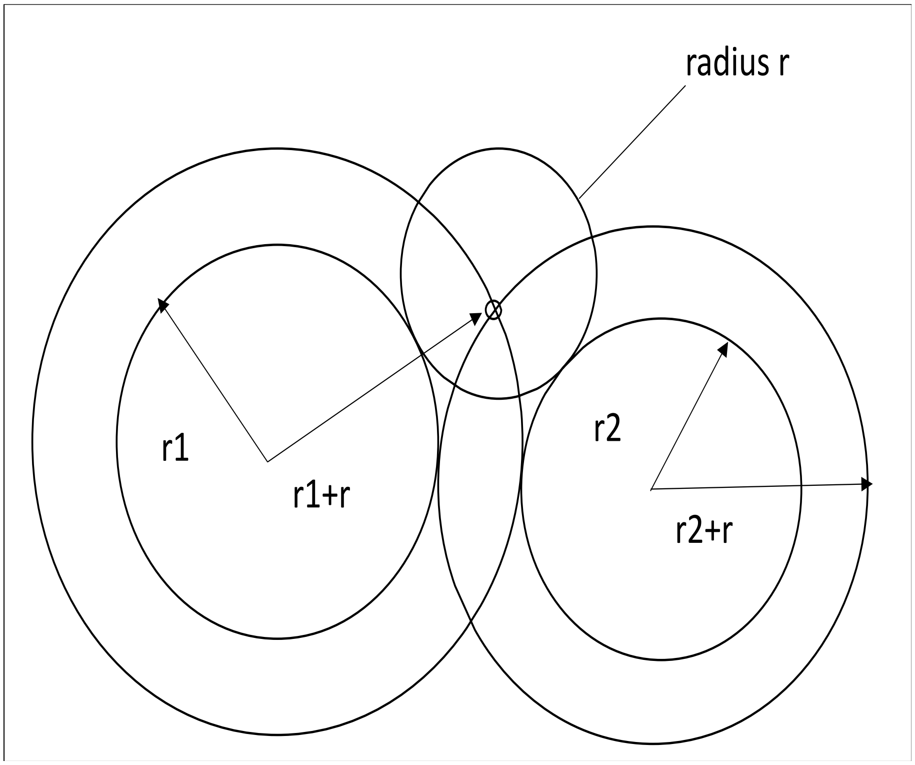

Figure 4.10: Intersection of three spheres within a plane

Solutions to the problem lie on a line which passes through the two possible solution points that two circles intersect in. In three dimensions, we can implement the same idea and find that the intersection of any two spheres is defined by a plane which contains the circle of intersection. An equilibrium point in 2D would be intersection of circles of radius $(r_1 + r)$ from centre of bubble 1 and $(r_2 + r)$ from centre of bubble 2. If we have two spheres then the quadratic forms that define them are given by,

$$Q_1 = \begin{pmatrix} 1 \\ x \\ y \\ z \end{pmatrix} \begin{pmatrix} c_1 & -x_1 & -y_1 & -z_1 \\ -x_1 & 1 & 0 & 0 \\ -y_1 & 0 & 1 & 0 \\ -z_1 & 0 & 0 & 1 \end{pmatrix} \begin{pmatrix} 1 \\ x \\ y \\ z \end{pmatrix}. \tag{4.25}$$

$$Q_2 = \begin{pmatrix} 1 \\ x \\ y \\ z \end{pmatrix} \begin{pmatrix} c_2 & -x_2 & -y_2 & -z_2 \\ -x_2 & 1 & 0 & 0 \\ -y_2 & 0 & 1 & 0 \\ -z_2 & 0 & 0 & 1 \end{pmatrix} \begin{pmatrix} 1 \\ x \\ y \\ z \end{pmatrix}. \tag{4.26}$$

Taking the difference between these quadratic forms gives (in vector notation)

$$2(x_1 - x_2).x + (c_2 - c_2) = 0 \tag{4.27}$$

which is the equation of a plane. We can write this in homogeneous coordinates as

$$\begin{pmatrix} p_0 \\ p_1 \\ p_2 \\ p_3 \end{pmatrix} \begin{pmatrix} 1 \\ x \\ y \\ z \end{pmatrix} = 0 \tag{4.28}$$

with $p_0 = c_2 - c_1, p_i = x_{1,i}, i = 1, 3$

With three bubbles, there are three planes $(p, q, r)$, obtained from the pairs, $Q1$,$Q2$, then $Q2$,$Q3$, then $Q2$,$Q1$ and which intersect generally in just one point. The solution to this construct the four minors with respect to $\begin{pmatrix} u_0 u_1 u_2 u_3 \end{pmatrix}$ of the matrix,

$$\begin{pmatrix} u_0 & u_1 & u_2 & u_3 \\ p_0 & p_1 & p_2 & p_3 \\ q_0 & q_1 & q_2 & q_3 \\ r_0 & r_1 & r_2 & r_3 \end{pmatrix} \tag{4.29}$$

This is equivalent to doing a matrix inversion. The answer is the homogeneous coordinates of the intersection point (which can be scaled to inhomogeneous coordinates). Incidentally in the unlikely case that the solution is not unique (as, for example, the planes all share a line in common). A vector or zeros would be obtained.

If $(1, x, y, z)$ are coordinates of a point $P$ and $(1, u, v, w)$ are coordinates of a plane $Q$. Then

$$(1, u, v, w).(1, x, y, z) = 0 \tag{4.30}$$

which implies that $P$ lies on the plane $Q$. The angle between point $P$ and plane $Q$ is mathematically expressed as

$$\theta = \cos^{-1} \frac{P \cdot Q}{|P||Q|} \tag{4.31}$$

and

$$P \cdot Q = |P||Q| \cos\theta \tag{4.32}$$

For $P \cdot Q = 0$ to be true, the angle $\theta$ between point P and plane Q should be equal to $90^o$ or $\frac{\pi}{2}$ radians. It is easily seen that P is perpendicular or orthogonal to the plane Q.

Figures 4.11-4.14 comprise of 3D (three dimensions) slices of randomly packed spheres in a unit cube. These slices were later translated to 2D slices of solid annuli. The conversion of 3D to 2D slices was achieved by calculating the radii of each individual circle intersecting the slices. The 2D slices were discretized with grid sizes $\Delta x$ and $\Delta y$ which leads to intersection of the circles bounded in a unit square with some grid points. The grid sizes were sampled such that the edges of the circles circumference which intersects with grid points farther from the inner grids bounded by the circles are negligible.

We were able to estimate the effective dielectric constant of sea foams by modelling the randomly packed bubbles as concentric spheres in 2-D where the outer sphere is seawater while the inner sphere contains about $80 - 95\%$ air, with these estimates we were able to calculate the area of the annulus (ring) as the radii of the outer spheres are known.

Table 2.1, 2.2 and 2.3 illustrate the dielectric constant of seawater at fixed salinity 34psu and sea surface temperature $20^oC$. The dielectric constant of air is taken as $1.00005 + j0.0000$. The area of the circles in each slice was calculated using the total number of grid points. The effective dielectric constants of sea foams at frequencies between 1.4 $GHz$ and 37.0 $GHz$ were calculated for 5 slices of randomly packed air-bubbles coated with thin layer of seawater.

Table 4.1 below gives the estimated effective dielectric constant of sea foam computed at frequencies 1.42 $GHz$, 6.8 $GHz$ and 23.8 $GHz$ for 5 $2D$ slices of randomly packed air bubbles covered with thin layer of seawater.

Table 4.1: Results for Dielectric constants of seafoam at frequencies of 1.42 $GHz$, 6.8 $GHz$ and 23.8 $GHz$ for 5 $2D$ slices of randomly packed air bubbles covered with thin layer of seawater.

| **Frequency in GHz** | **1.42GHz** | **6.8GHz** | **23.8GHz** |
|---|---|---|---|
| Slice 1 | 1.1598+j0.1297 | 1.1294+j0.1063 | 1.0008+j0.1267 |
| Slice 2 | 1.2032+j0.1562 | 1.1665+j0.1280 | 1.0117+j0.1526 |
| Slice 3 | 1.2563+j0.1876 | 1.2122+j0.1537 | 1.0263+j0.1833 |
| Slice 4 | 1.3060+j0.2148 | 1.2556+j0.1760 | 1.0427+j0.2098 |
| Slice 5 | 1.3457+j0.2357 | 1.2904+j0.1932 | 1.0567+j0.2302 |

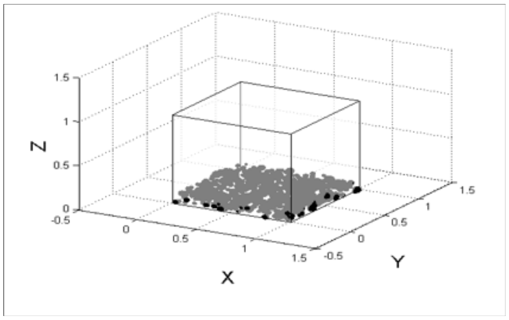

Figure 4.11: Randomly packed spheres in slice 1

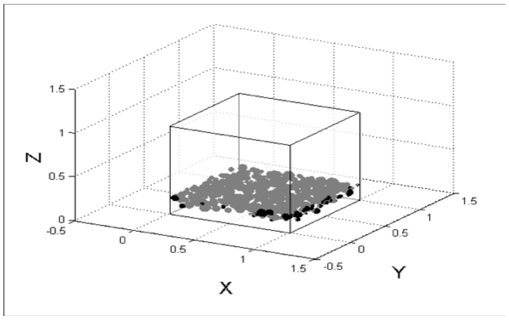

Figure 4.12: Randomly packed spheres in slice 2

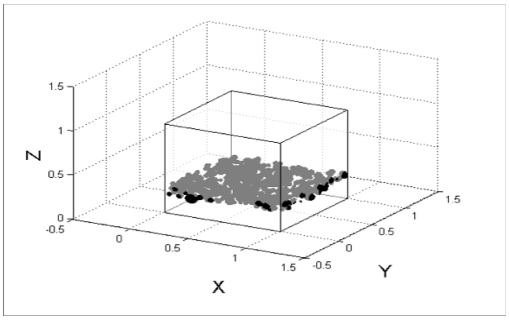

Figure 4.13: Randomly packed spheres in slice 3

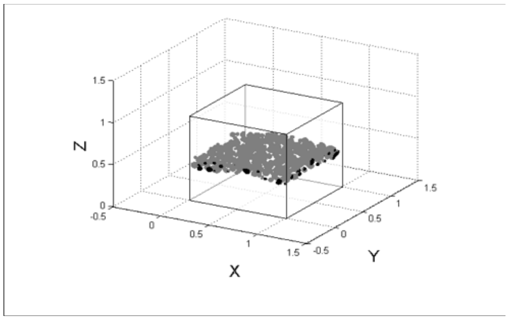

Figure 4.14: Randomly packed spheres in slice 4

## 4.6 Summary

In this chapter, we reviewed earlier models used to estimate the effect of sea-foam presence at the crest of ocean surface. Foam parameters such as shape, foam layer thickness, foam void fraction, physical micro-structure of foam, bubble radii, bubble size distribution and ocean wind vectors play significant role in ocean remote sensing.

Due to the need to obtain densely packed bubbles in (2-D) two dimension which best describe our model, as a thin phase scattering screen, we explain the various forms of closely packed sphere packing approach. The sea-foam model is developed as 3-D spheres packed into a 3-D finite domain mainly a cube/box. This was converted into sequences of 2-D thin layers which is suited for EM propagation using the split-step Fourier transform method. As earlier reported, SSFT scheme is a range matching one-way propagation that is widely used in 2-D radio-wave and ground wave propagation modelling.

A detailed description of how the 2-D sequences of thin foam layers were obtained is explained in this chapter. We also enumerate the generation of randomly distributed spheres and the procedures of fitting them into a finite 3-D cube/box.

Finally, we estimated the effective dielectric constant of sea-foam by modelling the randomly closed packed bubbles as concentric circles in 2-D, with the outer circle as sea-water and the inner circle as air. The next chapter explains the propagation of EM waves through the sequences of thin phase scattering screens using the split-step Fourier transform method.

# CHAPTER 5

# CODE IMPLEMENTATION OF SPLIT-STEP FOURIER METHOD

## 5.1 Introduction

In this chapter, the implementation process of the split-step Fourier method (SSFM) on the developed model of sea foam discussed in chapter 4 for investigation of the perturbations that the sea foam layer introduces when an incident plane wave travels through $n$ 2-D slices of sea foam layers containing isotropically distributed bubbles is reported. Early stages of the development of this algorithm was based on split-step PE for tropospheric radiowave propagation. PETOOL a parabolic equation toolbox has been developed in MATLAB with a user-friendly Graphical User Interface (GUI) for modelling radio-wave propagation over variable terrain and through homogeneous and inhomogeneous atmosphere which helps to ease the understanding process of how the split-step Fourier method works [97], [98].

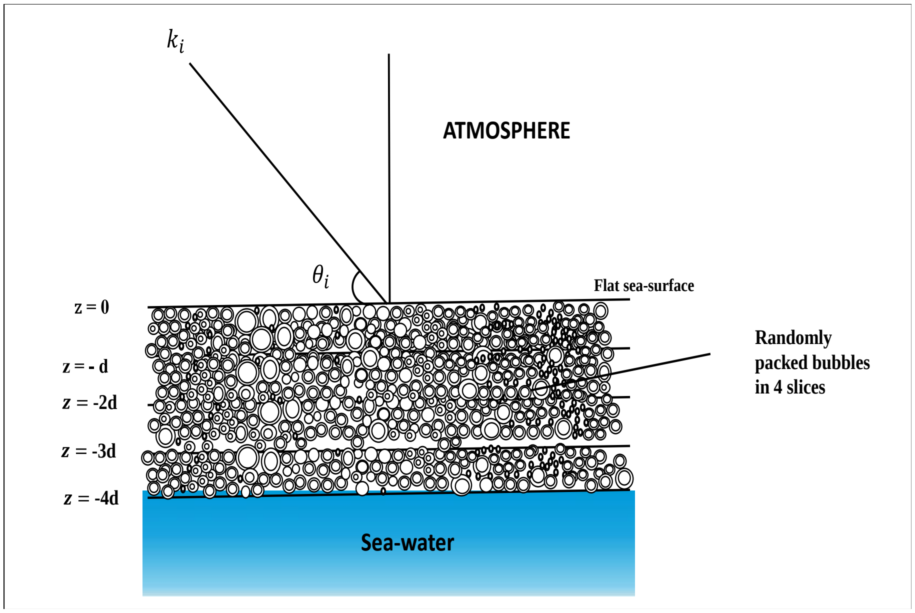

Figure 5.1: Schematic of incident E-Field propagated through slices of sea foam layers

## 5.2 Investigative approach

Considering a rough sea surface with height $z$ and an incident plane wave propagating at small angles from a preferred direction known as the paraxial direction. For simplicity, it is important that the rough sea surface is flattened or modelled as a smooth surface and the propagation medium treated as an inhomogeneous medium. The idea is to obtain sufficient information that will help to evaluate the scattering and absorption characteristics of oceanic foams which are visible at the rough sea surface in the form of oceanic whitecaps.

The flattening of the rough sea surface takes account of the fact that the interaction of high frequency energy at millimetre wavelength will result in significant diffuse reflections at the sea surface thereby attenuating the EM radiation.

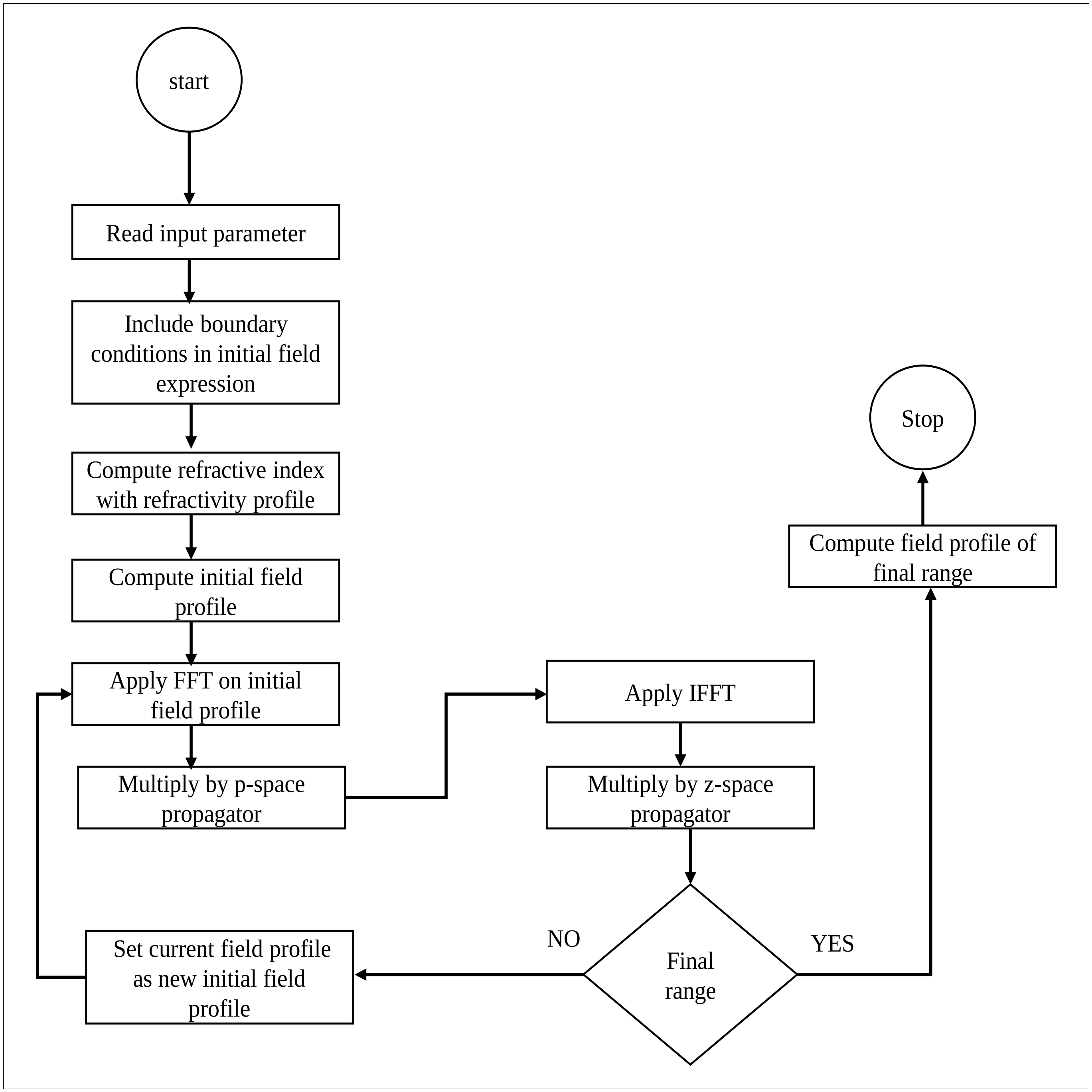
start
Read input parameter
Include boundary conditions in initial field expression
Compute refractive index with refractivity profile
Compute initial field profile
Apply FFT on initial field profile
Multiply by p-space propagator
Apply IFFT
Multiply by z-space propagator
Final range
NO
YES
Set current field profile as new initial field profile
Compute field profile of final range
Stop

Figure 5.2: Flowchat of Split-step Fourier Transform Algorithm

### 5.2.1 SSFM Computation for Investigation of seafoam layer model

The computer routines for the development of the sea foam layer model were written in FORTRAN 95 language with Silverfrost FTN95 compiler using a 64 bit machine in double precision. The SSFM code for observation of the amplitude and phase variations of the horizontal polarzised (TE) and vertical polarized (TM) electric field due to its interaction with $n$ layers of seafoams was written in MATLAB R2018b.

The SSFM routine was implemented to propagate the plane wave

$$E(z0, x, y) = E(z, x, y)exp(ik_x x + ik_y y + ik_z z) \tag{5.1}$$

with $E(z, x, y) \approx 1$ along the forward $+z$ direction. The plane wave was propagated through five (5) $2D$ slices of sea foam layers each containing isotropically distributed bubbles. The slices are equally dimensioned with area 50 $mm$ × 50 $mm$ with layer thickness $\delta_t = 0.1$ $mm$ separating adjacent layers. The foam layer thickness $d \gg \lambda_0$ is required to account for attenuation (E-field amplitude variation) and diffuse scattering (E-field phase variation) as the incident E-field travels through slices of the sea foam layer.

WindSat frequency channels (6.8 $GHz$, 10.8 $GHz$, 18.7 $GHz$, 23.8 $GHz$, 37.0 $GHz$) were used for propagation of the E-field through slices of sea foam layers. The following input parameters were used in investigating the perturbations of the amplitude and phase of E-field introduced by the presence of sea foams on the surface of seawater.

1. Speed of light ($C_0$) = $2.99 \times 10^8$ $ms^{-1}$
2. The frequency ($f$) in $GHz$

3. Wavelength ($\lambda_0$) $= C_0/f$

4. k-vector ($k_0$) $= 2\pi/\lambda_0$

5. Two polar angles namely zenith $\theta_i$ and azimuth $\phi_i$ are used to specify the direction of propagation of the incident wave.

6. Refractive indices of the sea foam layer $n(z,x)$ in each slices of randomly distributed bubbles.

7. Dimension of scatterer 50 $mm$ × 50 $mm$ × 50 $mm$ volume of $3D$ box and 50 $mm$ × 50 $mm$ area of $2D$ slices.

8. Foam layer thickness between adjacent slices ($\delta_t$)

9. Fourier transform length ($fr_l$) $= 256$

The incident wave is tilted from the normal so that there is an initial phase gradient along the surface of the sea foam model. This is done by assigning values of $0 \leq \theta_i \leq 90°$ for the zenith angle and fixed azimuthal angle for example $\phi_i = 0°$ or $45°$.

For each of the angles $\theta_i$ we compute the E-fields that emerges from the foam layer and calculate the FFTs of the fields. The contour plots of the intensity of the scattered field is displayed. Range of the depths of foam for realistic scenerios were observed to investigate the influence of the foam as a thin phase scattering screen and deep phase scattering screen. Checks for phase coherence of the wave field were done to see if there was strong coherence (coherent phase) or weak phase coherence (incoherent phase) between adjacent slices. For instance the difference between the phase of the E-field in layer 1 and the E-field in free space.

The figures shown in 5.13-5.18 illustrate random phase variations as the E-field propagates through thin slices of sea foam layers. At higher frequencies and large foam layer thickness, the E-field becomes more random which describe the scattering effect due to the presence of sea foam in the surface of sea water. The sea foam layer in this scenario acts like a deep phase scattering screen. The field is more perturbed and scattered as it propagates through the slices to the bottom of the sea foam layer. Conversely, the sea foam layer acts like a thin phase scattering screen at low frequencies and thin foam layer thickness, which leads to strong phase coherence between neighbouring sea foam layers and weak phase coherence between sea foam layers far apart from each other.

It is expected that the amplitude and phase variation will be intense for large sea foam layer thickness (deep scattering screen) and at high WindSat frequencies channels (10.8 $GHz$, 18.7 $GHz$, 23.8 $GHz$, 37.0 $GHz$). Hence, we expect more incoherent phase variations as the E-field will be more randomise as it propagates down to the bottom of the sea foam layer.

The field observations will continue as we propagate backwards to account for the Fresnel's reflection factor and its contibution to the field pertubations in the sea foam layer. The forward FFT of the diffuse scattered field estimates the angular spectrum of the field that emerges from the foam layer which will show the amount of distortion of the E-field due to the presence of sea foam in the surface of sea water. These conclusions will be drawn by comparing the contour plots of the angular spectrum at low and high frequencies and deep and thin phase scattering screens for two or more propagation angles. The essence is to establish that the extinction of the E-field is due to diffuse scattering caused by the effect of seafoams in sea water which introduces random phase fluctuations as the E-field propagates through the sea foam layer. or that the extinction is due to absorption as the sea foams acts like a black body at certain frequencies.

The analytical solution of the standard PE in 3.34 was solved by decomposition from its spatial form $(x, y)$ domains to spectral form $(p, q)$ via forward FFT and reformed to its original form by backward FFT. The refractive indices of each 2D slice $n(z, x, y)$ varies with the depth $z$ and length $x$ of the domain. This seems appropriate as the equation is solved at each grid-size $\Delta z$ such that the refractive indices vary through each grid-step size with respect to $z$.

The numerical split-step PE solution for $j = 1, 2, \dots M$ is expressed as

$$u(z_0+j\Delta z, x, y) = exp\big[i\frac{k}{2}(n^2-1)\Delta z\big]F^{-1}\left[exp\left(-i\frac{(p^2+q^2)\Delta z}{2k}\right)F\big[u(z_0+(j-1)\Delta z, x, y)\big]\right] \tag{5.2}$$

The was used to compute the intensity of the field $u(z, x, y)$ along the depth $z$ with steps of $\Delta z$, for known source distribution $u(z_0, x, y)$. We used a 2-D array to store the transverse field profiles of $Nz$ vertical depth points and $Nx$ and $Ny$ discrete width and length, with replacement. Here, the initial field $u(z_0, x, y)$ profile generated as an incident plane wave was propagated along +z direction from $z_0$ to $\Delta z$, for $j = 1$ using 5.2 until the solution $u(z_0 + j\Delta z, x, y)$ is obtained. This process is repeated for $j = 1, 2, \dots M$, the field solution for $j = 2$ is used as the initial field for $u(z_0 + 2\Delta z, x, y)$ and the depth field profiles are computed for each width and length of the domain until the desired depth is reached.

**Algorithm 1** Numerical Computation of Split-Step Fourier Transform

```
procedure SSFM($u_0, u^n, N$)
    REQUIRE : Input parameters ($f_0, c_0, \lambda_0, k_0, ref_{index}, N, u_0$)
    $f_0 \leftarrow$ frequency (GHz)
    $c_0 \leftarrow$ speed of light(m/s)
    $\lambda_0 \leftarrow c_0/f_0(mm)$
    $k_0 \leftarrow$ wavenumber ($mm^{-1}$)
    $N \leftarrow$ Fourier mode or transform length
    $u_0 \leftarrow$ Propagating initial field
    $ref_{index}(x_j, z_n) \leftarrow$ COMPLEX REFRACTIVE INDICES OF SEA FOAM LAYER
    COMPUTE VECTOR $u(0, x)$ as initial plane wave at $z = 0$
    SET SPATIAL GRID POINTS ON X DOMAIN
    $x_J, J = 1..........L$
    SET SPECTRAL GRID POINTS ON P DOMAIN
    $P_k, k = 1..........L$
    Set step-size $\Delta z$
    ENSURE: $U(z + \Delta z, x)$ or $u^n$ vector containing the output propagated wave
    Initializations
    for $J = 1 : N_x$ do
        $u(J) \leftarrow exp(ik0x(J)(cos\theta - 1))$
    end for
    $u_0 \leftarrow u(J)$
    $u^n \leftarrow u_0$
    $P \leftarrow \frac{2\pi}{L}(-N/2 : 1 : N/2 - 1)$
    LOOP OVER THE PROPAGATION INTERVAL
    If Number of Slices $\leq 10$
    for $n = 1 : M$ do
        $u^{(n+1/2)} \leftarrow exp(i\Delta z \frac{P^2}{2k_0})u^n$ Computing the Diffractive term
        $\hat{u}^{(n+1/2)} \leftarrow FFT(u^{(n+1/2)})$ Compute forward fast Fourier transform
        $\hat{u}^{(n+1)} \leftarrow exp(-i\Delta z k_0((ref_{index}(x_j, z_n)^2 - 1)))\hat{u}^{(n+1/2)}$ Compute Scattering term
        $u^{n+1} \leftarrow IFFT(\hat{u}^{(n+1)})$ BACKWARD OR INVERSE FFT
        RETURN $u^n$
    end for
    else
    Exit loop
    EndIf
end procedure
```

### 5.2.2 Sea-foam Boundary Condition

Forward propagation above the sea-surface is implemented using split-step Fourier technique. Here, we use Fresnel's boundary condition. To model the dielectric interface in the split-step Fourier resolution, the Fresnel's reflection coefficient is one of the popular methods deployed for both TE and TM modes. The field continuity at the interface is insured by the use of reflection coefficient above the sea-foam layer and transmission coefficient in the sea-foam layer. For slice 1 to slice 5, where the contrast in average dielectric constant of the layers are negligible, the E-fields are propagated stepwise in depth but for the sea-foam layer bottom and seawater interface where there is significant difference in dielectric constant, the Fresnel's reflection coefficient is multiplied with the E-field at the sea-foam bottom layer and propagated forward in the spectral domain.

### 5.2.3 Phase Fluctuations in Thin Phase Scattering Screen at Low Windsat Frequencies and slice thicknessses

The extended medium $0 \leq d \leq 50\ mm$ were modelled as a series of random phase-screens with irregularities in refractive index. For slice thicknesses $\delta_t = 0.1\ mm$ and $\delta_t = 0.2\ mm$ which acts as thin phase scattering screens and low WindSat frequency channels of 1.42 $GHz$ and 6.8 $GHz$ the field fluctuations due the propagation of a coherent plane wave through series of sea foam layers are shown in figures 5.13-5.18. We observe that the phase factors $exp(j(\theta_m - \theta_n))$ are random and don't cancel out. The E-fields don't vary uniformly between $-\pi$ to $\pi$ as is the case for the coherent incident plane wave which appears similar to the propagated plane wave in free space as shown in figures 5.7-5.8. Also, the phase delays don't present an inverted phase of the incident field and don't sum up to zero. Hence, we can say that the phase variations of the E-fields through the slices of seafoam with refractive index $n(z, x, y)$ heterogeneities appears incoherent which exemplifies diffuse scattering. The contour plots of the phase differences between successive slices of seafoam shows varying phase distributions that are randomized through the sampled domain for both TE and TM polarizations.

The deep phase scattering screen ($\delta_t = 2\ mm$) at low WindSat frequency channels of 1.42 $GHz$ and 6.8 $GHz$ when propagated upon reveals similar behaviour as the propagated E-field through the slices of the seafoam layer appears incoherent for successive slices but there is an exception as shown in figure, the bottom seafoam layer where the E-field obeys Huygen's principle as the phases interfere constructively to form an inverted phase (reflected) plane wave. The phase of the reflected E-field varies uniformly between $-\pi$ to $\pi$ as was the case of the incident coherent E-field, the phase distributions within the sampled domain are not random and do not cancel out (destructive interference). The field at the bottom of the seafoam layer is said to be coherent reflected field.

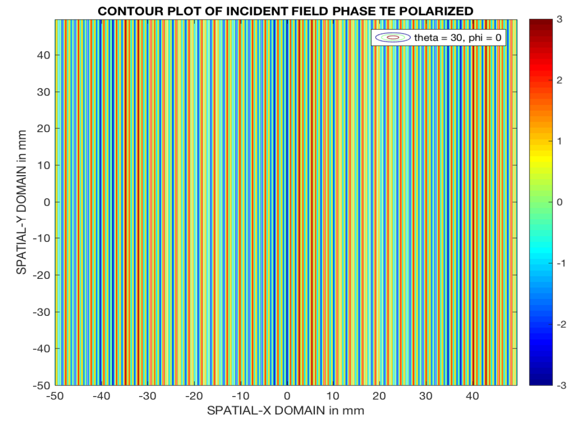

Figure 5.3: The phase gradient of an incident plane wave for horizontal polarization (TE) with zenith $\theta_i = 30°$ and azimuth $\phi = 0°$ as a function of the spatial coordinates X and Y of the propagation media at 1.42 $GHz$.

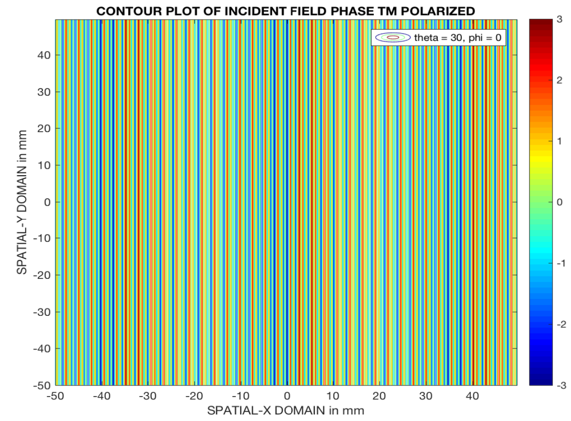

Figure 5.4: The phase gradient of an incident plane wave for vertical polarization (TM) with zenith $\theta_i = 30°$ and azimuth $\phi = 0°$ as a function of the spatial coordinates X and Y of the propagation media at 1.42 $GHz$.

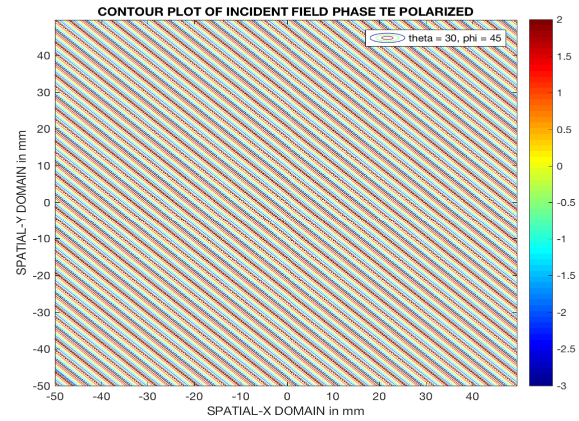

Figure 5.5: The phase gradient of an incident plane wave for horizontal polarization (TE) with zenith $\theta_i = 30°$ and azimuth $\phi = 45°$ as a function of the spatial coordinates X and Y of the propagation media at 1.42 $GHz$.

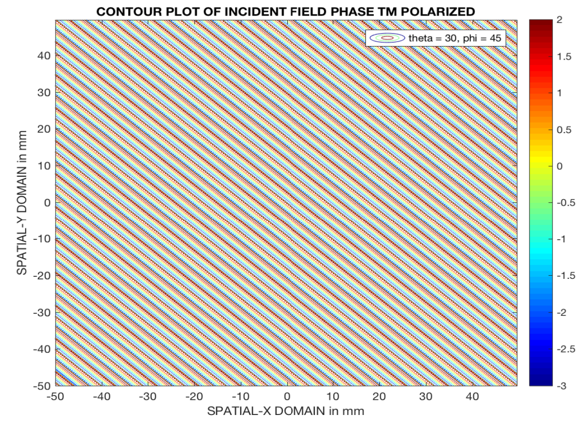

Figure 5.6: The phase gradient of an incident plane wave for vertical polarization (TM) with zenith $\theta_i = 30°$ and azimuth $\phi = 45°$ as a function of the spatial coordinates X and Y of the propagation media at 1.42 $GHz$.

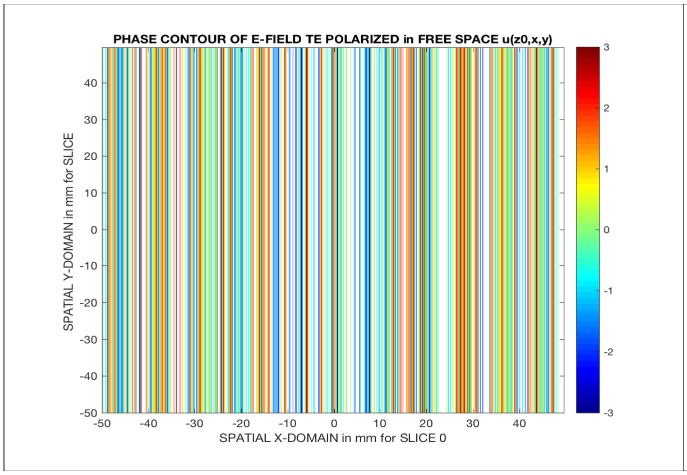

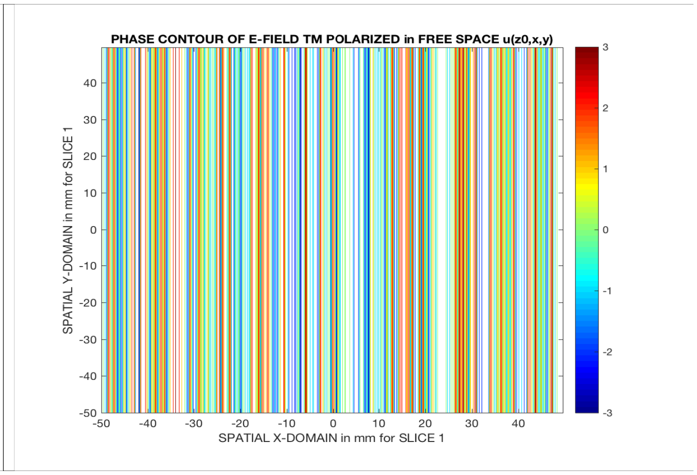

Figure 5.7: The phase gradient of E-field in free space for horizontal polarization (TE) with zenith $\theta_i = 30°$ and azimuth $\phi = 0°$ as a function of the spatial coordinates X and Y of the propagation media at 6.8 $GHz$.

Figure 5.8: The phase gradient of E-field in free space for vertical polarization (TM) with zenith $\theta_i = 30°$ and azimuth $\phi = 0°$ as a function of the spatial coordinates X and Y of the propagation media at 6.8 $GHz$.

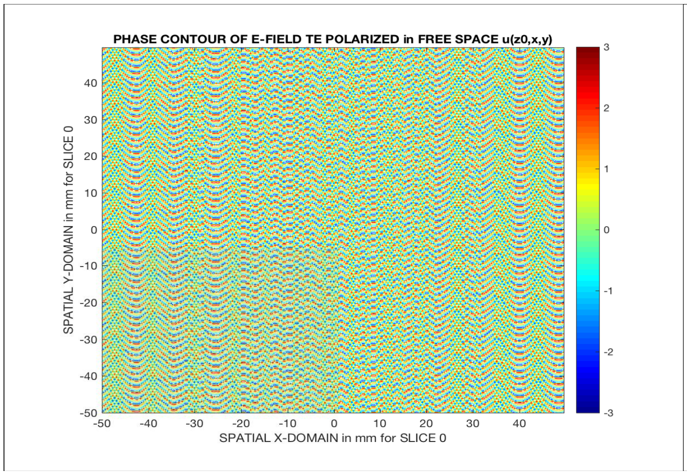

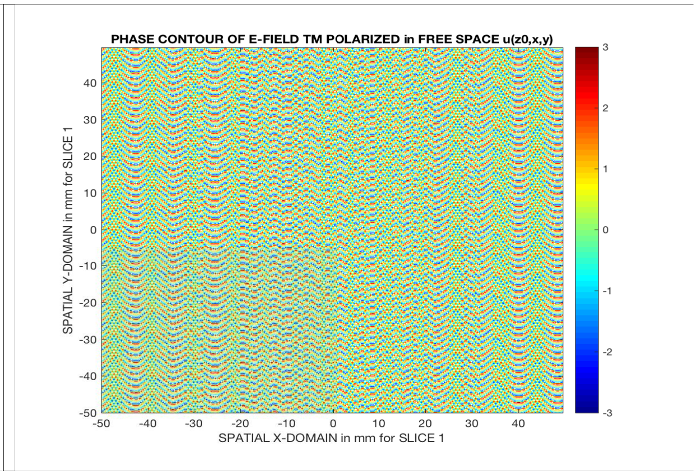

Figure 5.9: The phase gradient of an E-field in free space for horizontal polarization (TE) with zenith $\theta_i = 30°$ and azimuth $\phi = 45°$ as a function of the spatial coordinates X and Y of the propagation media at 6.8 $GHz$.

Figure 5.10: The phase gradient of E-field in free space for vertical polarization (TM) with zenith $\theta_i = 30°$ and azimuth $\phi = 45°$ as a function of the spatial coordinates X and Y of the propagation media at 6.8 $GHz$.

At low frequency and small slice thickness, the phase fluctuation of the E-field is expected to be weak and leads to weak scattering. The high refractive index of sea water at low frequencies contributes significantly in evaluating the effective dielectric constant of sea foam, the foam void fraction and varying effective dielectric constant of sea foam plays a significant role in determining if there will be weak or strong phase fluctuation of the wave field. At high frequencies, the short wavelength of signals makes them more sensitive to reflection. Microwave frequency can be refracted by smaller objects than low frequency signals. At high frequencies, the E-field with more energy will be strongly scattered due the microscopic irregularities and random boundaries of the extended random media. The figures below illustrate phase variation at low frequencies with thin and deep sea foam slices.

Figures 5.11 and 5.12 illustrate phase variation of the incident field in free space. We can clearly see that the phase gradient of the E-field is similar to what was generated as there was very weak interaction between the E-field and the media of propagation which was due to very low dielectric loss factor in free space and lower frequency signals having high penetration depth. The phase variation of the E-field in 5.13 and 5.14 shows random phase variation of the E-field from $-\pi$ to $\pi$ as the E-field interacts with closely packed random air bubbles with varying dielectric loss factor. The phase gradient of the E-field are randomised as the field propagates through successive slices of sea foam layer with microscopic irregularities and random boundaries. It is expected that there will be more interactions between the E-field and the air bubbles which will lead to multiple reflections or diffused scattering.

For thin sea foam slices in figures 5.13-5.18 we observe that the phase variation of the E-field intensifies as the wave field travels through successive slices of sea foam due to more interactions with the air bubble population. The rapid variation could be accounted for by the varying effective dielectric constants of the sea foams (dielectric loss factors) as the scatterers are closely packed with irregular boundaries.

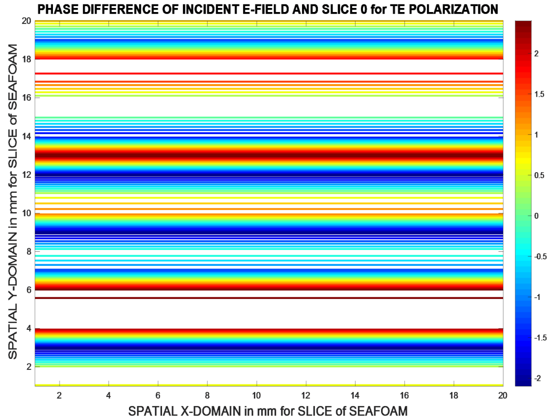

Figure 5.11: The phase variation of E-field in free space for horizontal polarization (TE) with zenith $\theta_i = 30°$ and azimuth $\phi = 0°$ as a function of the spatial coordinates X and Y of the propagation media at 6.8 $GHz$, $\delta_t = 0.1$ $mm$.

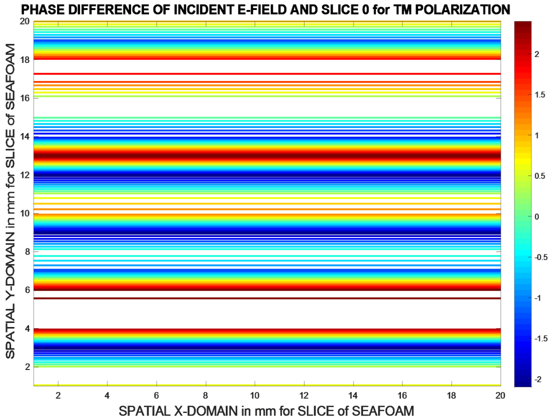

Figure 5.12: The phase variation of E-field in free space for vertical polarization (TM) with zenith $\theta_i = 30°$ and azimuth $\phi = 0°$ as a function of the spatial coordinates X and Y of the propagation media at 6.8 $GHz$, $\delta_t = 0.1$ $mm$.

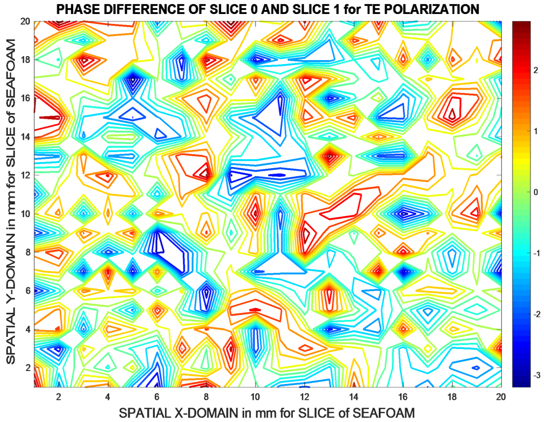

Figure 5.13: The phase variation of E-field in slice 1 for horizontal polarization (TE) with zenith $\theta_i = 30°$ and azimuth $\phi = 0°$ as a function of the spatial coordinates X and Y of the propagation media at 6.8 $GHz$,$\delta_t = 0.1$ $mm$.

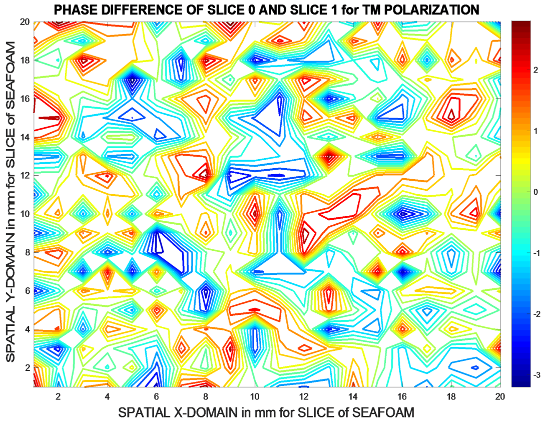

Figure 5.14: The phase variation of E-field in slice 1 for vertical polarization (TM) with zenith $\theta_i = 30°$ and azimuth $\phi = 0°$ as a function of the spatial coordinates X and Y of the propagation media at 6.8 $GHz$,$\delta_t = 0.1$ $mm$.

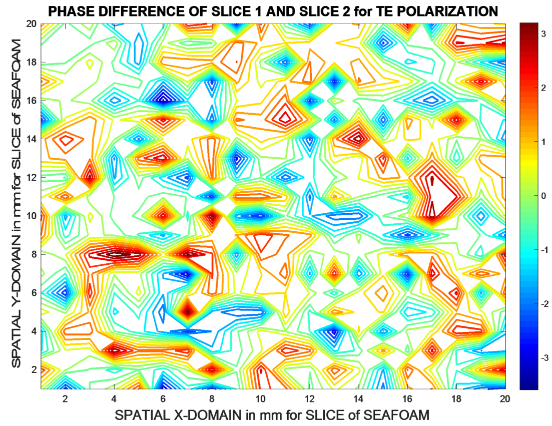

Figure 5.15: The phase variation of E-field in slice 2 for horizontal polarization (TE) with zenith $\theta_i = 30°$ and azimuth $\phi = 0°$ as a function of the spatial coordinates X and Y of the propagation media at 6.8 $GHz$,$\delta_t = 0.1$ $mm$.

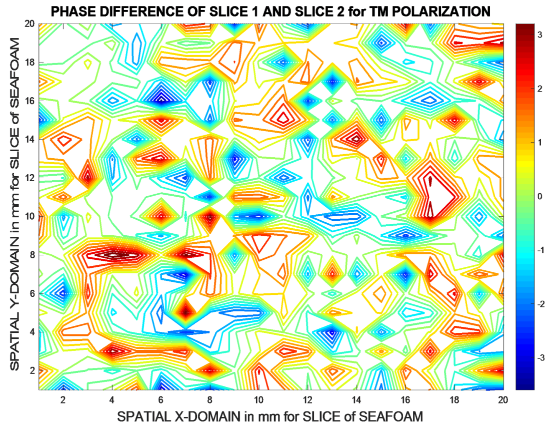

Figure 5.16: The phase variation of E-field in slice 2 for vertical polarization (TM) with zenith $\theta_i = 30°$ and azimuth $\phi = 0°$ as a function of the spatial coordinates X and Y of the propagation media at 6.8 $GHz$,$\delta_t = 0.1$ $mm$.

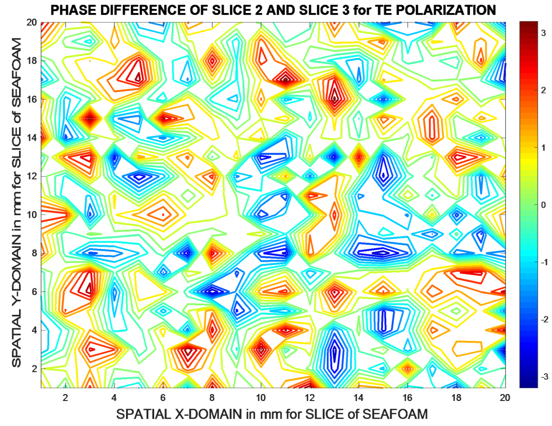

Figure 5.17: The phase variation of E-field in slice 3 for horizontal polarization (TE) with zenith $\theta_i = 30°$ and azimuth $\phi = 0°$ as a function of the spatial coordinates X and Y of the propagation media at 6.8 $GHz$,$\delta_t = 0.1$ $mm$.

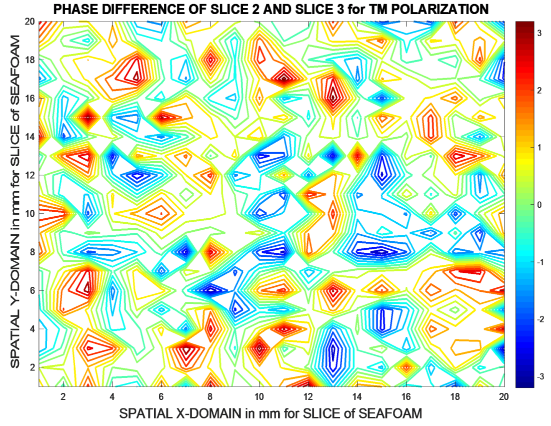

Figure 5.18: The phase variation of E-field in slice 3 for vertical polarization (TM) with zenith $\theta_i = 30°$ and azimuth $\phi = 0°$ as a function of the spatial coordinates X and Y of the propagation media at 6.8 $GHz$,$\delta_t = 0.1$ $mm$.

### 5.2.4 Phase Fluctuations in Deep Phase Scattering Screen at High Windsat Frequencies and slice thicknessses

The interactions between the incident coherent E-field and the randomly distributed bubbles with heterogeneous dielectric constants causes phase perturbations in the seafoam layer as shown in the contour plots as the phase of the resultant E-field varies randomly between $-\pi$ to $\pi$ within the sampled domain. At high frequencies, there are more interactions of the re-radiated E-fields within the seafoam layer. These interactions cause constructive or destructive coherent scattering which explains the phase inversion of the incident E-field or cancellation of the phases in the seafoam layer $exp(j(\theta_n - \theta_m)) = 0$.

For propagation frequency 23.8 $GHz$ with effective dielectric constant of seawater $\epsilon_{sw} = 28.924 + j33.233$ and slice thickness $\delta_t = 2\ mm$, the E-field undergoes significant loss due to destructive interference of the phases in the seafoam layer (phase difference in slice 2 and slice 3) as the phase cancels out to zero $exp(j(\theta_3 - \theta_2)) = 0$. This effect is a coherent scattering termed coherent destructive scattering. This was the case for both TE and TM polarized E-fields. Hence, the future phase delays of the successive phases of slices 4 and 5 are all zeros.

Correspondingly, the E-field undergoes significant loss in amplitude as it travels through slice 2 and slice 3 $exp(j(\theta_3 - \theta_2)) = 0$, due to destructive interference of the phase distributions. This occurs simultaneously for TM and TE polarized fields at frequency of 37 $GHz$ with effective dielectric constant of seawater $\epsilon_{sw} = 17.753 + j26.855$ and slice thickness $\delta_t = 2$ $mm$. The future amplitudes and phase of the series of phase screens are all zeros $\theta_4 - \theta_3$ and $\theta_5 - \theta_4$ are all zeros. The figures below illustrates random phase variations as the E-field propagates through thin and deep slices of sea foam layers at high WindSat frequencies.

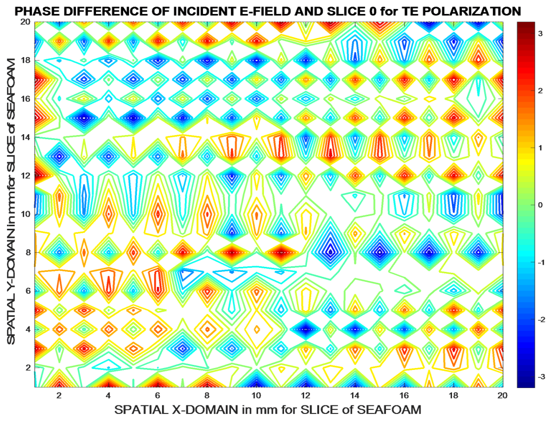

Figure 5.19: The phase variation of E-field in free space for horizontal polarization (TE) with zenith $\theta_i = 30°$ and azimuth $\phi = 45°$ as a function of the spatial coordinates X and Y of the propagation media at 23.8 $GHz$,$\delta_t = 2$ $mm$.

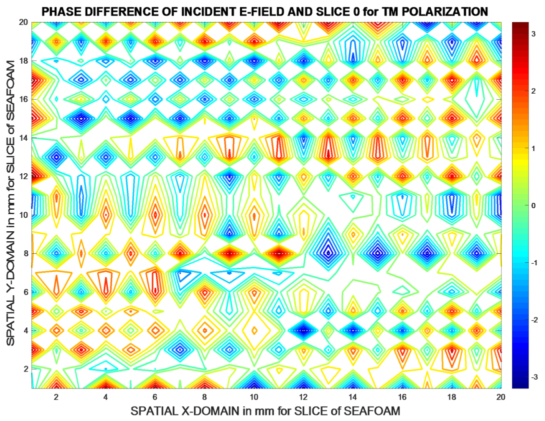

Figure 5.20: The phase variation of E-field in free space for vertical polarization (TM) with zenith $\theta_i = 30°$ and azimuth $\phi = 45°$ as a function of the spatial coordinates X and Y of the propagation media at 23.8 $GHz$ and $\delta_t = 2$ $mm$.

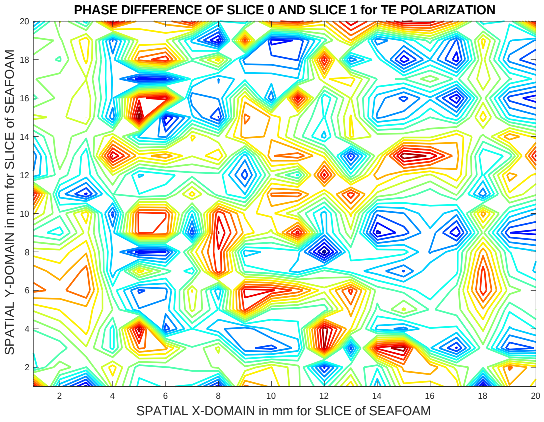

Figure 5.21: The phase variation of E-field in slice 1 for horizontal (TE) with zenith $\theta_i = 30°$ and azimuth $\phi = 45°$ as a function of the spatial coordinates X and Y of the propagation media at 23.8 $GHz$,$\delta_t = 2$ $mm$.

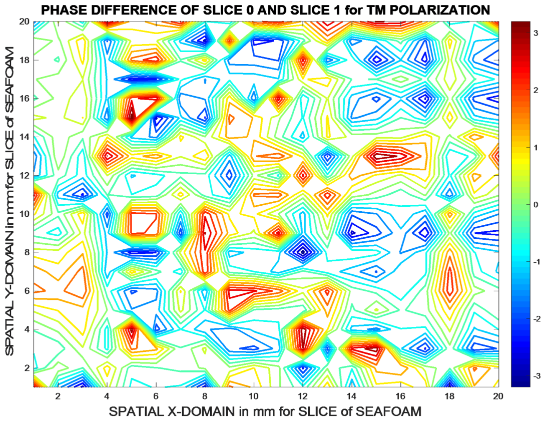

Figure 5.22: The phase variation of E-field in slice 1 for vertical polarization (TM) with zenith $\theta_i = 30°$ and azimuth $\phi = 45°$ as a function of the spatial coordinates X and Y of the propagation media at 23.8 $GHz$,$\delta_t = 2$ $mm$.

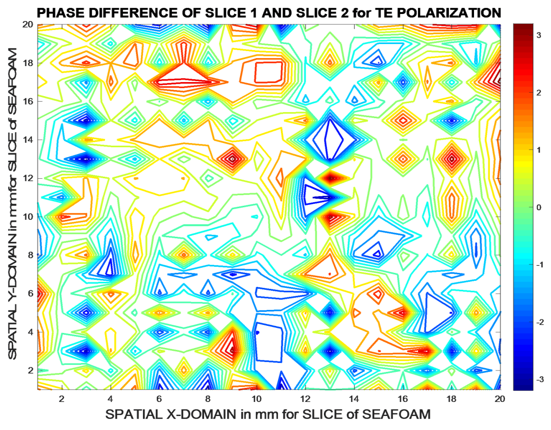

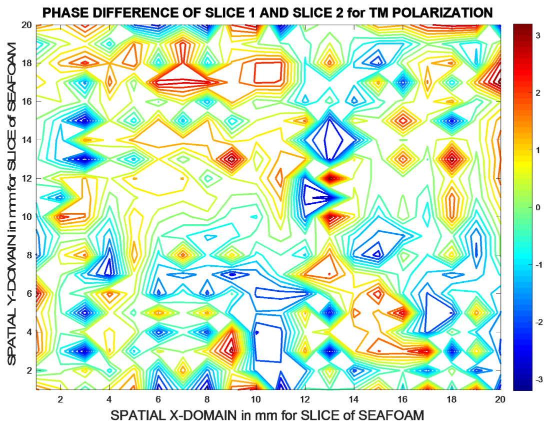

Figure 5.23: The phase variation of E-field in slice 2 for horizontal polarization (TE) with zenith $\theta_i = 30°$ and azimuth $\phi = 45°$ as a function of the spatial coordinates X and Y of the propagation media at 23.8 $GHz$,$\delta_t = 2$ $mm$.

Figure 5.24: The phase variation of E-field in slice 2 for vertical polarization (TM) with zenith $\theta_i = 30°$ and azimuth $\phi = 45°$ as a function of the spatial coordinates X and Y of the propagation media at 23.8 $GHz$ and $\delta_t = 2$ $mm$.

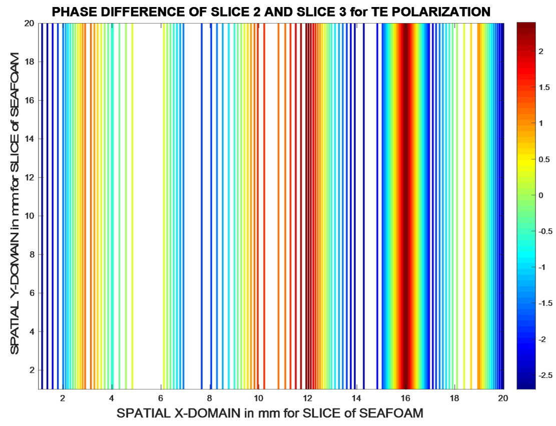

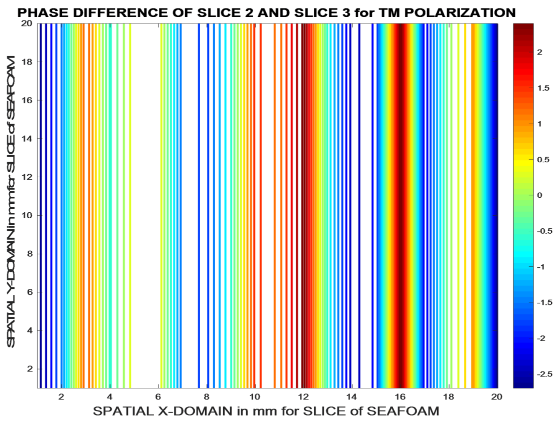

Figure 5.25: The phase variation of E-field in slice 3 for horizontal (TE) with zenith $\theta_i = 30°$ and azimuth $\phi = 45°$ as a function of the spatial coordinates X and Y of the propagation media at 23.8 $GHz$,$\delta_t = 2$ $mm$.

Figure 5.26: The phase variation of E-field in slice 3 for vertical polarization (TM) with zenith $\theta_i = 30°$ and azimuth $\phi = 45°$ as a function of the spatial coordinates X and Y of the propagation media at 23.8 $GHz$,$\delta_t = 2$ $mm$.

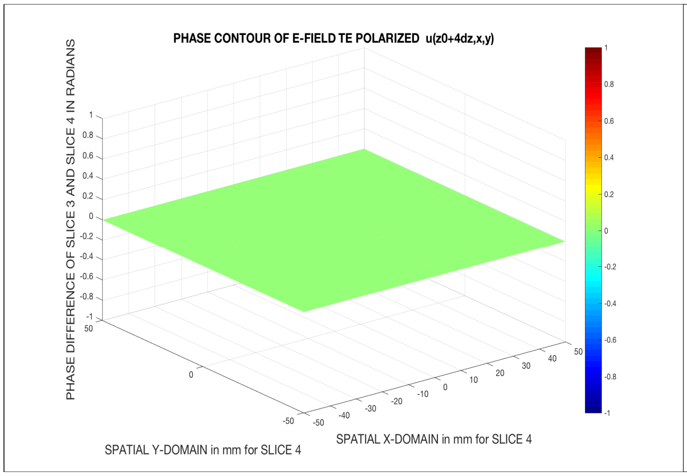

Figure 5.27: The phase variation of E-field in slice 4 for horizontal polarization (TE) with zenith $\theta_i = 30°$ and azimuth $\phi = 45°$ as a function of the spatial coordinates X and Y of the propagation media at 23.8 $GHz$,$\delta_t = 2$ $mm$.

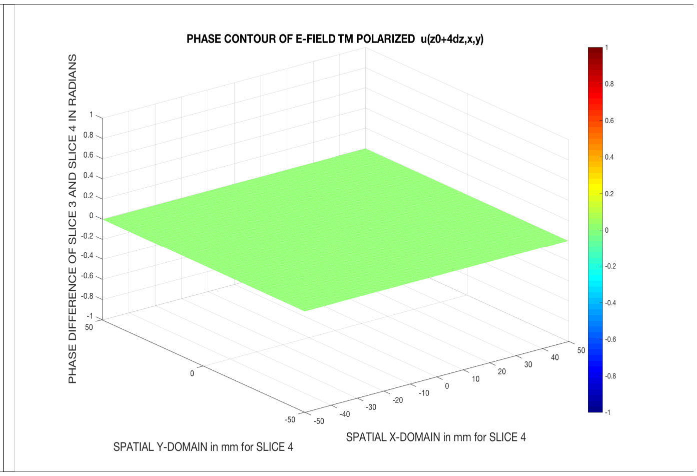

Figure 5.28: The phase variation of E-field in slice 4 for vertical polarization (TM) with zenith $\theta_i = 30°$ and azimuth $\phi = 45°$ as a function of the spatial coordinates X and Y of the propagation media at 23.8 $GHz$ and $\delta_t = 2$ $mm$.

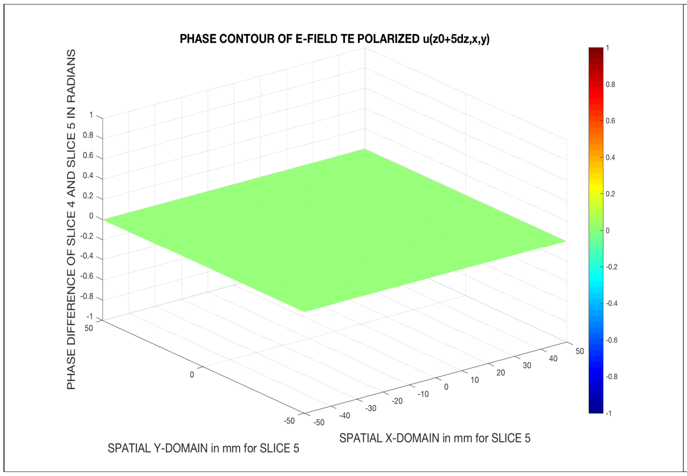

Figure 5.29: The phase variation of E-field in slice 5 for horizontal (TE) with zenith $\theta_i = 30°$ and azimuth $\phi = 45°$ as a function of the spatial coordinates X and Y of the propagation media at 23.8 $GHz$,$\delta_t = 2$ $mm$.

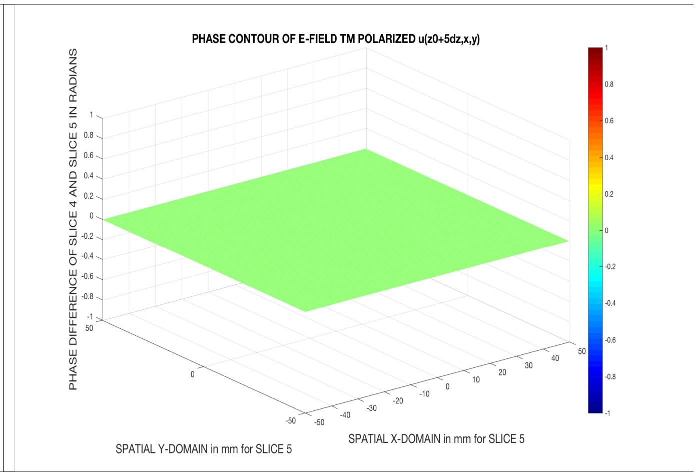

Figure 5.30: The phase variation of E-field in slice 5 for vertical polarization (TM) with zenith $\theta_i = 30°$ and azimuth $\phi = 45°$ as a function of the spatial coordinates X and Y of the propagation media at 23.8 $GHz$,$\delta_t = 2$ $mm$.

Plane waves attenuate as they propagate through a lossy medium. From the expression of skin depth, it is found that the depth of penetration of fields in a lossy medium is inversely proportional to the square-root of the conductivity of the medium. In the extreme case of conductivity close to infinity, this depth vanishes and in fact, time varying fields and induced currents can not exist within the medium. In other words, all fields and induced currents are confined near the skin region of the medium.

We observed an increased high frequency resistance of a thin sea-foam layer, which occurs as a result of current confinement through a smaller cross-section due to the skin effect.

In the ocean (seawater) with loss tangent greater than unity, we observe that attenuation of the E-field increased with depth. Antennas used for transmitting and receiving EM waves will cover more distance at lower propagating frequencies as the depth of penetration is inversely proportional to the attenuation constant. Attenuation is proportional to the square-root of the radian frequency in a lossy medium.

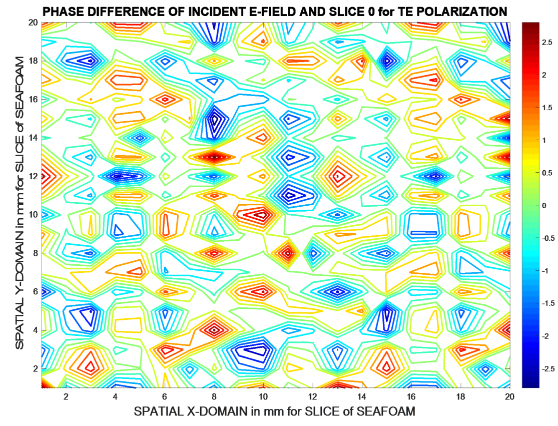

Figure 5.31: The phase variation of E-field in free space for horizontal polarization (TE) with zenith $\theta_i = 30°$ and azimuth $\phi = 45°$ as a function of the spatial coordinates X and Y of the propagation media at 37 $GHz$ and $\delta_t = 2$ $mm$.

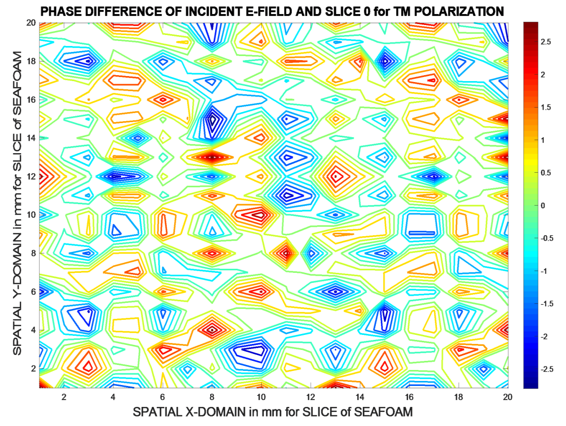

Figure 5.32: The phase variation of E-field in free space for vertical polarization (TM) with zenith $\theta_i = 30°$ and azimuth $\phi = 45°$ as a function of the spatial coordinates X and Y of the propagation media at 37 $GHz$ and $\delta_t = 2$ $mm$.

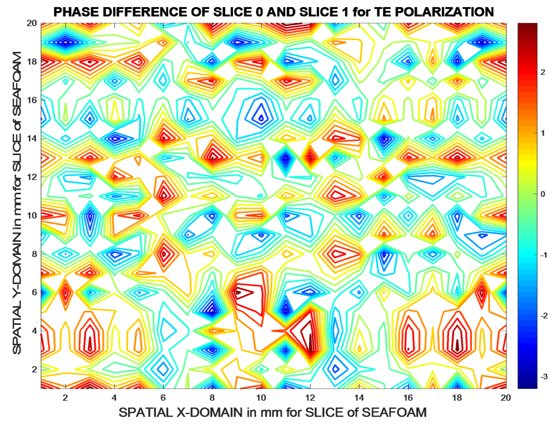

Figure 5.33: The phase variation of E-field in slice 1 for horizontal (TE) with zenith $\theta_i = 30°$ and azimuth $\phi = 45°$ as a function of the spatial coordinates X and Y of the propagation media at 37 $GHz$, $\delta_t = 2$ $mm$.

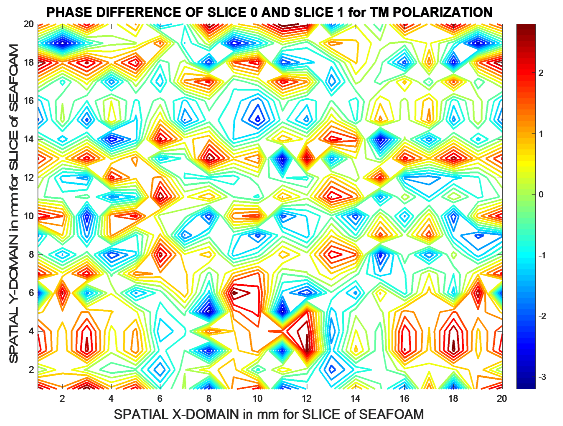

Figure 5.34: The phase variation of E-field in slice 1 for vertical polarization (TM) with zenith $\theta_i = 30°$ and azimuth $\phi = 45°$ as a function of the spatial coordinates X and Y of the propagation media at 37 $GHz$, $\delta_t = 2$ $mm$.

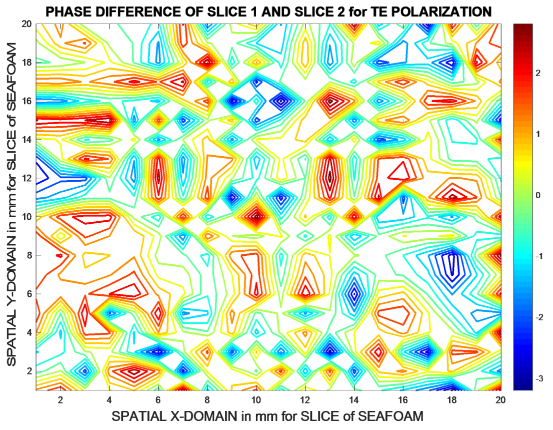

Figure 5.35: The phase variation of E-field in slice 2 for horizontal polarization (TE) with zenith $\theta_i = 30°$ and azimuth $\phi = 45°$ as a function of the spatial coordinates X and Y of the propagation media at 37 $GHz$ and $\delta_t = 2$ $mm$.

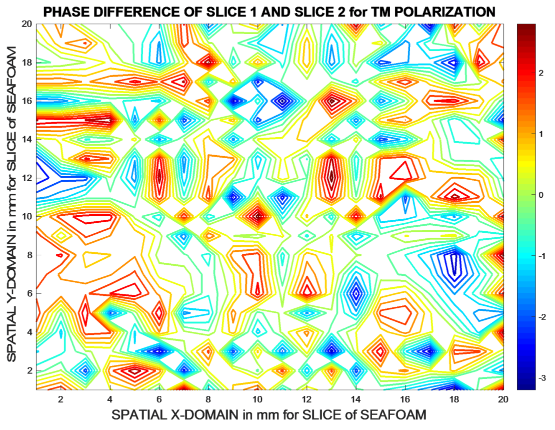

Figure 5.36: The phase variation of E-field in slice 2 for vertical polarization (TM) with zenith $\theta_i = 30°$ and azimuth $\phi = 45°$ as a function of the spatial coordinates X and Y of the propagation media at 37 $GHz$ and $\delta_t = 2$ $mm$.

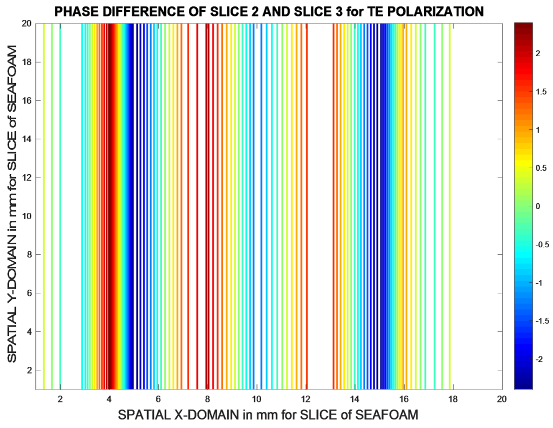

Figure 5.37: The phase variation of E-field in slice 3 for horizontal (TE) with zenith $\theta_i = 30°$ and azimuth $\phi = 45°$ as a function of the spatial coordinates X and Y of the propagation media at 37 $GHz$, $\delta_t = 2$ $mm$.

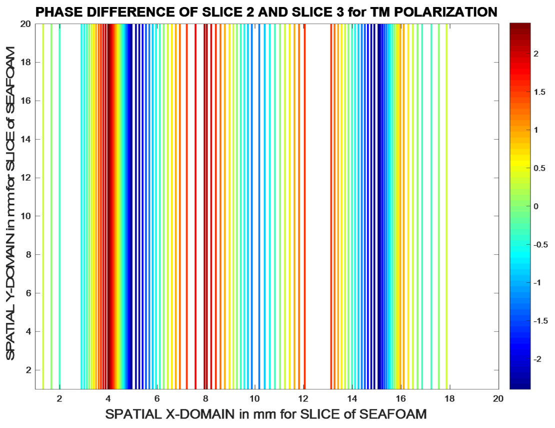

Figure 5.38: The phase variation of E-field in slice 3 for vertical polarization (TM) with zenith $\theta_i = 30°$ and azimuth $\phi = 45°$ as a function of the spatial coordinates X and Y of the propagation media at 37 $GHz$, $\delta_t = 2$ $mm$.

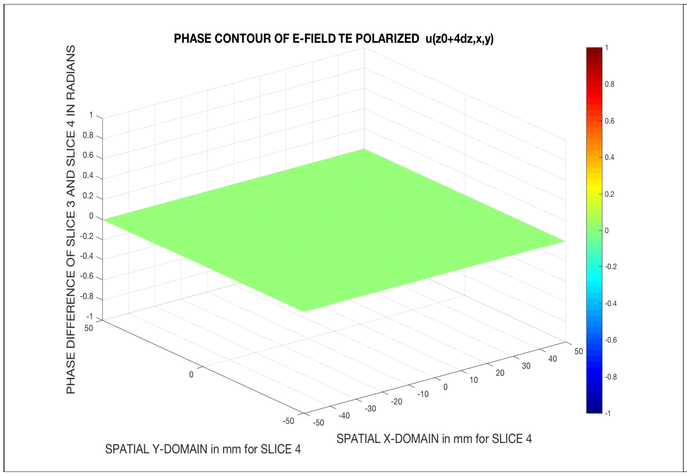

Figure 5.39: The phase variation of E-field in slice 4 for horizontal polarization (TE) with zenith $\theta_i = 30°$ and azimuth $\phi = 45°$ as a function of the spatial coordinates X and Y of the propagation media at 37 $GHz$ and $\delta_t = 2$ $mm$.

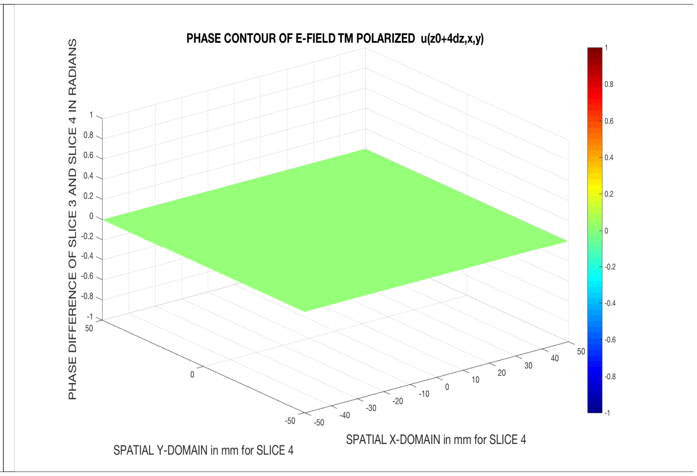

Figure 5.40: The phase variation of E-field in slice 4 for vertical polarization (TM) with zenith $\theta_i = 30°$ and azimuth $\phi = 45°$ as a function of the spatial coordinates X and Y of the propagation media at 37 $GHz$ and $\delta_t = 2$ $mm$.

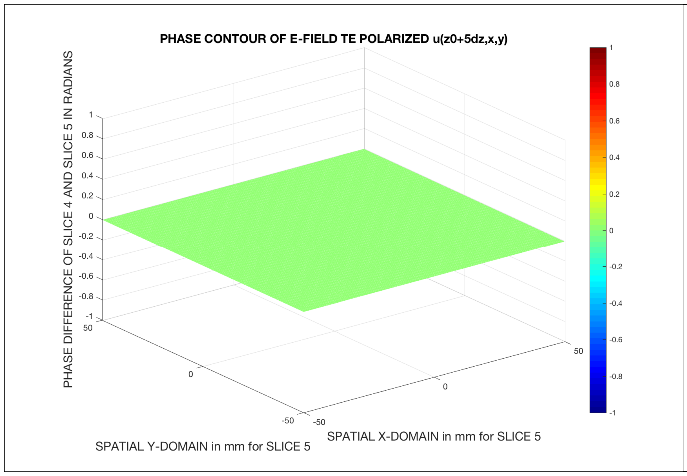

Figure 5.41: The phase variation of E-field in slice 5 for horizontal (TE) with zenith $\theta_i = 30°$ and azimuth $\phi = 45°$ as a function of the spatial coordinates X and Y of the propagation media at 37 $GHz$, $\delta_t = 2$ $mm$.

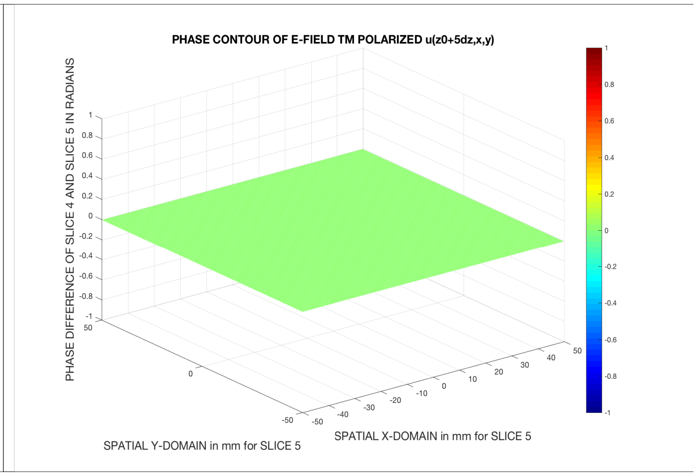

Figure 5.42: The phase variation of E-field in slice 5 for vertical polarization (TM) with zenith $\theta_i = 30°$ and azimuth $\phi = 45°$ as a function of the spatial coordinates X and Y of the propagation media at 37 $GHz$, $\delta_t = 2$ $mm$.

## 5.3 Angular Spectrum of Backscattered E-fields at WindSat Frequencies

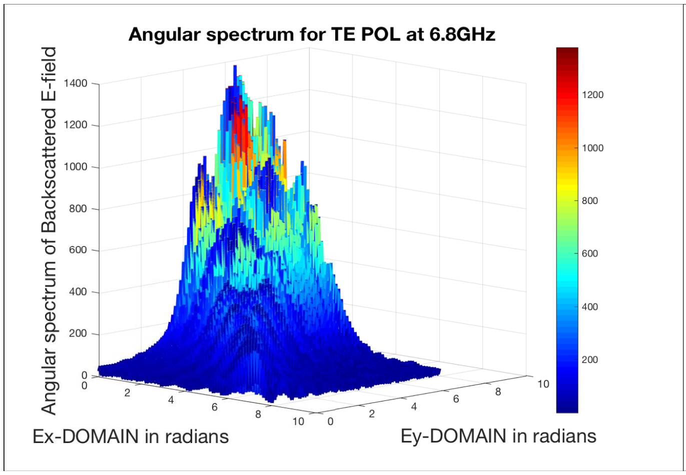

Figure 5.43: Angular spectrum of diffused reflected wave field at $6.8GHz$ and $\delta_t = 0.1mm$ for TE polarization with effective dielectric constant of seawater $\epsilon_{sw} = 62.6425 + j27.8729$ and foam void fraction $f_a = 0.8$ at constant $SST = 20°$ and salinity $(34psu)$ for seed $= 4$.

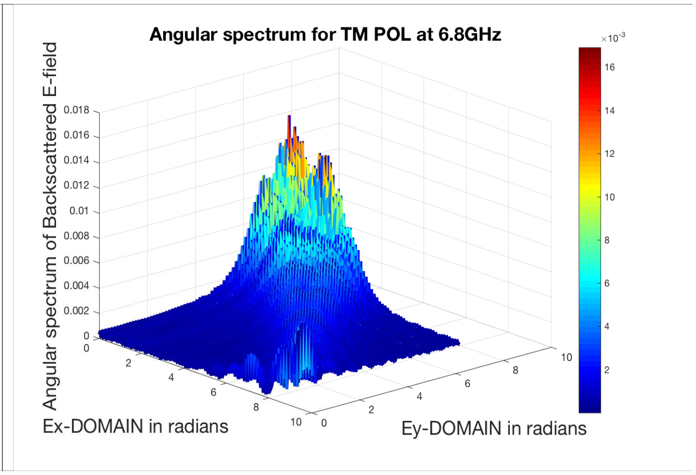

Figure 5.44: Angular spectrum of diffused reflected wave field at $6.8GHz$ and $\delta_t = 0.1mm$ for TM polarization with effective dielectric constant of seawater $\epsilon_{sw} = 62.6425 + j27.8729$ and foam void fraction $f_a = 0.8$ at constant $SST = 20°$ and salinity $(34psu)$ for seed $= 4$.

Figure 5.43 and figure 5.45 illustrate that the results are not artefact of the seed used in generating the log-normal distribution bubble radii.

The angular spectrum of the propagated E-field for both TE and TM modes through a foam covered sea-surface with $n$ log-normal distributed bubble radii, generated with seed $= 4$ and seed $= 5$ yields similar results as shown in figures 5.43, 5.44, 5.45 and 5.46.

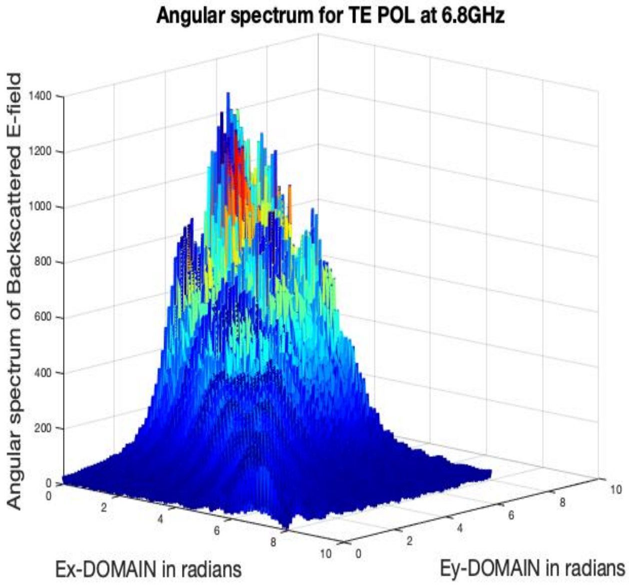

Figure 5.45: Angular spectrum of diffused reflected wave field at 6.8 $GHz$ and $\delta_t = 0.1$ $mm$ for TE polarization with effective dielectric constant of seawater $\epsilon_{sw} = 62.6425 + j27.8729$ and foam void fraction $f_a = 0.8$ at constant $SST = 20°$ and salinity $(34psu)$ for seed = 5

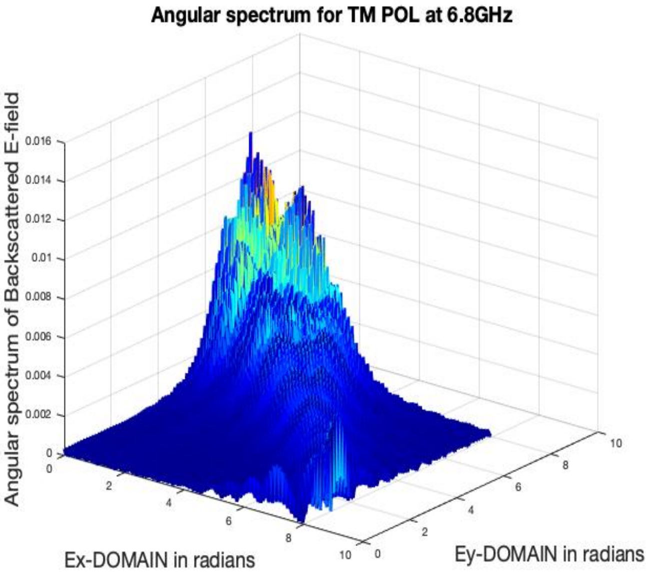

Figure 5.46: Angular spectrum of diffused reflected wave field at $6.8GHz$ and $\delta_t = 0.1$ $mm$ for TM polarization with effective dielectric constant of seawater $\epsilon_{sw} = 62.6425 + j27.8729$ and foam void fraction $f_a = 0.8$ at constant $SST = 20°$ and salinity $(34psu)$ for seed = 5.

We can see from figures 5.43 and 5.44 that there are many scattering paths due to the disordered air bubbles in the surface of the sea which makes the interaction between the incident E-field and isotropically distributed air bubbles diffusive and the air bubbles experiences series of random scattering. For sea foam layer thickness $\delta_t = 0.2$ $mm$ at frequency of 6.8 $GHz$ and same propagation conditions, the E-field distribution spectrum remains unchanged for a thin phase scattering screen as the angular spectrum of the scattered field is not influenced by the increase in sea foam layer thickness as shown in figures 5.47 and 5.48.

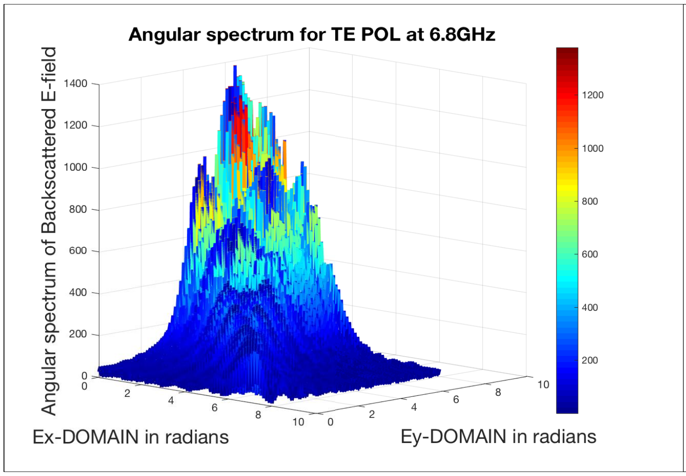

Figure 5.47: Angular spectrum of diffused reflected wave field at 6.8 $GHz$ and $\delta_t = 0.2\ mm$ for TE polarization with effective dielectric constant of seawater $\epsilon_{sw} = 62.6425 + j27.8729$ and foam void fraction $f_a = 0.8$ at constant $SST = 20°$ and salinity $(34psu)$

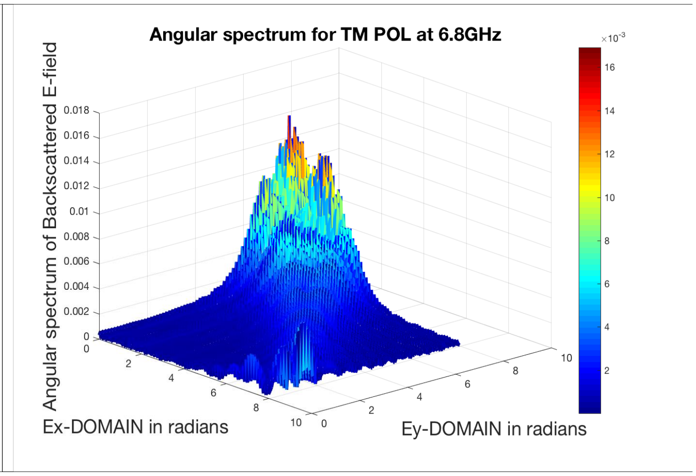

Figure 5.48: Angular spectrum of diffused reflected wave field at $6.8GHz$ and $\delta_t = 0.2\ mm$ for TM polarization with effective dielectric constant of seawater $\epsilon_{sw} = 62.6425 + j27.8729$ and foam void fraction $f_a = 0.8$ at constant $SST = 20°$ and salinity $(34psu)$

The refractive index of the layers increases with decrease in frequency. At low frequencies we have high refractive index of sea water which contributes to the effective refractive indices of the extended sea foam media. This explains the why the E-field is randomised and scattered in different directions as shown in 5.43, 5.44, 5.47 and 5.48 but the angular spectrum of the E-field remains unchanged when the slice thickness of the foam was altered from 0.1 $mm$ to 0.2 $mm$ which was due to negligible difference in the average effective dielectric constant of the sea foam media as the effective dielectric constant of each sea foam layer is approximately the same. This behaviour is expected for a thin phase scattering screen as most of the incident E-field are transmitted through the slice of sea foam. Each slice induces an independent random variation to the phase of the E-field, but doesn't influence a change in amplitude. The change in amplitude of the E-field build up as the E-field is diffracted over many slice thickness [99].

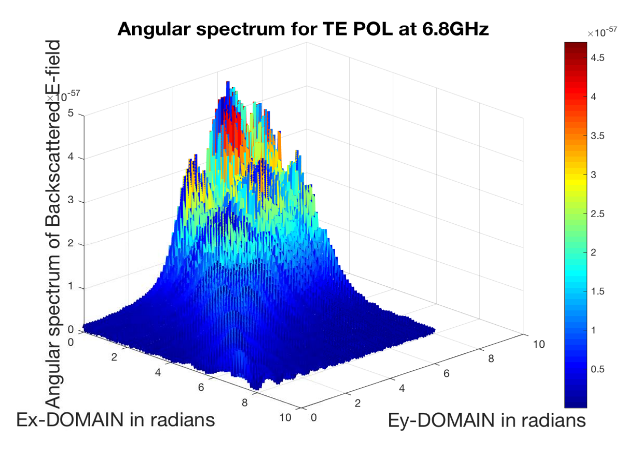

Figure 5.49: Angular spectrum of diffused reflected wave field at 6.8 $GHz$ and $\delta_t = 2\ mm$ for TE polarization with effective dielectric constant of seawater $\epsilon_{sw} = 62.6425 + j27.8729$ and foam void fraction $f_a = 0.8$ at constant $SST = 20°$ and salinity $(34psu)$

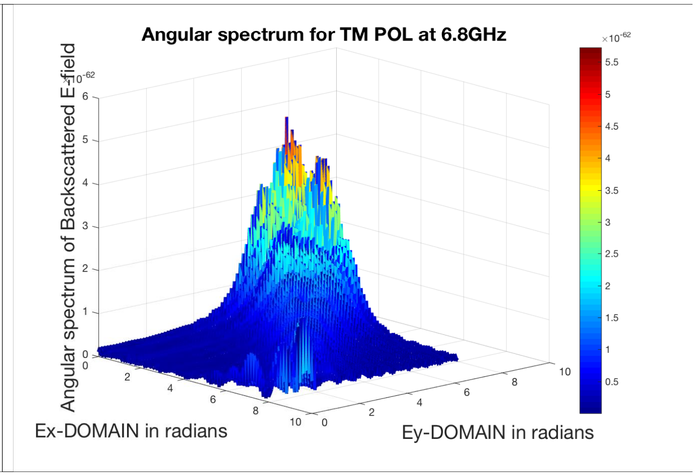

Figure 5.50: Angular spectrum of diffused reflected wave field at 6.8 $GHz$ and $\delta_t = 2\ mm$ for TM polarization with effective dielectric constant of seawater $\epsilon_{sw} = 62.6425 + j27.8729$ and foam void fraction $f_a = 0.8$ at constant $SST = 20°$ and salinity $(34psu)$

The angular spectrum of the diffused reflected wave field at $\delta_t = 2\ mm$ for a deep phase scattering screen is a function of the spectral wavenumbers $(p, q)$ for $1D$ problem and $(E_x, E_y)$ for $2D$ problem in the X and Y directions. The broadening of the peaks in figures 5.49 and 5.50 depends on the diffraction factor $\exp\left(i\Delta z\sqrt{k^2 - (p^2 + q^2)}\right)$. When $k^2$ approaches $(p^2 + q^2)$, the lobes of the angular spectrum are spread or broadened across the $(p, q)$ or $(E_x, E_y)$ spectral domain. This happens at low WindSat frequencies such as 6.8 $GHz$ and 10.7 $GHz$ but at higher frequencies 18.7 $GHz$, 23.8 $GHz$ and 37 $GHz$ where $k^2 \gg (p^2 + q^2)$, the lobes of the angular spectrum becomes sharper and narrower across the $(p, q)$ or $(E_x, E_y)$ spectral domain.

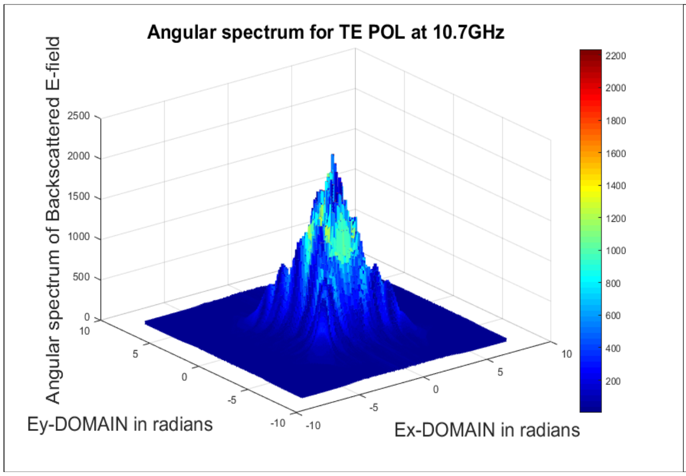

Figure 5.51: Angular Spectrum of Diffused Reflected Wavefront at 10.7 $GHz$ and $\delta_t = 0.1$ $mm$ for TE polarization with effective dielectric constant of seawater $\epsilon_{sw} = 53.5604 + j32.8054$ and foam void fraction $f_a = 0.8$ at constant $SST = 20°$ and salinity $(34psu)$.

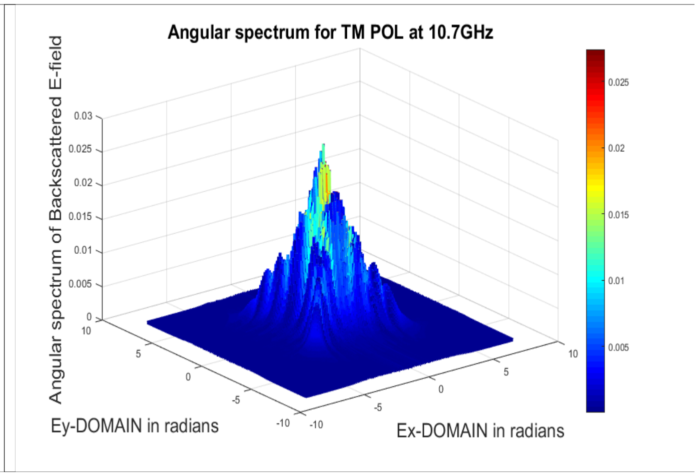

Figure 5.52: Angular Spectrum of Diffused Reflected Wavefront at 10.7 $GHz$ and $\delta_t = 0.1$ $mm$ for TM polarization with effective dielectric constant of seawater $\epsilon_{sw} = 53.5604 + j32.8054$ and foam void fraction $f_a = 0.8$ at constant $SST = 20°$ and salinity $(34psu)$.

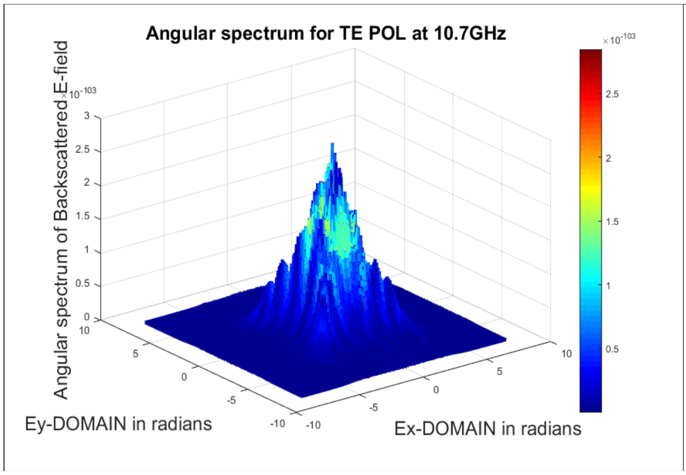

Figure 5.53: Angular Spectrum of Diffused Reflected Wavefront at 10.7 $GHz$ and $\delta_t = 2$ $mm$ for TE polarization with effective dielectric constant of seawater $\epsilon_{sw} = 53.5604 + j32.8054$ and foam void fraction $f_a = 0.8$ at constant $SST = 20°$ and salinity $(34psu)$.

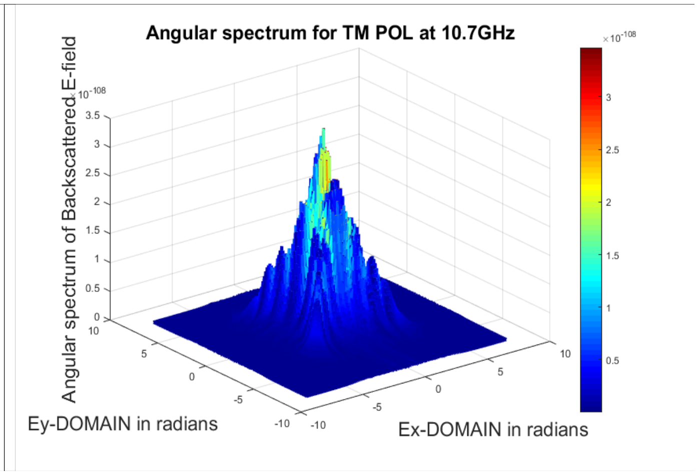

Figure 5.54: Angular Spectrum of Diffused Reflected Wavefront at 10.7 $GHz$ and $\delta_t = 2$ $mm$ for TM polarization with effective dielectric constant of seawater $\epsilon_{sw} = 53.5604 + j32.8054$ and foam void fraction $f_a = 0.8$ at constant $SST = 20°$ and salinity $(34psu)$.

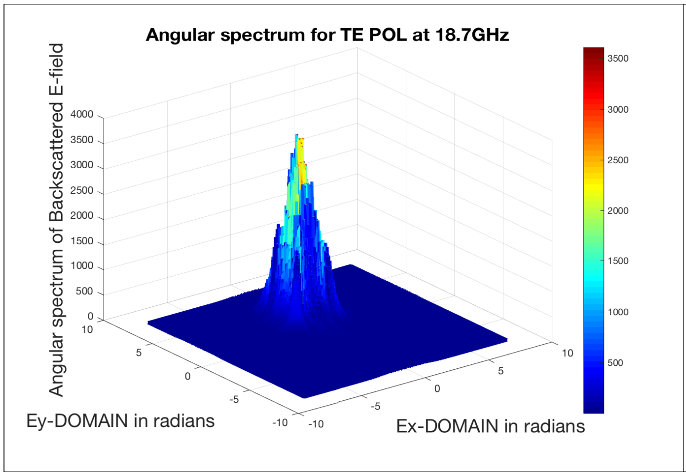

Figure 5.55: Angular Spectrum of Diffused Reflected Wavefront at 18.7 $GHz$ and $\delta_t = 0.1$ $mm$ for TE polarization with effective dielectric constant of seawater $\epsilon_{sw} = 36.5500 + j34.9728$ and foam void fraction $f_a = 0.8$ at constant $SST = 20°$ and salinity $(34psu)$.

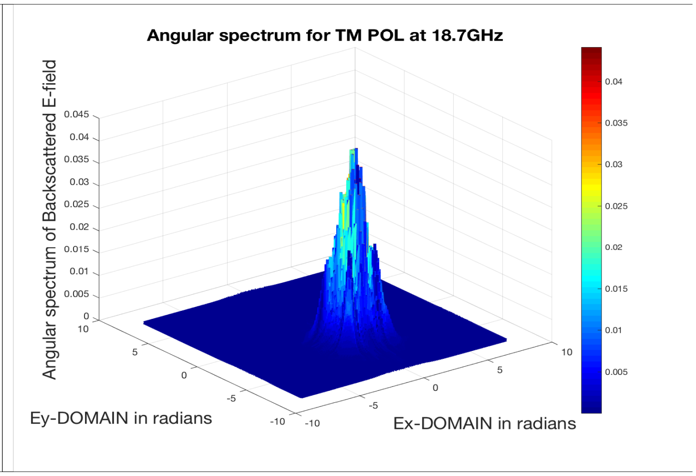

Figure 5.56: Angular Spectrum of Diffused Reflected Wavefront at 18.7 $GHz$ and $\delta_t = 0.1$ $mm$ for TE polarization with effective dielectric constant of seawater $\epsilon_{sw} = 36.5500 + j34.9728$ and foam void fraction $f_a = 0.8$ at constant $SST = 20°$ and salinity $(34psu)$.

The higher the frequency, the sharper and narrower the diffused reflected lobes because the diffraction effects of the scattering is reduced with increasing frequency. The is due to the relationship between the wavenumber $k$ and the spectral wavenumbers $(p^2 + q^2)$ as explained earlier in page 131. This is due to $k = 2\pi/\lambda$, where $\lambda$ is the wavelength of the incident wave field which decreases with increase in frequency. This implies that $k$ increases when there is increase in frequency. For an incident E-field propagating at a frequency of 18.7 $GHz$, $k = 339.1805$ and maximum value of $E_x + E_y = 129.3629$. For deep phase scattering screen $\delta_t = 2$ $mm$ the dorminant factor for attenuation of the wave-field is absorption at the sea-surface. This is shown in the figures below.

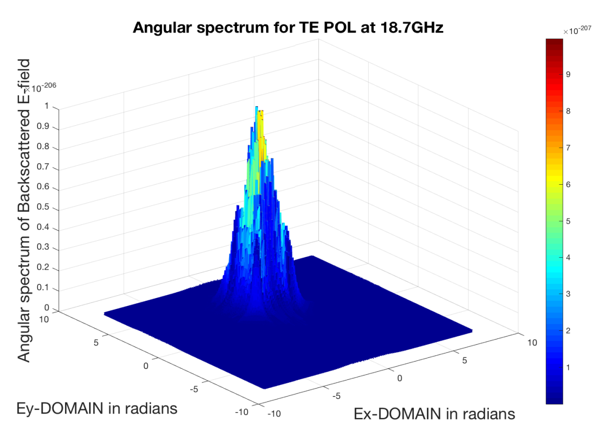

Figure 5.57: Angular Spectrum of Diffused Reflected Wavefront at 18.7 $GHz$ and $\delta_t = 2\ mm$ for TE polarization with effective dielectric constant of seawater $\epsilon_{sw} = 36.5500 + j34.9728$ and foam void fraction $f_a = 0.8$ at constant $SST = 20°$ and salinity $(34psu)$.

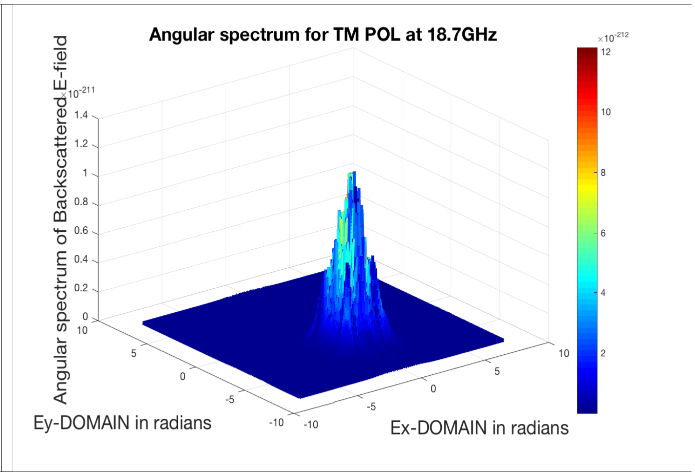

Figure 5.58: Angular Spectrum of Diffused Reflected Wavefront at 18.7 $GHz$ and $\delta_t = 2\ mm$ for TM polarization with effective dielectric constant of seawater $\epsilon_{sw} = 36.5500 + j34.9728$ and foam void fraction $f_a = 0.8$ at constant $SST = 20°$ and salinity $(34psu)$.

The angular spectrum of the diffused reflected wave field at $\delta_t = 2\ mm$ for a deep phase scattering screen is a function of the spectral wavenumbers $(p, q)$ for $1D$ problem and $(E_x, E_y)$ for $2D$ problem in the X and Y directions. The broadening of the peaks in figures 5.57 and 5.58 depends on the diffraction factor $\exp(i\Delta z\sqrt{k^2 - (p^2 + q^2)})$. When $k^2$ approaches $(p^2 + q^2)$, the lobes of the angular spectrum are spread or broadened across the $(p, q)$ or $(E_x, E_y)$ spectral domain. This happens at low WindSat frequencies such as 6.8 $GHz$ and 10.7 $GHz$ but at higher frequencies 18.7 $GHz$, 23.8 $GHz$ and 37 $GHz$ where $k^2 \gg (p^2 + q^2)$, the lobes of the angular spectrum becomes sharper and narrower across the $(p, q)$ or $(E_x, E_y)$ spectral domain.

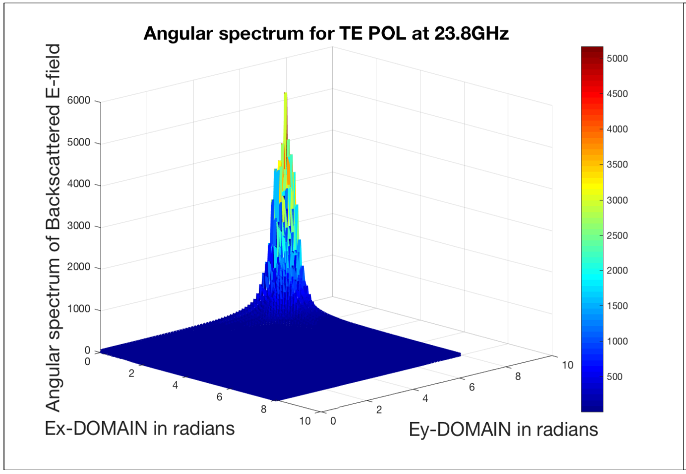

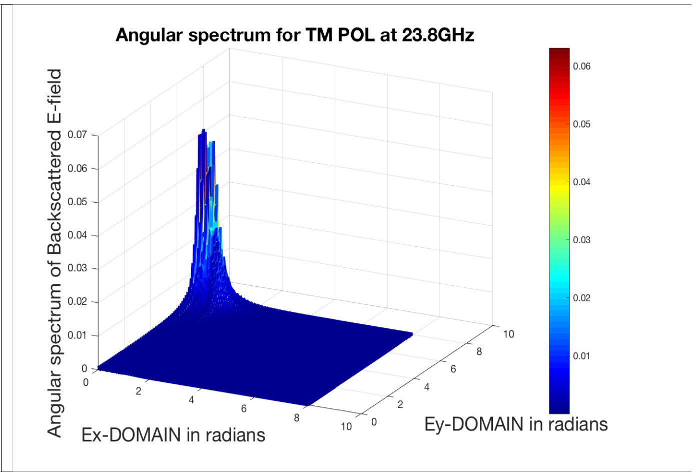

Figure 5.59: Angular Spectrum of Diffused Reflected Wavefront at 23.8 $GHz$ and $\delta_t = 0.2$ $mm$ for TE polarization with effective dielectric constant of seawater $\epsilon_{sw} = 28.9247 + j33.2233$ and foam void fraction $f_a = 0.8$ at constant $SST = 20^\circ$ and salinity $(34psu)$.

Figure 5.60: Angular Spectrum of Diffused Reflected Wavefront at 23.8 $GHz$ and $\delta_t = 0.2$ $mm$ for TM polarization with effective dielectric constant of seawater $\epsilon_{sw} = 28.9247 + j33.2233$ and foam void fraction $f_a = 0.8$ at constant $SST = 20^\circ$ and salinity $(34psu)$.

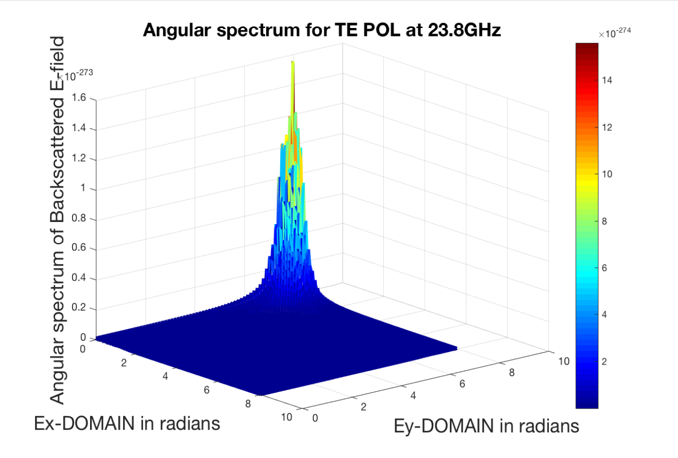

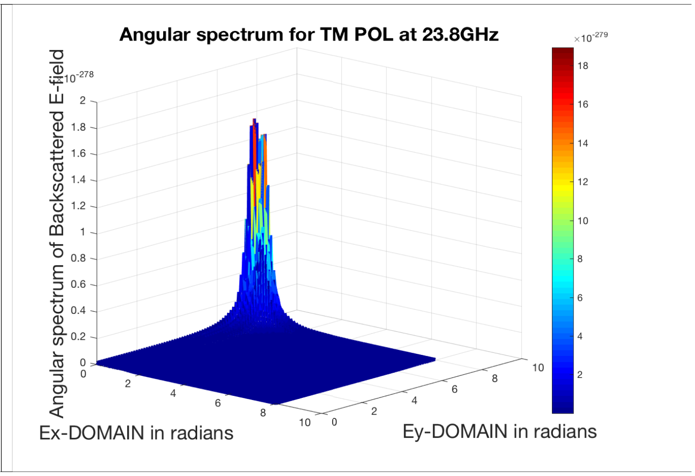

Figure 5.61: Angular Spectrum of Diffused Reflected Wavefront at 23.8 $GHz$ and $\delta_t = 2$ $mm$ for TE polarization with effective dielectric constant of seawater $\epsilon_{sw} = 28.9247 + j33.2233$ and foam void fraction $f_a = 0.8$ at constant $SST = 20^\circ$ and salinity $(34psu)$.

Figure 5.62: Angular Spectrum of Diffused Reflected Wavefront at 23.8 $GHz$ and $\delta_t = 2$ $mm$ for TM polarization with effective dielectric constant of seawater $\epsilon_{sw} = 28.9247 + j33.2233$ and foam void fraction $f_a = 0.8$ at constant $SST = 20^\circ$ and salinity $(34psu)$.

Figure 5.61 and 5.62 shows strong phase variations at $\delta_t$ and frequency of 23 $GHz$ which represents strong diffused reflections that occur at various slices of sea foam layer. We know that this is due to the increased population of randomly distributed bubbles present in the flat sea surface. This also represents accumulated diffractions at each individual sea foam layer with slice thickness $\delta_t$. Figure 5.59 and 5.60 shows random phase fluctuations of the E-field at frequency 23.8 $GHz$ and seafoam slice thickness $\delta_t = 0.2\ mm$ for the angular spectrum of the backscattered wavefront from the bottom of the seafoam layer. The field appears incoherent as the phase varies randomly from $-\pi$ to $\pi$. The angular spectrum of the diffused reflected wave field at $\delta_t = 2\ mm$ for a deep phase scattering screen is a function of the spectral wavenumbers $(p, q)$ for $1D$ problem and $(E_x, E_y)$ for $2D$ problem in the X and Y directions. The broadening of the peaks in figures 5.61 and 5.62 depends on the diffraction factor $\exp(i\Delta z\sqrt{k^2 - (p^2 + q^2)})$. When $k^2$ approaches $(p^2 + q^2)$, the lobes of the angular spectrum are spread or broadened across the $(p, q)$ or $(E_x, E_y)$ spectral domain. This happens at low WindSat frequencies such as 6.8 $GHz$ and 10.7 $GHz$ but at higher frequencies 18.7 $GHz$, 23.8 $GHz$ and 37 $GHz$ where $k^2 \gg (p^2 + q^2)$, the lobes of the angular spectrum becomes sharper and narrower across the $(p, q)$ or $(E_x, E_y)$ spectral domain.

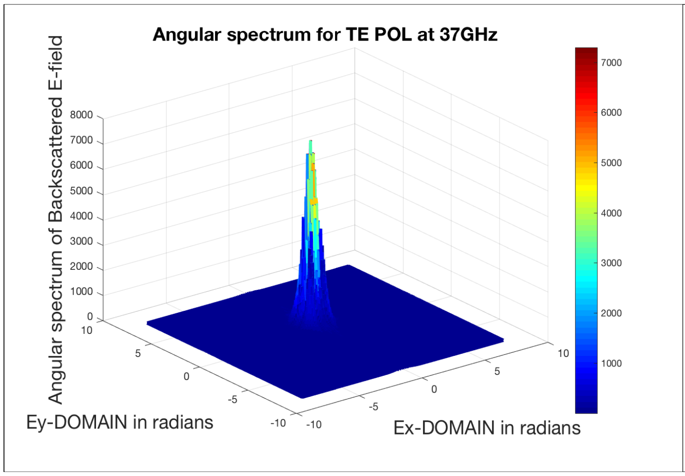

Figure 5.63: Angular Spectrum of Diffused Reflected Wavefront at 37 $GHz$ and $\delta_t = 0.1\ mm$ for TE polarization with effective dielectric constant of seawater $\epsilon_{sw} = 17.7537 + j26.8554$ and foam void fraction $f_a = 0.8$ at constant $SST = 20°$ and salinity $(34psu)$.

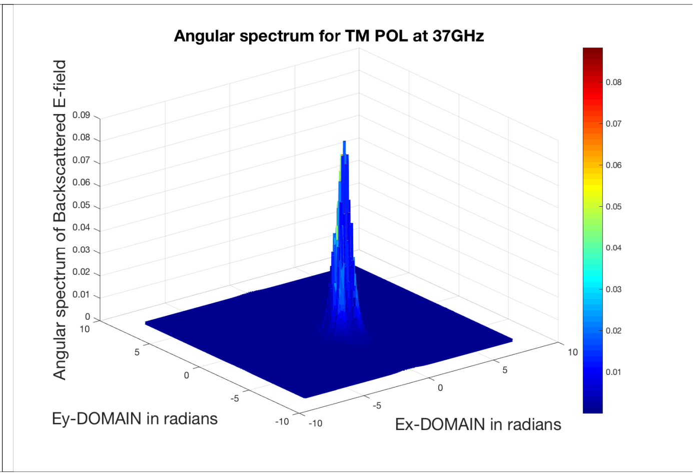

Figure 5.64: Angular Spectrum of Diffused Reflected Wavefront at 37 $GHz$ and $\delta_t = 0.1\ mm$ for TM polarization with effective dielectric constant of seawater $\epsilon_{sw} = 17.7537 + j26.8554$ and foam void fraction $f_a = 0.8$ at constant $SST = 20°$ and salinity $(34psu)$.

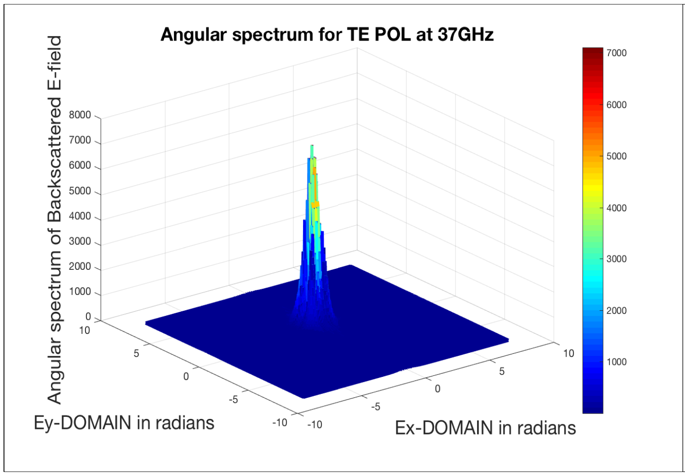

Figure 5.65: Angular Spectrum of Diffused Reflected Wavefront at 37 $GHz$ and $\delta_t = 0.2\ mm$ for TE polarization with effective dielectric constant of seawater $\epsilon_{sw} = 17.7537 + j26.8554$ and foam void fraction $f_a = 0.8$ at constant $SST = 20°$ and salinity $(34psu)$.

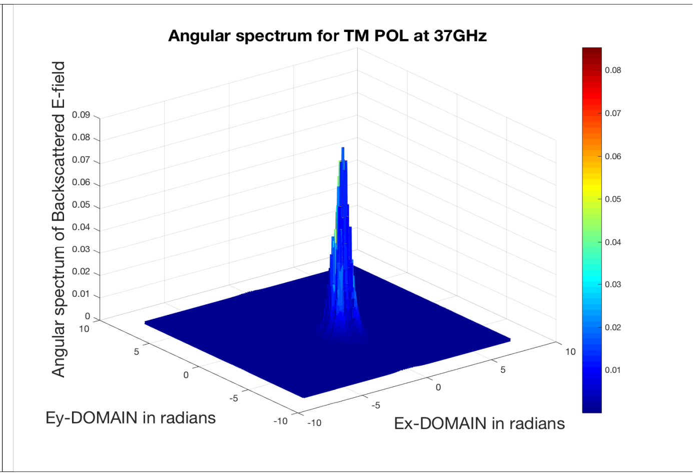

Figure 5.66: Angular Spectrum of Diffused Reflected Wavefront at 37 $GHz$ and $\delta_t = 0.2\ mm$ for TM polarization with effective dielectric constant of seawater $\epsilon_{sw} = 17.7537 + j26.8554$ and foam void fraction $f_a = 0.8$ at constant $SST = 20°$ and salinity $(34psu)$.

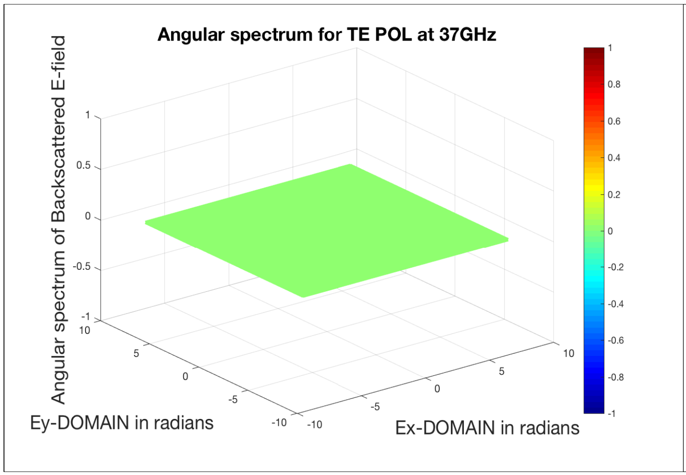

Figure 5.67: Angular Spectrum of Diffused Reflected Wavefront at 37 $GHz$ and $\delta_t = 2\ mm$ for TE polarization with effective dielectric constant of seawater $\epsilon_{sw} = 17.7537 + j26.8554$ and foam void fraction $f_a = 0.8$ at constant $SST = 20°$ and salinity ($34psu$).

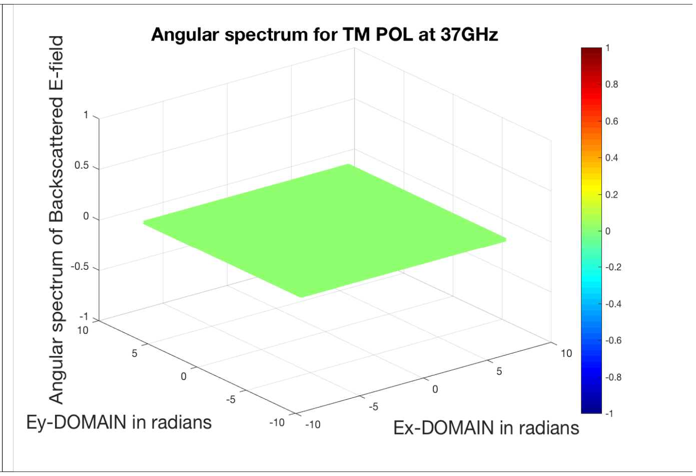

Figure 5.68: Angular Spectrum of Diffused Reflected Wavefront at 37 $GHz$ and $\delta_t = 2\ mm$ for TM polarization with effective dielectric constant of seawater $\epsilon_{sw} = 17.7537 + j26.8554$ and foam void fraction $f_a = 0.8$ at constant $SST = 20°$ and salinity ($34psu$).

The phase pertubations clearly varies randomly from $-\pi$ to $\pi$ but the low phase contours occupies most region in the contour plots at higher frequencies. We observe that the low phase contour lines increases with increasing frequency and more interactions takes place at higher frequencies and deep phase screens. Comparing the contour plots for lower frequencies (6.8 $GHz$, and 10.7 $GHz$) with those of higher frequencies (23.8 $GHz$, and 37 $GHz$), it was obvious that diffuse scattering increases at higher frequencies with increase in bubble population i.e seafoam slice thickness. This is evident as the angular spectrum of the backscattered E-field at the sea surface have phase and amplitude values equal to zero for very large seafoam slice thickness $\delta_t = 2\ mm$ at high WindSat frequencies. The E-field was first absorbed, then reflected as shown in the contour plots of the phase difference between slice 3 and slice 4 see 5.25, 5.26, 5.37 and 5.38 at high WindSat frequencies (23.8 $GHz$ and

37 $GHz$). At these frequencies and large seafoam slice thicknesses, we observe that the foam covered layer of randomly distributed air bubbles acts like a blackbody as it absorbs the E-field that is incident on it.

## 5.4 Field Intensity $|E|^2$ at WindSat Frequencies

The amplitude of the E-field attenuates as it propagates through successive layers of seafoam. The diffractive factor of the split-step propagator $\exp(i\Delta x\sqrt{k^2-(p^2+q^2)})$ accounts for the attenuation of the E-field as it travels through the 5 slices of seafoam layers. The field intensity of the scattered E-field at various WindSat frequencies shows that attenuation increase with increasing depth of the seafoam slices. We illustrate this in the figures below

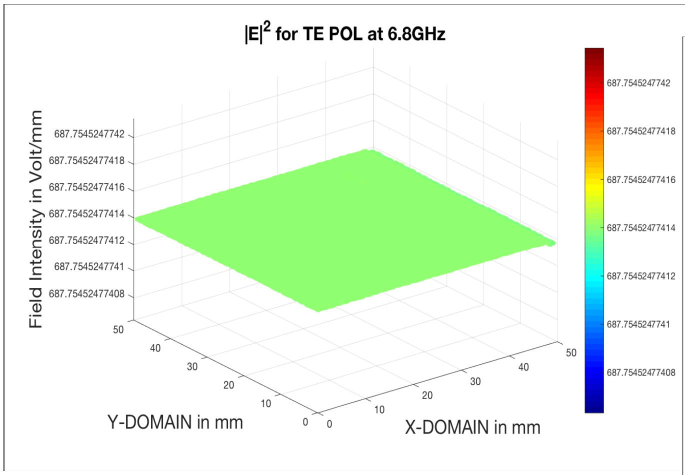

Figure 5.69: Field intensity of backscattered wave for horizontal polarization (TE) with zenith $\theta_i = 30°$ and azimuth $\phi = 0°$ as a function of the spatial coordinates X and Y of the propagation media at 6.8 $GHz$ and $\delta_t = 0.1$ $mm$.

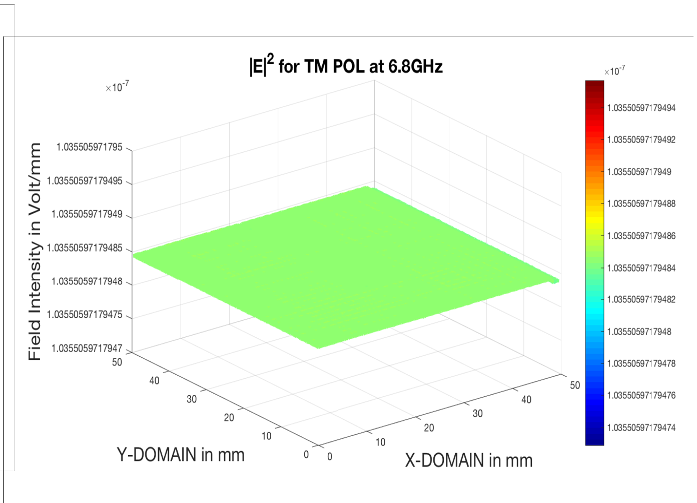

Figure 5.70: Field intensity of backscattered wave for vertical polarization (TM) with zenith $\theta_i = 30°$ and azimuth $\phi = 0°$ as a function of the spatial coordinates X and Y of the propagation media at 6.8 $GHz$ and $\delta_t = 0.1$ $mm$.

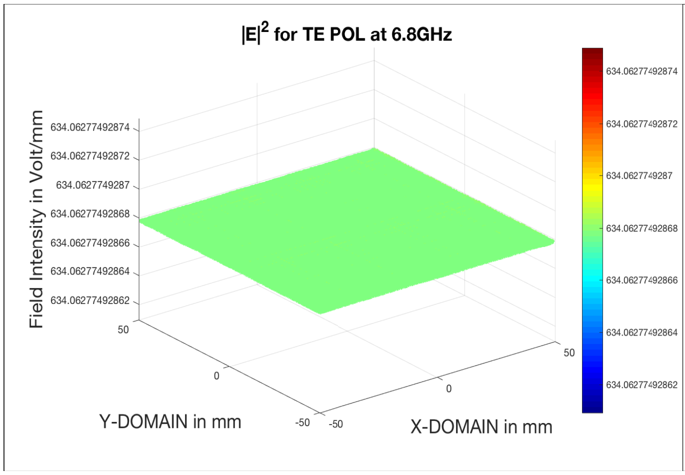

Figure 5.71: Field intensity of backscattered wave for horizontal polarization (TE) with zenith $\theta_i = 30°$ and azimuth $\phi = 0°$ as a function of the spatial coordinates X and Y of the propagation media at 6.8 $GHz$ and $\delta_t = 0.2$ $mm$.

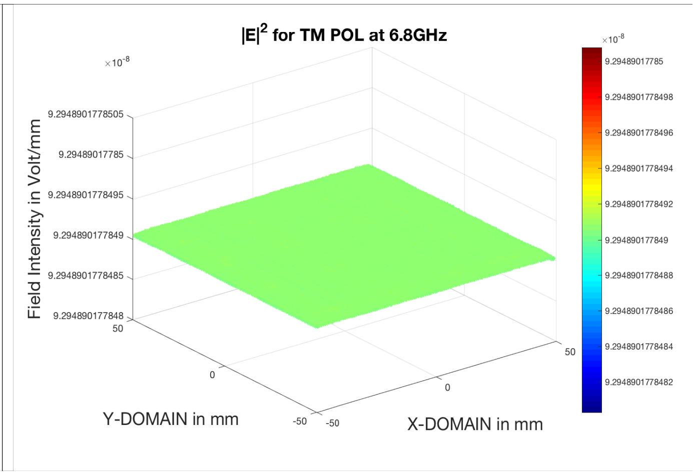

Figure 5.72: Field intensity of backscattered wave for horizontal polarization (TM) with zenith $\theta_i = 30°$ and azimuth $\phi = 0°$ as a function of the spatial coordinates X and Y of the propagation media at 6.8 $GHz$ and $\delta_t = 0.2$ $mm$.

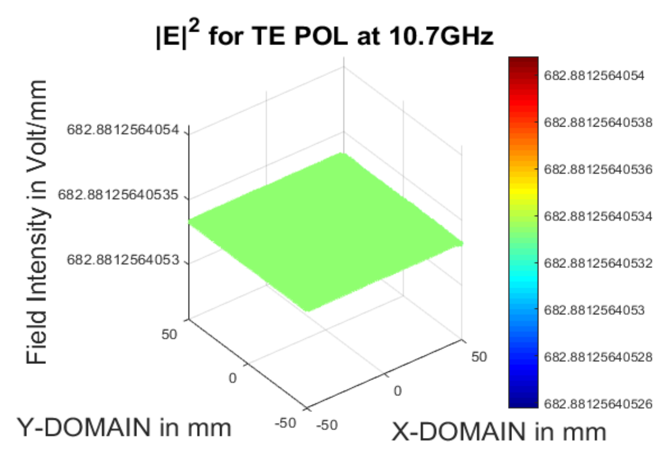

Figure 5.73: Field intensity of backscattered wave for horizontal polarization (TE) with zenith $\theta_i = 30°$ and azimuth $\phi = 0°$ as a function of the spatial X and Y of the propagation media at 10.7 $GHz$ and $\delta_t = 0.1$ $mm$.

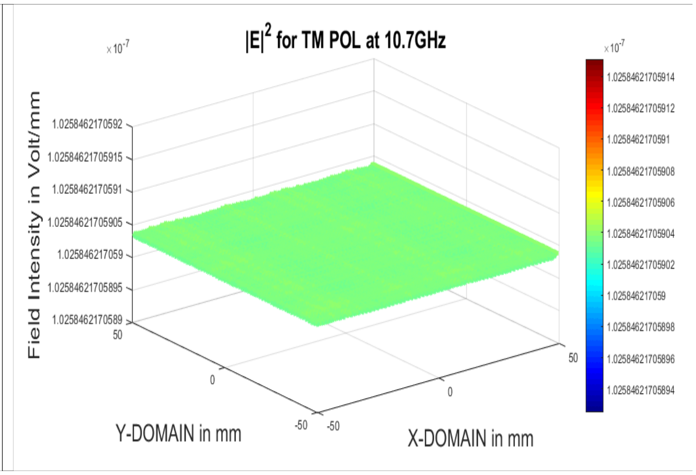

Figure 5.74: Field intensity of backscattered wave for vertical polarization (TM) with zenith $\theta_i = 30°$ and azimuth $\phi = 0°$ as a function of the spatial X and Y of the propagation media at 10.7 $GHz$ and $\delta_t = 0.1$ $mm$.

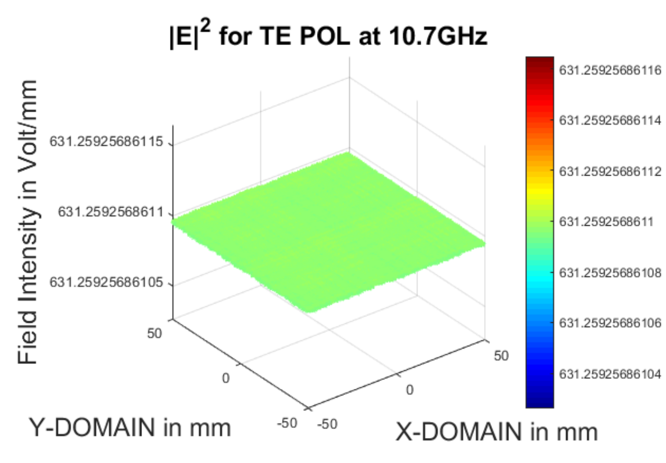

Figure 5.75: Field intensity of backscattered wave for horizontal polarization (TE) with zenith $\theta_i = 30°$ and azimuth $\phi = 0°$ as a function of the spatial coordinates X and Y of the propagation media at 10.7 $GHz$ and $\delta_t = 0.2$ $mm$.

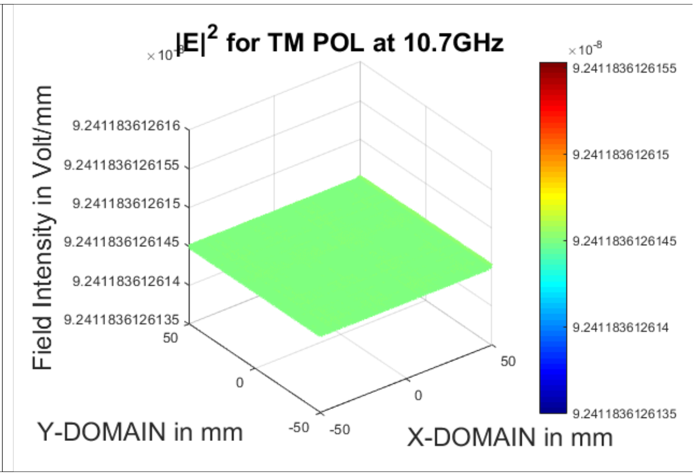

Figure 5.76: Field intensity of backscattered wave for horizontal polarization (TM) with zenith $\theta_i = 30°$ and azimuth $\phi = 0°$ as a function of the spatial coordinates X and Y of the propagation media at 10.7 $GHz$ and $\delta_t = 0.2$ $mm$.

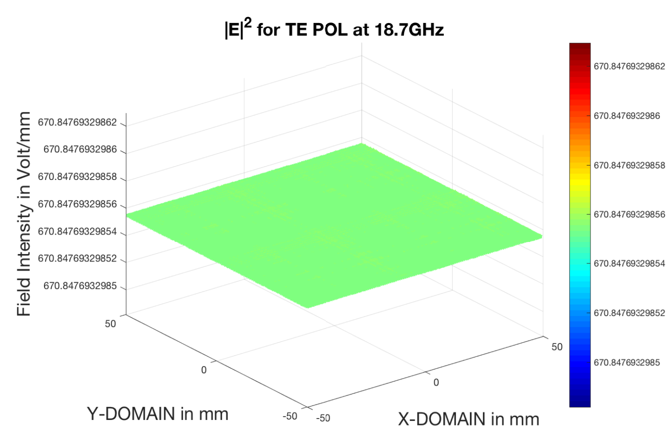

Figure 5.77: Field intensity of backscattered wave for horizontal polarization (TE) with zenith $\theta_i = 30°$ and azimuth $\phi = 0°$ as a function of the spatial X and Y of the propagation media at 18.7 $GHz$ and $\delta_t = 0.1$ $mm$.

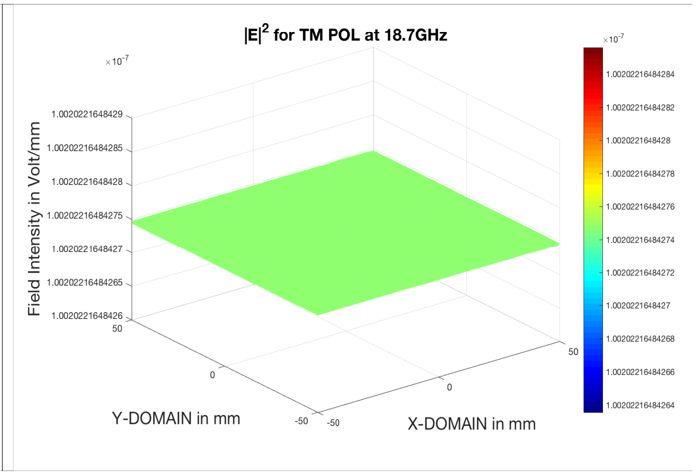

Figure 5.78: Field intensity of backscattered wave for vertical polarization (TM) with zenith $\theta_i = 30°$ and azimuth $\phi = 0°$ as a function of the spatial X and Y of the propagation media at 18.7 $GHz$ and $\delta_t = 0.1$ $mm$.

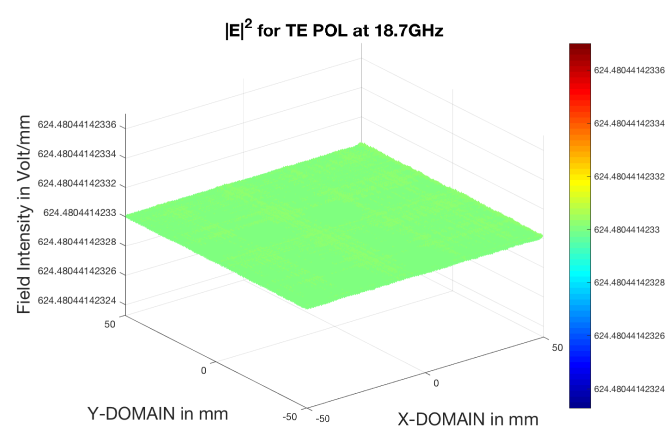

Figure 5.79: Field intensity of backscattered wave for horizontal polarization (TE) with zenith $\theta_i = 30°$ and azimuth $\phi = 0°$ as a function of the spatial coordinates X and Y of the propagation media at 18.7 $GHz$ and $\delta_t = 0.2$ $mm$.

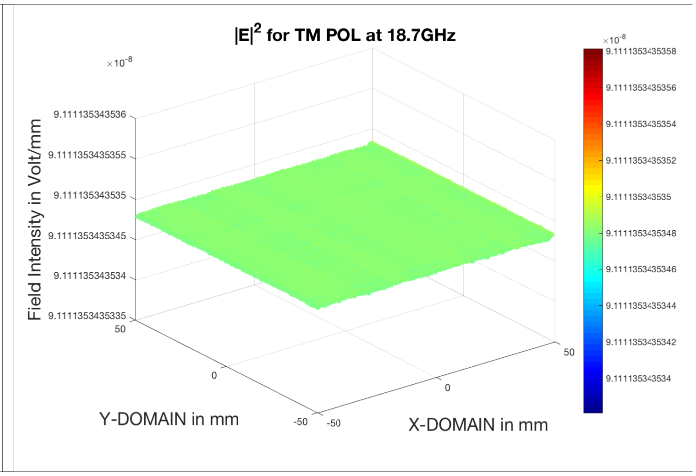

Figure 5.80: Field intensity of backscattered wave for horizontal polarization (TM) with zenith $\theta_i = 30°$ and azimuth $\phi = 0°$ as a function of the spatial coordinates X and Y of the propagation media at 18.7 $GHz$ and $\delta_t = 0.2$ $mm$.

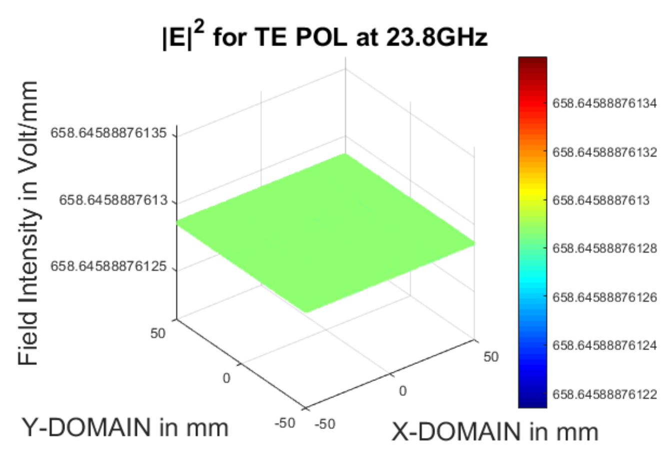

Figure 5.81: Field intensity of backscattered wave for horizontal polarization (TE) with zenith $\theta_i = 30°$ and azimuth $\phi = 0°$ as a function of the spatial X and Y of the propagation media at 23.8 $GHz$ and $\delta_t = 0.1$ $mm$.

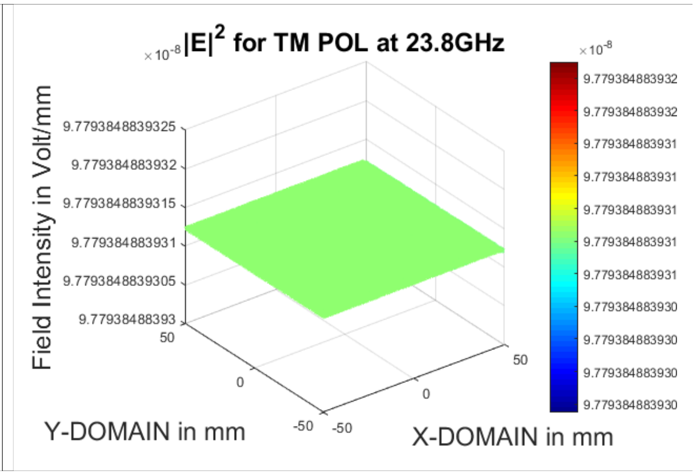

Figure 5.82: Field intensity of backscattered wave for vertical polarization (TM) with zenith $\theta_i = 30°$ and azimuth $\phi = 0°$ as a function of the spatial X and Y of the propagation media at 23.8 $GHz$ and $\delta_t = 0.1$ $mm$.

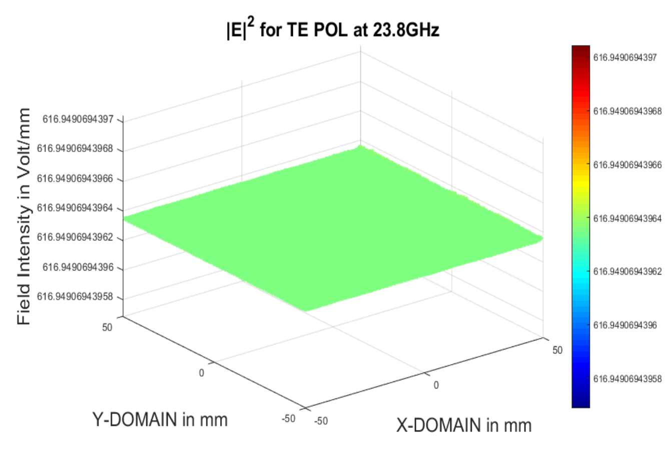

Figure 5.83: Field intensity of backscattered wave for horizontal polarization (TE) with zenith $\theta_i = 30°$ and azimuth $\phi = 0°$ as a function of the spatial coordinates X and Y of the propagation media at 23.8 $GHz$ and $\delta_t = 0.2$ $mm$.

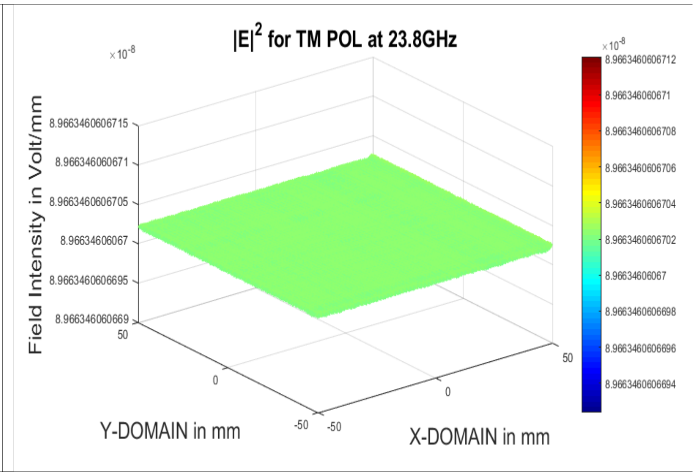

Figure 5.84: Field intensity of backscattered wave for horizontal polarization (TM) with zenith $\theta_i = 30°$ and azimuth $\phi = 0°$ as a function of the spatial coordinates X and Y of the propagation media at 23.8 $GHz$ and $\delta_t = 0.2$ $mm$.

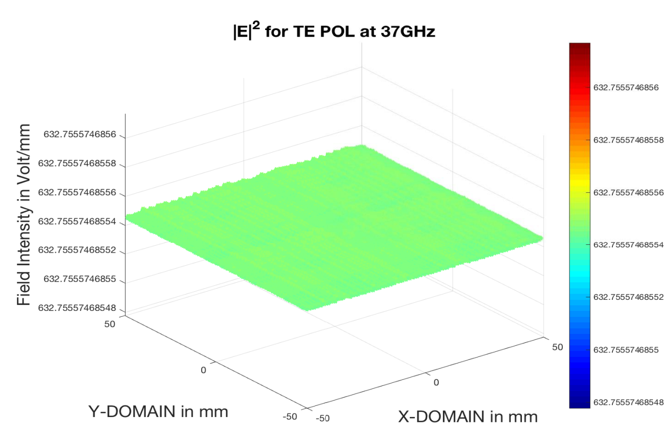

Figure 5.85: Field intensity of backscattered wave for horizontal polarization (TE) with zenith $\theta_i = 30°$ and azimuth $\phi = 0°$ as a function of the spatial X and Y of the propagation media at 37 $GHz$ and $\delta_t = 0.1\ mm$.

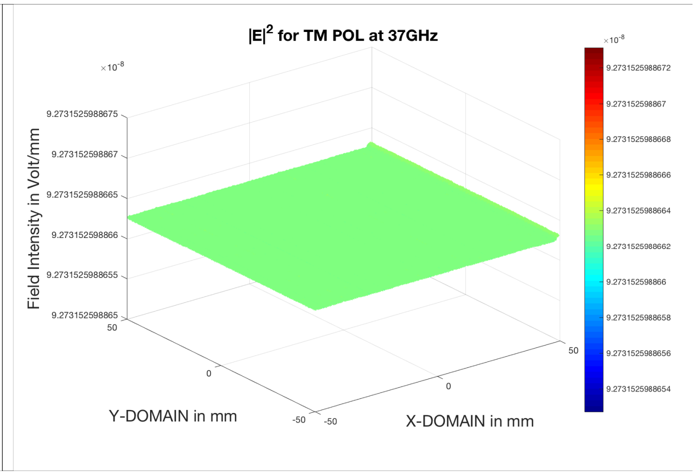

Figure 5.86: Field intensity of backscattered wave for vertical polarization (TM) with zenith $\theta_i = 30°$ and azimuth $\phi = 0°$ as a function of the spatial X and Y of the propagation media at 37 $GHz$ and $\delta_t = 0.1\ mm$.

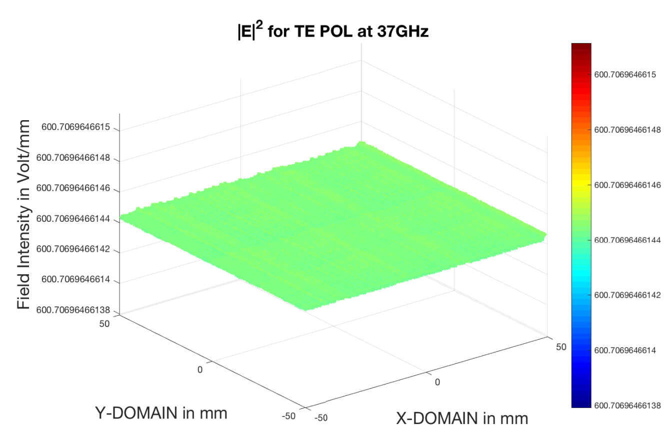

Figure 5.87: Field intensity of backscattered wave for horizontal polarization (TE) with zenith $\theta_i = 30°$ and azimuth $\phi = 0°$ as a function of the spatial coordinates X and Y of the propagation media at 37 $GHz$ and $\delta_t = 0.2\ mm$.

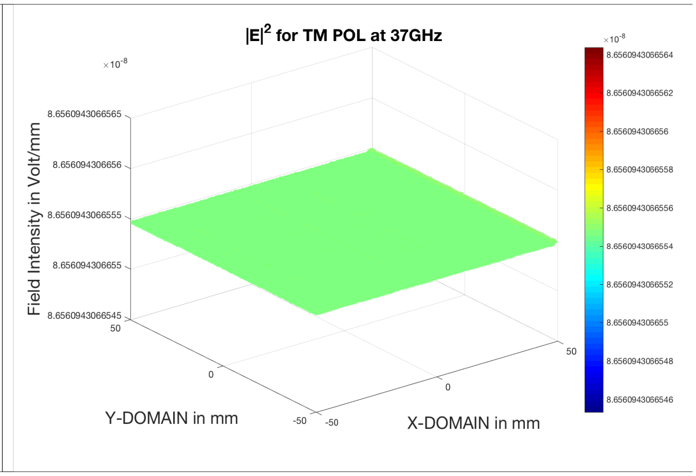

Figure 5.88: Field intensity of backscattered wave for horizontal polarization (TM) with zenith $\theta_i = 30°$ and azimuth $\phi = 0°$ as a function of the spatial coordinates X and Y of the propagation media at 37 $GHz$ and $\delta_t = 0.2\ mm$.

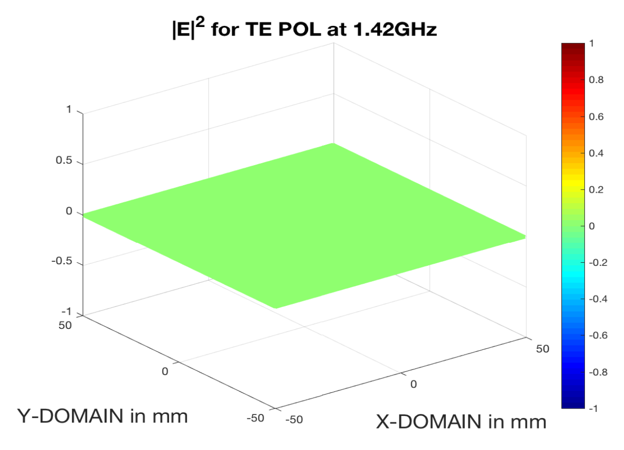

Figure 5.89: Field intensity of backscattered wave for horizontal polarization (TE) with zenith $\theta_i = 30°$ and azimuth $\phi = 0°$ as a function of the spatial X and Y of the propagation media at 1.42 $GHz$ and $\delta_t = 2\ mm$.

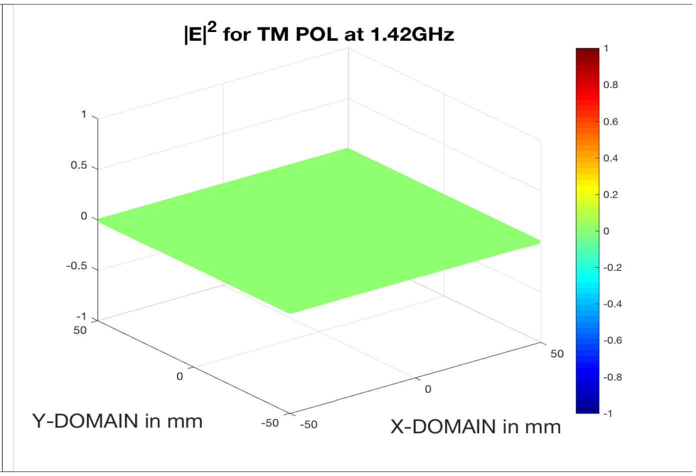

Figure 5.90: Field intensity of backscattered wave for vertical polarization (TM) with zenith $\theta_i = 30°$ and azimuth $\phi = 0°$ as a function of the spatial X and Y of the propagation media at 1.42 $GHz$ and $\delta_t = 2\ mm$.

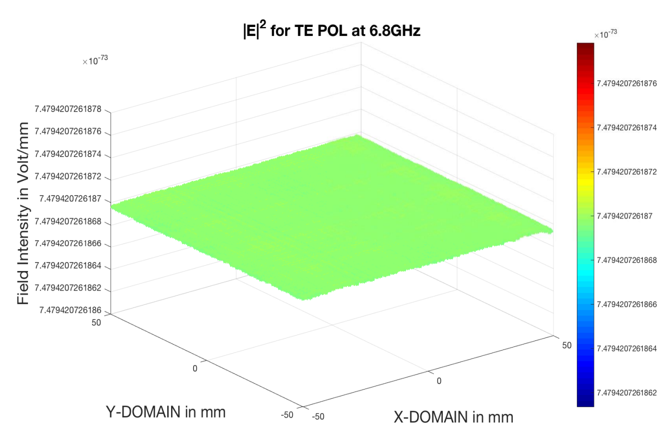

Figure 5.91: Field intensity of backscattered wave for horizontal polarization (TE) with zenith $\theta_i = 30°$ and azimuth $\phi = 0°$ as a function of the spatial coordinates X and Y of the propagation media at 6.8 $GHz$ and $\delta_t = 2\ mm$.

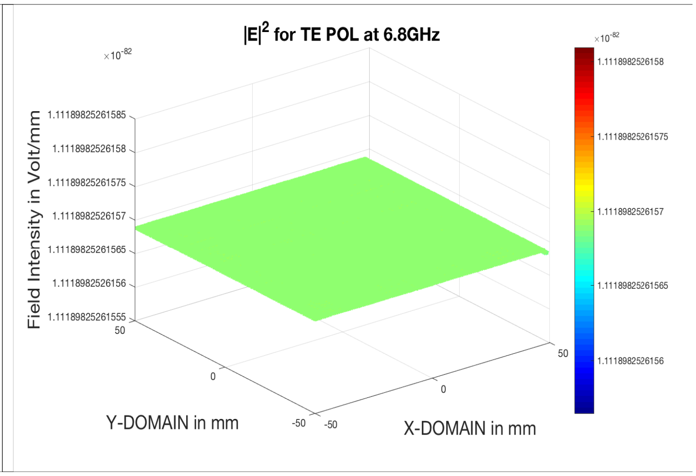

Figure 5.92: Field intensity of backscattered wave for horizontal polarization (TM) with zenith $\theta_i = 30°$ and azimuth $\phi = 0°$ as a function of the spatial coordinates X and Y of the propagation media at 6.8 $GHz$ and $\delta_t = 2\ mm$.

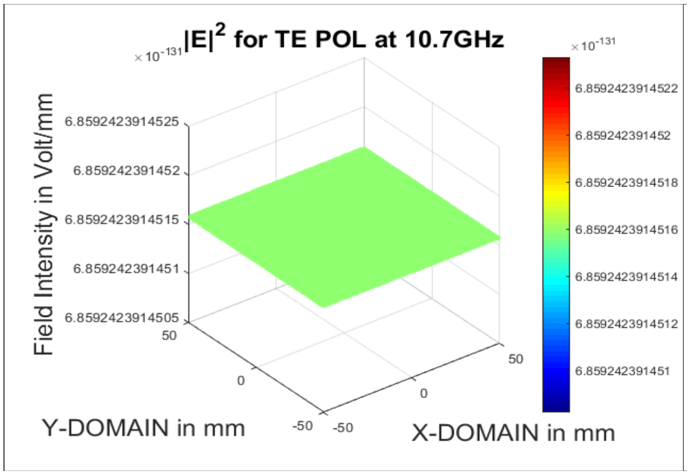

Figure 5.93: Field intensity of backscattered wave for horizontal polarization (TE) with zenith $\theta_i = 30°$ and azimuth $\phi = 0°$ as a function of the spatial X and Y of the propagation media at 10.7 $GHz$ and $\delta_t = 2\ mm$.

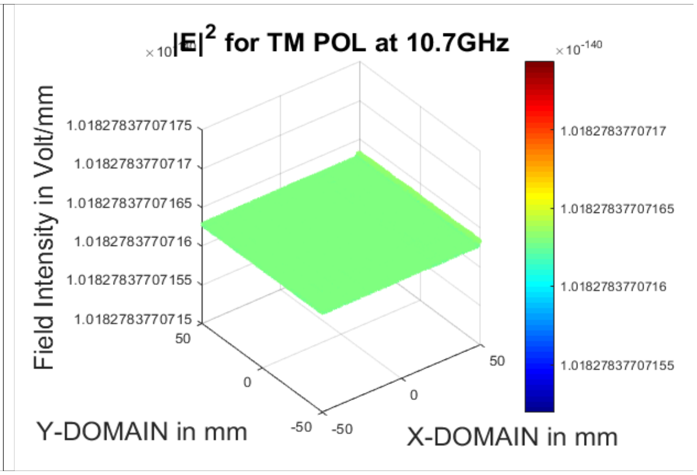

Figure 5.94: Field intensity of backscattered wave for vertical polarization (TM) with zenith $\theta_i = 30°$ and azimuth $\phi = 0°$ as a function of the spatial X and Y of the propagation media at 10.7 $GHz$ and $\delta_t = 2\ mm$.

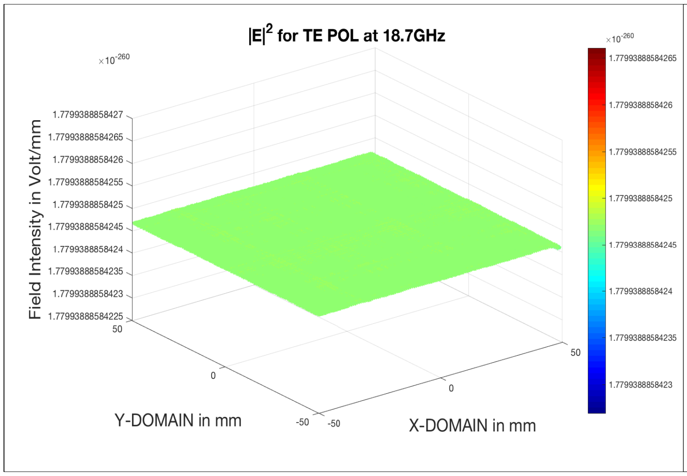

Figure 5.95: Field intensity of backscattered wave for horizontal polarization (TE) with zenith $\theta_i = 30°$ and azimuth $\phi = 0°$ as a function of the spatial coordinates X and Y of the propagation media at 18.7 $GHz$ and $\delta_t = 2$ $mm$.

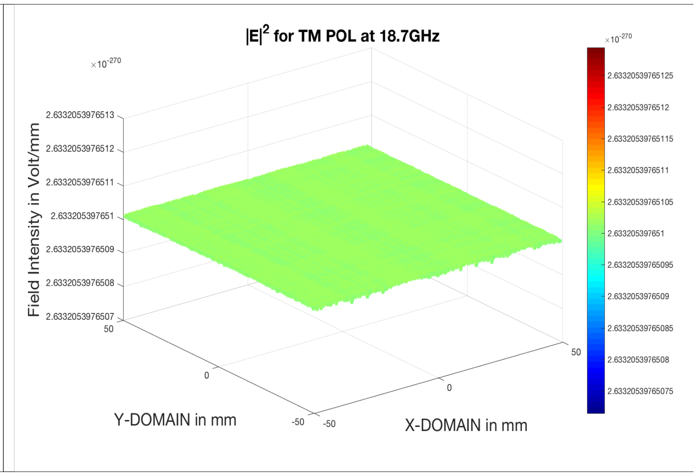

Figure 5.96: Field intensity of backscattered wave for horizontal polarization (TM) with zenith $\theta_i = 30°$ and azimuth $\phi = 0°$ as a function of the spatial coordinates X and Y of the propagation media at 18.7 $GHz$ and $\delta_t = 2$ $mm$.

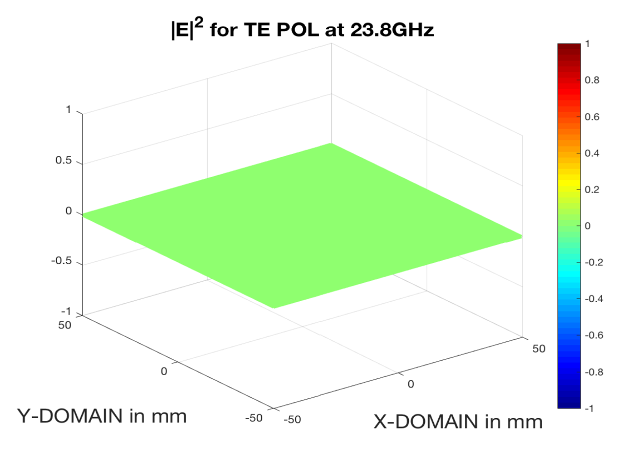

Figure 5.97: Field intensity of backscattered wave for horizontal polarization (TE) with zenith $\theta_i = 30°$ and azimuth $\phi = 0°$ as a function of the spatial X and Y of the propagation media at 23.8 $GHz$ and $\delta_t = 2\ mm$.

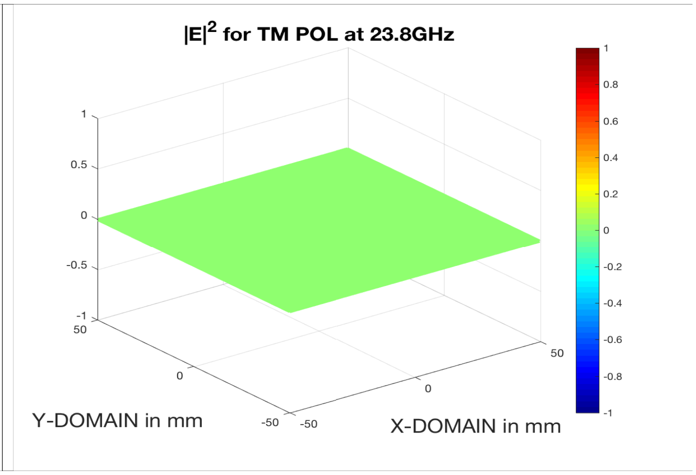

Figure 5.98: Field intensity of backscattered wave for vertical polarization (TM) with zenith $\theta_i = 30°$ and azimuth $\phi = 0°$ as a function of the spatial X and Y of the propagation media at 23.8 $GHz$ and $\delta_t = 2\ mm$.

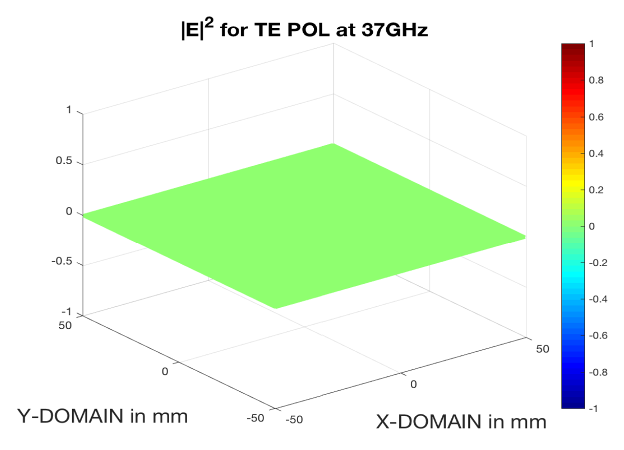

Figure 5.99: Field intensity of backscattered wave for horizontal polarization (TE) with zenith $\theta_i = 30°$ and azimuth $\phi = 0°$ as a function of the spatial coordinates X and Y of the propagation media at 23.8 $GHz$ and $\delta_t = 2$ $mm$.

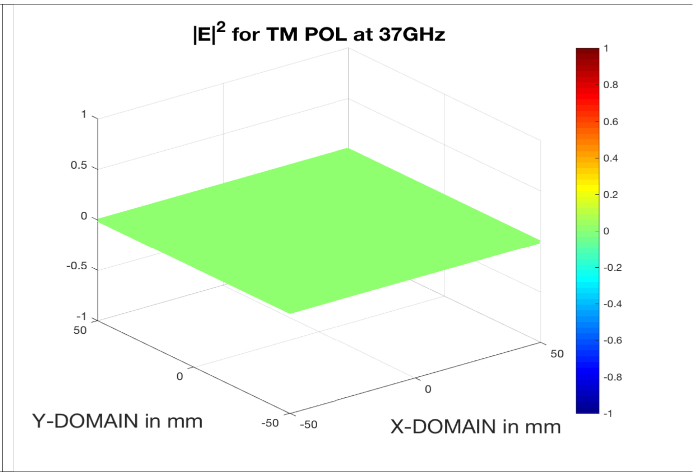

Figure 5.100: Field intensity of backscattered wave for horizontal polarization (TM) with zenith $\theta_i = 30°$ and azimuth $\phi = 0°$ as a function of the spatial coordinates X and Y of the propagation media at 23.8 $GHz$ and $\delta_t = 2$ $mm$.

The amplitude of the E-field varies with angular wave-number in radians as it propagates through slices of the sea foam layer. Figures above illustrates variation of field intensity of the E-field for both TE and TM polarizations with spatial domains which describe attenuation of the propagated E-field along the spatial directions. We can see the fluctuation in peaks of the diffracted E-field is due to the random varying effective dielectric constants of sea-foam with varying size distributions.

We have shown that the amplitude of the E-field attenuates with depth of seafoam slices with exception to the scenerio where the wave field is absorbed for large seafoam slice thickness $\delta_t = 2\,mm$. It was apparent that this phenomenon is true for all WindSat frequency channels. We can conclude that the amplitude of the E-field attenuates with increase in frequency and depth of seafoam slice thicknesses.

### 5.4.1 Attenuation of the Field Intensity in dB with Depth of Sea Foam at WindSat Frequencies

The attenuation of the field intensity in decibel ($dB$) at a low frequency of 6.8 $GHz$ and sea foam slice thickness $\delta_t = 0.1\ mm$ and $\delta_t = 0.2\ mm$, which represents a thin phase scattering screen, increases as the depth of the sea foam layer increases. Figures 5.101-5.104 illustrate the variation of attenuation of the E-field in dB with depth in mm of sea foam layer.

Test data from measurements by Bordonskiy et.al [56] at wavelengths $\lambda = 0.26, 0.86, 2.08, 8$ and 18 $cm$ and sensitivity fluctuation of $(0.1 - 0.2)\ K$ was used to probe brightness temperature changes induced by foam layer structural transformation. The following results were reported

1. Emissivity of a foam layer dominates at $\lambda = 0.26 - 8\ cm$, due to thin ($\approx 0.1$) $cm$ thickness monolayer of bubble located at the air-water interface.

2. Emissivity of a foam layer at $\lambda = 0.26 - 2cm$, due to thick ($\approx 1 - 2$) $cm$ thickness of foam is about 1 and represents an absolute black-body.

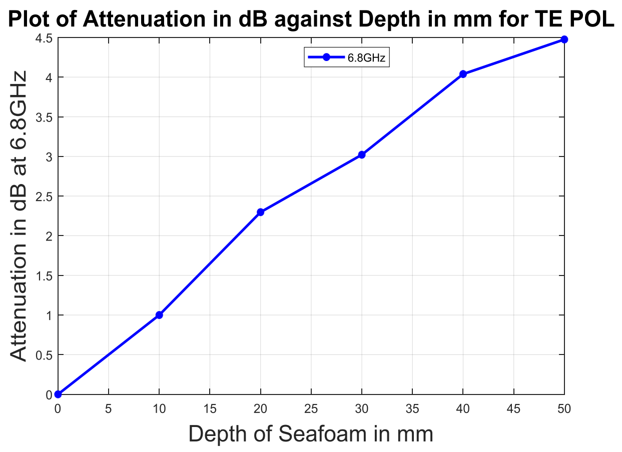

Figure 5.101: Attenuation of Field Intensity for horizontal polarization (TE) with zenith $\theta_i = 30°$ and azimuth $\phi = 0°$ with depth of sea foam at 6.8 $GHz$ and $\delta_t = 0.1\ mm$.

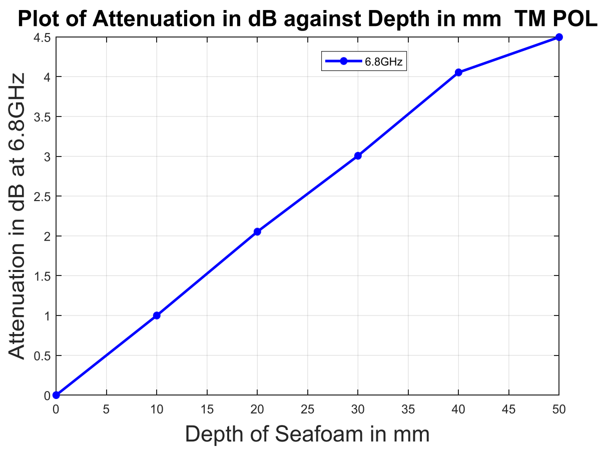

Figure 5.102: Attenuation of Field Intensity for vertical polarization (TM) with zenith $\theta_i = 30°$ and azimuth $\phi = 0°$ with depth of sea foam at 6.8 $GHz$ and $\delta_t = 0.1\ mm$.

As earlier reported in section 2.13 Table 2.2, the refractive index of seawater decreases with increase in frequency at constant temperature and salinity. The effective dielectric constant of seawater was estimated as $62.6425 + j27.8729$ at 6.8 $GHz$ by Stogryn's model [68]. The high dielectric constant of seawater contributes immensely in evaluating the effective dielectric constant of sea foam with 0.8 foam void fraction. The computed average dielectric constant of sea foam was $1.1629 + j0.2066$ for a thin phase scattering screen which explains why the attenuation of the E-field increases linearly with increasing depth of sea foam layer. When $\delta_t = 0.2\ mm$ there was no significant change of this linear relationship between attenuation

$\alpha_{dB}$ and depth of sea foam layer. It is well known that in an extended random media modelled as 2-D slices of $N$ layers, the E-fields build up with propagation through successive layers of the media.

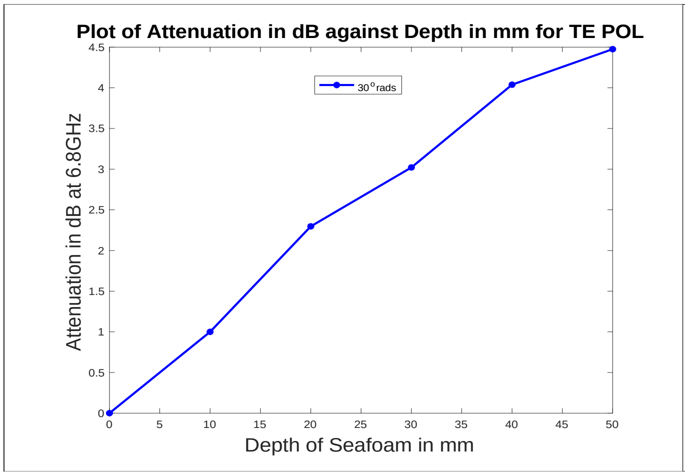

Figure 5.103: Attenuation of Field Intensity for horizontal polarization (TE) with zenith $\theta_i = 30°$ and azimuth $\phi = 0°$ with depth of sea foam at 6.8 $GHz$ and $\delta_t = 0.2\ mm$.

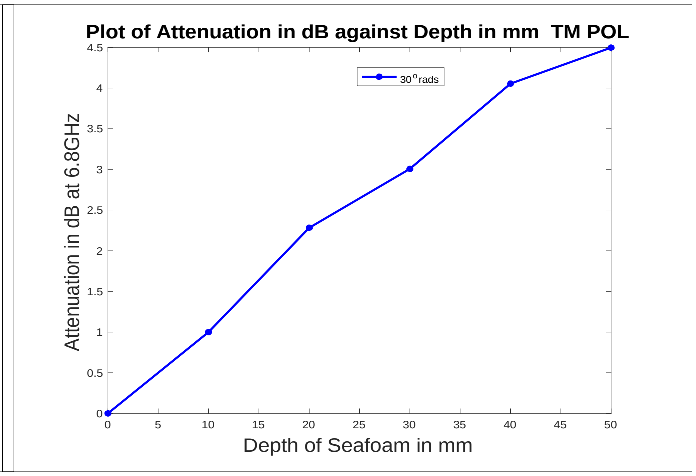

Figure 5.104: Attenuation of Field Intensity for vertical polarization (TM) with zenith $\theta_i = 30°$ and azimuth $\phi = 0°$ with depth of sea foam at 6.8 $GHz$ and $\delta_t = 0.2\ mm$.

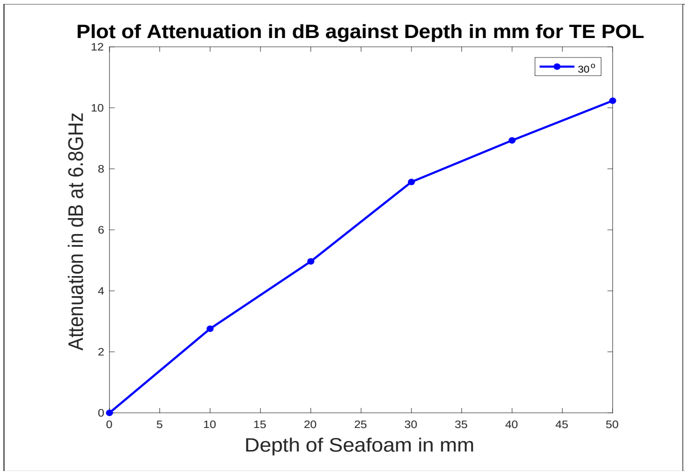

Figure 5.105: Attenuation of Field Intensity for vertical polarization (TM) with zenith $\theta_i = 30°$ and azimuth $\phi = 0°$ with depth of sea foam at 1.42 $GHz$ and $\delta_t = 2\ mm$.

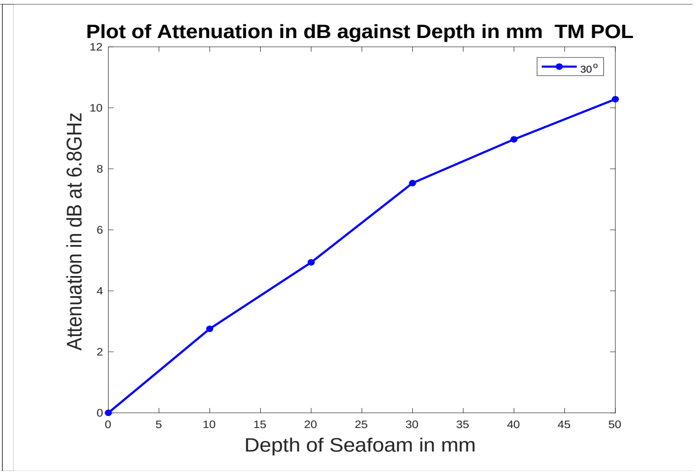

Figure 5.106: Attenuation of Field Intensity for vertical polarization (TM) with zenith $\theta_i = 30°$ and azimuth $\phi = 0°$ with depth of sea foam at 1.42 $GHz$ and $\delta_t = 2\ mm$.

For $\delta_t = 2\ mm$ which represents a deep phase scattering screen, we observe that the attenuation in dB increases in greater amount than the case for $\delta_t = 0.1\ mm$ and $\delta_t = 0.2\ mm$.The field intensity attenuates linearly with increase in depth of sea foam layer as shown in figures 5.105 and 5.106 above. We were able to illustrate that extinction of propagated E-field through thin phase scattering screens are due to diffused reflections by the sea foam covered sea-surface which builds up as the E-field travels further through the slices of the sea foam layers. For deep phase scattering screens, the E-field is absorbed within the sea foam layer as it travels further through the deep phase screens. These behaviours of the E-field extinction is dependent on the frequency of the propagated field, the slice thickness $\delta_t$, the depth of sea foam layer, effective dielectric constant of sea foam, foam void fraction and incident angle of propagating E-field.

The attenuation in dB for increasing depth of sea foam layer at higher frequency channel are shown below. There is no significant intensity fluctuations at small slice thickness $\delta_t = 0.1\ mm$ at 6.8 $GHz$ as the amplitude variation of the E-field appears constant with increasing depth of sea foam layer. For increased slice thickness $\delta_t = 0.2\ mm$ the behaviour of the E-field as it travels through the slices of sea foam remains constant which validates the idea that intensity fluctuations of propagated plane waves do not undergo strong scattering through thin phase scattering screens at low frequencies.

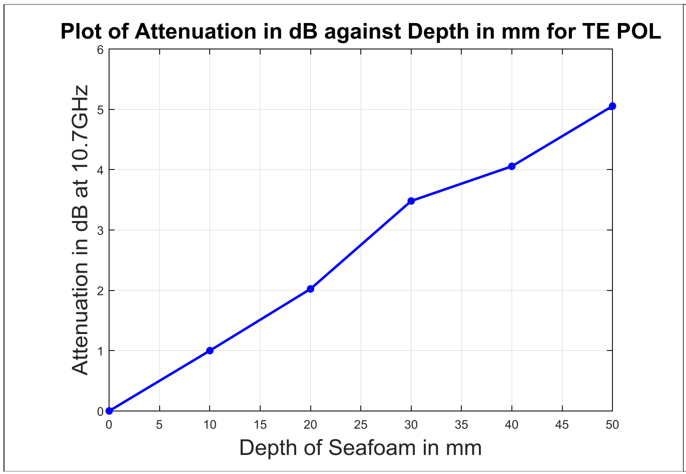

Figure 5.107: Attenuation of Field Intensity for horizontal polarization (TE) with zenith $\theta_i = 30°$ and azimuth $\phi = 0°$ with depth of sea foam at 10.7 $GHz$ and $\delta_t = 10\ mm$.

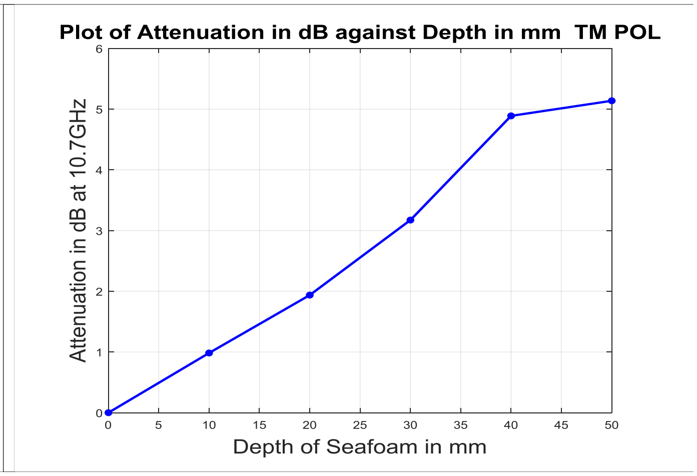

Figure 5.108: Attenuation of Field Intensity for vertical polarization (TM) with zenith $\theta_i = 30°$ and azimuth $\phi = 0°$ with depth of sea foam at 10.7 $GHz$ and $\delta_t = 10\ mm$.

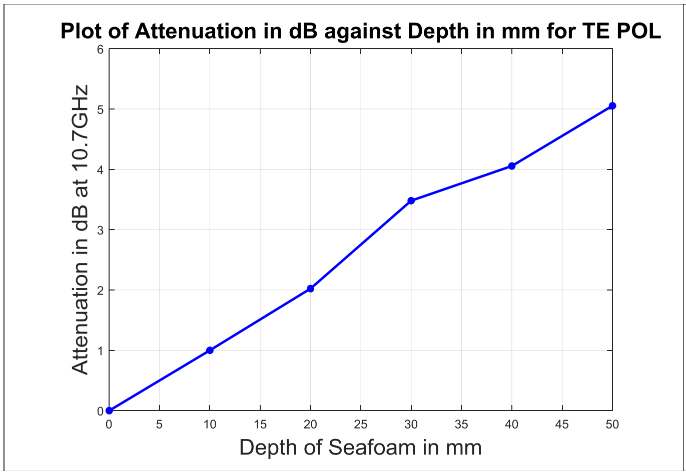

Figure 5.109: Attenuation of Field Intensity for vertical polarization (TM) with zenith $\theta_i = 30°$ and azimuth $\phi = 0°$ with depth of sea foam at 10.7 $GHz$ and $\delta_t = 20\ mm$.

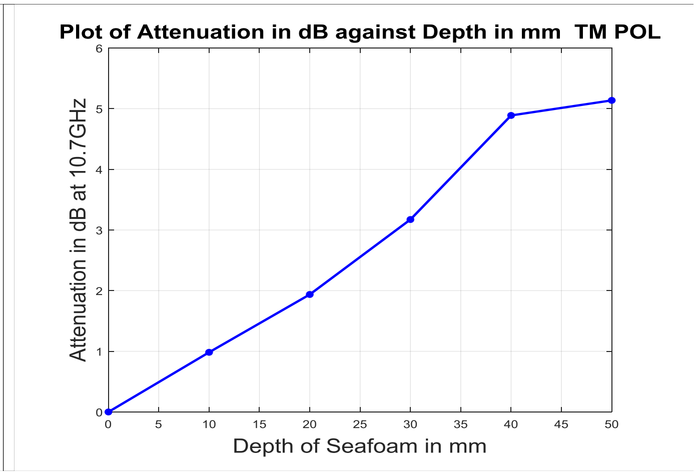

Figure 5.110: Attenuation of Field Intensity for vertical polarization (TM) with zenith $\theta_i = 30°$ and azimuth $\phi = 0°$ with depth of sea foam at 10.7 $GHz$ and $\delta_t = 20\ mm$.

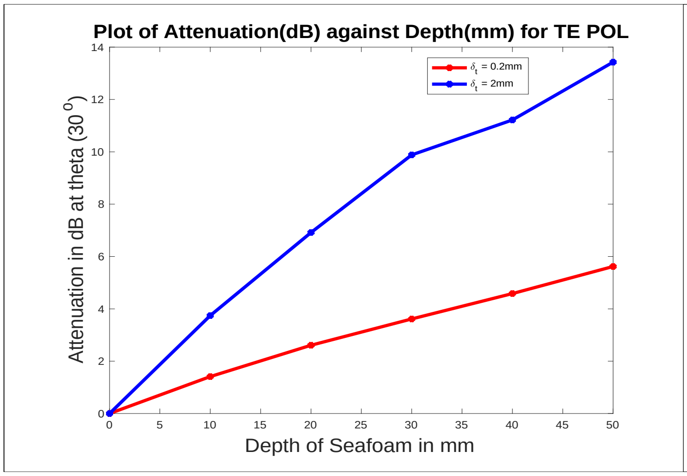

Figure 5.111: Attenuation of Field Intensity for horizontal polarization (TE) with zenith $\theta_i = 30°$ and azimuth $\phi = 0°$ with depth of sea foam at 18.7 $GHz$ and $\delta_t = 0.2\ mm$, and 2 $mm$.

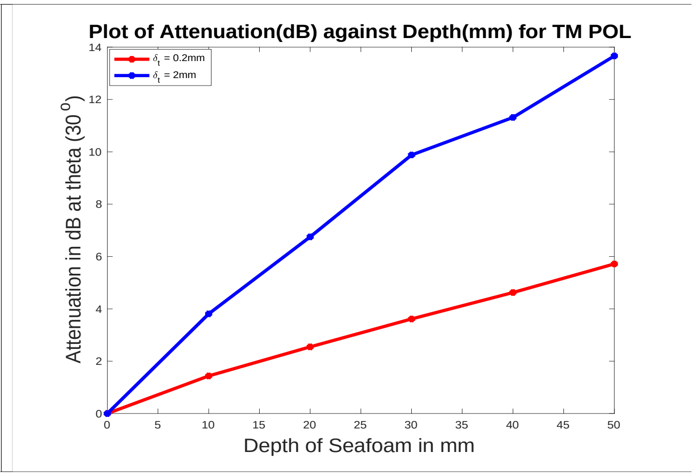

Figure 5.112: Attenuation of Field Intensity for vertical polarization (TM) with zenith $\theta_i = 30°$ and azimuth $\phi = 0°$ with depth of sea foam at 18.7 $GHz$ and slice thickness $\delta_t = 0.2\ mm$, and 2 $mm$.

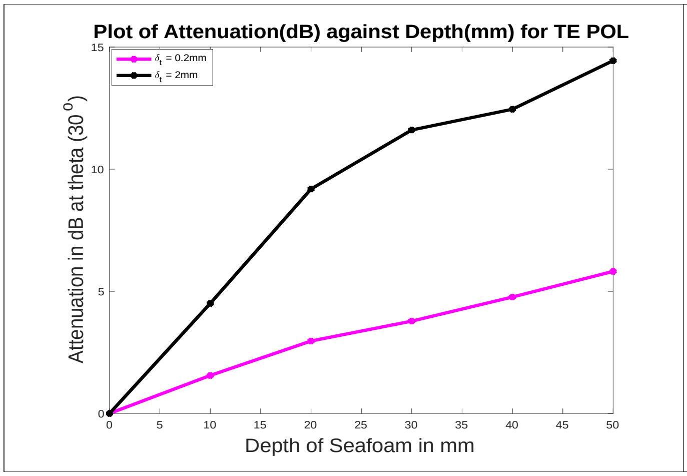

Figure 5.113: Attenuation of Field Intensity for vertical polarization (TM) with zenith $\theta_i = 30°$ and azimuth $\phi = 0°$ with depth of sea foam at 23.8 $GHz$ and $\delta_t = 0.2\ mm$, and 2 $mm$.

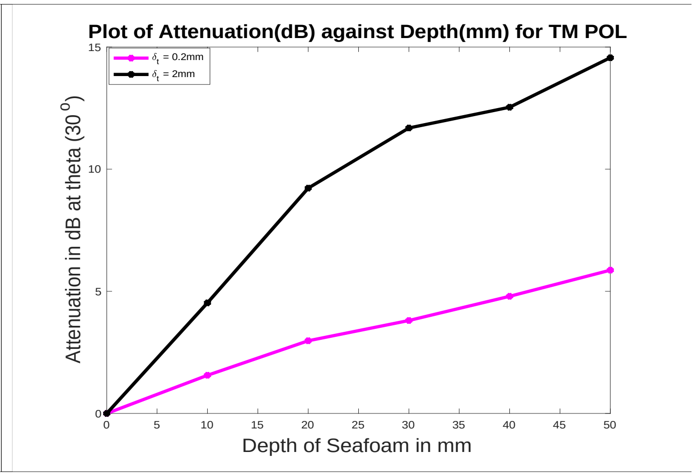

Figure 5.114: Attenuation of Field Intensity for vertical polarization (TM) with zenith $\theta_i = 30°$ and azimuth $\phi = 0°$ with depth of sea foam at 23.8 $GHz$ and $\delta_t = 0.2\ mm$, and 2 $mm$.

We observe that propagation of incident E-field with incident angle $\theta_i = 30^\circ$ and azimuth $\phi = 0^\circ$ for thin phase screens $\delta_t = 0.2$ $mm$ in figure 5.111 illustrates that the attenuation (dB) is a linear function of depth of sea foam with values between 0 $dB$−5.6168 $dB$ at 18.7 $GHz$ for TE polarized field while the TM polarized field varies from 0 $dB$ − 5.762 $dB$. These observations represent increase in diffuse scattering as the field travels through the slices of foam layers which is due to strong interactions between the E-field and dipoles of the randomly oriented scatterers as the field travels to greater depths. The attenuation $\alpha_{dB}$ increases with frequency 23.8 $GHz$ as shown in figures 5.112-5.114, $\alpha_{dB}$ increases from 0 $dB$ − 5.8171 $dB$ with increasing depth of foam layer for TE polarize field and 0 $dB$ − 5.8656 $dB$ for TM polarized field.

The attenuation $\alpha_{dB}$ for deep phase scattering screen $\delta_t = 2$ $mm$ validates the fact that attenuation generally increases with frequency as $\alpha_{dB}$ varies from 0 $dB$ − 14.4420 $dB$ for TE polarize field and 0 $dB$ − 14.5623 $dB$ at 23.8 $GHz$ while it ranges from 0 $dB$ − 13.4266 $dB$ at 18.7 $GHz$ for TE polarize field and 0 $dB$ − 13.6642 $dB$ for TM polarize field. From these findings we can say that there are more diffuse scattering due to large slice thickness of sea-foam which can be attributed to increased bubble population in adjacent slices at 18.7 $GHz$ and 23.8 $GHz$.

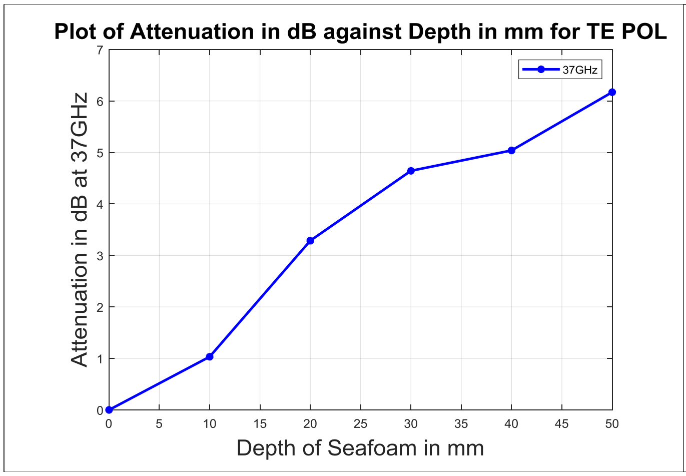

Figure 5.115: Attenuation of Field Intensity for horizontal polarization (TE) with zenith $\theta_i = 30°$ and azimuth $\phi = 0°$ with depth of sea foam at 37 $GHz$ and $\delta_t = 0.1$ $mm$

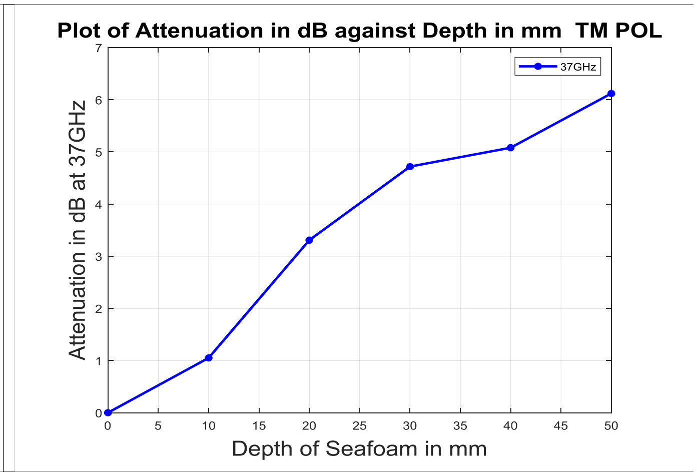

Figure 5.116: Attenuation of Field Intensity for vertical polarization (TM) with zenith $\theta_i = 30°$ and azimuth $\phi = 0°$ with depth of sea foam at 37 $GHz$ and $\delta_t = 0.1$ $mm$

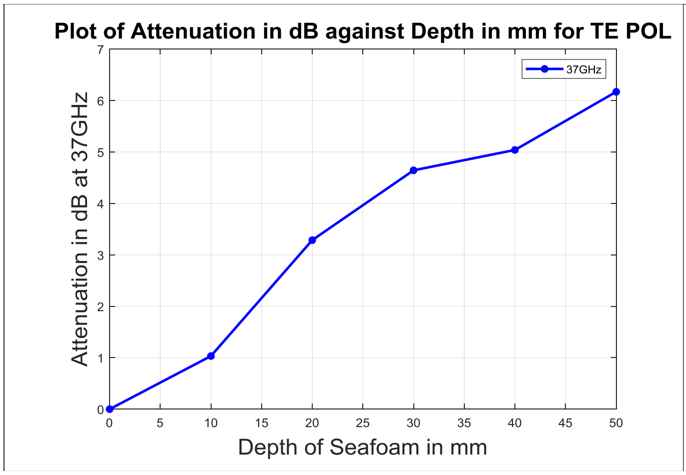

Figure 5.117: Attenuation of Field Intensity for vertical polarization (TM) with zenith $\theta_i = 30°$ and azimuth $\phi = 0°$ with depth of sea foam at 37 $GHz$ and $\delta_t = 0.2$ $mm$

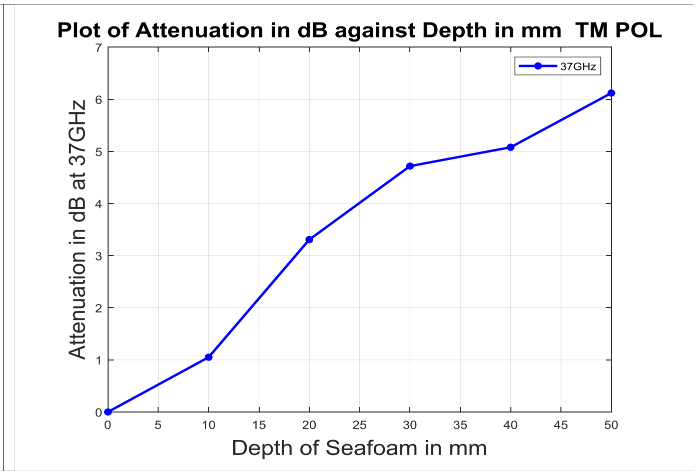

Figure 5.118: Attenuation of Field Intensity for vertical polarization (TM) with zenith $\theta_i = 30°$ and azimuth $\phi = 0°$ with depth of sea foam at 37 $GHz$ and $\delta_t = 0.2$ $mm$

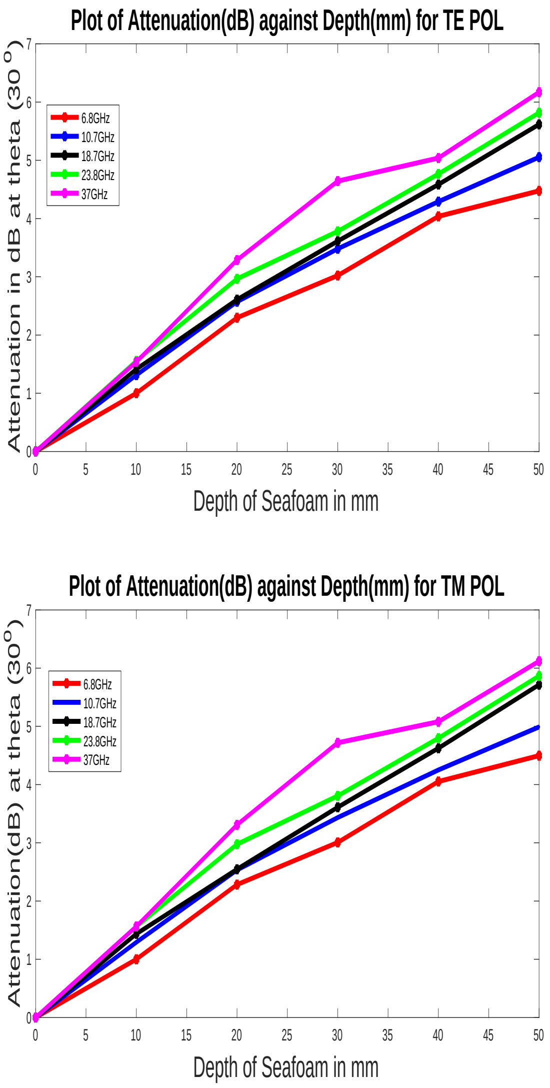

Figure 5.119: Attenuation $(dB)$ of $|E|^2$ for TE and TM POL against depth of sea foam with zenith $\theta_i = 30°$ and azimuth $\phi = 0°$ for thin phase scattering screens.

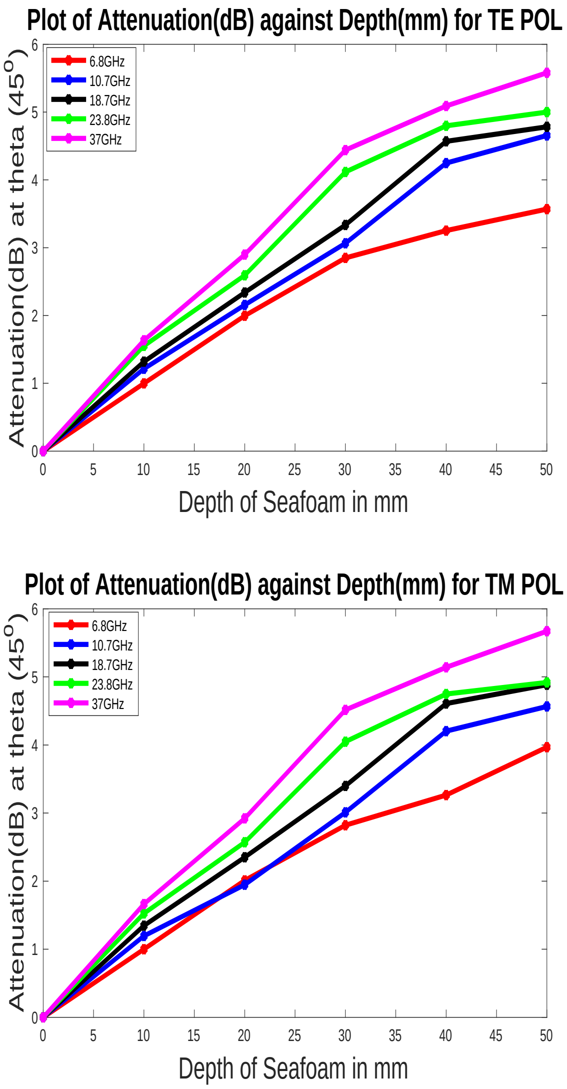

Figure 5.120: Attenuation $(dB)$ of $|E|^2$ for TE and TM POL against depth of sea foam with zenith $\theta_i = 45°$ and azimuth $\phi = 0°$ for thin phase scattering screens.

Attenuation $\alpha_{dB}$ of the field intensity $|E|^2$ for both TE and TM polarized fields increases with increase in frequency and depth of sea foam layer for thin phase screens $\delta_t = 0.1$ $mm$ and $\delta_t = 0.2$ $mm$, with zenith $\theta_i = 30°$ and azimuth $\phi = 0°$ as show in 5.119. The attenuation $\alpha_{dB}$ is highest at frequency 37 $GHz$ with a value of $\alpha_{dB} = 6.1695$ $dB$ for TE mode and $\alpha_{dB} = 6.1199$ $dB$ for TM mode. We have an attenuation of 0 $dB$ at slice 1, 1.5384 $dB$ at slice 2, 3.2864 $dB$ at slice 3, 4.6431 $dB$ at slice 4 and 5.0390 $dB$ at slice 5 and 6.1695 $dB$ at the sea-surface for TE polarized field. Similarly, attenuation at slice 1 is 0 $dB$, 1.5649 $dB$ at slice 2, 3.3080 $dB$ at slice 3, 4.7179 $dB$ at slice 4 and 5.0797 $dB$ at slice 5 and 6.11695 $dB$ at the sea-surface for TM polarized field.

The attenuation $\alpha_{dB}$ at 6.8 $GHz$ gives the least variation of attenuation with depth as shown in figure 5.119. We obtain an attenuation $\alpha_{dB} = 0$ $dB$ at slice 1, $\alpha_{dB} = 1$ $dB$ at slice 2, $\alpha_{dB} = 2.2969$ $dB$ at slice 3, $\alpha_{dB} = 3.0210$ $dB$ at slice 4, $\alpha_{dB} = 4.0385$ $dB$ at slice 5 and $\alpha_{dB} = 4.4751$ $dB$ at the sea surface for TE polarized field and $\alpha_{dB} = 0$ $dB$ at slice 1, $\alpha_{dB} = 1$ $dB$ at slice 2, $\alpha_{dB} = 2.2820$ $dB$ at slice 3, $\alpha_{dB} = 3.0065$ $dB$ at slice 4, $\alpha_{dB} = 4.0539$ $dB$ at slice 5 and $\alpha_{dB} = 4.4970$ $dB$. It is apparent that the attenuation at various WindSat frequencies $(6.8 - 37)$ $GHz$ increases with depth of sea foam layer for thin phase scattering screens.

The plots in 5.120 shows that attenuation also reduces with increase in zenith angle $\theta_i$ from 30° to 45° for both TE and TM polarized fields. We observe that as $\theta_i$ approaches 90°, the attenuation reduces due to weaker interaction between the E-field and randomly distributed scatterers. There is more diffuse scattering at smaller angles of incidence and multiple reflections in sea foam layer increases with frequency at deeper sea foam layers.

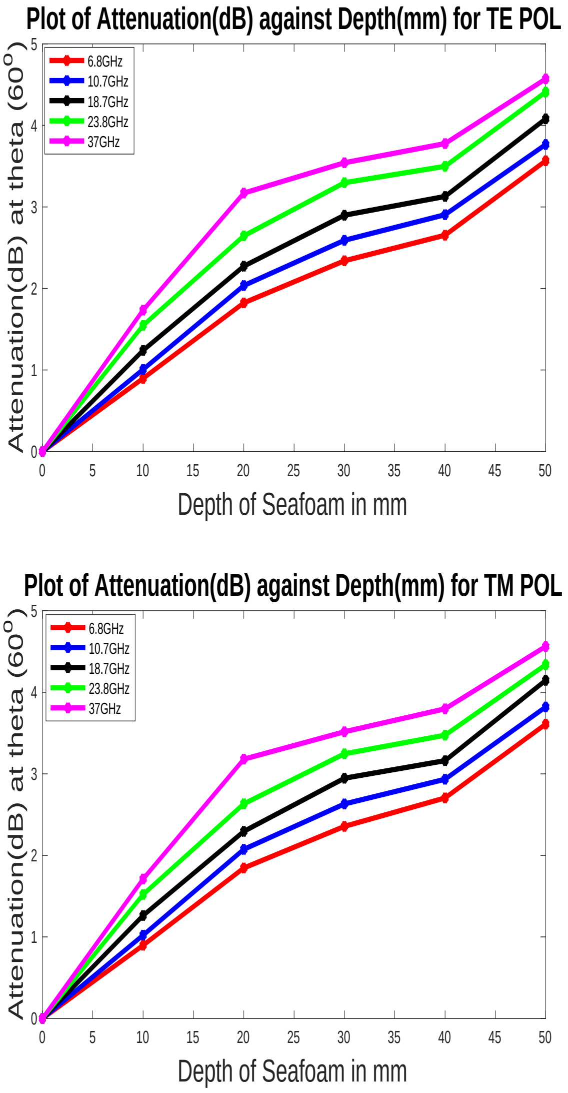

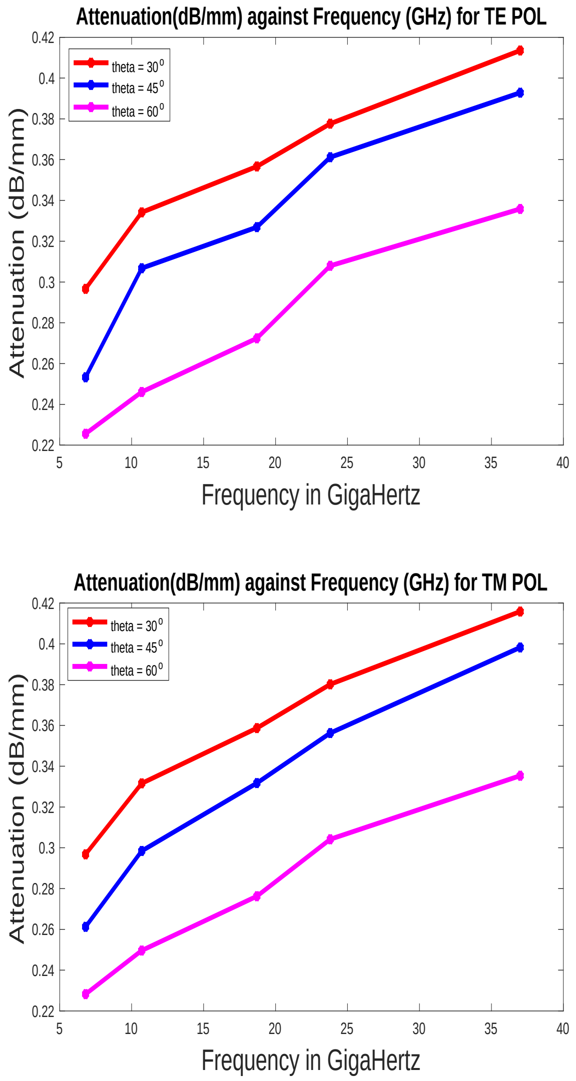

Figure 5.121: Attenuation $(dB)$ of $|E|^2$ for TE and TM POL against depth of sea foam with zenith $\theta_i = 60°$ and azimuth $\phi = 0°$ for thin phase scattering screens.

Figure 5.122: Specific attenuation $(dB/mm)$ against frequency $(GHz)$ with propagation angles zenith $\theta_i = 30°, 45°$ and $\theta = 60°$ for thin phase scattering screens.

For thin-phase scattering screens $\delta_t = 0.1\ mm$ and $\delta_t = 0.2\ mm$ with a given zenith $\theta_i = 60^\circ$ and azimuth $\phi = 0^\circ$, the attenuation $\alpha_{dB}$ increases with depth $d(mm)$ of sea foam. Figure 5.121 shows this to be true for all WindSat frequencies $(6.8 - 37)\ GHz$ as the E-field travels through successive slices of sea foams. For both TE and TM polarized fields, the attenuation $\alpha_{dB}$ at $\theta_i = 60^\circ$ is less than that of $\theta_i = 30^\circ$ and $\theta_i = 45^\circ$. This agrees with earlier report that the attenuation due to backscattered E-field by foam covered sea-surface reduces with increase in angle of incidence. Figure 5.121 validates these findings for all WindSat frequencies $(6.8 - 37)\ GHz$.

Figure 5.122 shows that the specific attenuation in $dB/mm$ increases with increase in WinSat frequencies $(6.8 - 37)\ GHz$ and also with decreases with angle of incidence of the propagated E-field for both TE and TM polarized fields. We can clearly see that specific attenuation is due to diffuse scattering when the incident E-field is multiple reflected by sea foam - seawater interface at the ocean bottom and propagates backward through the various slices of sea foam layers. The E-field is re-radiated by randomly distributed scatterers with varying dielectric constants which absorbs and re-radiates the incident E-field in different directions on the sea-surface. The specific attenuation in $dB/mm$ at $\theta_i = 30^\circ$ are 0.2966 $dB/mm$ at 6.8 $GHz$, 0.3341 $dB/mm$ at 10.7 $GHz$, 0.3567 $dB/mm$ at 18.7 $GHz$, 0.3776 $dB/mm$ at 23.8 $GHz$ and 0.4135 $dB/mm$ at 37 $GHz$ for TE polarized field. For TM polarize field, the specific attenuation in $dB/mm$ are 0.2968 $dB/mm$ at 6.8 $GHz$, 0.3316 $dB/mm$ at 10.7 $GHz$, 0.3587 $dB/mm$ at 18.7 $GHz$, 0.3801 $dB/mm$ at 23.8 $GHz$ and 0.4158 $dB/mm$ at 37 $GHz$. The specific attenuation in dB/mm shows the same relationship for incident angles $\theta_i = 45^\circ$ and $\theta_i = 60^\circ$ for both TE and TM mode.

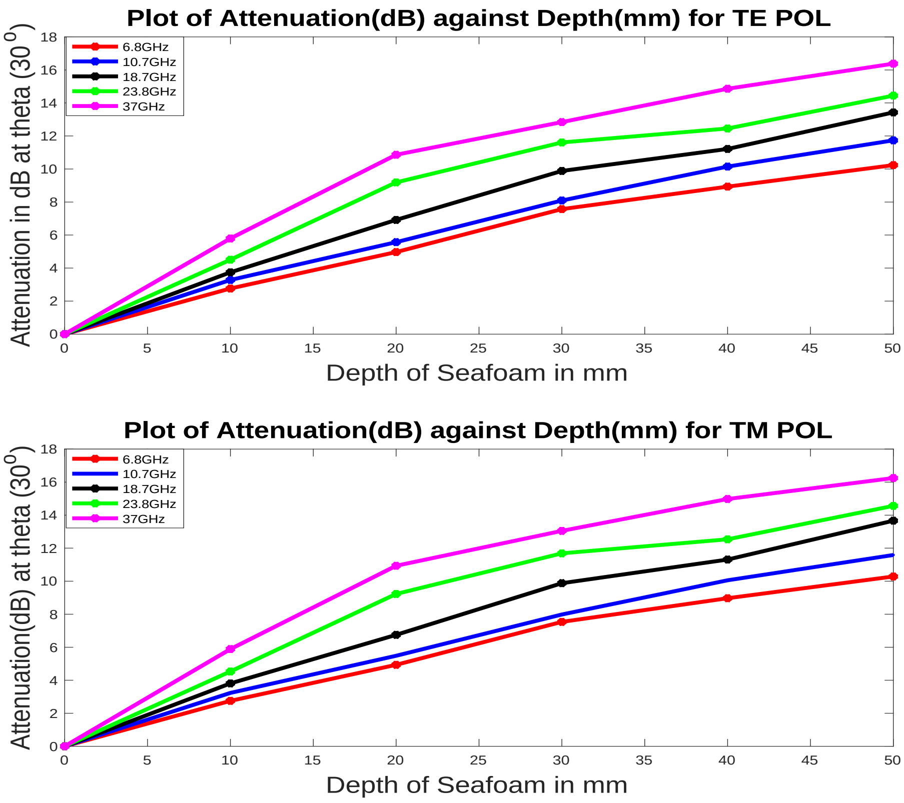

Figure 5.123: Attenuation $(dB)$ of $|E|^2$ for TE and TM POL against depth of sea foam with zenith $\theta_i = 30°$ and azimuth $\phi = 0°$ for deep phase scattering screens.

Figure 5.123 illustrate that attenuation increases with frequency $(GHz)$ as the depth of sea foam increases for deep phase screens $\delta_t = 2\ mm$. At lower frequencies the attenuation of the E-field is dominated by diffuse scattering which intensifies as frequency of the signal increases but at higher frequencies such as 18.7 $GHz$, 23.8 $GHz$ and 37 $GHz$ the foam bubbles cause strong absorption of the E-field providing effects such as a black-body.

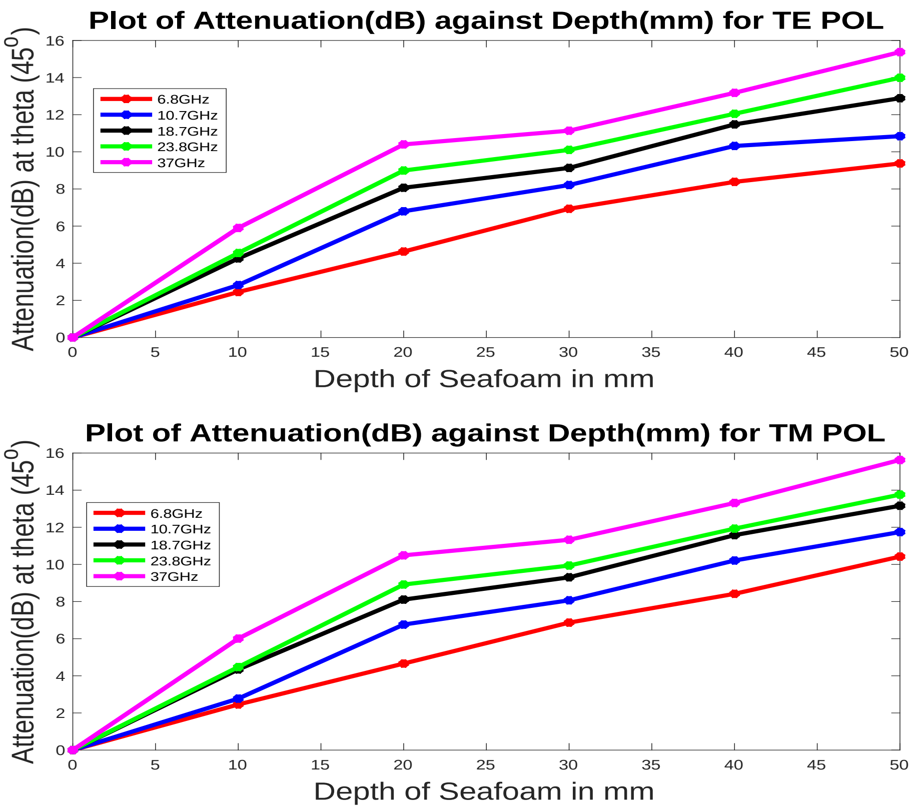

Figure 5.124: Attenuation $(dB)$ of $|E|^2$ for TE and TM POL against depth of sea foam with zenith $\theta_i = 45°$ and azimuth $\phi = 0°$ for deep phase scattering screens.

This shows similar behaviour as figure 5.123, the increase in attenuation for deep phase screens is due to strong interactions between the E-field and air-bubbles which leads to more diffuse scattering within the foam layers. The figures above shows that the attenuation $\alpha_{dB}$ reduces with increase in propagation angle $\theta_i$ as is the case for thin phase scattering screens. Absorption is the major factor responsible for attenuation of the E-field at higher frequencies while diffuse scattering is dominant for lower frequencies.

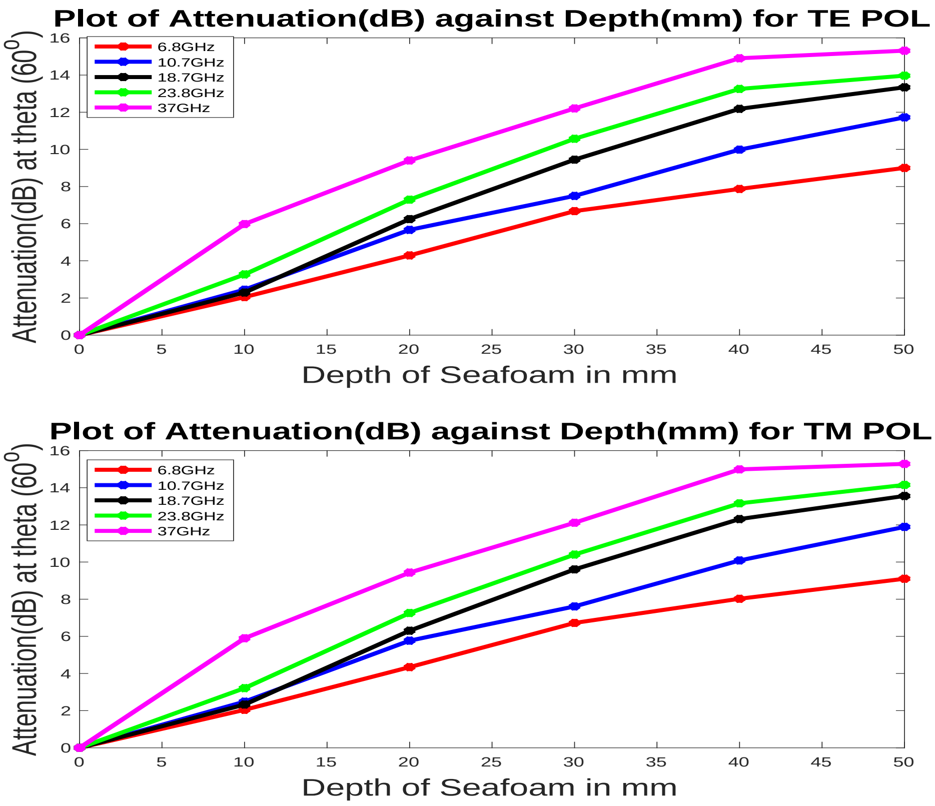

Figure 5.125: Attenuation $(dB)$ of $|E|^2$ for TE and TM POL against depth of sea foam with zenith $\theta_i = 60°$ and azimuth $\phi = 0°$ for deep phase scattering screens.

This illustrates that attenuation increase with depth of sea foam at WindSat frequencies $(6.8 - 37)$ $GHz$ for deep phase screens at $\delta_t = 2$ $mm$. The behaviour is similar to figure 5.123 and figure 5.124. Absorption remains a major contributor to attenuation at higher frequencies such as 23.8 $GHz$ and 37 $GHz$ while diffuse scattering is the cause of attenuation at lower frequencies $(6.8 - 10.7)$ $GHz$ for $\theta_i = 60°$.

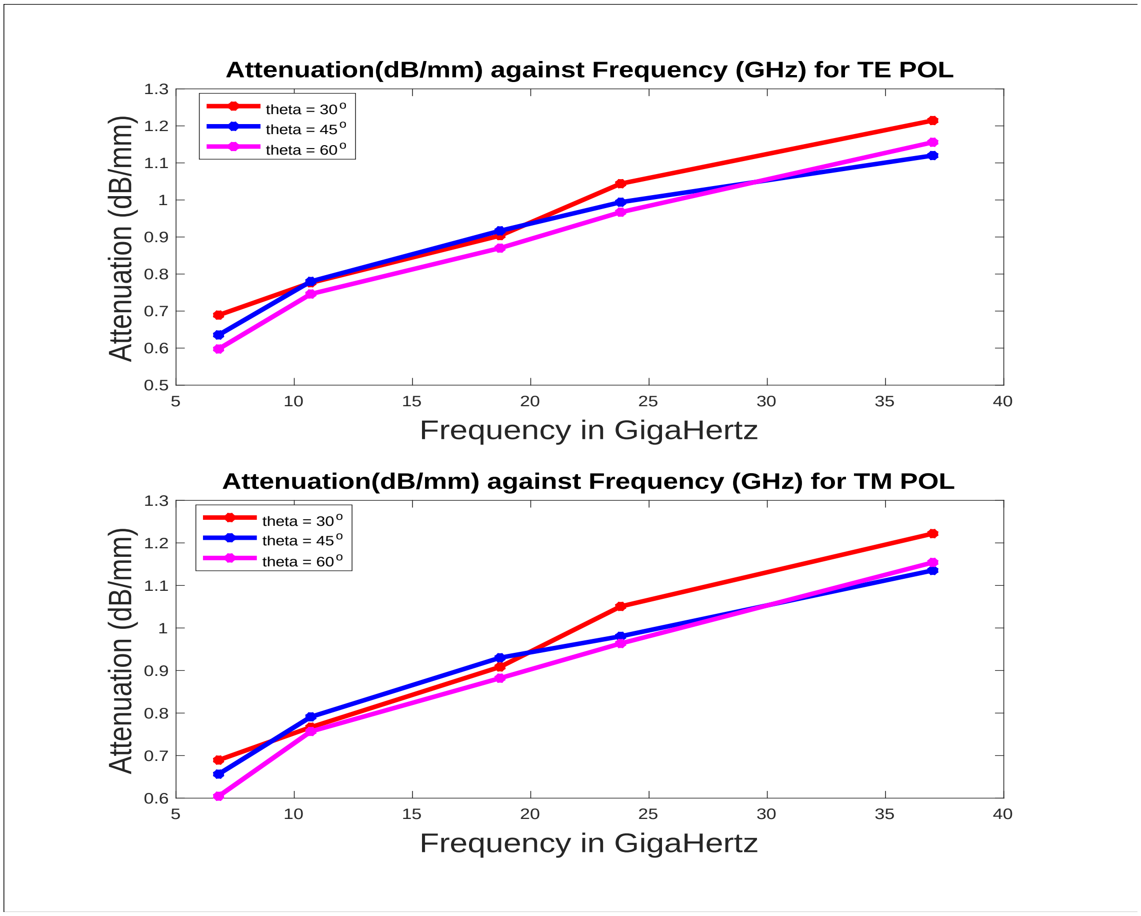

Figure 5.126: Specific attenuation $(dB/mm)$ against frequency $(GHz)$ with propagation angles zenith $\theta_i = 30°, 45°$ and $\theta = 60°$ for deep phase scattering screens.

The specific attenuation in $dB/mm$ increases with WindSat frequencies for deep phase screens $\delta_t = 37\ GHz$. This behaviour is similar to that of thin phase screen but the attenuation increase is due to absorption by air-bubbles at higher frequencies and diffuse scattering at lower frequencies. The specific attenuation also reduces with increase in incidence angle of the E-field for both TE and TM polarized fields.

Table 5.1: Results for Dielectric Constant of sea foam at 10.7 $GHz$ and 37 $GHz$ for 5 2-D slices of randomly packed air-bubbles covered with thin-layer of sea water

| **Frequency (GHz)** | **10.7 GHz** | **37 GHz** |
|---|---|---|
| Slice 1 | 1.0948+j0.1251 | 1.0006+j0.0332 |
| Slice 2 | 1.1248+j0.1507 | 1.0108+j0.0239 |
| Slice 3 | 1.1622+j0.1810 | 1.0225+j0.0344 |
| Slice 4 | 1.1983+j0.2072 | 1.0315+j0.0569 |
| Slice 5 | 1.2271+j0.2277 | 1.0465+j0.0637 |

## 5.5 Comparison of Simulated Emissivity of Sea Foam with Experimental Results

For fixed salinity 34 $psu$, sea surface temperature $20°C$ and frequency range between 1.4 $GHz$ and 37 $GHz$ , the estimated effective dielectric constant of sea water in pages 41 and 42 was used to compute the effective dielectric constants of sea foams at frequencies 10.7 $GHz$ and 37 $GHz$ for 5 slices of randomly packed air-bubbles coated with thin-layer of sea water.

The effective dielectric constant of sea foam increases with increase in thickness of foam layer and decreases with increase in frequency as illustrated in Table 5.1. The effective dielectric constant of sea foams are used in the computation of Fresnels reflection coefficients for both horizontal $R_p^{foam}$ and vertical $R_v^{foam}$ polarized fields, at the air-foam interface and the foam-ocean interface. The Fresnels reflection coefficients are used for the computation of sea surface emissivity $e^{foam}$ and brightness temperature $T_B$ in the radiative transfer equations given in pages 17 and 18 .

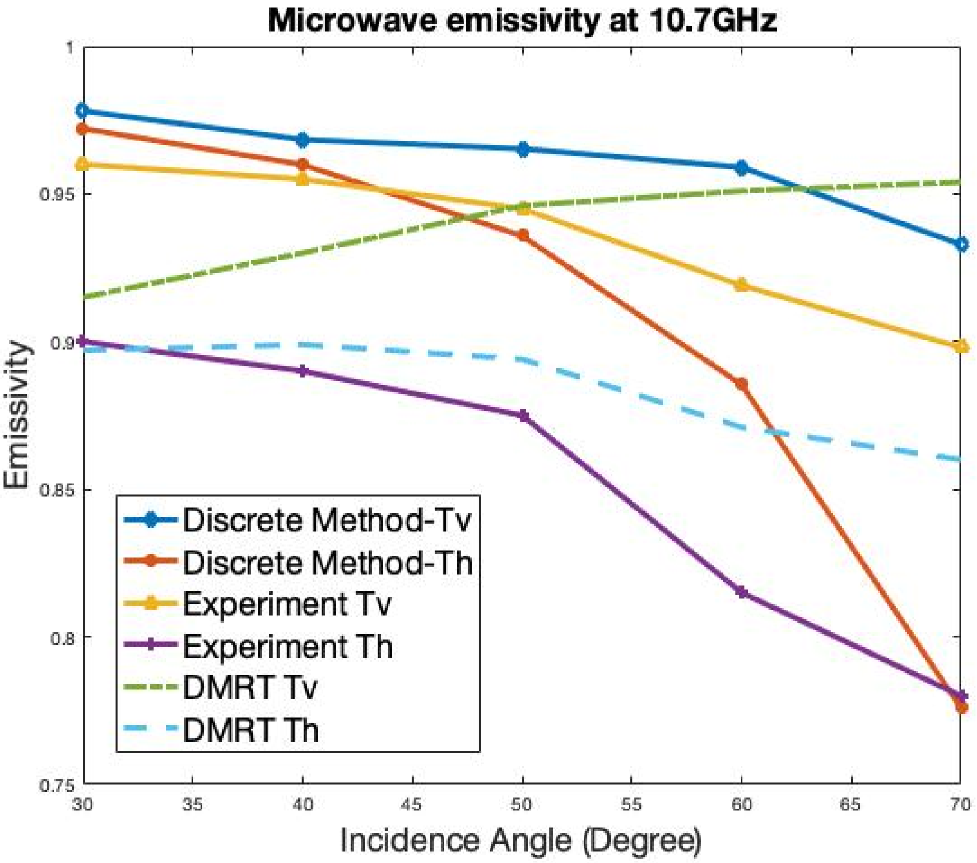

Figure 5.127: Comparison between simulation results and measurements of microwave emissivity at 10.7 $GHz$ for horizontal and vertical polarization as a function of incidence angle.

Figures 5.127 and 5.128 show plots of microwave emissivity dependence on the incidence angles at 10.7 $GHz$ and 37 $GHz$ respectively, for both vertical and horizontal polarizations. We can see explicitly that foam emissivity using experimental data, increases at angles $\theta_i =$ 30°, 35° and $\theta = 40°$, then undergoes a decrease at angles 45°, 50°, 55° and 60° for both horizontal and vertical polarizations. The discrete method correspondingly, decreases with increase in angle of incidence for both horizontal and vertical polarizations at 10.7 $GHz$

and 37 $GHz$. We can see that the (DMRT) dense media radiative transfer yield results in reasonably good agreement with experimental measurements. The results show comparable emissivities at 10.7 $GHz$ and 37 $GHz$. Absorption effect at 37 $GHz$ is larger than 10.7 $GHz$ while scattering effect is more significant at 37 $GHz$. The results are in good agreement at small incidence angles. The disparity in results is explicit at larger angles of incidence.

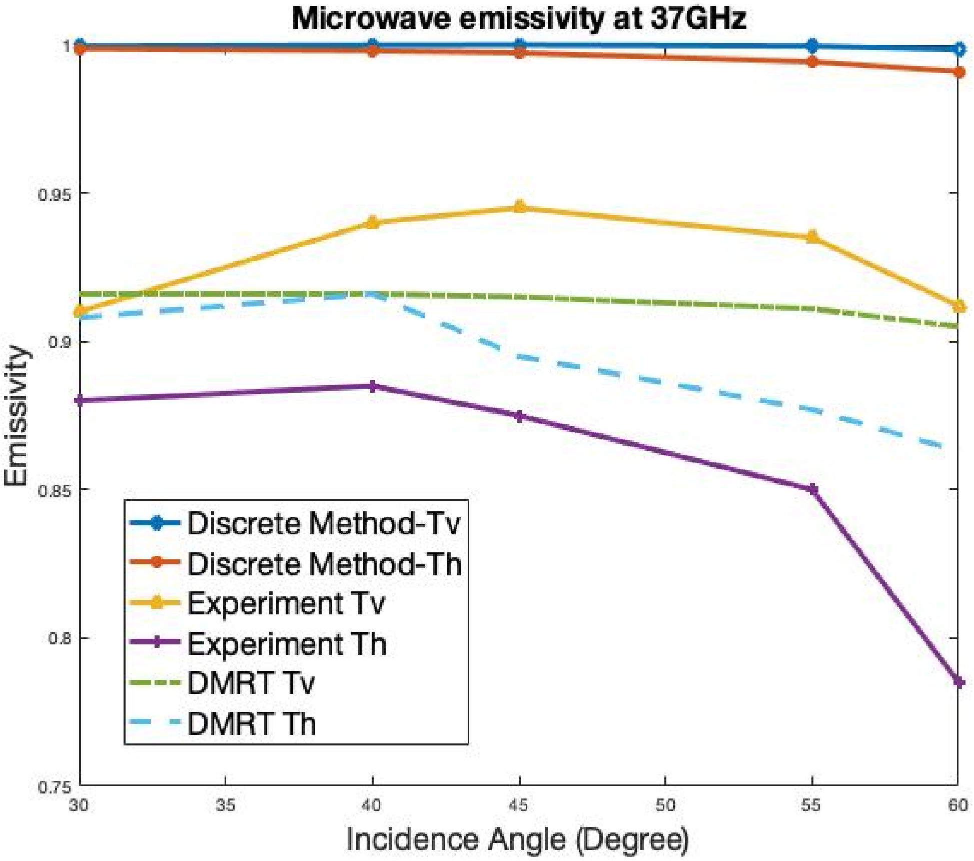

Figure 5.128: Comparison between simulation results and measurements of microwave emissivity at 37 $GHz$ for horizontal and vertical polarization as a function of incidence angle.

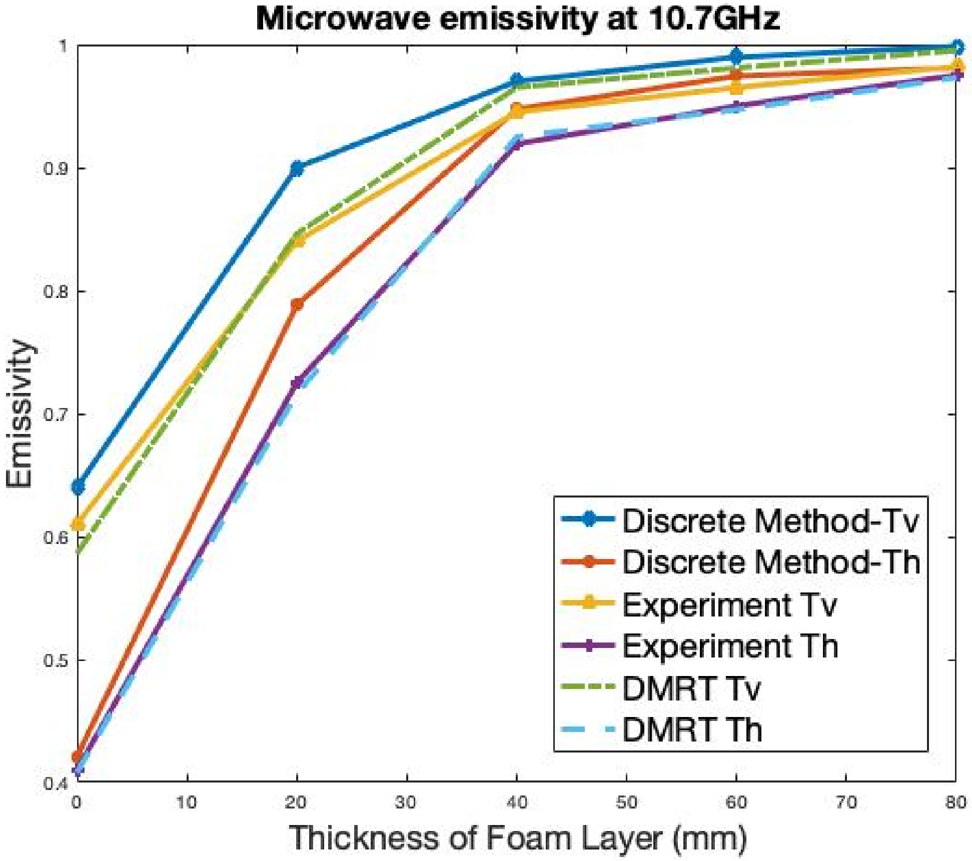

Figure 5.129: Comparison between simulation results and measurements of microwave emissivity at 10.7 $GHz$ for horizontal and vertical polarization as a function of foam layer thickness.

Figures 5.129 and 5.130 show the emissivity for horizontal and vertical polarization at WindSat frequencies 10.7 $GHz$ and 37 $GHz$, with dependence on foam layer thickness for randomly distributed air bubbles at incidence angle $\theta_i = 53°$. The coated bubbles are $80\% - 95\%$ of the actual foam radii. We used foam parameters; mean bubble radius $r_{mean} = 500\ \mu m$, minimum bubble radius $r_{min} = 6.9\ mm$ and maximum bubble radius $r_{max} = 0.95\ cm$. Scattering increases with particle size and the effective scattering mean size of the DMRT and experimental models was reported substantially larger than the mean size of the radius. The discrete method used randomly distributed size particles with mean radius $r_{mean} = 500\ \mu m$, which was chosen as its comparable to bubble radius used by Chen et.al [30], which represent the effective mean scattering. In actual foam, the coating thicknesses vary as a function of foam depth. Figures 5.129 and 5.130 show that scattering effect increases with increase in size of bubbles, and the albedo increases also which leads to decrease in brightness temperatures.

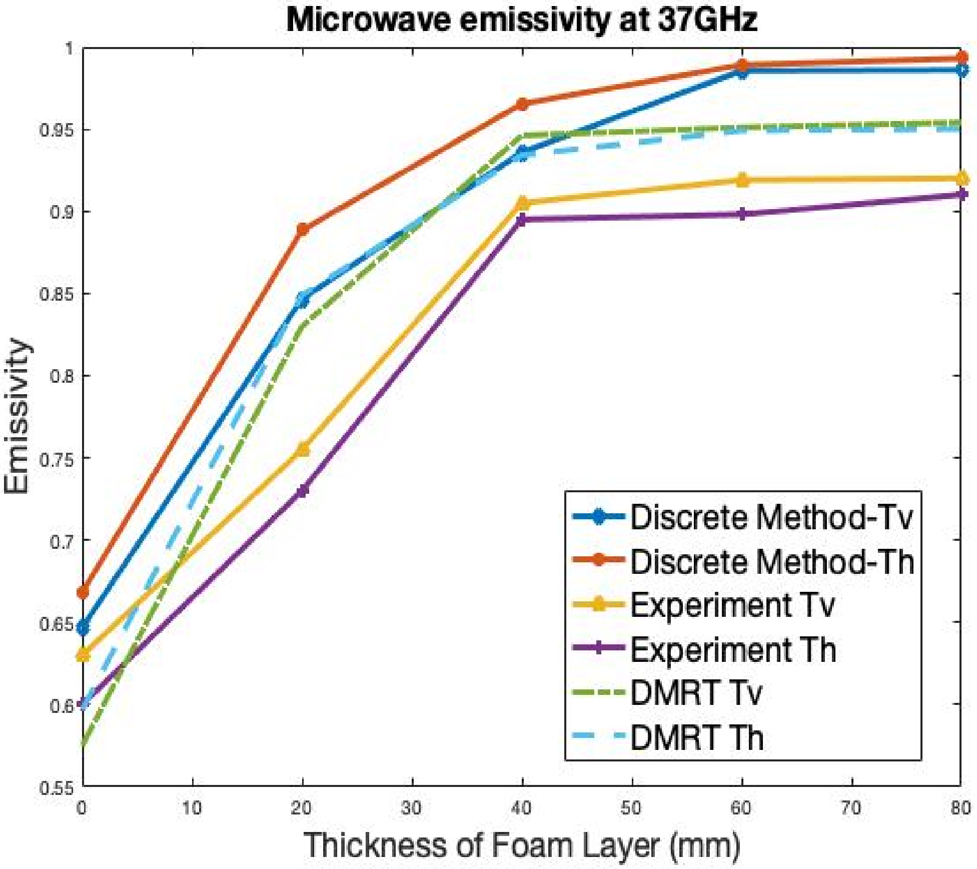

Figure 5.130: Comparison between simulation results and measurements of microwave emissivity at 37 $GHz$ for horizontal and vertical polarization as a function of foam layer thickness.

## 5.6 Comparison of Simulated Brightness Temperature of Sea Foam with Experimental Results

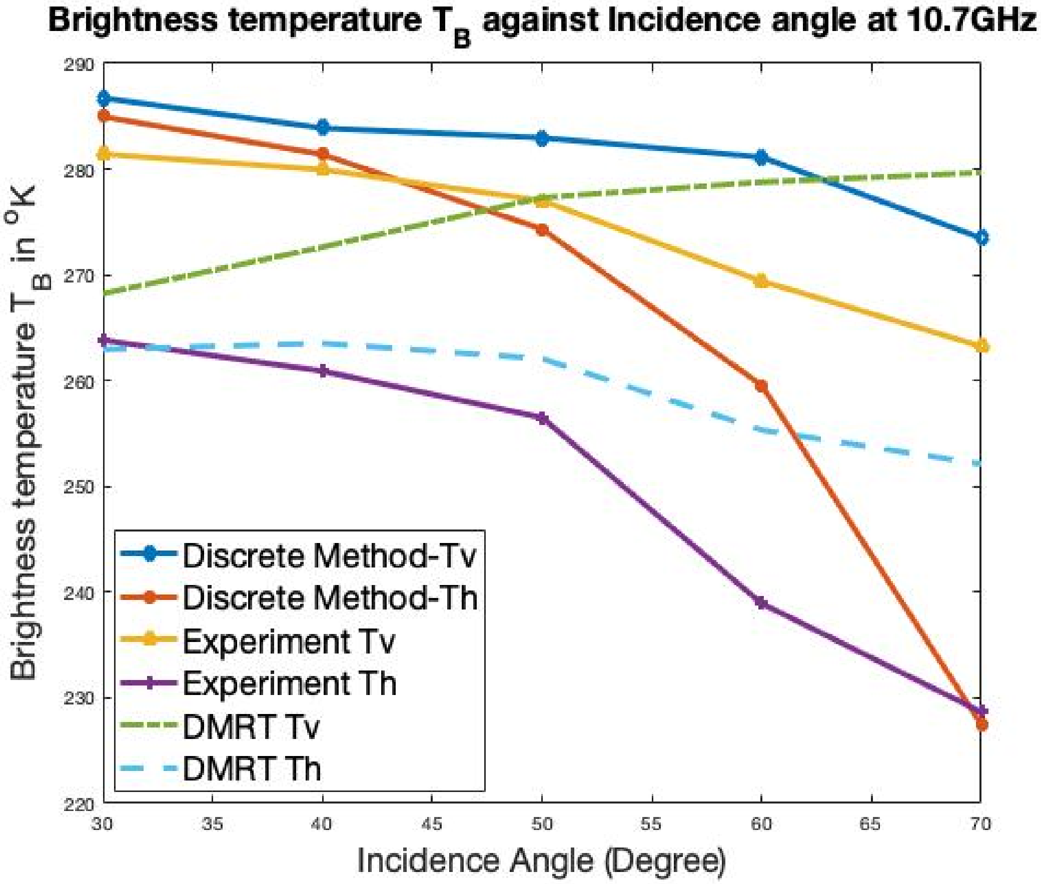

Figure 5.131: Comparison between simulation results and measurements of brightness temperature at 10.7 $GHz$ for horizontal and vertical polarization as a function of incidence angle.

Figures 5.131 and 5.132 illustrate brightness temperature variation with incidence angles at 10.7 $GHz$ and 37 $GHz$ respectively, for both vertical and horizontal polarizations. The brightness temperature as a measure of the radiance of the upward millimetre wave radiation from the sea surface decreases with increase in incident angle. Experimental data used in computation of the brightness temperature, yields brightness temperature that increases at angles $\theta_i = 30°$, $35°$ and $\theta = 40°$, then undergoes a decrease at angles 45°, 50°, 55° and 60° for both horizontal and vertical polarizations.

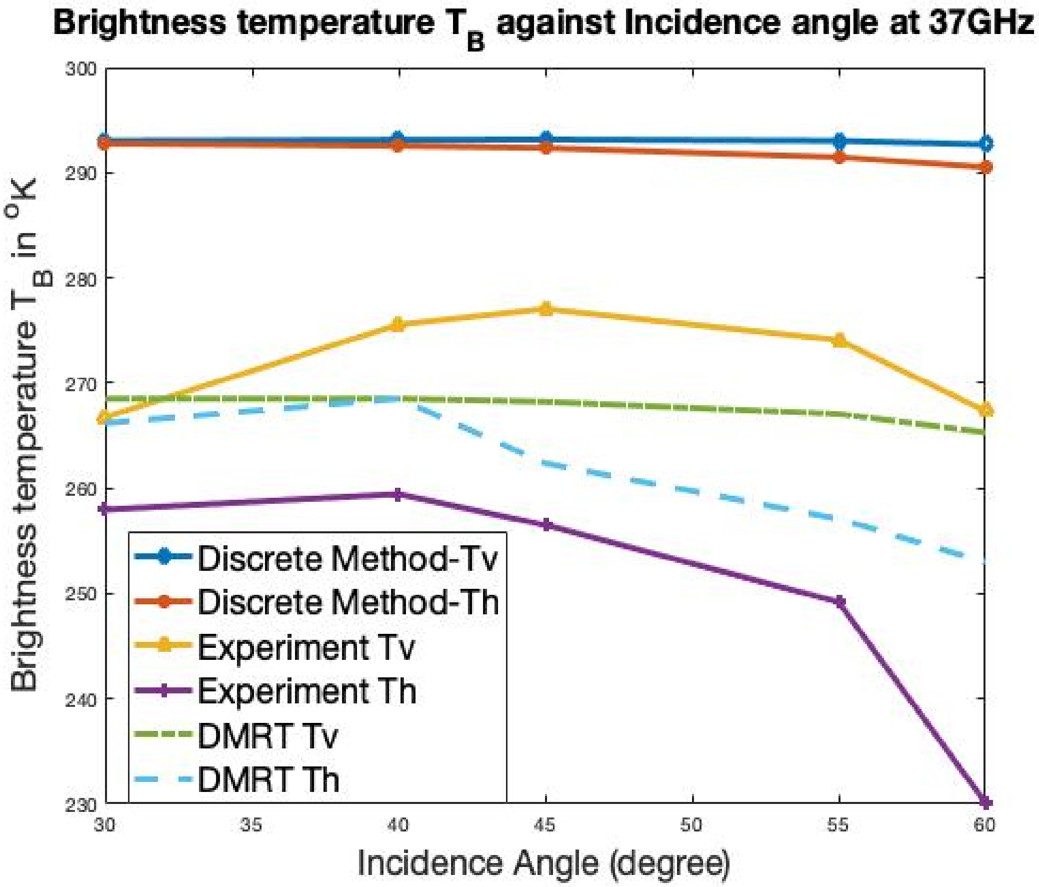

Figure 5.132: Comparison between simulation results and measurements of brightness temperature at 37 $GHz$ for horizontal and vertical polarization as a function of incidence angle.

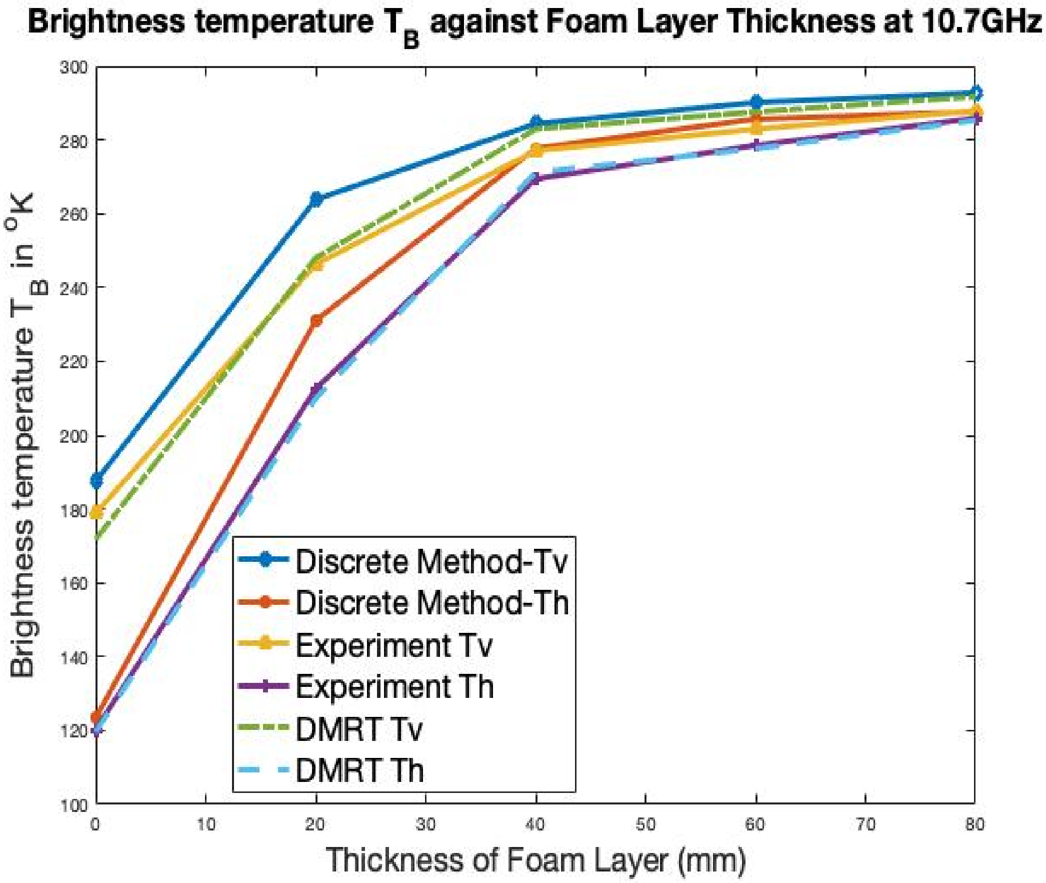

Figure 5.133: Comparison between simulation results and measurements of brightness temperature at 10.7 $GHz$ for horizontal and vertical polarization as a function of foam layer thickness.

Figures 5.133 and 5.134 show that brightness temperature of the sea surface covered by foam increases with increase in foam layer thickness at frequencies 10.7 $GHz$ and 37 $GHz$. The discrete method used for computation of the brightness temperature of foam covered sea surface which is our method, follows similar pattern as experimental and DMRT methods shown in figures 5.133 and 5.134.

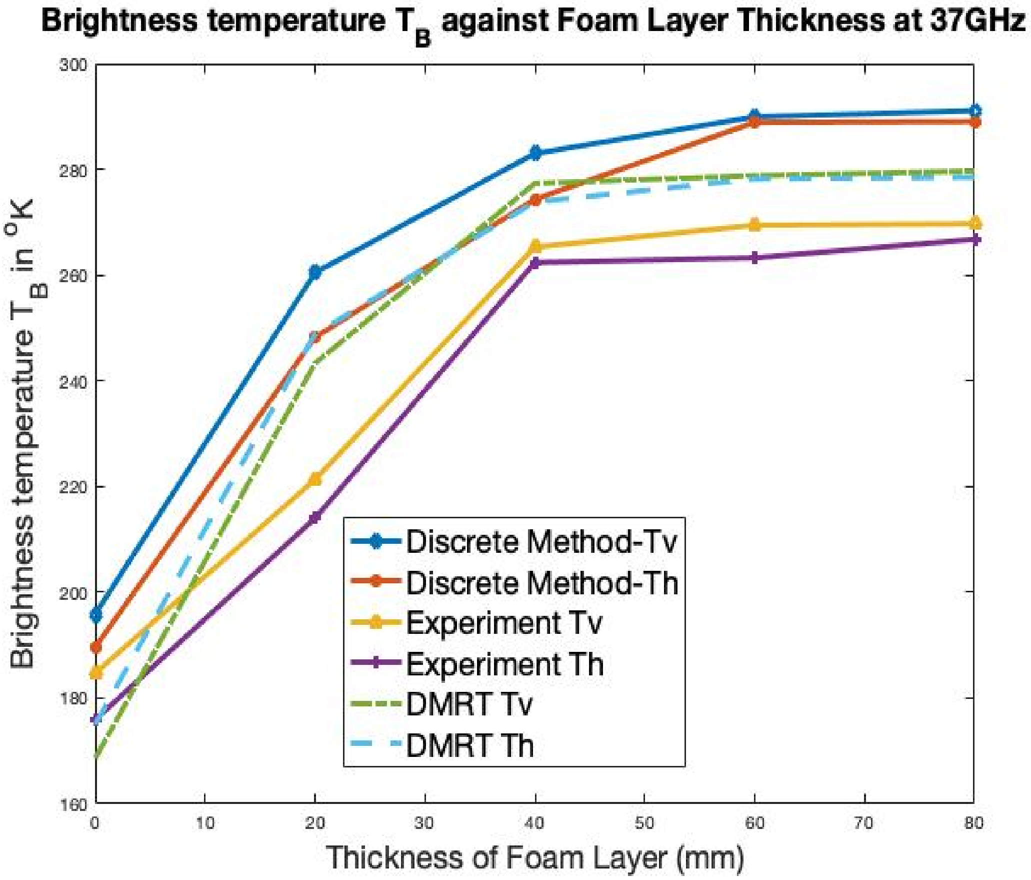

Figure 5.134: Comparison between simulation results and measurements of brightness temperature at 37 $GHz$ for horizontal and vertical polarization as a function of foam layer thickness.

We can see explicitly that brightness temperature increases as the foam layer thickness increases and later saturates at a specific foam thickness, for both horizontal and vertical polarization. Chen et.al [30] DMRT simulation results show that the saturation point of horizontal polarization was slightly larger than that of vertical polarization. The discrete method results shows reasonably good agreement with DMRT and experimental measurements.

## 5.7 Summary

It was reported that cloud content of liquid water induces absorption and scattering of EM energy for frequencies above 10 $GHz$, but less intensity than that of rain [100]. Attenuation of cloud in addition to propagation parameters such as signal frequency and angle of elevation $\theta$, rely on parameters of the cloud such as average cloud height, thickness and columnar content of liquid water (liquid water contents) LWC and temperature.

Salomen and Uppala [101], ITU-R [102], DAH [103], and Altshuler et.al [104] developed various models to estimate cloud attenuation. Ali M. Al-Saegh et.al [100] reported an attenuation below 1 $dB$ at 22 $GHz$ for different liquid water content at $\theta > 45^0$, and below 3 $dB$ for lower $\theta$ at 2 and 3 $kg/m^2$ LWC. 50 $GHz$ frequency band gives a great amount of cloud attenuation exceeding 10 $dB$ for $LWC = 3$ $kg/m^2$ and $\theta$ below $20^0$. Cloud attenuation increases from 1.8 $dB$, 3.6 $dB$ and 5.3 $dB$ for $\theta = 41.1^0$ and $LWC = 1, 2$ and 3 $kg/m^2$, respectively. Accordingly, the attenuation of cloud increases from 1.17 $dB$,2.3 $dB$, and 3.5 $dB$ for $\theta = 77^0$ and $LWC = 1, 2$, and 3 $kg/m^2$. The specific attenuation of cloud in $dB/km$ increases with frequency and thickness of $LWC$ but decreases with elevation angle. This is very interesting as our results have similar behaviour because the attenuation in dB of the E-field increases with increase in frequency $(GHz)$ and depth $d(mm)$ of sea foam. Also, attenuation in $dB$ decreases with increase in incident angle $\theta_i$. The specific attenuation in $dB/mm$ as a function of frequency shows similar behaviour.

# CHAPTER 6

# CONCLUSION AND FURTHER WORK

The split-step Fourier method for evaluating the diffraction and scattering effects of a sea-surface covered by foam which was modelled as sequences of random thin phase scattering screens has been presented.

The code implementation of the sea-foam model as a log-normal distribution of randomly packed spheres was done in FORTRAN 95 with version 7.10 FTN95 Silverfrost 64bit compiler, which has the capacity to define modules, functions, subroutines and derived data types for implementation of complex multi-dimensional arrays and vector algorithms. With the aid of the FTN95 compiler a well structured algorithm was translated to an elementary top level code for computation of the random sphere packing problem. Random packing of spheres into a unit cube and slicing of the sea-foam model into $n$ thin layers was a challenge that was encountered and surmounted by the use of Matlab R2016a software. The sea-foam model was assumed to be spherical. However, it can be modelled as an ellipsoid, cylinder, cone, prolate and oblate spheroids. Future models can assume other statistics than a log-normal distribution for example Poisson distribution, power law distribution, Weibull distribution, exponential distribution and etc.

Earlier reported estimates of the effective complex dielectric constants was based on the macroscopic properties of sea-foam such as foam void fraction and foam thickness which ignores the effect of scattering due to foam presence in seawater. Limited knowledge of microscopic properties of sea-foam from previously published work and experiments, which can be attributed to foam emissivity models that computed the attenuation and permittivity of foam, and several scattering theories by microscopic properties of foam introduce uncertainties which affected accuracy of the foam emissivity model. To account for scattering effects of foam presence on the sea surface at fixed salinity (34psu), SST $20°C$ and frequency range 1.4 $GHz$ - 37 $GHz$, we computed the dielectric constant of seawater by adopting Strogyn's model. The estimates were recorded using Maxwell Garnett's and Bruggeman methods with the permittivity of phytoplantones as a major contributor to impurities in seawater taken into consideration. This accounts for the optical effects of impurities in seawater as dead and decay organisms and phytoplanktones contributes impurities in 95% of the world ocean.

The randomly packed spheres in a unit-cube were translated to 2D slices of solid annuli. The conversion of 3D to 2D slices was achieved by calculating the radius of each individual circle intersecting a plane. The 2D slices were discretized with grid sizes $\Delta x$ and $\Delta y$ which leads to intersection of the circles bounded in a unit square with some grid points. The grid sizes were sampled such that the edges of the circles circumference which intersects with grid points farther from the inner grids bounded by the circles are negligible. With this assumption, we estimated the effective dielectric constant of sea foams by modelling the randomly packed bubbles as concentric spheres in 2-D where the outer sphere is seawater while the inner sphere contains about 80%-95% air, with these estimates we were able to calculate the area of the annulus (ring) as the radii of the outer spheres are known.

The PEM is a marching technique so to ignore the incoming PEM solution implies neglecting the incoherent backscatter. The backscattered field is worth considering as it enables us to get the exact solution of the PEM. For the present, we are ignoring the fine scale backscattered field which appears reasonable since the bubbles are mostly air.

We reported phase perturbations induced by the presence of sea foam on the surface of the ocean. Results obtained shows that in free-space, the phase gradient of the E-field for both TE and TM modes vary uniformly between $-\pi$ and $\pi$ with spatial X and Y domain in mm at frequencies 1.42 $GHz$ and 6.8 $GHz$. The phase variation of the E-field are random as it propagates through successive slices of sea foam layer with microscopic irregularities and varying effective dielectric constants of sea foam.

We also reported significant loss of amplitude of the propagating E-field at moderate to high frequencies for deep phase screens. It was asserted that unstable atmospheric conditions induced wind speeds between 7 $ms^{-1}$ $-$ 20 $ms^{-1}$, which contributes to a average weighted foam layer thickening of about 10 $mm$ and 35 $mm$, which explains why a foam layer of 50 $mm$ depth is used in this research. To evaluate millimetre wave scattering by sea foam it is significant to ensure that $d \gg \lambda$.

Calculations of the absorption, scattering and extinction coefficients of sea foam at WindSat frequencies are widely used in evaluation of microwave emissivity and scattering by sea foams. These parameters helps to estimate the brightness temperature of the ocean surface. WindSat frequencies $(6.8 - 37)$ $GHz$ were adopted because they are not prone to attenuation by cloud and absorption by atmospheric gases. Foam emissivity and brightness temperature are functions of incidence angle, polarization and frequency. Hence, we have shown that absorption is dominant at moderate to high frequencies with deep phase screens while scattering is dominant at moderate to high frequencies with thin phase screens. At high frequency and increasing depth of sea foam layer, the sea foam layer covering the sea surface behaves like a black or gray body . It will be an interesting research to model the sea surface as a rough surface and evaluate the effect of surface roughness on the brightness temperature of the ocean surface. Integrating our model with Monte-Carlo, Mie theory and radiative transfer theory for estimation of brightness temperature of the ocean surface should be a good future research interest. Evaluation of the sea surface emissivity and brightness temperature would be an interesting future work. The use of Pade's approximation method and Finite difference method to evaluate the remote sensing of foam covered ocean surface could also be a good research work.

# BIBLIOGRAPHY

[1] C.-T. Chen, J. Guo, L. Tsang, A. T. Chang, and K.-H. Din, “Analytical and numerical methods for the scattering by dense media,” in *Geoscience and Remote Sensing Symposium, 2000. Proceedings. IGARSS 2000. IEEE 2000 International*, vol. 5, pp. 2359–2361, IEEE, 2000.

[2] K. Schilling and M. Zessner, “Foam in the aquatic environment,” *water research*, vol. 45, no. 15, pp. 4355–4366, 2011.

[3] R. Jiang, P. Xu, K.-S. Chen, S. Tjuatja, and X. Wu, “A numerical study on physical characterizations of microwave scattering and emission from ocean foam layer,” *Progress In Electromagnetics Research*, vol. 75, pp. 91–109, 2017.

[4] Y. Li, P. Hoogeboom, and H. Russchenberg, “Radar observations and modeling of fog at 35 ghz,” in *Antennas and Propagation (EuCAP), 2014 8th European Conference on*,

pp. 1053–1057, IEEE, 2014.

[5] P. Rosenkranz and D. Staelin, "Microwave emissivity of ocean foam and its effect on nadiral radiometric measurements," *Journal of Geophysical Research*, vol. 77, no. 33, pp. 6528–6538, 1972.

[6] A. Stogryn, "The emissivity of sea foam at microwave frequencies," *Journal of Geophysical Research*, vol. 77, no. 9, pp. 1658–1666, 1972.

[7] J. Droppleman, "Apparent microwave emissivity of sea foam," *Journal of Geophysical Research*, vol. 75, no. 3, pp. 696–698, 1970.

[8] T. Oguchi, "Electromagnetic wave propagation and scattering in rain and other hydrometeors," *Proceedings of the IEEE*, vol. 71, no. 9, pp. 1029–1078, 1983.

[9] I. Tardy and O. Grondalen, "On the role of future high-frequency bfwa systems in broadband communication networks," *IEEE Communications Magazine*, vol. 43, no. 2, pp. 138–144, 2005.

[10] I. V. Cherny and V. Y. Raizer, *Passive microwave remote sensing of oceans.* John Wiley & Son Ltd, 1998.

[11] L. A. Dombrovsky and D. Baillis, *Thermal radiation in disperse systems: an engineering approach.* Begell House New York, 2010.

[12] A. Ishimaru, *Wave propagation and scattering in random media*, vol. 2. Academic press New York, 1978.

[13] A. Ishimaru, “Theory and application of wave propagation and scattering in random media,” *Proceedings of the IEEE*, vol. 65, no. 7, pp. 1030–1061, 1977.

[14] V. Twersky, “Interface effects in multiple scattering by large, low-refracting, absorbing particles,” *JOSA*, vol. 60, no. 7, pp. 908–914, 1970.

[15] V. Varadan and V. Varadan, “Acoustic, electromagnetic and elastic wave scattering-focus on the t-matrix approach; proceedings of the international symposium, ohio state university, columbus, ohio, june 25-27, 1979,” in *Acoustic, Electromagnetic and Elastic Wave Scattering-Focus on the T-Matrix Approach*, vol. 1, 1980.

[16] M. I. Mishchenko, L. D. Travis, and A. A. Lacis, *Multiple scattering of light by particles: radiative transfer and coherent backscattering.* Cambridge University Press, 2006.

[17] R. Jiang, P. Xu, K.-S. Chen, S. Tjuatja, and X. Wu, “Foam-scattering effects on microwave emission from foam-covered ocean surface,” *IEEE Geoscience and Remote Sensing Letters*, vol. 15, no. 5, pp. 649–653, 2018.

[18] W. J. Plant and V. Irisov, “Breaking waves effects on scatterometer and radiometer signatures of the ocean,” in *Oceans-San Diego, 2013*, pp. 1–5, IEEE, 2013.

[19] G. T. M. A. Sayer and R. G. Grainger, “A sea surface reflectance model for (a) atsr, and application to aerosol retrievals,” *Atmos.Meas. Tech*, vol. 3, pp. 813–838, 2010.

[20] A. Kokhanovsky, “Spectral reflectance of whitecaps,” *Journal of Geophysical Research: Oceans*, vol. 109, no. C5, 2004.

[21] L. Jiang and M. Wang, “Improved near-infrared ocean reflectance correction algorithm

for satellite ocean color data processing," *Optics express*, vol. 22, no. 18, pp. 21657–21678, 2014.

[22] G. de Leeuw, E. L. Andreas, M. D. Anguelova, C. Fairall, E. R. Lewis, C. O'Dowd, M. Schulz, and S. E. Schwartz, "Production flux of sea spray aerosol," *Reviews of Geophysics*, vol. 49, no. 2, 2011.

[23] R. Wanninkhof, W. E. Asher, D. T. Ho, C. Sweeney, and W. R. McGillis, "Advances in quantifying air-sea gas exchange and environmental forcing*," *Marine Science*, vol. 1, 2009.

[24] G. B. Deane, "Sound generation and air entrainment by breaking waves in the surf zone," *The journal of the acoustical society of America*, vol. 102, no. 5, pp. 2671–2689, 1997.

[25] L. Mitnik, V. Kuleshov, M. Mitnik, M. Pichugin, G. Chernyavsky, I. Cherny, and O. Nikitin, "Geophysical model functions of ocean surface winds for the meteor-m no. 2 mtvza-gy radiometer," in *2018 IEEE 15th Specialist Meeting on Microwave Radiometry and Remote Sensing of the Environment (MicroRad)*, pp. 20–23, IEEE, 2018.

[26] M. D. Anguelova, M. H. Bettenhausen, and P. W. Gaiser, "Passive remote sensing of sea foam using physically-based models," in *International Geoscience and Remote Sensing Symposium (IGARSS), Denver, CO, USA*, pp. 3676–3679, 2006.

[27] M. Anguelova, M. Bettenhausen, W. Johnston, and P. Gaiser, "Passive remote sensing of oceanic whitecaps: Further developments," in *AGU Fall Meeting Abstracts*, vol. 1, p. 0353, 2013.

[28] X. Yin, J. Boutin, N. Martin, and P. Spurgeon, "Optimization of l-band sea surface emissivity models deduced from smos data," *Geoscience and Remote Sensing, IEEE Transactions on*, vol. 50, no. 5, pp. 1414–1426, 2012.

[29] X. Yin, J. Boutin, N. Martin, and P. Spurgeon, "On systematic biases between modeled and measured smos brightness temperature," in *Geoscience and Remote Sensing Symposium (IGARSS), 2012 IEEE International*, pp. 5756–5759, IEEE, 2012.

[30] D. Chen, L. Tsang, L. Zhou, S. C. Reising, W. E. Asher, L. A. Rose, K.-H. Ding, and C.-T. Chen, "Microwave emission and scattering of foam based on monte carlo simulations of dense media," *Geoscience and Remote Sensing, IEEE Transactions on*, vol. 41, no. 4, pp. 782–790, 2003.

[31] C. O. Ao, *Electromagnetic wave scattering by discrete random media with remote sensing applications*. PhD thesis, Massachusetts Institute of Technology, 2001.

[32] G. Heygster, V. Alexandrov, G. Dybkjær, W. von Hoyningen-Huene, F. Ardhuin, I. Katsev, A. Kokhanovsky, T. Lavergne, A. Malinka, C. Melsheimer, *et al.*, "Remote sensing of sea ice: advances during the damocles project," *Cryosphere*, vol. 6, no. 6, pp. 1411–1434, 2012.

[33] H. Booker and W. Gordon, "A theory of radio scattering in the troposphere," *Proceedings of the IRE*, vol. 38, no. 4, pp. 401–412, 1950.

[34] L. L. Foldy, "The multiple scattering of waves. i. general theory of isotropic scattering by randomly distributed scatterers," *Physical Review*, vol. 67, no. 3-4, p. 107, 1945.

[35] M. Lax, “Multiple scattering of waves. ii. the effective field in dense systems,” *Physical Review*, vol. 85, no. 4, p. 621, 1952.

[36] V. Twersky, “Low-frequency scattering by mixtures of correlated nonspherical particles,” *The Journal of the Acoustical Society of America*, vol. 84, no. 1, pp. 409–415, 1988.

[37] U. Frisch, “Wave propagation in random media, in volume i of probabilistic methods in applied mathematics, edited by at barucha-reid,” 1968.

[38] M. J. Beran and R. Mazar, “Intensity fluctuations in a quadratic channel,” *The Journal of the Acoustical Society of America*, vol. 82, no. 2, pp. 588–592, 1987.

[39] V. Tartaskii, “The effects of the turbulent atmosphere on wave propagation. 1971,” *National Technical Information Service.*

[40] C. F. Bohren and D. R. Huffman, *Absorption and scattering of light by small particles.* John Wiley & Sons, 2008.

[41] F. T. Ulaby, E. Michielssen, U. Ravaioli, W. Hayt, and J. Buck, “Fundamentals of applied electromagnetics, isbn: 978-0-13-213931-1,” *Instructor*, 2013.

[42] P. W. Barber and S. C. Hill, *Light scattering by particles: computational methods*, vol. 2. World scientific, 1990.

[43] K. Holmberg, “Surfactant-templated nanomaterials synthesis,” *Journal of colloid and interface science*, vol. 274, no. 2, pp. 355–364, 2004.

[44] J. Heard, E. Harvey, B. B. Johnson, J. D. Wells, and M. J. Angove, "The effect of filamentous bacteria on foam production and stability," *Colloids and Surfaces B: Biointerfaces*, vol. 63, no. 1, pp. 21–26, 2008.

[45] S. Levitus, R. Burgett, and T. P. Boyer, "World ocean atlas 1994. volume 3. salinity," tech. rep., National Environmental Satellite, Data, and Information Service, Washington, DC (United States), 1994.

[46] M. H. Sharqawy, J. H. Lienhard, and S. M. Zubair, "Thermophysical properties of seawater: a review of existing correlations and data," *Desalination and Water Treatment*, vol. 16, no. 1-3, pp. 354–380, 2010.

[47] M. D. Anguelova, "Complex dielectric constant of sea foam at microwave frequencies," *Journal of Geophysical Research: Oceans (1978–2012)*, vol. 113, no. C8, 2008.

[48] I. MILITSKII, V. RAIZER, E. Sharkov, and V. Etkin, "Scattering of microwave radiation by foamy structures(honeycomb and emulsion type sea surfs)," *Radio Engineering and Electronic Physics*, vol. 22, pp. 46–50, 1977.

[49] I. MILITSKII, U. RAIZER, E. Sharkov, and V. Etkin, "Thermal radio emission from foam structures(remote microwave radiometry application)," *Soviet Physics-Technical Physics*, vol. 23, p. 601, 1978.

[50] R. D. Peltzer and O. M. Griffin, "Stability of a three-dimensional foam layer in seawater," *Journal of Geophysical Research: Oceans (1978–2012)*, vol. 93, no. C9, pp. 10804–10812, 1988.

[51] L. A. Rose, W. E. Asher, S. C. Reising, P. W. Gaiser, K. M. St Germain, D. J. Dow-

giallo, K. A. Horgan, G. Farquharson, and E. Knapp, "Radiometric measurements of the microwave emissivity of foam," *Geoscience and Remote Sensing, IEEE Transactions on*, vol. 40, no. 12, pp. 2619–2625, 2002.

[52] A. Camps, M. Vall-Llossera, R. Villarino, N. Reul, B. Chapron, I. Corbella, N. Duffo, F. Torres, J. J. Miranda, R. Sabia, *et al.*, "The emissivity of foam-covered water surface at l-band: Theoretical modeling and experimental results from the frog 2003 field experiment," *Geoscience and Remote Sensing, IEEE Transactions on*, vol. 43, no. 5, pp. 925–937, 2005.

[53] V. Y. Raiter and E. Sharkov, "Electrodynamic description of densely packed dispersed systems," *Radiophysics and Quantum Electronics*, vol. 24, no. 7, pp. 553–560, 1981.

[54] J. Guo, L. Tsang, W. Asher, K.-H. Ding, and C.-T. Chen, "Applications of dense media radiative transfer theory for passive microwave remote sensing of foam covered ocean," *Geoscience and Remote Sensing, IEEE Transactions on*, vol. 39, no. 5, pp. 1019–1027, 2001.

[55] V. Raizer, "Macroscopic foam–spray models for ocean microwave radiometry," *Geoscience and Remote Sensing, IEEE Transactions on*, vol. 45, no. 10, pp. 3138–3144, 2007.

[56] G. Bordonskii, I. Vasilkova, V. Veselov, N. Vorsin, I. MILITSKII, V. Mirovskii, V. Nikitin, V. Raizer, I. Khapin, and E. Sharkov, "Spectral characteristics of the emissivity of foam formations," *Academy of Sciences, USSR, Izvestiya, Atmospheric and Oceanic Physics*, vol. 14, pp. 464–469, 1979.

[57] Y. Zhang, Y. Yang, and J. Kong, “A composite model for estimation of polarimetric thermal emission from foam-covered wind-driven ocean surface,” *Prog. Electromagn. Res*, vol. 37, pp. 143–190, 2002.

[58] L. Dombrovskiy, “Absorption and scattering of microwave radiation by spherical water shells,” *Izv. Atmos. Ocean. Phys*, vol. 17, pp. 238–241, 1982.

[59] T. C. Choy, *Effective medium theory: principles and applications.* No. 102, Oxford University Press, 1999.

[60] M. D. Anguelova and P. W. Gaiser, “Dielectric and radiative properties of sea foam at microwave frequencies: Conceptual understanding of foam emissivity,” *Remote Sensing*, vol. 4, no. 5, pp. 1162–1189, 2012.

[61] A. Morel and A. Bricaud, “Inherent optical properties of algal cells including picoplankton: theoritical and experimental results,” *Can. Bull. Fish. Aquat. Sci*, 1986.

[62] M. Lentovich and V. Fock, “Solution of propagation of electromagnetic waves along the earths surface by the method of parabolic equations,” *Journal Physics USSR*, vol. 10, pp. 13–23, 1946.

[63] G. Malyuzhinets, “Progress in understanding diffraction phenomena,” *Sov. Phys. Usp*, vol. 69, pp. 321–334, 1959.

[64] R. Hardin and F. Tappert, “Applications of the split-step fourier method to the numerical solution of nonlinear and variable coefficient wave equations,” *Siam Rev*, vol. 15, no. 1, pp. 423–429, 1973.

[65] A. Radder, “On the parabolic equation method for water-wave propagation,” *Journal of fluid mechanics*, vol. 95, no. 01, pp. 159–176, 1979.

[66] M. Levy, *Parabolic equation methods for electromagnetic wave propagation.* No. 45, IET, 2000.

[67] A. Benjamin and D. Bebbington, “Millimetre wave scattering by sea foam using split-step fourier transform,” in *Progress in Electromagnetic Research Symposium (PIERS)*, pp. 4339–4339, IEEE, 2016.

[68] A. Benjamin and D. O. Bebbington, “Millimeter-wave propagation and attenuation in closed packed sea-foam layer and complex dielectric constant of sea-foam using split-step fourier transform,” in *Progress in Electromagnetics Research Symposium-Fall (PIERS-FALL), 2017*, pp. 2556–2563, IEEE, 2017.

[69] P. Suarez, “An introduction to the split step fourier method using matlab,” 2016.

[70] S. H. Yueh, “Modeling of wind direction signals in polarimetric sea surface brightness temperatures,” *Geosciences and Remote Sensing Transactions*, vol. Volume 35, no. 6, pp. 1400–1418, 1997.

[71] P. M. Smith, “The emissivity of sea foam at 19 and 37 ghz,” *Geoscience and Remote Sensing, IEEE Transactions on*, vol. 26, no. 5, pp. 541–547, 1988.

[72] G. Williams, “Microwave emissivity measurements of bubbles and foam,” *Geoscience Electronics, IEEE Transactions on*, vol. 9, no. 4, pp. 221–224, 1971.

[73] P. C. Pandey and R. K. Kakar, "An empirical microwave emissivity model for a foam-covered sea," *Oceanic Engineering, IEEE Journal of*, vol. 7, no. 3, pp. 135–140, 1982.

[74] X.-Z. Huang and Y.-Q. Jin, "Scattering and emission from two-scale randomly rough sea surface with foam scatterers," in *Microwaves, Antennas and Propagation, IEE Proceedings*, vol. 142, pp. 109–114, IET, 1995.

[75] E. C. M. W.Asher, Q. Wang and P. Smith, "Estimation of air-gas transfer velocities from apparent microwave brigthness temperature," *Mar. Technol. Soc. J.*, vol. Vol. 32, no. No. 2, pp. 32–40, 1998.

[76] S. L. Durden and J. F. Vesecky, "A physical radar cross-section model for a wind-driven sea with swell," *Oceanic Engineering, IEEE Journal of*, vol. 10, no. 4, pp. 445–451, 1985.

[77] K.-H. Ding, L. Tsang, and Q. Li, "Computational electromagnetic scattering models for microwave remote sensing," *Encyclopedia of RF and Microwave Engineering*, 2005.

[78] A. Ishmael, "Micro-mechanical modelling of metal powder," *Masters of Science Thesis in Computing, Royal Institute of Technology, Schoool of Engineering Science.*, 2012.

[79] L. Ma, F. Wang, C. Wang, C. Wang, and J. Tan, "Investigation of the spectral reflectance and bidirectional reflectance distribution function of sea foam layer by the monte carlo method," *Applied Optics*, vol. 54, no. 33, pp. 9863–9874, 2015.

[80] N. Reul and B. Chapron, "A model of sea-foam thickness distribution for passive microwave remote sensing applications," *Journal of Geophysical Research: Oceans*, vol. 108, no. C10, 2003.

[81] E. W. Weisstein, "Circle packing," 2002.

[82] R. L. Whetten, M. N. Shafigullin, J. T. Khoury, T. G. Schaaff, I. Vezmar, M. M. Alvarez, and A. Wilkinson, "Crystal structures of molecular gold nanocrystal arrays," *Accounts of chemical research*, vol. 32, no. 5, pp. 397–406, 1999.

[83] T. C. Hales, "The sphere packing problem," *Journal of Computational and Applied Mathematics*, vol. 44, no. 1, pp. 41–76, 1992.

[84] T. C. Hales, "Historical overview of the kepler conjecture," in *The Kepler Conjecture*, pp. 65–82, Springer, 2011.

[85] S. Torquato, T. M. Truskett, and P. G. Debenedetti, "Is random close packing of spheres well defined?," *Physical review letters*, vol. 84, no. 10, p. 2064, 2000.

[86] M. N. Sadiku, *Numerical techniques in electromagnetics with MATLAB.* CRC press, 2011.

[87] D. D. W.S.Winkel, S. L. Ceccio and M.Perlin, "Bubble-size ddistribution produced by wall injection of air into flowing fresh water, saltwater and surfactant ssolution,," *Exp. Fluids*, vol. 37, pp. 802–810, 2004.

[88] G.B.Dean and M. Stokes, "Scale dependence of bubble creation mechanisms in breaking waves," *Nature*, vol. 418, pp. 839–844, 2002.

[89] L. Dombrovskiy and V. Rayzer, "Microwave model of a two-phase medium at the ocean surface," *IZVESTIIA-RUSSIAN ACADEMY OF SCIENCES ATMOSPHERIC AND*

*OCEANIC PHYSICS C/C OF IZVESTIIA-ROSSIISKAIA AKADEMIIA NAUK FIZIKA ATMOSFERY I OKEANA*, vol. 28, pp. 650–650, 1992.

[90] R. Biondini, "Cloud motion and rainfall statistics," *Journal of Applied Meteorology*, vol. 15, no. 3, pp. 205–224, 1976.

[91] E. Limpert, W. A. Stahel, and M. Abbt, "Log-normal distributions across the sciences: Keys and clues: On the charms of statistics, and how mechanical models resembling gambling machines offer a link to a handy way to characterize log-normal distributions, which can provide deeper insight into variability and probabilitynormal or log-normal: That is the question," *AIBS Bulletin*, vol. 51, no. 5, pp. 341–352, 2001.

[92] R. Romero and T. Sutton, "Sensitivity of mycosphaerella fijiensis, causal agent of black sigatoka of banana, to propiconazole," *Phytopathology*, vol. 87, no. 1, pp. 96–100, 1997.

[93] G. Sugihara, "Minimal community structure: an explanation of species abundance patterns," *The American Naturalist*, vol. 116, no. 6, pp. 770–787, 1980.

[94] E. Limpert, M. Abbt, R. Asper, W. Graber, F. Godet, W. Stahel, and E. Windhab, "Life is log normal: Keys and clues to understand patterns of multiplicative interactions from the disciplinary to the transdisciplinary level," *Transdisciplinarity: Joint Problem-Solving among Science, Technology and Society. Zurich (Switzerland): Haffmans*, pp. 20–24, 2000.

[95] M. D. Anguelova and P. W. Gaiser, "Skin depth at microwave frequencies of sea foam layers with vertical profile of void fraction," *Journal of Geophysical Research: Oceans*, vol. 116, no. C11, 2011.

[96] V. Leroy, Y. Fan, A. Strybulevych, G. Bellido, J. Page, and M. Scanlon, "Investigating the bubble size distribution in dough using ultrasound," *Bubbles in food*, vol. 2, pp. 51–60, 2008.

[97] O. Ozgun, G. Apaydin, M. Kuzuoglu, and L. Sevgi, "Petool: Matlab-based one-way and two-way split-step parabolic equation tool for radiowave propagation over variable terrain," *Computer Physics Communications*, vol. 182, no. 12, pp. 2638–2654, 2011.

[98] G. Apaydin and L. Sevgi, "The split-step-fourier and finite-element-based parabolic-equation propagation-prediction tools: Canonical tests, systematic comparisons, and calibration," *IEEE Antennas and Propagation Magazine*, vol. 52, no. 3, pp. 66–79, 2010.

[99] J. Martin and S. M. Flatté, "Intensity images and statistics from numerical simulation of wave propagation in 3-d random media," *Applied Optics*, vol. 27, no. 11, pp. 2111–2126, 1988.

[100] A. M. Al-Saegh, A. Sali, J. Mandeep, and A. Ismail, "Extracted atmospheric impairments on earth-sky signal quality in tropical regions at ku-band," *Journal of Atmospheric and Solar-Terrestrial Physics*, vol. 104, pp. 96–105, 2013.

[101] E. Salonen and S. Uppala, "New prediction method of cloud attenuation," *Electronics Letters*, vol. 27, no. 12, pp. 1106–1108, 1991.

[102] I. Itu, "Attenuation due to clouds and fog," *International Telecommunication Union-Recommendation*, p. 840, 2012.

[103] A. Dissanayake, J. Allnutt, and F. Haidara, "Cloud attenuation modelling for shf and

ehf applications," *International journal of satellite communications*, vol. 19, no. 3, pp. 335–345, 2001.

[104] E. E. Altshuler and R. A. Marr, "Cloud attenuation at millimeter wavelengths," *IEEE Transactions on antennas and propagation*, vol. 37, no. 11, pp. 1473–1479, 1989.

# Appendices

# APPENDIX A

# DERIVATIONS

## A.1 Wide angle Split-step Algorithm

Li Dexin et.al implemented the forward -backward mixed Discrete Fourier transform which uses the first order forward-backward difference formula to substitute for the conventional second order central-difference formula to fill the impedance boundary condition. The idea solves the unstable problems and makes the method more robust and efficient.

We shall confirm the correctness and applicability of this improved method by verifying the simulated results with the conventional method in different boundary conditions and real terrain.

Let us consider a Cartesian coordinate system (x,y,z) with EM incident field propagating in +x paraxial the direction, z is the vertical height and x is the range. From two dimensional (2D) scalar wave equation and using the Feit-Fleck PE approximaion, we obtain the Feit-Fleck PE equation in the 2D range-height field as follows:

The Fiet and Fleck approximation yields

$$Q \sim \sqrt{1+A} + \sqrt{1+B} - 1 \tag{A.1}$$

Equation A.1 is exact in vacuum. For a case of homogeneous medium where $n = 1 + \delta n$. The pseudo-differential operator $Q$ in section 3.2, equations (3.15-3.18) can be expressed as

$$Q = \sqrt{1+A+B} = \sqrt{1+A} + \sqrt{1+B} - 1 \tag{A.2}$$

$$Q = 1 + \delta n + \sqrt{1 + \frac{1}{k^2}\frac{\partial^2}{\partial z^2}} - 1 \tag{A.3}$$

substituting the expression of Q in A.3 into the above expression for forward travelling wave

$$\frac{\partial u}{\partial x} = -ik(1-Q)u \tag{A.4}$$

gives

$$\frac{\partial u}{\partial x} = -ik(1 - (1 + \delta n + \sqrt{1 + \frac{1}{k^2}\frac{\partial^2}{\partial z^2}} - 1))u \tag{A.5}$$

substitute $\delta n = n - 1$ into $A.5$

$$\frac{\partial u}{\partial x} = -ik(1 - (1 + (n-1) + \sqrt{1 + \frac{1}{k^2}\frac{\partial^2}{\partial z^2}} - 1))u \tag{A.6}$$

This is further expanded to obtain

$$\frac{\partial u}{\partial x} = -ik(-(n-1) - \sqrt{1 + \frac{1}{k^2}\frac{\partial^2}{\partial z^2}} - 1))u \tag{A.7}$$

$$\frac{\partial u}{\partial x} = ik(n-1) + ik(\sqrt{1 + \frac{1}{k^2}\frac{\partial^2}{\partial z^2}} - 1)u \tag{A.8}$$

The split-step solution is obtained by solving successively for the refractive and diffractive terms . Using the simplest split, the formal solution is given as

$$\frac{\partial u(x,z)}{\partial x} = ik(\sqrt{1 + \frac{1}{k^2}\frac{\partial^2}{\partial z^2}} - 1)u(x,z) + ik(m-1)u(x,z) \tag{A.9}$$

The scalar $u(x,z)$ is the electromagnetic field at random locations, $k = \frac{2\pi}{\lambda}$ is the wavenumber in vacuum and $\lambda$ is the free-space wavelength, $m = n + \frac{z}{a_e}$ is the modified atmospheric refractive index, $n$ is the refractive index and $a_e$ equivalent earth radius. Theb formal solution by the SSFT method becomes:

$$u(x,z) = e^{ik(n-2+\frac{z}{a_e})\Delta x} F^{-1}(e^{i\Delta x\sqrt{k^2-p^2}} F[u(x_0,z)]) \qquad \text{(A.10)}$$

In this equation, the definition $M = exp(i\Delta x\sqrt{k^2-p^2})$ reflects the diffraction effect of obstacles in the path, $N = exp(ik(n-2+\frac{z}{a_e}))$ reflects the refraction effect of the media. $F$ and $F^{-1}$ indicate the Fourier transformation and inverse Fourier transformation.

# APPENDIX B

# PUBLICATIONS

## B.1 List OF Publications

The papers listed below have been presented and published in conference proceedings.

A. K. Benjamin and D. H .O. Bebbington. Millimetre wave scattering by sea foam using split-step Fourier transform. *In Progress in Electromagnetic Research Symposium PIERS*, pp. 4339-4339, IEEE, 2016.

A. K. Benjamin and D. H. O. Bebbington. Millimetre wave propagation and attenuation in closed packed sea-foam and complex dielectric constant of sea-foam using split-step Fourier transform. *In Progress in Electromagnetic Research Symposium-Fall PIERS-FALL*, 2017, pp. 2556-2563, IEEE, 2017.

A. K. Benjamin and D. H. O. Bebbington. Discrete method for computation of scattering by sea foam layer modelled as sequences of thin phase screens. Accepted for publication by Journal of Nanoelectronics and Optoelectronics.